EXAMINING THE MECHANISMS AND KINETICS OF TRANSIENT LIQUID PHASE BONDING OF TITANIUM ALLOYS USING COPPER AND NICKEL FILLER METALS

By

Colin Andrew Tadgell

Submitted in partial fulfilment of the requirements

for the degree of Doctor of Philosophy

at

Dalhousie University

Halifax, Nova Scotia

October 2019

Table of Contents

List of Tables

List of Figures

Abstract

Copper and nickel were examined as potential interlayers in transient liquid phase brazing (TLPB) of commercially pure titanium (CP-Ti) and Ti-6Al-4V. Experimental parameters were set such that the braze temperature was above intermetallic formation (1050°C) and was examined for all systems for the purpose of consistency. In addition, a foil width of 50 μm and a heating and cooling rate of 20 Kpm was used throughout experimentation. Using high temperature thermal analysis techniques (DSC, DIL), as well as microstructural observations (SEM, Optical Microscopy), the efficacy of these interlayers was monitored for levels and mechanisms of dissolution, rates of isothermal solidification, and the time to homogenization.

Dissolution in both titanium systems requires the development and evolution of a diffusion couple between Ti-Cu and Ti-Ni as dictated by the binary phase diagram. This involves the growth of intermetallic compound (IMC) layers and progresses with incipient melting at the lowest melting intermetallic. In copper systems this is found on the Cu-rich side whereas in the nickel systems it occurs on the Ti-rich side. For copper systems this led to a preferential dissolution of copper foil with minimal solute uptake. In nickel systems the IMC layer is slowly consumed by the liquid which delays homogenization. Overall gap widening is largest in Ni systems since the solubility of titanium in the liquid phase is higher, but this was found to be mitigated by a higher Ni solute uptake when compared to copper. These trends were also observed in Ti-6Al-4V samples.

Isothermal solidification studies showed that the rate of isothermal solidification is faster in nickel than in copper and faster in CP-Ti in comparison to Ti-6Al-4V. These trends can be explained by the apparent diffusivity of solute in these systems which was calculated. The higher rate of isothermal solidification led to shorter isothermal solidification times compared to copper-based joints. DSC analysis was able to produce $2W_{ISZ}$ curves with the capability of predicting complete isothermal solidification time for any starting gap, or foil, size. In addition, the time to homogenization can be calculated directly from these curves.

List of Abbreviations and Symbols Used

TLPB	Transient Liquid Phase Brazing
CP-Ti	Commercially Pure Titanium
Ti64	Ti-6Al-4V Titanium Alloy
γ	Surface Energy
P	Pressure
ρ	Density (g/cm^3)
T	Temperature (°C)
k	Partition Coefficient
J	Flux
D	Diffusion Coefficient (cm^2/s)
C, X	Composition (wt%)
ASZ	Athermally Solidified Zone
ISZ	Isothermally Solidified Zone
DAZ	Diffusionally Affected Zone
W	Width of Joint Microstructure (ASZ, ISZ, Foil) (µm)
W_{ASZ}	Width of the ASZ
W_{ISZ}	Width of the ISZ
W_{max}	Maximum Width of ASZ during Dissolution (µm)
W_o	Initial Foil Thickness (µm)
DSC	Differential Scanning Calorimetry
Q	Activation Energy (kJ/mol)
α-Ti	HCP (Hexagonally Close Packed) Structure of Titanium

β-Ti	BCC (Body Centered Cubic) Structure of Titanium
DIL	Dilatometer
L_f	Liquid Fraction Remaining
ΔH_m	Measured Enthalpy in DSC
$\Delta H_{theo.}$	Theoretical Enthalpy of Melting of ASZ
K	Kelvin
Kpm	Heating/Cooling Rate (Kelvin per minute)
EDS	Energy Dispersive X-Ray Spectrometry
h	Height of a Spherical Cap
D	Diameter of a Spherical Cap
V	Volume
BM	Base Metal
A	Cross-Sectional Area
MBC	Maximum Brazing Clearance (synonymous with $2W_{ISZ}$)
HV	Vickers Hardness
J/g	Joules per gram
D_e	Effective Diffusivity
LD	Liquid Duration
LR	Linear Regression
IMC	Intermetallic Compound

Acknowledgments

First and foremost, I would like to acknowledge my supervisor and mentor Dr. Stephen Corbin whose continued support, patience, and expertise guided me through the past five years. His passion for metallurgy and love for experimentation have only intensified my own appreciation for materials science. I would like to thank my supervisory committee, Dr. Zoheir Farhat and Dr. Ted Monchesky, for your continued assistance and insight throughout my time at Dalhousie. I would also like to thank Dr. Darrel Doman, Dr. Kevin Plucknett, Dr. Paul Bishop, and Kate Hide who assisted and advised me through both my academic and teaching pursuits at Dalhousie.

I would like to acknowledge the financial support that I have received through the NSERC discovery grant. I could not have finished my degree without this assistance.

I have been fortunate to meet many talented and wonderful people during my time at Dalhousie whom I am happy to call colleagues. The members of HTTAL have been such a tremendous group for help, support, and conversation; Clark Murray, Julian O' Flynn, Dan Cluff, Addison Rayner, Eric Moreau, Clare McIssac, and Joel Chapman. In addition, I would like to thank Greg Sweet, Mark Amegadzie, Marciel Gaier, Zhila Rashidi, Randy Cooke, and Patricia Scallion for your assistance and company over the years.

Finally, I would like to thank my friends, family, and my loving wife Jen whose continued compassion and grace have helped me through the darkest chapters of this journey. My caring parents, Brenda and Scott, and my siblings, Anne and Eric who I've counted on for love and support. My close friends Harrison Glachan, Jason Stewart, Nathan Biedermann, and Cameron Derry for always being there. None of it would be possible without you and many others.

1.0 Introduction

Incorporation of titanium, and titanium alloys is an established method of reducing the weight of launch vehicles and aircraft structures. This is achieved by the fixturing of titanium to titanium, or titanium to dissimilar metals such as stainless steel. Currently, over 100 brazing filler metals exist to facilitate the joining of titanium in the aerospace industry with the goal of improving strength and corrosion resistance at the joints of these fixtured materials [1]. Titanium possesses an excellent strength to weight ratio, corrosion resistance and thermal stability at high temperatures, see Table 1.1. These properties give titanium a competitive edge in lowering the overall structural weight of many commercial and military airframes whilst effectively protecting itself from weathering elements [2][3].

Table 1.1 - Comparing Materials Properties of Pure Titanium and Other Common Structural Pure Metals [3]

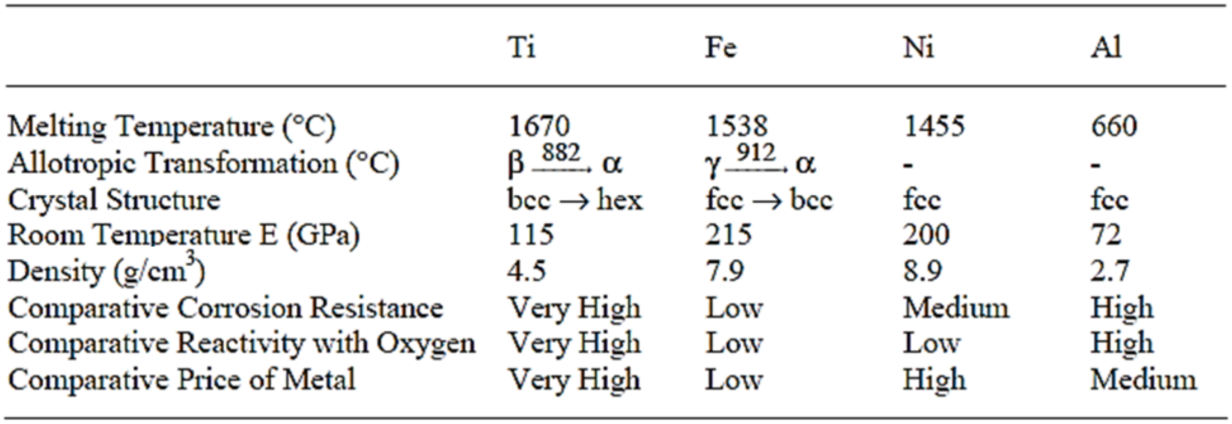

	Ti	Fe	Ni	Al
Melting Temperature (°C)	1670	1538	1455	660
Allotropic Transformation (°C)	$\beta \xrightarrow{882} \alpha$	$\gamma \xrightarrow{912} \alpha$	-	-
Crystal Structure	bcc → hex	fcc → bcc	fcc	fcc
Room Temperature E (GPa)	115	215	200	72
Density (g/cm^3)	4.5	7.9	8.9	2.7
Comparative Corrosion Resistance	Very High	Low	Medium	High
Comparative Reactivity with Oxygen	Very High	Low	Low	High
Comparative Price of Metal	Very High	Low	High	Medium

1.1 Titanium Industry and Applications

Large scale production and fabrication of titanium began in the late 1940's and early 1950's. Due to the properties described above, titanium is sought after in areas where a strong, lightweight, corrosion resistant material can be used in high, or low, temperature applications. A large sector for the consumption of titanium lies in aerospace technologies. In the U.S. alone, 70-80% of all titanium requests are for aerospace with the remainder being in industrial applications [4].

Table 1.2 outlines common components which are made of titanium, or titanium alloy, in aerospace and automotive. The primary reasons for titanium use in these fields are weight reduction (as a replacement for steels), space limitation (high strength needed in small area, replaces aluminum alloys), operating temperatures, and corrosion resistance. Over 80% of the titanium market is centered on commercially pure titanium and the α+β alloy Ti-6Al-4V [3].

Table 1.2 - Applications of Titanium Alloys in the Aerospace and Automotive Industries [4]

Systems and parts	Aerospace Materials
Airframe structures	
Hydraulic tubing	Ti-3Al-2.5V
Floors	CP-Ti
Landing gear	Ti-10V-2Fe-3Al; Ti-6-6-2
Windows frames	Ti-6Al-4V
Springs	Ti-15V-3Cr-3Sn-3Al
Gas turbine engines	
Fan discs and blades	Ti-6Al-4V; Ti-6-2-4-2S
Compressor disc	Ti-6Al-4V; Ti-6-2-4-2S
Compressor blades	Ti-6Al-4V; Ti-6-2-4-2S
Compressor stators	Ti-35V-15Cr
Nozzle assembly	TIMETAL 21S

Systems and parts	Automotive Materials
Frame structures	
Suspension springs	Ti-6.8Mo-4.5Fe-1.5Al; Ti-6Al-4V
Armor	Ti-6Al-4V
Body	CP-Ti (Grade 4); Ti-6Al-4V
Engines	
Outlet valves	γ(TiAl); Grade 2; Ti-6Al-4V; Ti-6Al-2Sn-4Zr-2Mo-0.1Si
Intake valves	Ti-6Al-4V
Turbocharger rotors	γ(TiAl)
Connecting rods	Ti-6Al-4V
Exhaust system	Grade 2

Commercially pure titanium (or CP-Ti) is used in annealed conditions for the floor support structure in the galley and lavatory areas to replace aluminum alloys due to space limitations. It is also used in the tubes and pipes of the lavatory systems, clips and brackets, ducting for anti-icing, and environmental control systems operating at temperatures of 230°C (above aluminum alloy operating temperatures) [4].

The Ti-6Al-4V alloy is the most prominent titanium structural alloy and can be found in gas turbine engines (typically in cooler sections) as static or rotating components. In terms of aircraft, Ti-6Al-4V can be found in all sections, but is used largely in the fuselage, nacelles, landing gear, wings, empennage, as well as the floor support structure (galleys and lavatories). This particular alloy is also used in high end performance cars in a large number of areas [3][4].

The usage of titanium in automotive is relatively low compared to aerospace with the major limitation being overall material and production costs. Peters *et al.* noted the expectation within European automakers that the cost of saving one kilogram of weight should not exceed 10€ whereas aerospace companies were willing to pay as high as 10,000€ to achieve the same results. There is a higher payoff to weight reduction in aerospace due to the fact that one third of take-off weight for aircraft is held in fuel. Added savings can be achieved from reducing weight on other components (landing gear, wings, support structure) due to a lighter plane [5].

This is further exacerbated in automotive due to titanium possessing a lower young's modulus and therefore a lower stiffness. Titanium is therefore limited to areas such as the overall frame and powertrain. Additionally, Ti-6Al-4V and Grade 4 titanium have been shown to be useful in crash elements where energy absorption during deformation is needed [6].

1.2 Motivation

As discussed, one of the prime limiting factors from titanium use in automotive and more importantly aerospace applications lies in the overall cost to construct complex components. A term often used in aerospace which helps illustrate this issue is called the buy-to-fly ratio. This ratio is the amount of material in kilograms used in fabricating a component versus the amount in kilograms remaining in the completed part. As of 2013, Titanium aerospace components required 8:1 buy to fly ratios on engine components and as high as 6:1 for new jets such as the Boeing 787 [7].

One large reason for these high ratios is due to overall problems of machining and joining titanium. Typical practice in titanium component manufacture involves casting or forging large scale parts which are machined into the final product. It is not uncommon for the final product of a complex forged component to have less than 10% of the initial weight following machining [7]. Titanium itself poses considerable problems due to its poor machinability [3].

If smaller scale components could be brazed into large scale products considerable savings could be achieved in machining alone. This is the motivation for the improving the titanium brazing process which is currently not a primary method of manufacture. Welding is not uncommon to see in fabrication, but transient liquid phase brazing (TLPB) of titanium has yet to be proven efficient despite the large number of braze fillers available. Therefore, the focus of this work revolves around detailed examination of the mechanisms and kinetics of TLPB of titanium and titanium alloys (namely grade two and grade five titanium). In addition, this study examines the fundamentals of TLPB over all stages of interaction with the braze foil; heating, dissolution, isothermal solidification, and homogenization. Several models and process maps were developed in this work to describe TLPB of, not just titanium, but any binary system. Examination of quaternary systems showed good agreement with these models.

1.3 Objectives

1. Fundamental investigation of TLPB in binary systems to better understand this process and its individual stages (dissolution, isothermal solidification, homogenization). This includes preparing a process map for the extent of dissolution/gap widening, solute uptake, remaining liquid at a given time during the brazing process.
2. Implementation and continuation of examination of TLPB using Differential Scanning Calorimetry (DSC) to model isothermal solidification at a given braze temperature.
3. To relate these results back to industrial processing through examination of capillary and sandwich assemblies and to use these experiments as a validation for the previous two objectives.
4. To effectively braze grade two (commercially pure (CP) titanium) and grade five (Ti-6Al-4V) titanium assemblies by transient liquid phase bonding using copper and nickel such that deleterious intermetallic phases are subverted by depletion of the filler material into the base metal.

2.0 Background

2.1 Brazing Process

Brazing is a process where a filler metal is heated above its melting temperature and allowed to solidify into a joint between other metals. It is predominantly controlled through the use of alloying and diffusion. It differs from soldering by the higher melting temperatures (above 450°C) of the filler metal. Often in brazing, a flux is used to help remove the surface oxide from the parent materials and ensure a strong metallurgical bond is formed between the parent material and braze material. The filler metal is heated above its melting temperature whilst in a protective environment (typically through use of a flux or controlled atmosphere) to provide the best conditions for brazing [8].

Key parameters in the brazing process involve surface energy and tension. These properties can be illustrated in the sessile drop experiment (shown in Figure 2.1) where knowledge of the surface energy of the liquid in atmosphere (γ_{LV}) and the surface of the metal to the atmosphere (γ_{SV}) can be used to find the relative surface energy between the liquid and solid (γ_{SL}) using Young's equation:

$$\boldsymbol{\gamma_{SV} = \gamma_{SL} + \gamma_{LV} cos\theta} \qquad \textbf{(2.1)}$$

There is a balance of these three energies creating an overall tension at the triple point which seeks to minimize its free energy. The contact angle of the droplet on the surface indicates the wettability of the liquid, where θ<90° indicates wetting of the liquid on the surface. Wetting can be improved by decreasing θ through proper selection and alloying of the filler metal and solid, removal of metal oxides, dust and water from the surface, and control of pressure and temperature in the process [8].

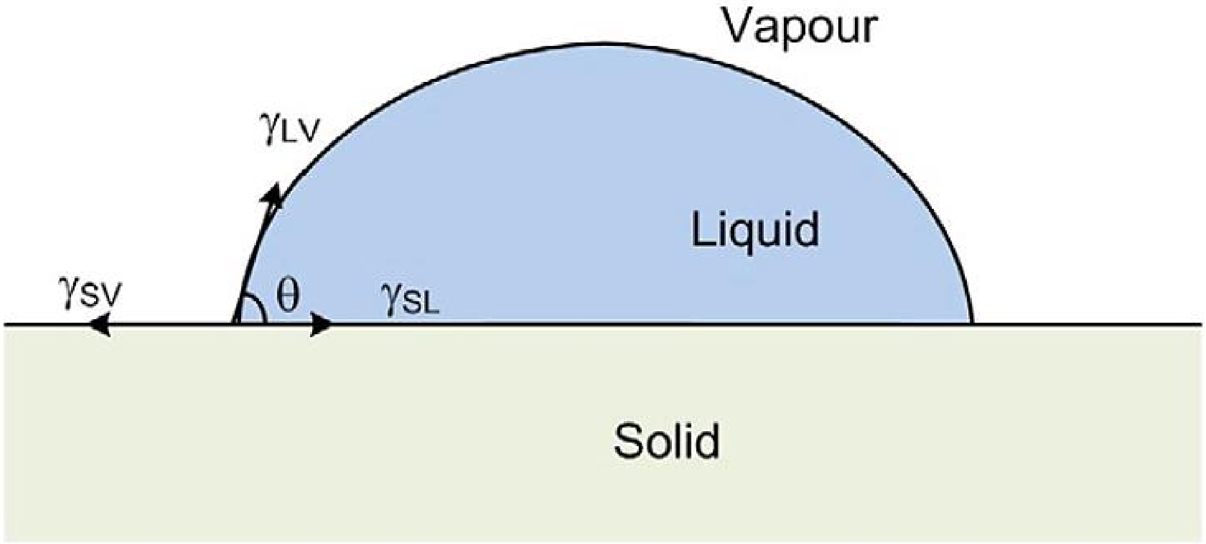

Figure 2.1 - Deriving Young's Equation from the Sessile Drop Method [9]

An important effect in braze joint formation is capillary action in pulling molten clad into the joint cavity. This helps ensure that no voids, or gaps, are present and that the joints remain liquid/gas tight while under heavy pressures. This drawing action phenomenon is the result of two combative forces; the adhesive forces of molten clad to the surface of the joint and the cohesive forces felt within the clad itself. A common expression for capillary action is Jurin's law for liquid drawn or pulled (Δh) from a vertical capillary tube:

$$\Delta h = \frac{2\gamma_{LV}\cos\theta}{\rho g r} \quad \textbf{(2.2)}$$

Where θ is the contact angle, ρ is the density of the liquid, g is acceleration due to gravity, and r is the radius of the tube [10] . Note the associated terms from Young's equation (see Equation 2.1). This will be discussed further in the next section.

Common factors affecting capillary forces are the mutual surface tensions of the base metal, molten clad, flux, and the present atmosphere, in addition there are other dynamic considerations such as viscosity, vapor pressure, and metallurgical reactions between the base/filler metal [11][12].

2.2 Brazing Configuration

Depending on the application, brazing assemblies can make use of either a sandwich assembly or by using capillary action to draw filler into the joint, shown in Figure 2.2. In a sandwich assembly the filler material, or braze, is placed between the two parts to be joined (Figure 2.2a). For capillary action the braze is applied at, or near, the joint entrance and when molten will infiltrate the joint gap (Figure 2.2b). The materials to be joined can be dissimilar, or similar in either case [13].

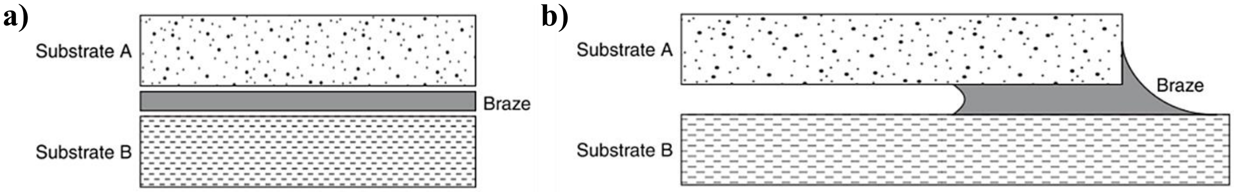

Figure 2.2 - Schematic of Brazing Assemblies (a) Sandwich Assembly; (b) Capillary Action Assembly [13]

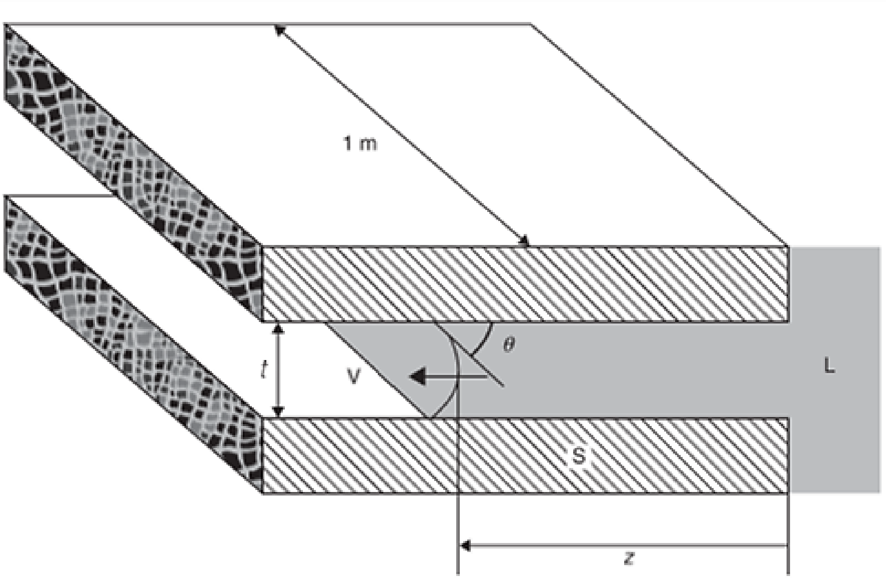

Figure 2.3 - Modelling Capillary Flow into a Horizontal Joint Gap [13]

In capillary action we have a mechanism similar to Jurin’s law mentioned above drawing in the molten filler metal. The variation of the surface energy can be expressed by the free energy difference at the opening of the joint to some distance z further in. Figure 2.3 outlines this state showing two parallel plates of the same material drawing in a molten filler liquid (L). The filler is exposed to vapor (V) inside the joint and in contact with the solid plate surface (S) as it is drawn further in making a contact angle which follows Youngs equation [13].

From the joint opening to some distance z, the variation in surface energy per unit length can be derived from Youngs equation as $2z(\gamma_{SL} - \gamma_{SV})$. This term is then further expanded to $-2z(\gamma_{LV})\cos\theta$. If the assembly was rearranged to a vertical position with the positive z-axis pointing upward, then the work necessary for the molten filler to overcome gravity is $zt\rho g(z/2)$. Putting these two terms together yields:

$$\Delta \boldsymbol{G} = \boldsymbol{G}(\boldsymbol{z}) - \boldsymbol{G}(\boldsymbol{z} = \boldsymbol{0}) \tag{2.3}$$

$$\Delta G = -2z\gamma_{LV}cos\theta + zt\rho g\frac{z}{2} \quad (2.4)$$

Where ΔG is the total free energy, t is the joint gap thickness and ρ is the density of the liquid. This relation then can be minimized by setting the derivative with respect to z of Equation 2.4 to zero:

$$\frac{d\Delta G}{dz} = -2\gamma_{LV}cos\theta + t\rho gz = 0 \quad (2.5)$$

$$P_c = \rho gz = \frac{2\gamma_{LV}cos\theta}{t} \quad (2.6)$$

The hydrostatic pressure (ρgz) is represented as Pc and the resultant equation 2.6 represents the pressure variation across the filler from the joint opening to its current location. If we use some values for copper ($\gamma_{LV} \approx 1.35$ J/m^2, $\rho = 8020$ kg/m^3, and a joint thickness of 50 μm) we find that the equivalent value for z of 0.485 m. Actual values of z for real brazing applications will be much lower than this value and therefore the effects of gravity can be ignored compared with capillary forces. Therefore, the total pressure applied to the molten filler metal is nearly equal to the capillary pressure and is mainly dictated by the wetting properties of the liquid and the joint gap thickness [13].

Another equation worth noting when discussing capillary action of a braze material is Washburn's infiltration law. This relation equates the distance travelled by the filler metal and the time taken to reach that far in a horizontal assembly:

$$z^2 = x\frac{\gamma_{LV}cos\theta}{3\eta}t \quad (2.7)$$

Where x is now the joint gap thickness as t now represents time and η is the dynamic viscosity of the liquid. This is a parabolic relation where a large intake of filler material would occur in a short period of time which would then begin to taper over time. Increased intake is favored by a molten metal with a low viscosity, high surface energy of the liquid, and an overall low viscosity [13].

When discussing sandwich assemblies, the contact angle of the filler and the base metal dictate the resultant braze quality. Figure 2.4 illustrates the different macrostructures expected when the contact angle is much greater than 90° to when it is lower than 45°. These results are expected with both similar and dissimilar materials provided there is not a large difference in the overall contact angle of the filler with material A or B. Figure 2.4 a-b shows the resultant macrostructure for when the contact angle is above 90° where contact with the solid is difficult, especially for situations where $\theta >> 90°$. Despite better contact of the solid/liquid interface, a tendency to dewetting exists such that porosities and bubbles occur either during melting, liquid flow, or solidification [13].

For contact angles below 90°, there is intimate contact between the braze and the base metal (Figure 2.4 c-d). The importance of the wetting angle now lies in determining the flow of the liquid outside of the braze gap. This is determined by a pressure threshold between the capillary pressure and the external pressure which will be discussed shortly.

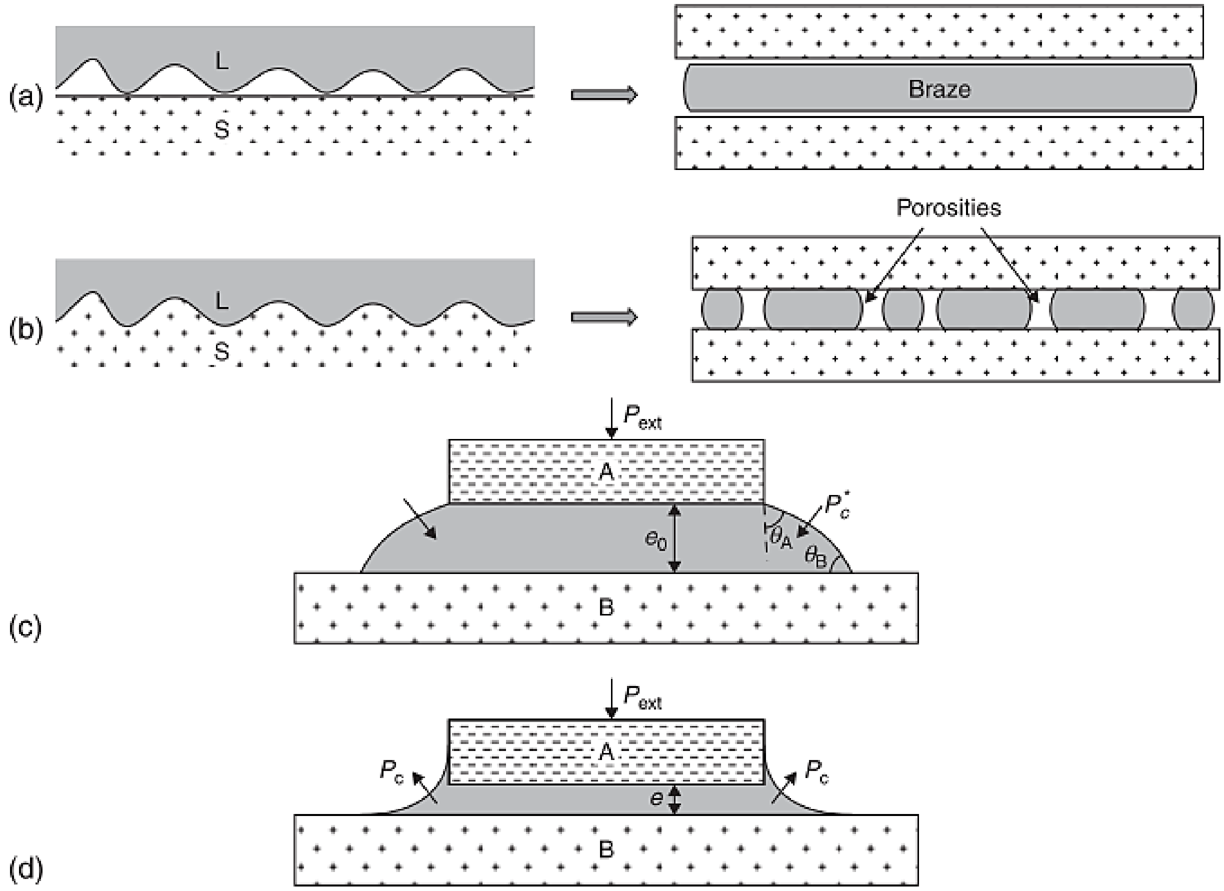

Figure 2.4 - Sandwich Assembly Brazing where the Contact Angle (θ) is Found to be (a) θ >> 90°; (b) θ >90° and Dewetting or Porosity is Observed. This also Applies When Considering Fillets where the Contact Angle is (c) 45°> θ >90° and (d) θ <45° [13]

Table 2.1 outlines the differences across contact angles with the resultant braze in a sandwich assembly. For all contact angles below 90°, bonding is intimate along the base metal surface aside from issues discussed above such as clean mating surfaces appropriate pressure and temperature. Contact angles above 90° lead to imperfect joining along the surfaces creating porosities and leading to joint failure on cooling or during operation.

Table 2.1 – Expected Microstructural Results for Varied Contact Angles in Figure 2.4 [13]

Contact Angle	Macrostructure
Θ>>90°	Contacts solid at limited points, small stresses on cooling could detach.
Θ>90°	Contact intimate at any point on interface. Tendency to detach creating porosities/bubbles along the joint detrimental to mech. performance.
90°>Θ>45°	Intimate joining. If $P_{ext}<P_c^*$ then molten filler will stay within the joint.
Θ<45°	Intimate joining. P_c^* is negative and pulls joint in. Lowers joint thickness.

For contact angles below 90°, liquid will only leave the joint gap when a pressure threshold P_c^* is lower than the external pressure felt by the molten filler, P_{ext}. This pressure threshold is found using the following equation:

$$P_c^* = \frac{\gamma_{LV}(\sin\theta_A - \cos\theta_B)}{t_o} = \frac{\gamma_{LV}(\sin\theta - \cos\theta)}{t_o} \tag{2.8}$$

Where the first set of terms refers to the contact angles of two dissimilar materials A and B and the second set simplifies with two similar materials to be joined. The initial thickness of the joint gap is referred to as t_o. The external pressure, P_{ext}, is due to the weight of the upper joining plate experienced by the liquid, ρgh. Here ρ is the density of the solid upper plate and h represents the thickness of the plate [13].

As a quick example, assume an assembly of two titanium plates with a piece of copper foil sandwiched between them. Since the plates are similar, it is not necessary to find two distinct contact angles between the upper and lower plate. To simplify things further assume that the contact angle is 90° such that P_c^* simplifies to γ_{LV}/ t_o. From Amin *et al.* the average surface energy of the liquid is 1.35 J/m^2 and, with a joint gap of 50 μm, P_c^* resolves to 27 kPa [13][14]. The upper plate of titanium has a density of 4506 kg/m^3 and a thickness of 1.5 mm such that P_{ext} becomes 66.3 Pa. Since $P_{ext} < P_c*$, liquid will not leave the joint gap of the sandwich braze. These parameters are close to actual experimental values discussed later during actual sandwich brazing of titanium and copper.

2.3 Titanium Braze Fillers

As stated in the opening of this thesis, titanium brazing has been in development since the early 1950's with over 100 brazing filler metals developed and tested. Despite this surplus of braze materials, very little brazing is currently observed when examining scientific literature of the joining of titanium. Partly this is due to a lack of flexibility in braze temperature as very few can operate below 800°C to avoid the beta transus for α and near α alloys. Another issue that persists in titanium brazing is avoiding the formation of brittle intermetallics [1].

All known titanium brazing fillers can be classed into five categories based on the base metal of each alloy: silver, titanium, aluminum, palladium, and zirconium-based alloys. These alloys dictate the temperature and time limits of braze operations and each have known issues in generating intermetallic layers. There is an added difficulty in that the higher the braze temperature is raised, the thicker the intermetallic compound (IMC) layer. These intermetallic layers become the source of microcracks which develop during mechanical testing. However, it has been shown that a higher brazing temperature of 950-1000°C can lead to an increase in the static strength of braze joints at room temperature [15][16].

Table 2.2 outlines some common brazes across the five categories that are used currently. Silver based alloys have been in circulation since the beginning of titanium brazing due to their accessibility and well understood behavior. Titanium braze joints heated to 1100°C show high tensile strengths (150 MPa) and good ductility due to the relatively ductile nature of TiAg intermetallics. Low melting filler metals such as BAg-8 have a eutectic temperature of 780°C [1][15][16].

Table 2.2 - Existing Filler Metals for Brazing of Titanium and Titanium Alloys [1]

Brazing Filler Metal		**Titanium Base Metal**	**Brazing Temp. (°C)**	**Holding Time (min.)**	**Shear Strength (MPa)**
Tradename	**Composition**				
Silver	Fine Ag	CP-Ti	970	30	104
Bag-8	Ag-28Cu	Ti-6Al-4V	800	20	142
Gapasil-9	Ag-9Pd-9Ga	Ti-6Al-4V	890	1	166-193
TiCuNi	Ti-15Cu-15Ni	Ti-6Al-4V	950	5	Not Provided
AA3003	Al-1.2Mn-0.6Si-0.7Fe-0.2Cu	Ti-6Al-4V	680	3	65
BAlSi-4	Al-10Si-1Mg	CP-Ti	620	25	84
Stemet® 1406	Zr-11Ti-14Ni-13Cu	CP-Ti	900	15	236
BTi43ZrNiBe	Zr-43Ti-12Ni-2Be	Ti-6Al-4V	900	10	152

Aluminum alloys show promise due to their low melting points and densities coupled with excellent wetting of titanium surfaces in vacuum and under flux. However, they possess very low strength compared to any of the other braze base metals. They also suffer from insufficient corrosion resistance and a strong tendency to form brittle intermetallics [1].

Filler metals such as palladium and zirconium see limited use due to their increased cost. More recently amorphous foils of zirconium alloys have seen more increased use as they provide much higher strengths compared to silver and aluminum. Typically, these alloys must be heated well above their liquidus temperatures to achieve quality brazes (800-900°C) [1].

Worth noting is the use of copper and nickel in the braze filler Ti-15Cu-15Ni which shows great compatibility with titanium and is brazed at 950°C to create higher static strength in brazing of Ti-6Al-4V [1]. It should be noted that none of the above filler metals or studies have been used in TLPB or diffusion brazing applications, with the exception of Wells *et al.* [16]. These two elements will be discussed further in the braze filler selection section following a discussion of transient liquid phase brazing.

2.4 Transient Liquid Phase Bonding

Transient Liquid Phase Bonding (TLPB) is a joining process, which improves upon traditional brazing, where an interlayer is heated and held at the braze temperature until it has undergone isothermal solidification (IS). This is achieved by a process where the formed liquid is slowly reduced in volume fraction by diffusion of some of the interlayer elements into the base metal. Advantages for this method include forming a joint that has a higher melting point than the braze temperature, less concern for surface oxide layers and joint preparation, little melting of the substrate (as opposed to processes such as welding), and improved microstructural/mechanical properties.

Figure 2.5 outlines all the steps of the TLPB process including a later option to homogenize the joint if desired. Initially, the assembly is heated to a temperature which is usually above the interlayers melting point to achieve complete melting and higher rates of diffusion. Following melting, the liquid layer undergoes a stage known as dissolution which will be discussed in more detail later. Heavy dissolution can lead to large expansions in the liquid layer, in some systems as much as 5-15 times the original thickness [18]. In order to minimize this effect, the interlayer should be thin and of eutectic composition which has the added benefit of lowering the time to isothermal solidify.

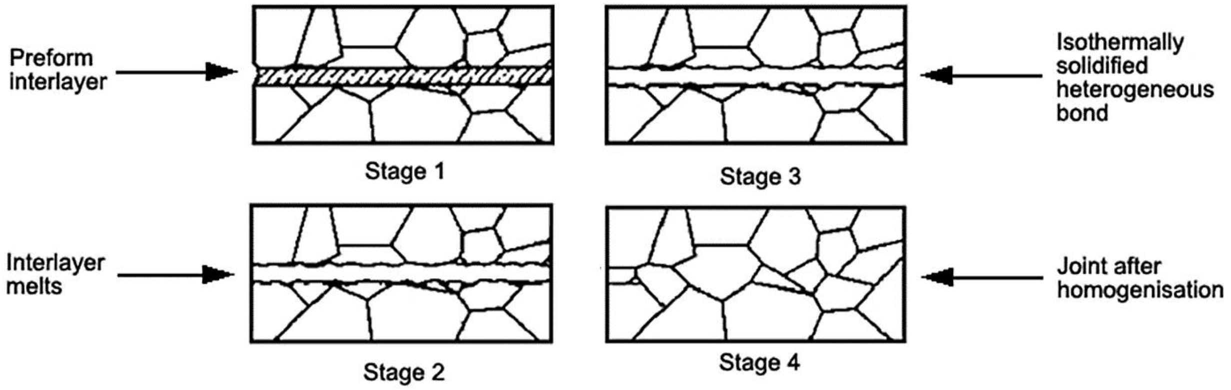

Figure 2.5 - Four Basic Stages of Transient Liquid Phase Brazing including Dissolution, Isothermal Solidification, and Homogenization [17]

After the liquid layer reaches a maximum width, the interlayer elements diffuse out into the base metal with a diffusivity somewhere between the liquid and the solid diffusivities. Diffusion continues isothermally at the braze temperature and the liquid layer reaches equilibrium with the adjacent solid. This is referred to as liquid homogenization As equilibrium is established, a mass balance occurs across the interface which favors the solid growing into the liquid. The result is a movement in the solid/liquid interface towards the joint centerline as more and more liquid solidifies. Eventually, the entire liquid layer solidifies, at the braze temperature, as shown in stage three [19].

There is an optional step following isothermal solidification where the joint can be further homogenized to the base metal composition. This is especially important in systems with highly sensitive microstructures. The homogenization temperature can be at the braze temperature or lower depending on whether brittle intermetallic formation is anticipated. An adequate homogenization temperature is often dictated by later measured bond strength or by economic considerations (energy costs etc.) [18].

This process is better illustrated by Cook *et al.* using composition profiles as the interlayer is heated and later homogenized, see Figure 2.6. These are labelled composition profiles one through five (CP1-CP5). At room temperature, the compositional profile (CP1) is flat with the base metal at a

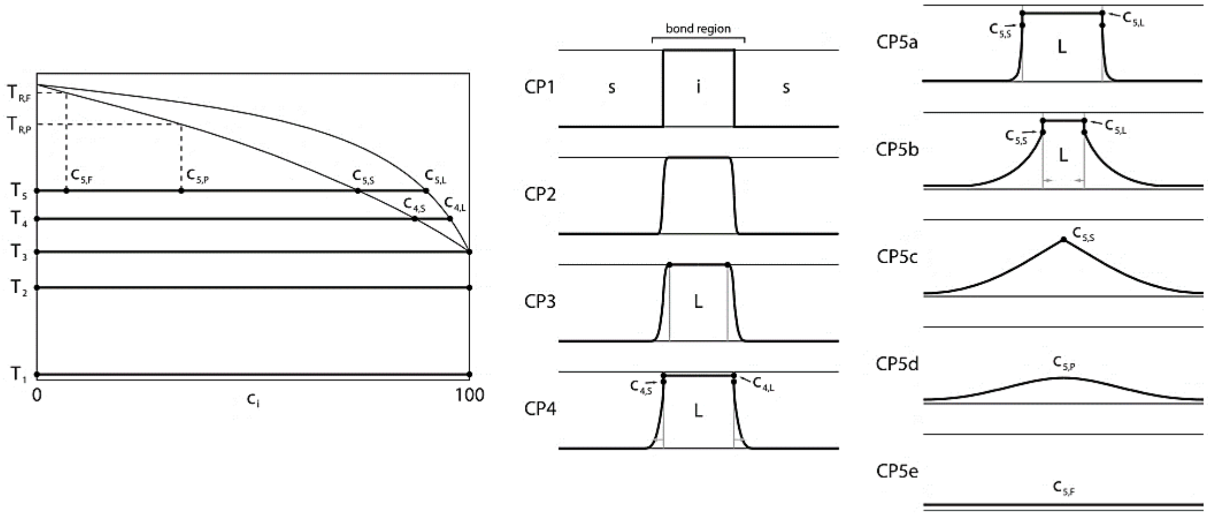

Figure 2.6 - Isomorphous Binary System with Compositions at Varying Temperatures. Compositional profiles included show the Progression of Transient Liquid Phase Bonding while Holding at the Braze Temperature [18]

lower concentration of the diffusing element compared to that in the interlayer. Prior to melting some solid-state diffusion may occur as diffusion rates increase with temperature. The interlayer melts locally at the base metal/interlayer interfaces where there is intimate contact. Upon forming a liquid, diffusion rates in the bond region become much more pronounced and dissolution of the base metal begins [18].

Heating past the melting point causes some of the solid at the solid/liquid interface to dissolve into the liquid as dictated by the phase diagram. The concentration in the liquid region is no longer the pure interlayer element but a new concentration $c_{4,L}$ shown in CP4. Near the interface the composition of the solid is given by the solidus, $c_{4,S}$. Movement of the solid/liquid interface will continue until the braze temperature (T_5) is reached at which point the liquid layer reaches its maximum width (CP5a). Over time (CP5b to CP5c), the liquidus composition width shrinks to a point until the maximum concentration is the solidus at the centerline. The motion of this width is governed by a mass balance at the interface which will be discussed further in section 2.4.1.1. At this point, no more liquid remains. CP5e demonstrates how a low concentration of the interlayer element can result with continued heating and diffusion. At this point, the joint region is only saturated base metal and it is possible for the grain structure to regrow forming a homogenous microstructure. This is ideal for creating a joint strength near comparable to that of the base metal [18].

An important aspect of TLPB is to find an interlayer element which will lead to minimal dissolution, if possible, and result in shorter overall braze times. The amount of dissolution expected is dictated by the solidus and liquidus compositions given by the phase same diagram, as is shown in Figure 2.6. In addition to these compositions, dissolution can be lowered by promoting solid state diffusion prior to reaching the braze temperature or by loss of liquid due to wetting, or high bonding pressures, removing volume from the joint [18].

Figure 2.6 illustrates four separate half joint systems where there are variances in the solidus/liquidus lines in terms of concavity and convexity, as well as differences in the partition coefficient. The partition coefficient is defined as the ratio of solidus and liquidus compositions:

$$\boldsymbol{k = \frac{c_S}{c_L}} \tag{2.9}$$

This term provides a measure of the overall solubility of the interlayer element into the base metal. It is important to note that in these systems it is assumed that the diffusion coefficients are all the same and that they are heated instantaneously to the braze temperature. So, the main differences between the systems are that a and b are convex while c and d are concave; and that both a and c have a partition coefficient of 0.9 while b and d have a partition coefficient of 0.4.

Systems possessing a convex liquidus line are found to prevent melt back as can be seen by a and c having liquidus compositions moving towards the joint centerline over time. The opposite is true when discussing concave liquidus lines where a higher degree of dissolution is observed. In terms of the partition coefficient, isothermal solidification is more rapid in systems with a higher value which intuitively makes sense as the base metal can accommodate more of the diffusing species. Systems c and d show a high degree of dissolution initially whereas b and d will take a much longer time to isothermally solidify (dictated by the difference in the solidus and liquidus values, or a low partition coefficient)[18]. This can be understood as a solute rich liquid layer in contact with a base metal of a much lower solubility which will take time for solute to be completely removed.

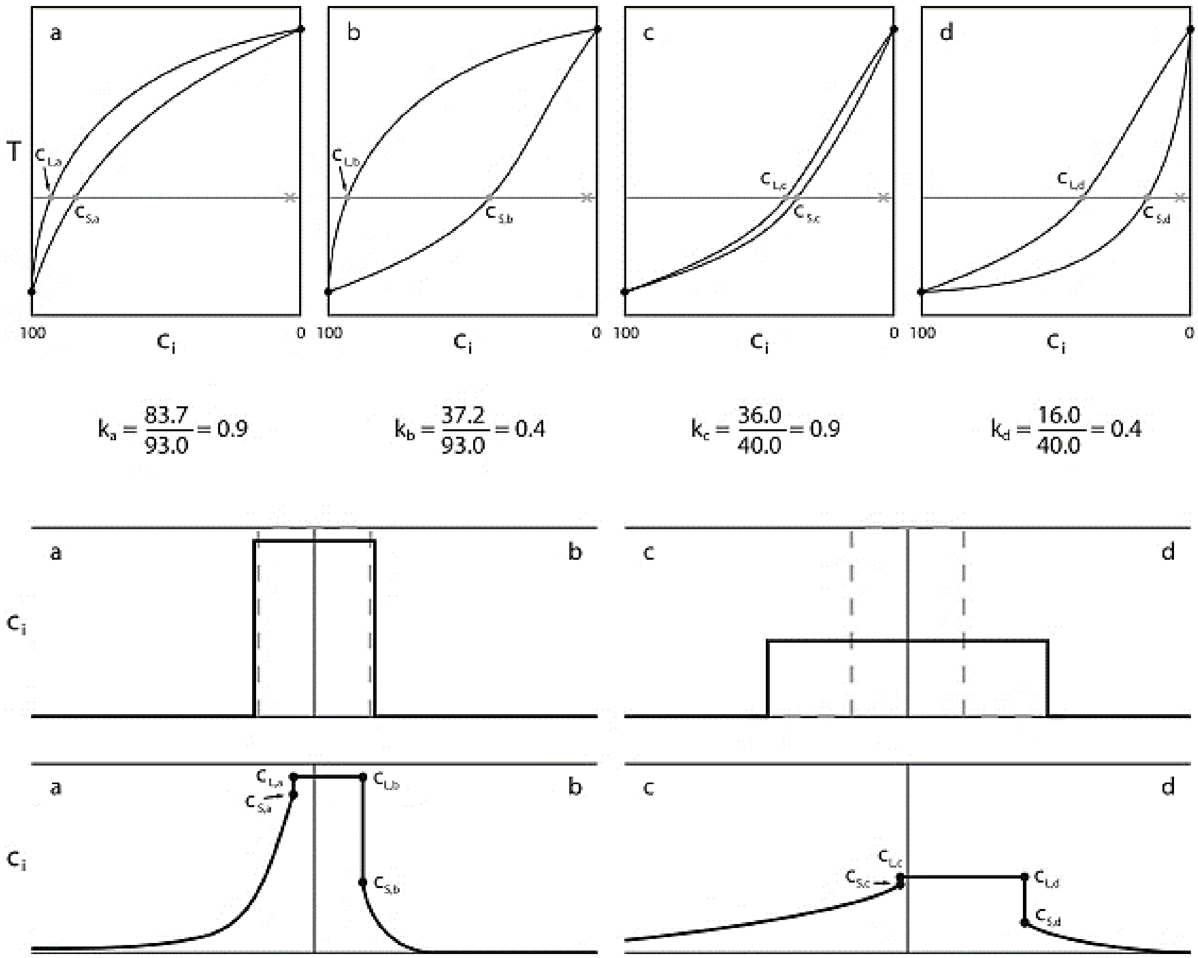

Figure 2.7 - The Effect of the Partition Coefficient on Dissolution and Resultant Composition Profiles. The Initial Condition (Dashed Line) Resolves to Initial Dissolution (Solid Line) and Finally the Resulting Liquid Homogenization in the Bottom Profiles. Each System Resolves to the Respective Liquidus and Solidus Values Dictated by the Above Isomorphous Phase Diagrams [18]

2.4.1 TLPB Modelling

Modelling of the TLPB process has been ongoing for the last fifty years and focuses mostly on the dissolution and isothermal solidification stages [19][20][21]. The kinetics of TLPB at all stages are diffusion-based with the main driving force being a solid-state compositional gradient beyond the solid-liquid interface. The rate at which each stage of TLPB can occur is therefore determined by the shape of this concentration gradient. During dissolution the gradient is developing and the concentrations at the solid/liquid interface are being established. In isothermal solidification the concentration gradient changes, with the restriction that the maximum solubility is fixed at the solidus composition. Finally, the homogenization stage (after all the liquid is removed) no longer has the restriction of a fixed centerline composition, allowing the gradient to flatten this profile across the brazed area.

To simplify the understanding of these processes, several assumptions are made when modelling TLPB. The flux of the solute is modelled as one-dimensional and is a function of the concentration gradient along a distance x away from the joint centerline. Diffusivity is considered to be constant and complete mixing is assumed in the liquid such that it forms a homogenous mixture following dissolution. The diffusion distance available to the solute is semi-infinite in the base metal and the concentration far away from the solid-liquid interface is the original solute concentration of the base metal (C_o). Finally, the interface is assumed to obey local equilibrium and that a constant planar interface parallel to the centerline is maintained [22].

Since TLPB is diffusion controlled, modelling of TLPB is based around the fundamental equations established by Fick. Fick's first law describes the mass flux of diffusing solute (J) and when applied in one dimension can be modified to:

$$\boldsymbol{J} = -\boldsymbol{D} \cdot \boldsymbol{\nabla C} = -\boldsymbol{D}\frac{\partial \boldsymbol{C}}{\partial \boldsymbol{x}} \qquad \textbf{(2.10)}$$

Where D is the diffusion coefficient, C is the composition of the solute, and x is in the direction of mass transfer. The diffusion coefficient can be assumed to be independent of concentration, position, and time in one-dimensional systems when the concentration differences are small.

Fick's second law describes the change in concentration in any control volume through conservation of mass. This equation can be expressed in a one-dimensional form:

$$\frac{\partial C}{\partial t} = -\nabla \cdot \boldsymbol{J} = -\left(\frac{\partial C}{\partial x}\right)\left(-\boldsymbol{D} \cdot \frac{\partial C}{\partial x}\right) = \boldsymbol{D}\left(\frac{\partial^2 C}{\partial x^2}\right) \tag{2.11}$$

Equations 2.10 and 2.11 form the fundamental equations for modelling of TLPB [20][21][22]. From these equations, modelling of dissolution and isothermal solidification can now be discussed.

2.4.1.1 Modelling of Dissolution

Tuah-Poku *et al*. stated that the driving force for continuous dissolution is the difference in composition between the starting liquidus ($c_{3,L}$ in Figure 2.6 which is $T_{m,B}$) of the insert and the final liquidus determined by the simple binary phase diagram ($c_{5,L}$ in Figure 2.6) [21]. Upon melting the liquid layer is supersaturated with an average concentration beyond $c_{3,L}$. Therefore, some solid uptake (dissolution) is necessary to lower the average composition. Using Fick's second law and an error function type solution common to 2D planar diffusion, a simplified equation was found where the interface displacement is described by:

$$\boldsymbol{y} = \boldsymbol{K_1}\sqrt{\boldsymbol{4D_L t}} \tag{2.12}$$

Where y equals zero at the initial faying surface, t is time, and K_1 is a constant described by the compositions of the solidus and liquidus for both the interlayer and the base metal. This equation describes the total distance traveled by the solid/liquid interface after heating to the braze temperature. Zhou *et al.* have shown that there are no suitable analytical solutions for the dissolution stage and it has not been studied to the same degree as isothermal solidification due to the rapidity of interlayer incorporation into the base metal [20][22].

2.4.1.2 Modelling of Isothermal Solidification

Following dissolution, Wmax will begin to recede as the isothermal solidification stage begins. Previously, the interlayer rapidly melted and incorporated the base metal until the liquidus composition ($C_{liq.}$) was obtained. At this point equilibrium is established at the solid-liquid interface which fixes the liquid composition to $C_{liq.}$ and the solid to C_{sol} at the interface. The position of the interface [x(t)] is now dictated by a mass balance between the solid and liquid:

$$\left(C_{liq.} - C_{sol.}\right)\frac{d}{dt}x(t) = D_{sol.}\frac{\partial}{\partial x}C_{sol.} - D_{liq.}\frac{\partial}{\partial x}C_{liq.} \qquad \textbf{(2.13)}$$

Equation 2.16 includes the diffusivities of the solute in the solid ($D_{sol.}$) and the liquid ($D_{liq.}$) and can be explained schematically in Figure 2.9. Figure 2.9a shows the interface moving from the solid line compositional profile to the dashed line. Note that the compositions of the liquidus and the solidus (C_L and C_s) are fixed at the interface as it moves a distance Δx.

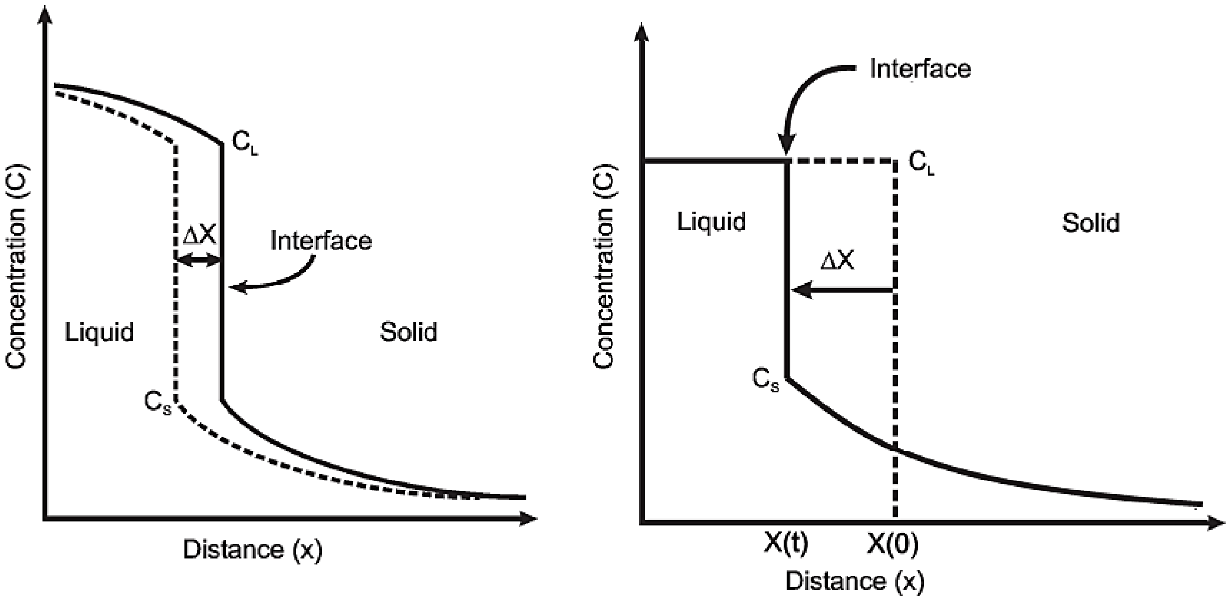

Figure 2.8 - Motion of the Solid-Liquid Interface by a Mass Balance (a) for an Established Interface following Liquid Homogenization; (b) Initial Melting Transitioning to Liquid Homogenization with Perfect Mixing in the Liquid [22]

Recall that an assumption made when modelling TLPB was that the composition of the liquid was homogenous due to perfect mixing and a much higher diffusivity than the solid. The resultant compositional profile of the liquid is flat, and Equation 2.16 simplifies to the following:

$$\left(C_{liq.} - C_{sol.}\right)\frac{d}{dt}x(t) = D_{sol.}\frac{\partial}{\partial x}C_{sol.} \tag{2.14}$$

Equation 2.17 favors motion of the interface towards the liquid and solid will grow into the liquid until isothermal solidification is complete. A convenient schematic for viewing isothermal solidification under these conditions is shown in Figure 2.9b. The dashed line shows the interface just following dissolution where x(0) would be W_{max}. This assumes that there is no initial uptake of solute prior to time zero. After equilibrium is established, the compositional profile in the liquid becomes flat and constant at $C_{liq.}$. The solute concentration for the solid at x(t) is fixed at the solidus concentration ($C_{sol.}$) and depletes in solute concentration further into the semi-infinite base metal [21][22].

This compositional profile established in the solid will be controlled by the rate of diffusion of solute into base metal. Therefore, the time to complete isothermal solidification will be dependent on how quickly solute can be pulled from the liquid. The time can be found experimentally by monitoring the growth of the saturated base metal into the liquid, or can be evaluated by Equation 2.18 found by Tuah-Poku et al [21].

$$\boldsymbol{t_{IS} = \frac{\pi W_{max}^2}{16 \cdot D_{sol.}} \left(\frac{C_{sol.} - C_{liq.}}{C_{liq.}} \right)} \qquad \textbf{(2.15)}$$

Note that the time to complete isothermal solidification is dictated not only by the diffusivity in the solid but by the difference in the solidus and liquidus concentrations (given by the phase diagram) and the maximum liquid width established following dissolution. Thus, there is a constant competition in TLPB between dissolution necessary for liquid generation and homogenization of the liquid which subsequently must remove it before isothermal solidification.

Isothermal solidification was also described by a value K_3, replacing the K_1 value in the previous section, in a similar equation.

$$\boldsymbol{y = K_3 \sqrt{4 D_S t}} \qquad \textbf{(2.16)}$$

K_3 is dictated entirely by the base metal solidus and liquidus ($c_{5,S}$ and $c_{5,L}$) as the average composition of the liquid is no longer supersaturated and lies somewhere between these values, c_o. K_3 can be found as the solution to the general equation:

$$\boldsymbol{K_3\left(e^{-K_3^2}\right)(1+\mathrm{erf}(K_3))\sqrt{\pi} = \frac{c_S-c_o}{c_L-c_S}} \qquad \textbf{(2.17)}$$

Typically, both K_1 and K_3 are values between 0.01 and 1.1 though this will vary depending on the phase diagram of the system. During isothermal solidification and later homogenization, the rate of these processes is controlled by the diffusion of solute into the base metal and therefore controlled by the rate of solid-state diffusion [21].

The maximum width attained from dissolution, W_{max}, can be determined from the phase diagram using the initial width (W_o) of the interlayer, the relative densities of base metal and interlayer (ρ_A and ρ_B), as well as the composition of the interlayer ($c_B = 1$ if pure) and the composition of the liquidus.

$$\boldsymbol{W_{max} = W_o\left[1+\left(\frac{c_B-c_L}{c_L}\right)\left(\frac{\rho_A}{\rho_B}\right)\right] = W_o\left(\frac{c_B}{c_L}\right)} \qquad \textbf{(2.18)}$$

The second part of the equation assumes the densities of the base metal and the interlayer are similar, and that the interlayer is a pure metal [21]. The relationship is shown schematically in Figure 2.8 where a simple eutectic binary phase diagram is used. At t_{start}, the foil is placed between the two plates of base metal A and has a measured thickness of W_o. The foil (pure B) will melt with some of A at the braze temperature as the $C_{sol.}$ and $C_{liq.}$ compositions are established, until a maximum thickness (W_{max}) is reached and dissolution ends (t_{finish}).

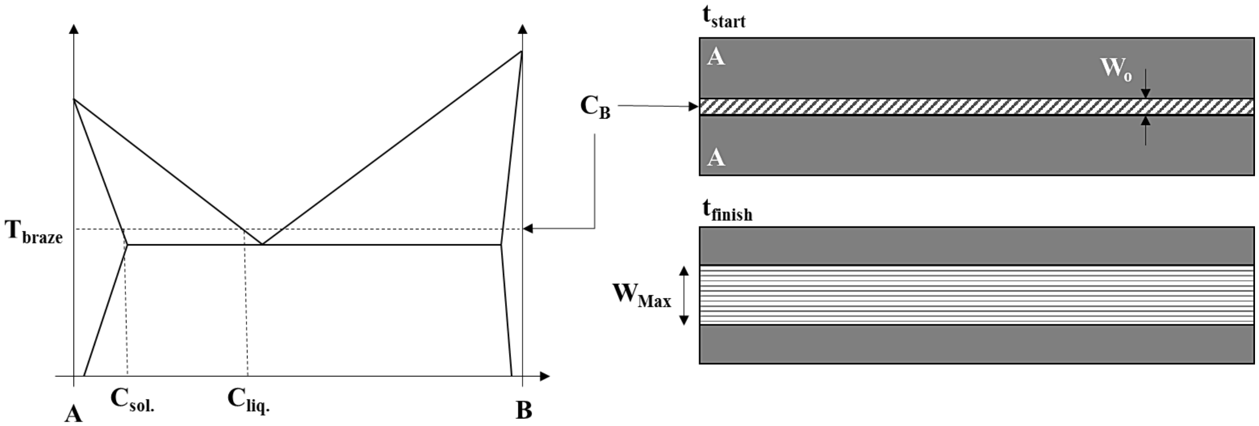

Figure 2.9 - Schematic of Dissolution Where a Starting Foil of Width, W_o, Dissolves and Incorporates Base Metal to a Width, W_{max}, as Modelled by Toah-Poku *et al.* [21]

2.5 Titanium Composition and Microstructure

A large contribution to the final product in brazing lies in appropriate alloy additions of the parent metal. Commercially pure titanium is graded by its purity and contains residual iron and oxygen from the Kroll process and exposure to atmosphere. Alloying additions are implemented to change the transus temperature of titanium (α to β) and to change the overall microstructure of the final alloy [3].

Titanium and titanium alloys can be simplified into three major microstructural categories: α alloys and CP titanium, α and β alloys such as Ti-6-4, and finally β alloys. Table 2.3 outlines these different alloys with focus on common commercially used titanium alloys. Notice that the chemistries of these alloys not only dictate their classification but also shift the transus temperature above which α transitions to β. This is due to the tendency of certain alloying elements to either preferentially stabilize the α or the β phase [3].

Table 2.3 - Transus Temperatures for Titanium and α /α + β Titanium Alloys. ELI is an acronym for Extra Low Interstitial Limit. Modified from [3]

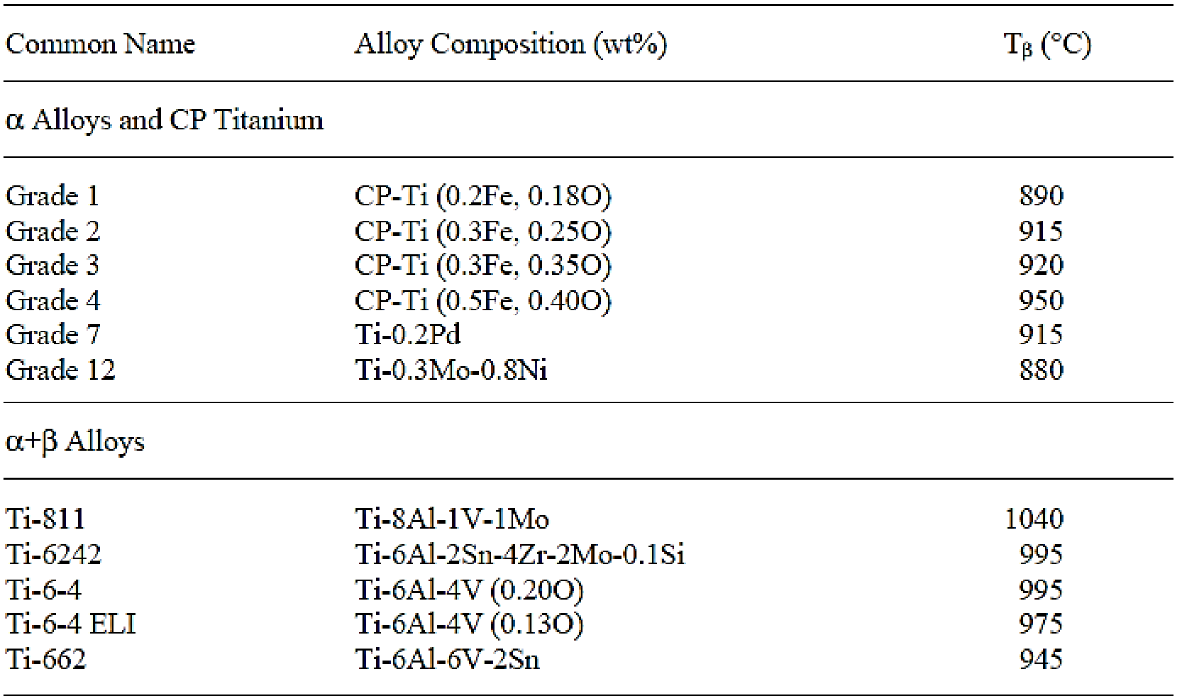

Common Name	Alloy Composition (wt%)	T_β (°C)
α Alloys and CP Titanium		
Grade 1	CP-Ti (0.2Fe, 0.18O)	890
Grade 2	CP-Ti (0.3Fe, 0.25O)	915
Grade 3	CP-Ti (0.3Fe, 0.35O)	920
Grade 4	CP-Ti (0.5Fe, 0.40O)	950
Grade 7	Ti-0.2Pd	915
Grade 12	Ti-0.3Mo-0.8Ni	880
α+β Alloys		
Ti-811	Ti-8Al-1V-1Mo	1040
Ti-6242	Ti-6Al-2Sn-4Zr-2Mo-0.1Si	995
Ti-6-4	Ti-6Al-4V (0.20O)	995
Ti-6-4 ELI	Ti-6Al-4V (0.13O)	975
Ti-662	Ti-6Al-6V-2Sn	945

Figure 2.10 shows the effect these alloying elements have on the transus temperature of titanium. Common elements in these alloys such as aluminum or oxygen have an α stabilizing effect whereas vanadium, iron, or hydrogen instead stabilize the β phase. Elements such as zirconium, hafnium, or strontium have no effect on the transus temperature. These effects are predicated on similar temperature-composition behavior seen in the equilibrium phase diagrams. β isomorphous elements in sufficient quantities can stabilize the β phase at room temperature whereas β eutectoid will produce a eutectoid mixture of α and β [3][4].

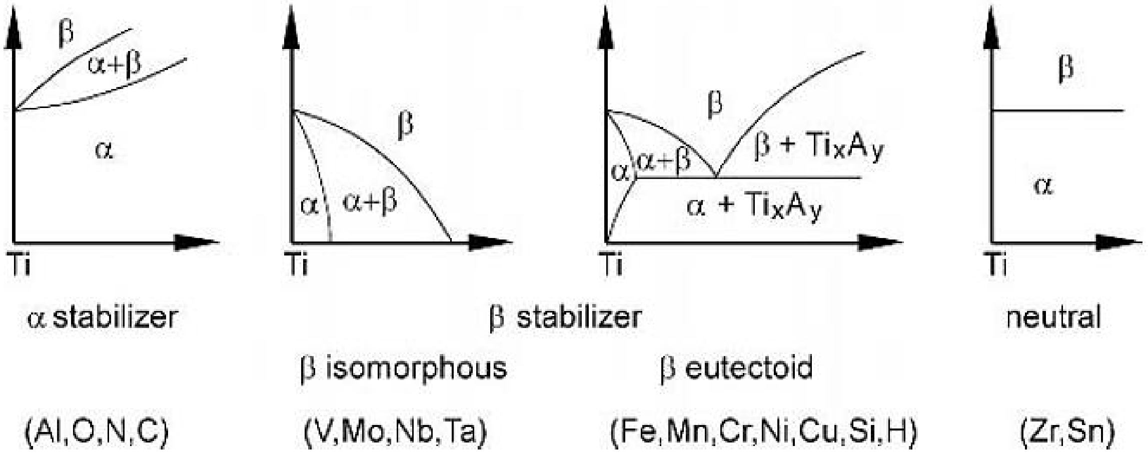

Figure 2.10 - Effect of Alloying Elements on the Transus Temperature [3]

α alloys and CP titanium contain substitutional elements of aluminum and tin, as well as soluble interstitial elements such as oxygen, carbon, and nitrogen. Some of these are byproducts of the Kroll process or a byproduct of manufacture. A maximum limit of 0.4 wt% oxygen is permitted in almost all titanium alloys as it becomes detrimental to the alloy due to its embrittling properties [22]. The role of oxygen will be discussed later in this section. Iron, vanadium, and molybdenum may be added as well in limited quantities. These alloys all derive strength from their substitutional and interstitial alloying elements, microstructure (grain size, orientation), and precipitation hardening of secondary α particles; and also offer excellent corrosion resistant due to the low addition of elements typically found in them. Because of this they are ideal for chemical and petrochemical processing equipment as well as heat exchangers and other piping applications [3].

The constitution of these alloys is almost entirely α with small volume fractions of β. Due to the low additions of alloying elements, these alloys essentially don’t respond to heat treatment. The only influence of heating lies in influencing crystallographic texture and overall grain size. These alloys are largely produced as rolled products, either sheet or plate. Typical processing would take a large ingot or slab and hot roll it before coiling. From there the coiled alloy would be uni-directionally rolled and deformed to a desired grain size and crystallographic orientation. The product is finally annealed to a certain grain size. Typically, these alloys are not cold rolled as this offers little in terms of strength due to low work hardening and also reduces ductility [4].

The microstructure as stated consists of recrystallized α grains with dispersed β phase. The β phase remains due to low quantities of iron always present in CP titanium. Iron has a low solubility in titanium and is rejected to form β upon cooling which remains stable at room temperature. This is a desired formation as the β phase pins the α grain boundaries and helps control grain size during recrystallization. It also improves hydrogen solubility in the alloy [22][24]. Figure 2.11 shows an α alloy heat treated to 675°C for an hour where it has formed an equiaxed grain structure.

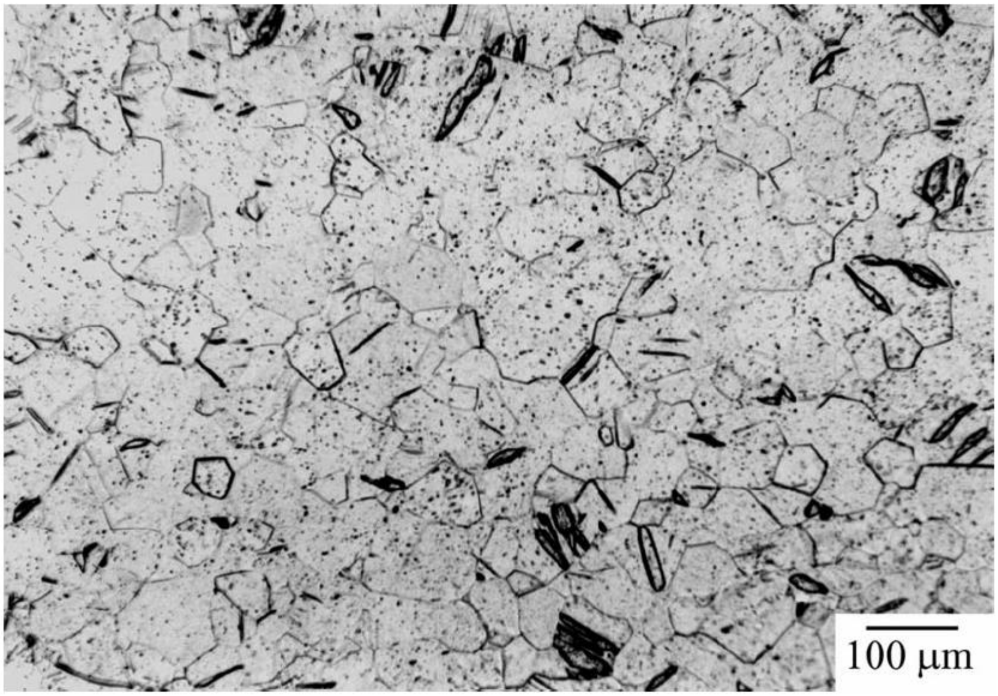

Figure 2.11 – Commercially Pure Titanium Heated to 675°C for One Hour and Cooled in Air Showing Recrystallized Equiaxed Alpha Grains [22]

Another common microstructural form is a Widmannstätten structure. This particular structure is more prevalent and visible in α and β alloys where the β phase is present at a much higher volume fraction. Figure 2.12 helps to explain this formation. Depicted in the figure is an alloy with the composition of Ti-6Al-6V (close to Ti-6Al-4V) which is cooled from a temperature above the β transus temperature into an α and β region to various temperatures. The α phase nucleates in preferential directions on the β grains and continues to grow in a lamellar fashion. The resulting Widmannstätten structure at room temperature is shown on the right of the image. This structure is beneficial in fatigue and fracture toughness applications, but comes with a loss in overall strength and ductility [24][25][26].

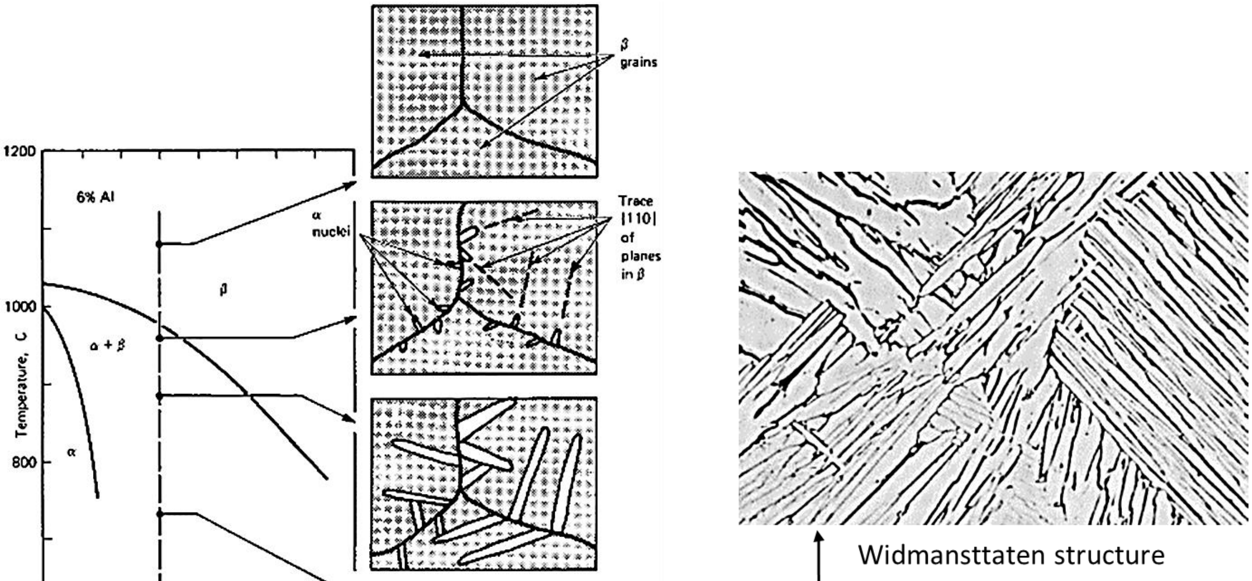

Figure 2.12 - Formation of Widmanstatten Structure in Titanium and Titanium Alloys [28]

Half of the titanium market is focused on α and β alloys used for structural aircraft components, the front section of aero engines, fan and compressor blades, automotive parts and in biomedical applications. The abundant use of these alloys is due to their ability to retain larger amounts of beta phase and its effect to alter the overall microstructure [2].

2.6 Filler Metal Considerations

As stated in Section 1.3, the modelling of dissolution and isothermal solidification was to be investigated using titanium as a base metal. An appropriate filler metal was necessary for undergoing TLPB and successfully joining CP-Ti and Ti-6Al-4V. This required an appropriate experimental design to evaluate braze evolution and quality, as well as selection of an appropriate filler metal. With minimal literature available on the subject, the experimental design required simplicity in terms of compositional complexity (due to expected gradients in concentration and evaluation of efficacy).

Filler selection was therefore restricted to simple binary systems and all variations of Ti-X phase diagrams were evaluated (where X represents a metalloid/metallic binary constituent). All metalloid/metallic systems were considered initially before eliminating candidates based on criteria outlined in Table 2.4.

Parameters of interest include the solubility of solute available in the base metal as well as the concentration of base metal that can dissolve into the solute. Also, of importance was at what temperature could a maximum degree of solubility of the filler be obtained both in the alpha and beta phase of the titanium. If brazing in the alpha phase was desired, it was also necessary to know the maximum solubility below 800°C into the base metal. The number of intermetallics and the lowest melting temperature/composition are included as well as the diffusivities in the alpha and beta phase (when available).

From this selection, elements such as carbon, nitrogen, and oxygen could be immediately removed as well as all metals where the base metal would melt with the foil (Mo, Nb, etc.). Peak temperatures when friction stir welding Ti-6Al-4V have been shown to reach temperatures in the range of 1000-1200°C which was considered as a maximum limit for acceptable braze temperatures [27]. Diffusion bonding is typically done in 900-950°C regime and brazing can occur as low as 767°C if a Ti-Zr-Ni-Be amorphous foil is used [1][16]. Lee *et al.* were able to implement these amorphous foils in TLPB joints at temperatures of 830°C with isothermal solidification completing with 300-1800 seconds [29].

All constituents with a melting point minimum above 1200°C were discarded leaving ten candidates remaining. From these, certain metals proved either too dangerous due to toxicity (beryllium) or too costly for serious industrial application (palladium). Table 2.4 contains the remaining choices for pure filler metals.

Table 2.4 - Decision Matrix for Potential Filler Metals in the Brazing of Titanium [30]

	Solubility in α (wt%)	**Max Solubility Temp.**	**Solubility in β (wt%)**	**Max Solubility Temp.**	**Max Solubility below 800°C**	**Intermetallics**	**Highest IMC Melting Point**	**Lowest Melting Point**	**Liquid Solubility at 1050°C (wt%)**
Ag	10	885	35	1325	9	Ti_2Ag TiAg	1020	962	98%
Al	31	1280	32	1480	<10	Ti_3Al TiAl Al_3Ti	1500	660	99%
Co	1.5	685	17	1020	1.5	Ti_2Co TiCo $TiCo_2$	1325	1020	27%

Cu	2	803	18	989	2	Ti_2Cu $TiCu$,Ti_3Cu_4 $TiCu_2$	989	875	50%
Fe	0.047	595	24.7	1085	0.047	TiFe $TiFe_2$	1427	1085	33%
Mg	1	882	5	>1600	1	-	-	650	99%
Mn	1	550	32	1180	1	TiMn $TiMn_2$ $TiMn_{3-4}$	1325	1180	42%
Ni	0.5	765	10.5	942	0.5	Ti_2Ni TiNi $TiNi_3$	984 1310 1380	942	28%

In addition, intermetallics in each of the systems were considered. A system with very low melting intermetallics would be an ideal candidate for brazing at lower temperatures saving energy costs in an industrial application. This made copper and silver excellent candidates for the binary study to isothermally solidify the titanium base metals. Of the two, copper was chosen as a result of existing literature and a smaller liquidus region.

Apart from aluminum, a large increase in solubility is observed when transitioning from the alpha to beta. In the interest of increasing isothermal solidification kinetics a braze temperature in beta phase was chosen (T_{braze} > 880°C). This removed any benefit in using aluminum and made candidates such as iron, cobalt, and nickel more applicable. Due to a lower melting eutectic and ease of accessibility nickel was chosen from these constituents.

Figure 2.13 shows the titanium copper binary phase diagram. The system has two eutectic points (875 and 960°C) and six intermetallic compounds forming from 860 to 1015°C. Copper in its pure state melts at 1083°C and commercially titanium as a base metal would be expected to melt at 1670°C. In order to achieve isothermal solidification without the formation of intermetallics, a braze temperature above 989°C is necessary. With a temperature of 1050°C, the liquidus concentration near the solid/liquid interface would be 40 wt% copper and the solidus concentration is 18 wt%. At this temperature the partition coefficient is 0.45.

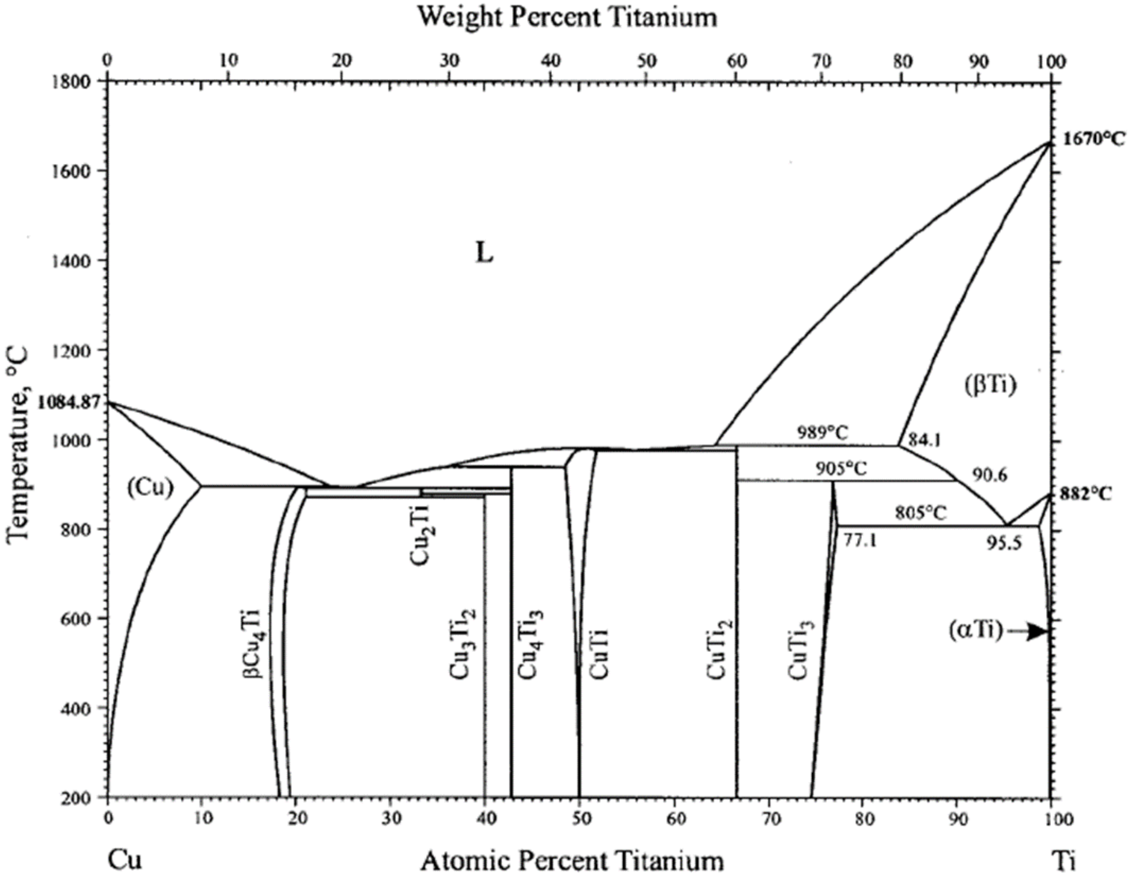

Figure 2.13 - Titanium-Copper Binary Phase Diagram [31]

The titanium nickel phase diagram is shown in Figure 2.14 with three eutectics (1304, 1118, and 942°C) and with three intermetallic phases melting at 984, 1310 and 1380°C. Nickel in its pure state melts at 1465°C. To achieve isothermal solidification without the formation of intermetallics in this system it is necessary for a rapid shift in concentration somewhere below roughly 40 wt% nickel. This could be achieved through dissolution providing the braze temperature was above 942°C. At a braze temperature of 1050°C, the liquidus and solidus concentration become 25.5 wt% and 10.5 wt% Ni respectively, creating a partition coefficient of 0.41.

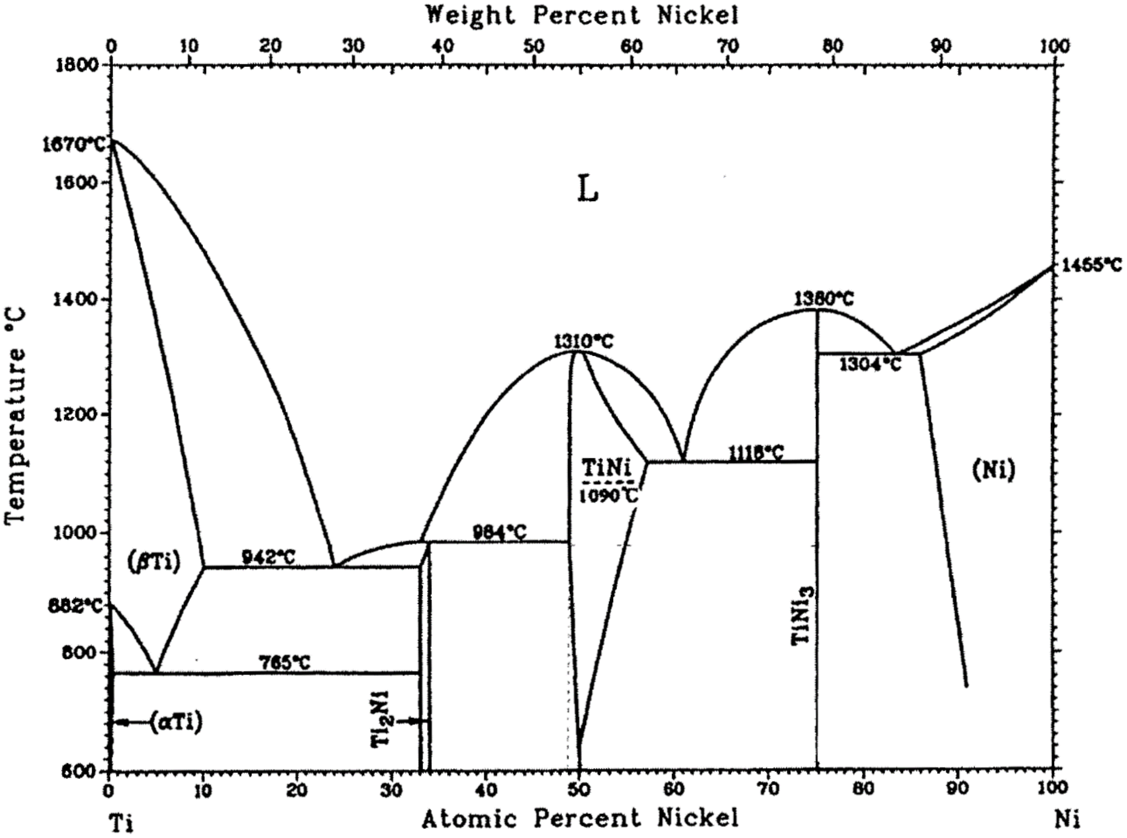

Figure 2.14 - Titanium-Nickel Binary Phase Diagram [30]

Both copper and nickel encapsulated the bulk of this work in joining titanium by TLPB. These studies focused on the thermal and microstructural characteristics using differential scanning calorimetry (DSC), optical and scanning electron microscopy, as well as lab scale brazing and hardness testing of these joints.

2.6.1 Prior Art in Joining of Titanium and Titanium Alloy

Joining of titanium using pure copper and nickel interlayers has been studied previously and a summary of the prior art is included in this section [32-51]. Twenty studies were examined looking into joining of titanium by conventional high temperature brazing (mainly diffusion bonding and TLPB). The results are listed in Table 2.5. Deng. et al highlights the importance of high temperatures when using TLPB to join Ti-6Al-4V and provides an excellent summary of other joining techniques (friction stir welding, fusion welding, etc.). Deng also notes that an advantage for conventional brazing is that post welding heat treatments can be avoided entirely [41]

Table 2.5 - Summary of Prior Art in Joining of Titanium and Titanium Alloy

Base Metal [Interlayer]	Bonding Temp. (°C)	Hold Times (min.)	Foil Thickness (µm)	TLPB Studies	Diffusion Bonding Studies	Welding/ Other Joining
Grade 2 [Cu]	850 - 1000	20 - 180	10 - 300	[16] [33]	[34]	[35]
Grade 2 [Ni]	700 - 950	5 - 100	30 - 300	-	[36] – [38]	[39] – [40]
Grade 5 [Cu]	800 - 1020	10 - 150	20 - 150	[41] – [47]	[48]	-
Grade 5 [Ni]	760 - 950	15 - 90	20 - 400	-	[49] – [50]	[51]

Twelve of the twenty citations examined the joining of dissimilar materials, often joining titanium to stainless steel or duplex stainless steel (four of these involved TLPB). This is due to cost savings and optimization of engine capacity by joining titanium engine blades to stainless steel discs in the front section of aeroengines [43]. Additional industries that benefit from the joining of these metals include accessories in oil rigs, cryogenic plumbing, biomedical applications and dental implants. Norouzi cites that fusion welding is not applicable for these applications as it forms brittle cast structures (intermetallics) in the weld zone [43].

Many studies were reluctant to use a braze temperature above the α to β transus temperature of both commercially pure titanium and Ti-6Al-4V (890°C and 975°C respectively from Table 2.3) despite improved diffusion of the interlayer in the BCC structure of β-Ti. Issues of grain growth and retained β were often quoted as reasons to avoid this transformation. As a result, seven of the studies attempt lower temperatures (such that no liquid is formed) using diffusion brazing which is a lengthier diffusional process relying on diffusion in the solid state.

The application of TLPB using copper interlayers was first investigated in work by Wells [16]. Wells examined brazing of commercially pure titanium and copper between the temperatures of 817°C and 982°C. These temperatures lie below the peritectic and intermetallic formation was still prevalent. Samples were held from 20-400 minutes and a foil size of 10 μm was used. With these experiments Wells created a time-temperature-copper concentration curve which is shown in Figure 2.15. The dashed line in the figure was constructed by Wells as the recommended hold time and temperature to ensure a quality braze joint.

The desired composition of 7 wt% Cu is below the solidus composition of beta titanium and would lead to development of the eutectoid phase along the centerline. Wells also examined using copper as interlayer with Ti-6Al-4V which also created quality joints. In addition, mechanical properties of commercially pure and Ti-6Al-4V were comparable to the base metal when the composition at the centerline of the joint was found to be 7 wt% Cu or less. Wells was the only reference that discusses the kinetics of brazing titanium with copper. However, there was no investigation into liquid kinetics, dissolution, or homogenization. The work demonstrates that copper is an effective interlayer for joining titanium and can produce joints with quality mechanical properties in the absence of intermetallics.

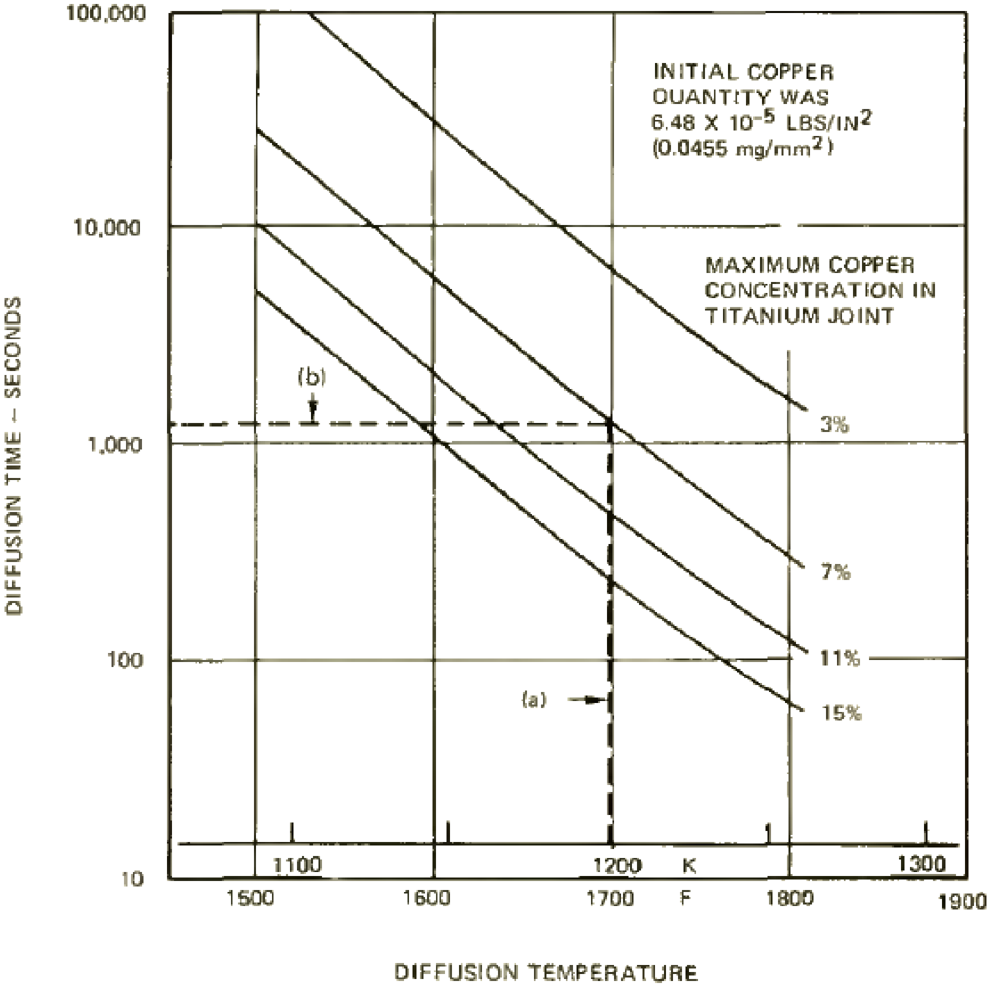

Figure 2.15 - Time-Temperature-Concentration Curve Mapping Copper Concentration in Experiments by Wells [16]

Figure 2.16 shows a eutectoid microstructure (α + Ti_2Cu) transitioning into a α + β Ti64 base metal as the composition of copper decreases. Wells found that microstructural control of titanium alloys with copper proved less difficult than using pure titanium as the base metal. It was observed that generally the liquid would form into either a eutectic or peritectic reaction. Wells noted a high degree of dissolution in the titanium-copper diffusion-brazed joints when an excess of thin film (above 10µm) was used. Wells brazed between roughly 820°C and 984°C with an effort to avoid the peritectic melt and a base metal that was predominantly α-phase [16].

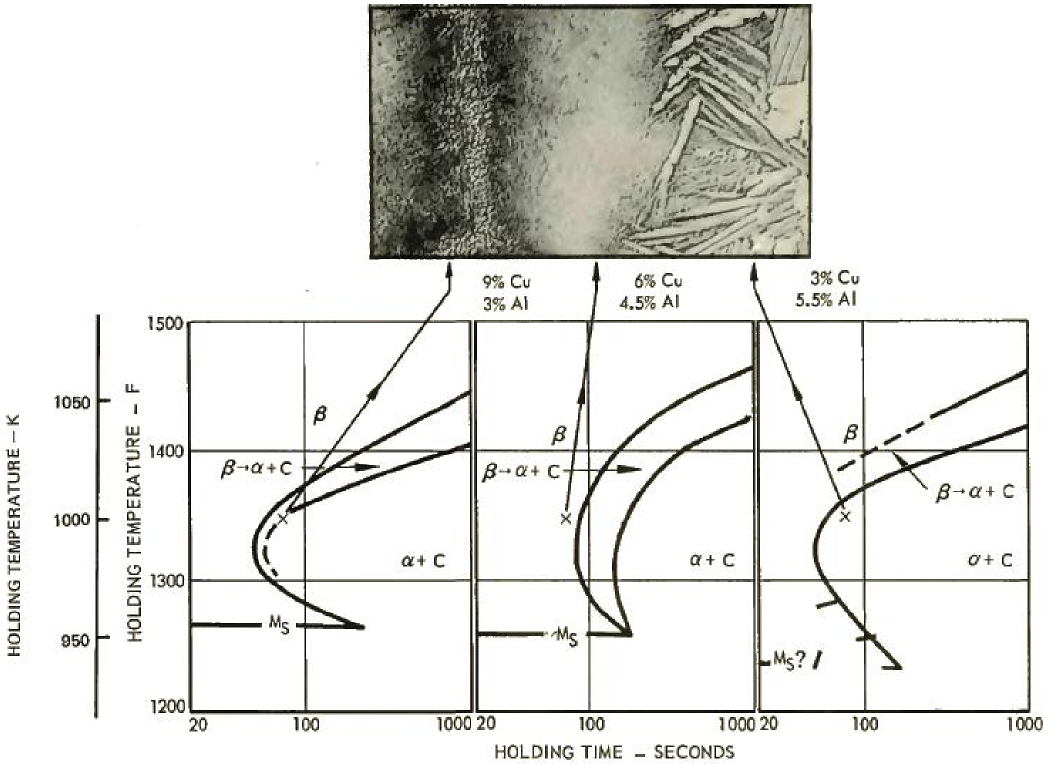

Figure 2.16 - TTT Diagrams Derived from Ti-6Al-4V Microstructure Joined with Copper where Presumably C Denotes the Formation of Intermetallic Compounds [16]

Work by McDonald *et al.* included a brief summary of TLPB of titanium and copper at one braze temperature for two hold times [33]. This work examined brazing from 920-955°C and recommends a Type 1 interlayer (using pure copper) for the joining of titanium structural shapes.

Deng. *et al.* investigated the microstructure and properties of Ti-6Al-4V when using a pure copper interlayer at a braze temperature of 930°C [41]. These samples were held from 1-30 minutes using a 20 μm foil. Deng observed the formation of TiCu and Ti_2Cu and that these intermetallics can be eliminated with increased hold time. The presence of Ti_2Cu on the joint centerline lead to poor strength during mechanical testing at 20 minutes duration. By holding for 30 minutes Deng noted that the optimized joints had excellent structural integrity. Again, the removal of intermetallics in the joint lead to quality joints in both Deng and Song when examining titanium alloys [41][42].

In addition to titanium to titanium joints, several studies examined the joining of Ti-6Al-4V to stainless steel using TLPB of copper foil. Norouzi *et al.* implemented a 25 μm foil which was brought to a braze temperature of 960°C and isothermally held from 15-90 minutes [43]. When joining to AISI 304 stainless steel (SS), Norouzi found TiCu, Ti_2Cu, $TiCu_4$, $TiCu_2$, FeTi and Fe_2Ti along the joint centerline. This study included the use of EBSD at the joint to map the progression of phases as well as the grain structure. This was used to monitor the density of Ti-Cu intermetallics and there was a noted decrease after an 80 minute hold time. Bond strengths during tensile testing were found to be close to the values of the base metal.

In a similar manner; Özdemir, Eroglu, and Zakipour examined the joining of Ti-6Al-4V to AISI 304SS, microduplex SS, and AISI 316L SS [45-47]. Özdemir used a 60 μm foil heating from 800-1000°C and holding from 50-150 minutes. Similar microstructures to Norouzi are mentioned with the addition $CuTi_3$, Ti_3Al and $Ti_{33}Cu_{67-x}Fe_x$ confirmed by EDS [43]. Eroglu investigated a 20 μm foil heating to 900°C and holding from 5-60 minutes. Mapping the composition of the interfaces, the eutectoid and a layer of Ti_2Cu were identified on the side of Ti64. Finally, Zakipour examined bonding with a 50 μm foil and heating from 900°C to 960°C for 50-150 minutes. Again, similar EDS results were found to Norouzi and Özdemir [43][45]. All studies found a region of increased microhardness values away from Ti-6Al-4V and the eutectoid which are likely due to copper and iron rich intermetallics. The presence of copper in Ti64 did not show mechanical properties that deviated far from the base metal, provided that copper was in the eutectoid phase.

An article by Kundu examined using pure Ni and Cu interlayers sandwiched between dual phase stainless steel and Ti64 such that a DSS/Ni/Cu/Ti64 couple was created [44]. These layers were reacted at 875°C to 950°C and held for 60 minutes. The reaction of these phases leads to a complex microstructure at higher temperatures, but brazing would only occur in the solid state when reacted at 875°C from the Ti-Cu and Ti-Ni phase diagrams discussed later in this section. Since thick foils were used (150 μm), this reaction still leaves pure copper near the centerline and a diffusion couple is created which is included in Chapter 6. Due to the formation of intermetallics at the centerline, there was an increased hardness across the joint and a decrease in overall shear strength.

The use of nickel as an interlayer has never been investigated in titanium when using TLPB despite its repeated use in diffusion bonding. Only five studies were noted examining diffusion bonding of grade two and five titanium with nickel as outlined in Table 2.5. Bond temperatures chosen were low, typically from 800°C to 950°C. In studies which heat to 950°C, there is a noted change in the microstructure to the formation of a eutectic (β-Ti + Ti_2Ni) which would suggest that some amount of liquid was present. All studies note the formation of a $TiNi_3$/TiNi/Ti_2Ni intermetallic compound layer within the range of brazing temperatures. He *et al.* notes that after 15 minutes of diffusion bonding at 800°C that shear strength begins to drop due to an increase in the rate of intermetallic growth [36]. Kundu shows that above 900°C (held for 75 minutes) there is a sharp decrease in both tensile and shear strength in the joints of Ti-6Al-4V and microduplex stainless steel. In all studies, microstructural and mechanical properties were examined but there was no investigation of the Ti-Ni liquid or system kinetics.

The benefits of transient liquid phase bonding of Ti and its alloys remain relatively untapped with only the recent study by Deng in 2017 noting its advantages [41]. Out of all twenty studies only, Wells examined the kinetics of brazing titanium and a pure interlayer, in this case copper [16]. All studies state the benefits of using a pure interlayer to create near base metal mechanical properties. However, none examine the kinetics of dissolution or isothermal solidification and even fewer take advantage of using TLPB to remove persistent intermetallics. Only the work by Song *et al.* operated at a temperature that was above the melting point of all intermetallics in the Ti-Cu binary phase diagram and the hold times used in this study were not sufficient to remove intermetallics from the joint centerline [42]. Many studies are running an assay-like approach where a matrix of brazing parameters is selected, and the strongest option is chosen. Up to this point, no literature exists to describe the mechanisms and kinetics of TLPB in titanium and no study has examined these material systems using differential scanning calorimetry (DSC).

As stated in Section 1.3, one of the objectives of this study is to examine the extent of dissolution, gap widening, solute uptake and the remaining liquid for a given hold. With these parameters, the optimal brazing time and temperature can be found for any industrial joint using commercially pure titanium or Ti-6Al-4V. The benefits of using a pure interlayer have been outlined in the previous studies and the only caveat to successful implementation is in the removal of intermetallic layers. Using a braze temperature above the intermetallic melting temperature, a diffusion couple can be created between the base metal and the resultant dissolved liquid where isothermal solidification can proceed to completion. If these samples are allowed to homogenize, it is possible to remove any intermetallics from the joint and achieve optimal mechanical properties as a result. Using DSC, the interactions of pure copper and nickel were monitored when heated to the braze temperature in contact with commercially pure titanium and Ti-6Al-4V. With an understanding of the overall system kinetics at each stage of TLPB, the ideal braze conditions could be found for any gap size in an industrial assembly.

2.6.2 Diffusion in Ti-Cu and Ti-Ni Systems

It was quickly discovered that the titanium-copper and titanium-nickel systems experience a rapid dissolution and uptake of titanium base metal into the melt zone, especially when the amount of filler metal is small. This large uptake quickly dilutes the pure filler metals into titanium rich intermetallics which will remain present upon cooling until complete isothermal solidification is achieved. Throughout this study the predominant phases discovered were TiNi, Ti_2Ni, TiCu, Ti_2Cu and Ti_3Cu_4 (in small amounts when joining Ti-6Al-4V). These intermetallics become important in the various solidification structures that result and will be discussed briefly individually.

Table 2.6 outlines major diffusing species in the systems to be discussed including constituents of Ti64 as these become important following dissolution and over long liquid durations. Allotropic transformation from hcp to bcc allows for higher diffusion rates due to the β-phase possessing lower atomic packing factor. The diffusing species Cu and Ni are faster diffusing species than titanium during counter diffusion which is beneficial for isothermal solidification and homogenization. Nickel is the fastest diffusing species within β titanium. It is worth noting also the slow rates of diffusion both aluminum and vanadium display, as low amounts were found in the filler when joining Ti64. It was assumed that the presence of these elements in the filler area was due to dissolution only. These values remain low enough to avoid any Al-rich or V-rich intermetallics as dictated by the Al-Ti-Ni and Al-Ti-Cu phase diagrams in Appendix A.

Table 2.6 – Relative Diffusion Values of Titanium, Copper, Nickel, Aluminum, and Vanadium [52]

	D_o (cm^2/s)	Q (kJ/mol)	$D_{1050°C}$ (cm^2/s)	Temperature Range (°C)
α-Ti Self Diffusion	1.7×10^{-4}	192.8	4.15×10^{-12}	585-855
β-Ti Self Diffusion	1.27×10^{-4}	119.7	2.39×10^{-9}	900-1620
Diffusion of Cu in β-Ti	2.1×10^{-3}	122.3	3.12×10^{-8}	960-1460
Diffusion of Ti in Cu	0.693	196	1.27×10^{-8}	700-1010
Diffusion of Ni in β-Ti	9.2×10^{-3}	123.9	1.18×10^{-7}	940-1240
Diffusion of Ti in Ni	1.4	263.8	5.38×10^{-11}	750-1150
Diffusion of Al in β-Ti	0.114	213.1	4.4×10^{-10}	920-1600
Diffusion of Al in Cu	0.131	185.2	6.39×10^{-9}	710-1000
Diffusion of Al in Ni	1.0	260	5.43×10^{-11}	640-940
Diffusion of V in β-Ti	3.1×10^{-4}	134.8	1.48×10^{-8}	900-1540
Diffusion of V in Cu	2.48	215	8.05×10^{-9}	720-1070
Diffusion of V in Ni	0.87	278.4	8.87×10^{-12}	800-1300

2.6.3 Ti-Ni Intermetallics

Titanium-rich intermetallics (Ti_2Ni, TiNi) were encountered during this study following interaction of pure nickel and titanium. Their overall structure and composition are included in

Table 2.7. These results agree with earlier studies such as the work by Bastin and Reick examining titanium nickel diffusion couples. These studies were conducted in the temperature range of 650-940°C and found that β-Ti (Ni), Ti_2Ni and NiTi all showed diffusion-controlled growth [52].

Table 2.7 - Titanium-rich Phases in the Titanium Nickel System [54]

Phase	Stability Range (at%)	Pearson Symbol	Space Group	Structure	Type
α-Ti	0-1.0	hP2	$P6_3/mmc$	Mg	Hexagonal
β-Ti	0-10.5	cI2	$Im\bar{3}m$	W	Cubic
(Ni)	86-100	*cF4*	$Fm\bar{3}m$	Cu	Cubic
Ti_2Ni	32.5-33.8	*cF96*	$Fd\bar{3}m$	CFe_3W_3	Cubic
TiNi	49.3-56.9	*cP2*	$Pm\bar{3}m$	CsCl	Cubic

The microstructures following interaction were mapped and are included in Figure 2.17. During interaction of these couples, Ti_2Ni tends to show a slower growth than TiNi. At 900°C, the Ti_2Ni

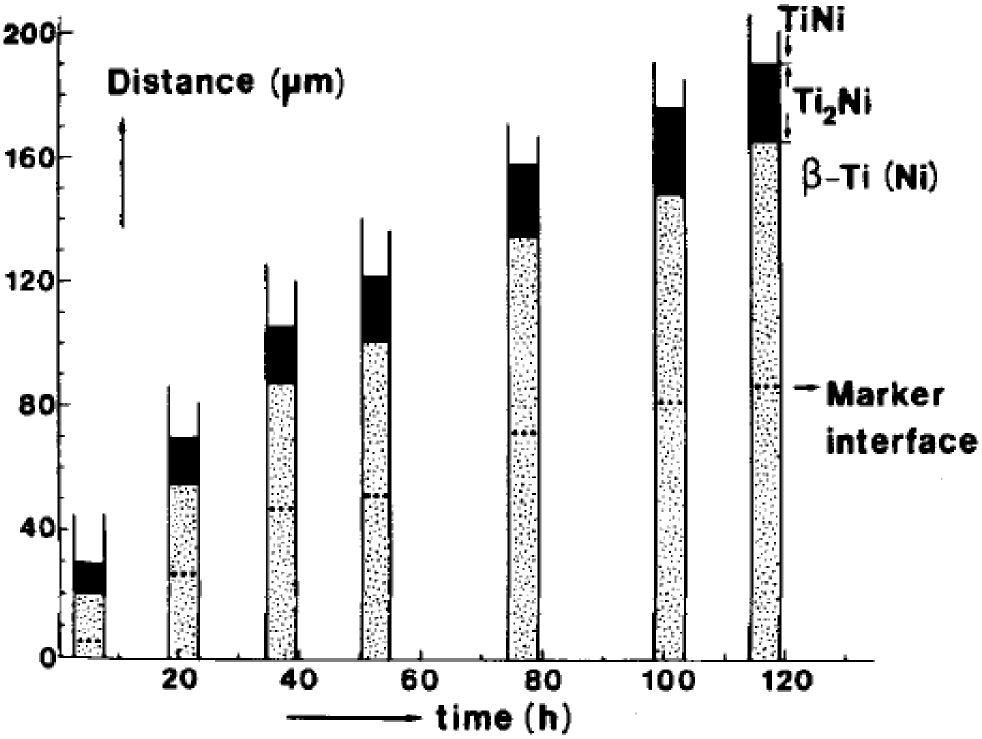

Figure 2.17 - Growth of Intermetallics Layers in a Titanium-Nickel Diffusion Couple [52]

layer consisted of short columnar crystals with grain boundaries roughly parallel to the diffusion direction. Included in the figure is the marker interface where fine tungsten wires and radioactive thoria particles were used to delineate the original interface. Due to the large imbalance in diffusion rates between titanium and nickel, it is possible for nickel to diffuse away leaving a local buildup of vacancies leading to porosity [52].

Interaction between the base metal and the interlayer show a delayed response in this work. Bastin *et al.* noted rapid growth of solid solution Ni in (β-Ti) at 770°C when examining Ti-Ni diffusion couples [52]. Enhanced diffusion was seen at 880°C due to high diffusivity paths along α/β grain boundaries in specimens using lower purity titanium (99.5 wt% Ti). Finally, it was found that the growth rate of Ti_2Ni and TiNi were impeded when in the presence of β-Ti. In powder studies, Cluff *et al.* mapped the growth of intermetallic layers over temperatures from 600°C to 1200°C (shown in Figure 2.18) [55]. Cluff found that intermetallic formation was impeded until dissolution of the surface oxide occurred at around 600°C.

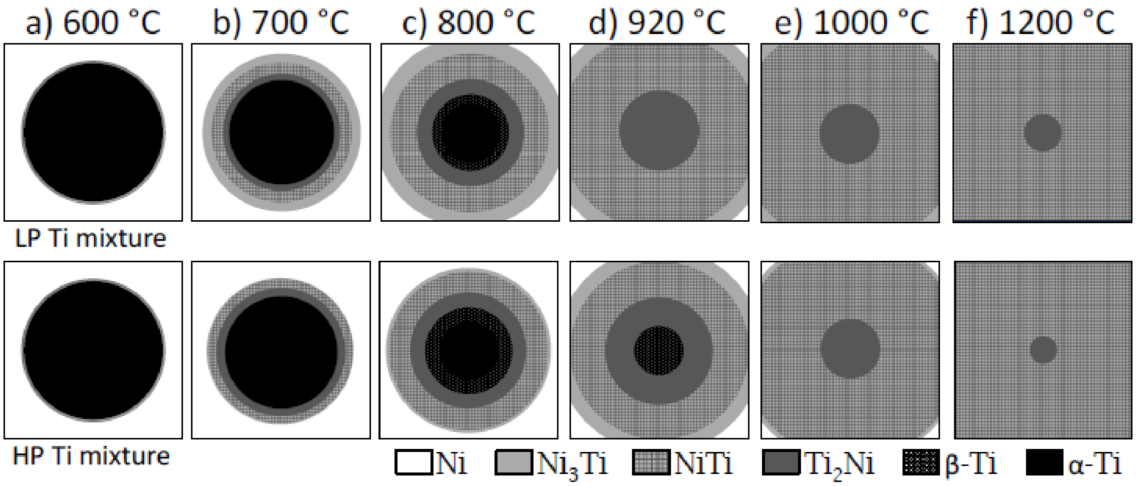

Figure 2.18 - Progression of Intermetallic Formation In High Purity (HP) and Low Purity (LP) Titanium Nickel Powders [55]

2.6.4 Ti-Cu Intermetallics

Titanium-rich intermetallics (Ti_2Cu, TiCu) were also observed in this study with the addition of Ti_3Cu_4 when using Ti64. Table 2.8 includes their structures and compositions.

Table 2.8 - Titanium-rich Phases in the Titanium Copper System [56]

Phase	Stability Range (at%)	Pearson Symbol	Space Group	Structure	Type
α-Ti	0-1.6	hP2	$P6_3/mmc$	Mg	Hexagonal
β-Ti	0-13.5	c/2	$Im\bar{3}m$	W	Cubic
(Cu)	92-100	*cF4*	$Fm\bar{3}m$	Cu	Cubic
Ti_2Cu	33.3	*tI6*	I4/mmm	$MoSi_2$	Tetragonal
TiCu	48-52	*tP4*	P4/nmm	γ-CuTi	Tetragonal
Ti_3Cu_4	57.1	t/14	I4/mmm	Ti_3Cu_4	Tetragonal

For the Ti-Cu system, diffusion bonding studies by Elrefaey *et al.* demonstrate the formation of intermetallic layers at 850°C when bonding commercially pure titanium and a 100 μm copper alloy foil [34]. Figure 2.19 shows the progression of the diffusion couple from 30 minutes to 180 minutes at 850°C. There is a transient period at 30 minutes (Figure 2.19a) where the intermetallic phases are developed but the interfaces are curvy, and the phases are mixed. By 60 minutes there is a clearly defined layer of Ti_2Cu (lighter phase) and TiCu (darker phase) which have developed and remain throughout the rest of the isothermal holds (Figures 2.19b to 2.19d). A eutectoid α + Ti_2Cu phase has developed close to the base metal and progresses slowly outwards. Note that no identification of Cu-rich intermetallics was discussed in either microstructural characterization or in EDS phase identification [34]. This suggests the growth rate of Cu-rich intermetallics is slow, at least in comparison to Ti_2Cu and TiCu.

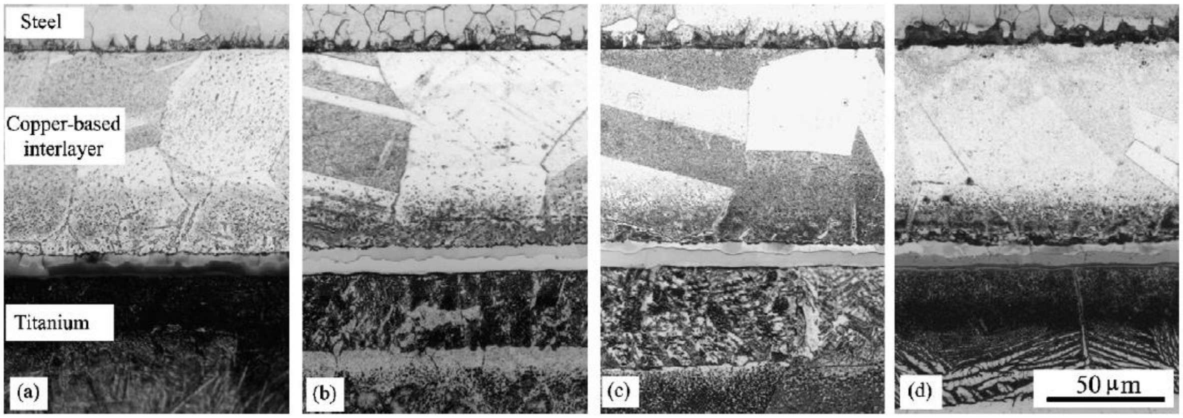

Figure 2.19 - Titanium Copper Diffusion Couple with Cu-Based Alloy (Cu-12Mn-2Ni) Heated to 850°C and Held Isothermally for (a) 30 min.; (b) 60 min.; (c) 90 min. and; (d) 120 min. [34]

2.7 Differential Scanning Calorimetry

Höhne *et al.* states that 'the objective of calorimetry is the measurement of heat' and from this heat comes an intrinsic temperature change in a body [57]. By monitoring this temperature change, the amount of heat can be measured and quantified. This technique has been used previously to quantify heat capacities of low melting substances, organic and polymer studies, and the study of chemical reactions. With the advent of high temperature DSC, metallurgical studies became possible in the evaluation of phase diagrams, intermetallics, and melting/solidification phenomena [57].

Figure 2.20 shows the change in enthalpy of a sample as it is heated. Any change in the solid-state chemistry that takes in or gives off heat will lead to a change in the enthalpy curve (called the latent heat). This change in enthalpy can be observed by monitoring the temperature difference of the sample and reference pan. Latent heats appear on DSC traces as a peak, the area under which is the total enthalpy of the event. Further discussion of the DSC can be found in earlier work [58].

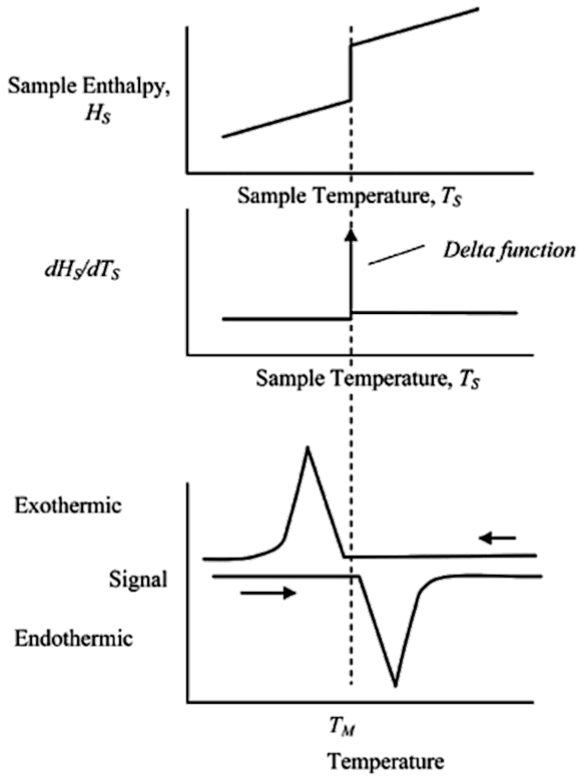

Figure 2.20 - Conversion of Enthalpies into DSC Signal Showing a Sample Melting with Temperature Increasing from Left to Right [57]

The measure of changes in enthalpy occur in the study of isothermal solidification as the repeated melting and solidification of a material which can be quantified. In addition, major metallurgical changes (phase formation, incipient melting) can be observed concurrently. This lead Corbin *et al.* to the investigation of transient liquid phase bonding in metallic systems using DSC as a main investigative technique. Kuntz *et al.* examined a binary Ag-Cu eutectic foil in contact with a pure silver base metal [22]. The events during melting and solidification are represented both microstructurally and thermally by the DSC trace in Figure 2.21 a and b.

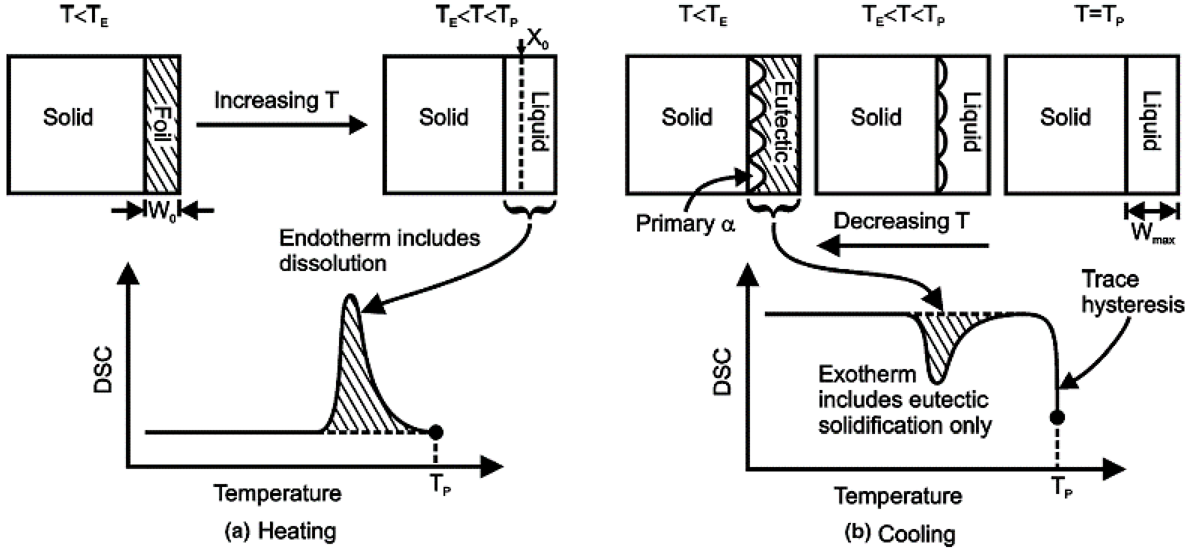

Figure 2.21 - Comparing Microstructural Evolution of Ag-Cu Eutectic Foil to DSC Signals Observed During (a) Heating and; (b) Cooling [22]

Examining Figure 2.21a, the foil in contact with the solid base metal reaches a eutectic temperature, T_E, where the foil proceeds to melt after exceeding it. The resulting liquid does not remain at the original foil thickness, W_o, but expands due to dissolution of the base metal into the newly formed liquid pool. The value T_P denotes where the melting event and dissolution complete. This is both advantageous, in that the dissolution event is recorded also, and an issue as it can be difficult to separate these two enthalpy events [22]. It is worth noting that the peaks broaden and are not perfectly sharp due to thermal lag experienced at interfaces between the liquid and the base metal, the liquid and the crucible, as well as the crucible and the thermocouple.

While the original foil was eutectic in composition, heating above T_E formed a hypoeutectic composition. Upon cooling, the growth of primary α dendrites into the molten eutectic was observed first in Figure 2.21b. Due to the absence of primary phase undercooling it was theorized that primary dendrite solidification was not measured in the DSC trace. Only the eutectic solidification that follows below T_E was documented as a sharp peak. The enthalpy of this dendritic formation can be accounted for in the subtraction of the enthalpy of melting from solidification. However, some of this will be due to diffusional motion of solute into the base metal [22].

In subsequent studies by Turriff *et al.*, the Al-Si eutectic system was examined for use in aluminum braze sheet in automotive heat exchangers. Work by Turriff observed that with increased hold time in the liquid state (above the braze temperature) there was a decrease in the freezing exotherm peaks on cooling, see Figure 2.22. This decreased area was attributed to lowering in liquid fraction as more silicon diffused into the base 3003 aluminum alloy. Both Kuntz and Turriff noted a linear dependence on the liquid fraction with the square root of time [22][60].

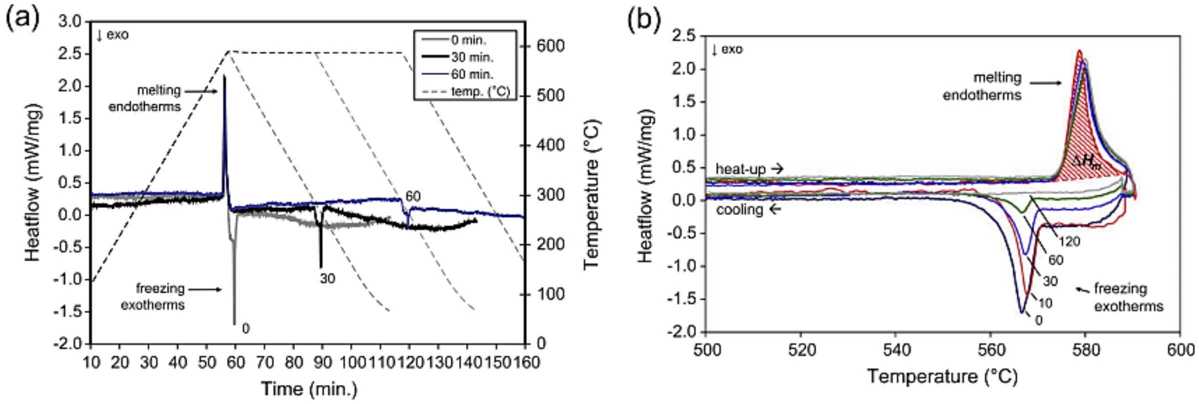

Figure 2.22 - DSC Measurement of Isothermal Solidification by Measuring the Melting Enthalpy of Aluminum Silicon Braze Sheet. Independent Isothermal Holds are Displayed with Heat Flow versus (a) Time and; (b) Temperature [60]. Note the Decreasing Enthalpy of Solidification

The liquid fraction here is defined as the measured enthalpy recorded from the DSC trace (the peak area) divided by the theoretical enthalpy of fusion for the pure eutectic:

$$f_L = L_f = \frac{\Delta H_m}{\Delta H_{theo.}} \tag{2.19}$$

When plotted against the square root of time, the liquid fraction decreases linearly. The slope of this curve is referred to as the rate constant, k. The intercept of this line is the initial weight fraction of liquid ($f_{L,o}$) following cooling and the first stage of isothermal solidification, homogenization. Figure 2.23 illustrates this relationship. It is worth noting that in this work the liquid fraction term will be denoted as L_f.

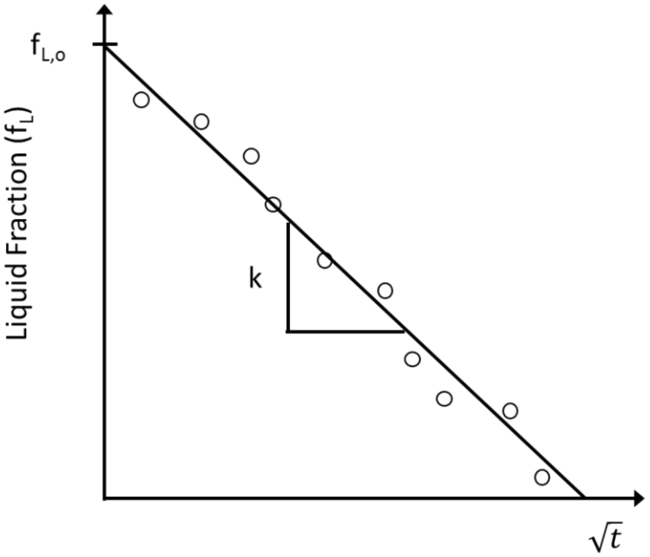

Figure 2.23 - Plotting Liquid Fraction against Square Root Time of Liquid Duration [22]

For a planar geometry where a foil is placed in contact with a flat base metal (or sandwiched between two), the motion of the interface during isothermal solidification will move concurrently with this decreasing liquid fraction. Maximum brazing clearance is a term used to define the gap size at which the joint is free of centerline eutectic. Due to difficulties arising from the interpretation of this term, Moreau *et al* define this interface motion by a $2W_{ISZ}$ curve where the motion of the interface is indexed with respect of time for a given foil/gap thickness [61]. The

$2W_{ISZ}$ is the maps the width of the isothermally solidified zone over the square root of liquid duration and will be discussed further in Chapter 4.

2.7.1 Undercooling in DSC

Advancing solidification fronts are constantly rejecting solute enriching the liquid ahead and as a consequence there are concentration gradients in the liquid near the base metal. Depending on the temperature, composition, and the shape and speed of the interface, there can be significant difficulties in solidification concerning nucleation. As discussed previously, such difficulties in nucleation (necessary to solidify) can lead to undercooling below freezing temperatures. These differences in freezing temperature can be detected in DSC in terms of the onset of the freezing exotherm.

Wanbing *et al.* examined undercooling in DSC using aluminum powders with respect to cooling rates applied. Figure 2.24 shows the results of heating and cooling these powders with cooling rates ranging from 5-25 K/min (Kpm). T_M is used to indicate the onset of melting of the powder and T_N indicates nucleation of the solid in the liquid [62].

Experimental undercooling was calculated using a definition by Mueller *et al.* where ΔT is the difference between the melting temperature and the temperature of nucleation on cooling [63]. Figure 2.25 shows the results of these experiments plotting undercooling (ΔT) in relation to the cooling temperature. It is evident that as the cooling rate increases, less time is provided to the liquid to react and solidify. In the current thesis work, a cooling rate of 20 Kpm was adopted for all samples with the exception of samples where it was imperative to freeze as much liquid as possible following dissolution.

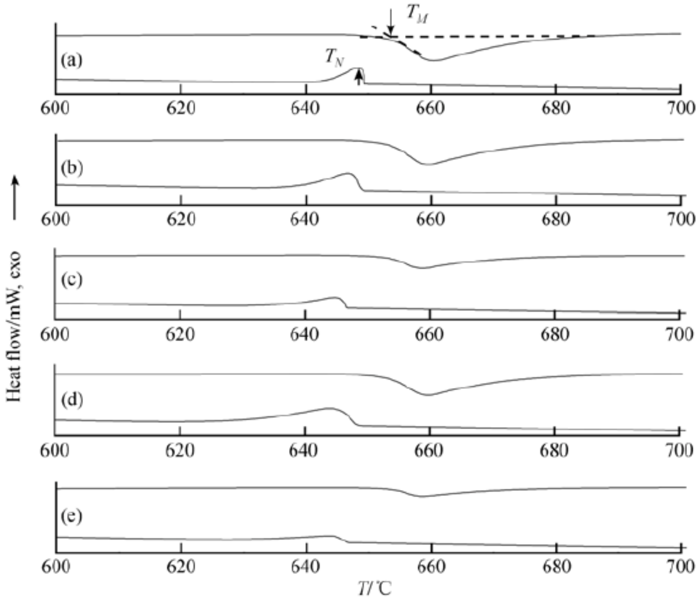

Figure 2.24 - Effect of DSC Cooling Rate on the Undercooling of Pure Aluminum Powder (a) 5 K/min; (b) 10 K/min; (c) 15 K/min; (d) 20 K/min; (e) 25 K/min [62].

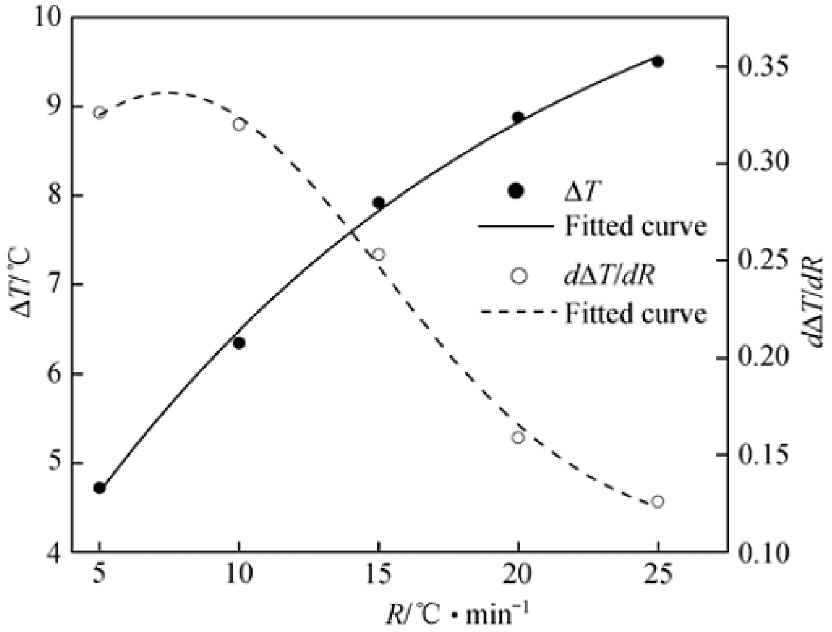

Figure 2.25 - Undercooling of Pure Aluminum Powder (ΔT) Plotted with the Rate of Undercooling as a Function of DSC Cooling Rate [62]

3.0 Experimental Methods

3.1 Materials

In the interest of reproducibility, samples of the same weight and dimensions were desired for the proper comparison of enthalpies and microstructural developments. Commercially pure (CP-Ti, or grade 2) and Ti-6Al-4V (Ti64, or grade 5) sheet measuring 1.6 mm in thickness, copper and nickel foils (50 µm in thickness) were purchased from McMaster Carr, and Alfa Aesar respectively. Each of the interlayers was graded at N2.0 level of purity. Both grade two and grade five titanium sheets met ASTM B265 specifications which are included in Table 3.1 [64]. It should be noted for iron, oxygen, carbon, nitrogen, and hydrogen that these values are the maximum allowable concentrations. Surface testing along the top and bottom of the sheets gave maximum values for carbon (<0.01 wt%), nitrogen (<0.03 wt%), iron (<0.15 wt%), and oxygen (<0.12 wt%) for both grade two and grade five titanium sheets (provided by the manufacturer).

Table 3.1 - ASTM Specifications for Grade Two and Five Titanium Sheets [64]

	Al (wt%)	V (wt%)	Fe (wt%)	O (wt%)	C (wt%)	N (wt%)	H (wt%)	Ti (wt%)
Grade 2 (ASTM B265)	-	-	0.30	0.25	0.08	0.03	0.015	Bal.
Grade 5 (ASTM B265)	5.5 - 6.75	3.5 - 4.5	0.40	0.20	0.08	0.05	0.015	Bal.

Titanium sheets were originally sectioned by water jet cutting into 4.76 mm (3/16") size specimens appropriate for fitting in a Differential Scanning Calorimetry (DSC) alumina crucible. However, issues with inconsistent sample tolerances led to the use of wire Electric Discharge Machining (EDM). A comparison of the two techniques is shown in Figure 3.1. There is no observable

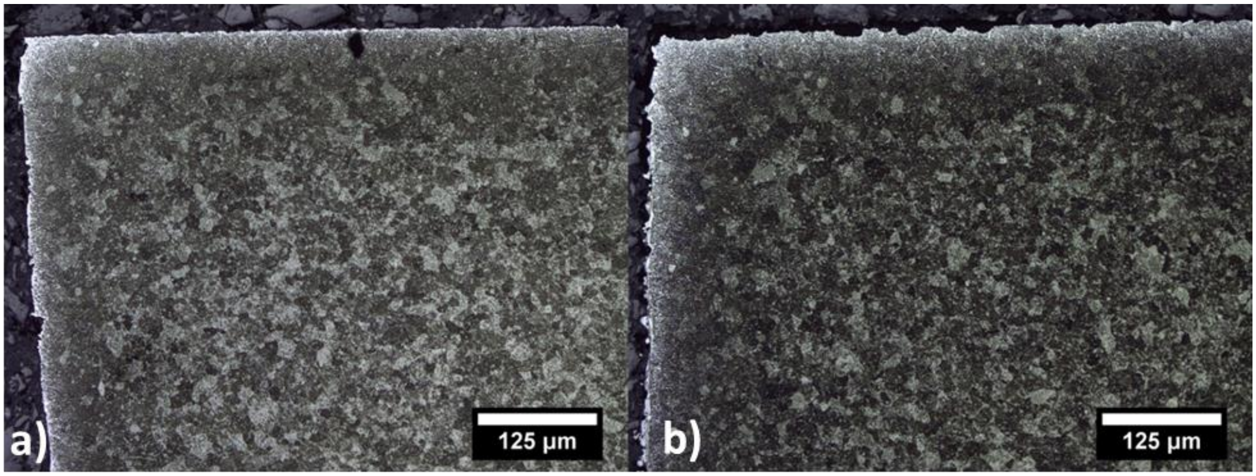

Figure 3.1 – Optical Microscopy of As-Received CP-Titanium Sectioned by (a) Water-Jet Cutting and; b) Electric Discharge Machining

distinction between the internal grain structures of the two samples with the only difference being an inherent oxide visible on the EDM sample surface. With improved tolerances, the oxide was removed by grinding with 500 grit silica paper (FEPA) which was also done in previous testing with the water jet cut samples.

Interlayer foils were punched using a 1/8" (3.175 mm) punch so that the filler metal was undersized on the titanium faying surface. This allowed for post DSC observance of wetting and spreading across the surface. As mentioned previously, the titanium samples were ground on the faying surface and a StopOff^{TM} coating (liquid titania within an organic solvent) was applied on the sides of the slug to prevent spreading on any other surface. Prior to testing, both the titanium slug and the foil of interest were cleaned in acetone.

3.2 Differential Scanning Calorimetry

Thermal analysis was conducted using a Netzsch DSC 404 F1 Pegasus® outfitted with a roughing pump and turbo pump. The purging gas used was argon at a flow rate of 50 mL/min. Figure 3.2a shows the equipment in the lab and Figure 3.2b shows a close up of the stem which carries the thermocouples to the alumina crucibles used in testing. The reference crucible is empty and shown with the lid placed on top. A titanium sample is in the sample crucible prior to applying the lid. A titanium getter can be seen below for removal of oxygen during testing.

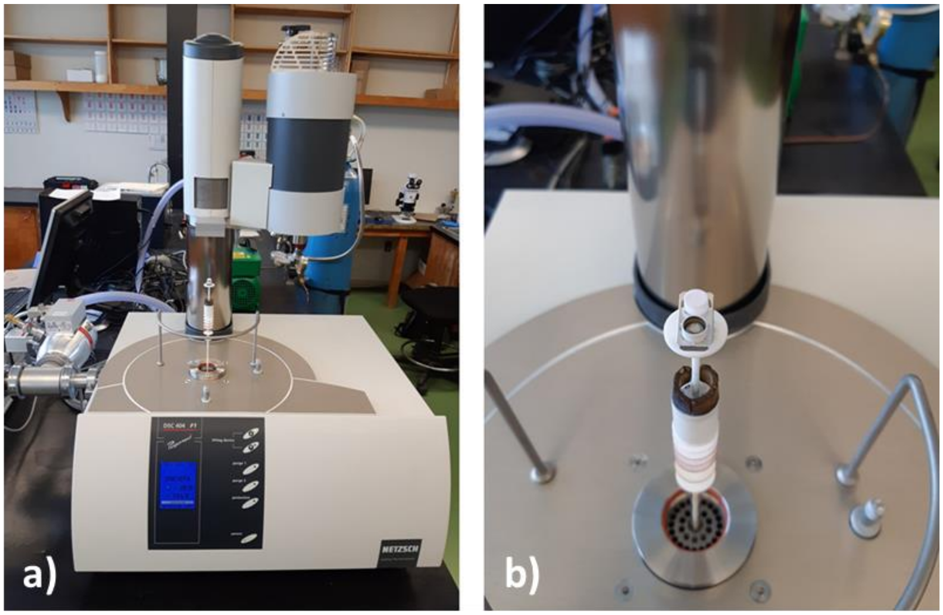

Figure 3.2 - Netzsch DSC 404 F1 Pegasus at HTTAL Laboratory a) Open Furnace Chamber and; (b) Imaging of Alumina Stem and Crucibles

Samples were arranged such that an undersized interlayer foil was placed on the top surface of the titanium base metal which was an added source of thermal lag during testing. To accommodate thermal lag (which was discussed in Section 2.7), a filler metal foil that undergoes a transition from amorphous to crystalline was placed on the surface of titanium slugs and heated to the transition temperature. The value of this enthalpy (ex. 60.68 J/g for CP-Ti) was compared to running the foil alone (72 J/g) in the DSC and a correction factor was assigned to each base metal studied. These values were 0.842 for grade two titanium and 0.865 for grade five titanium. They were applied for all DSC measurements.

In the discussion of DSC in Section 2.7, a flat baseline was assumed when considering heating and cooling curves. This would be valid if the specific heat of the sample has not changed significantly and if other events were not occurring simultaneously. In this situation, a linear baseline as shown in Figure 3.3a would be most appropriate and has been implemented in the previous Figures 2.21 and 2.22. If the specific heat of the sample changes following the phase transformation due to

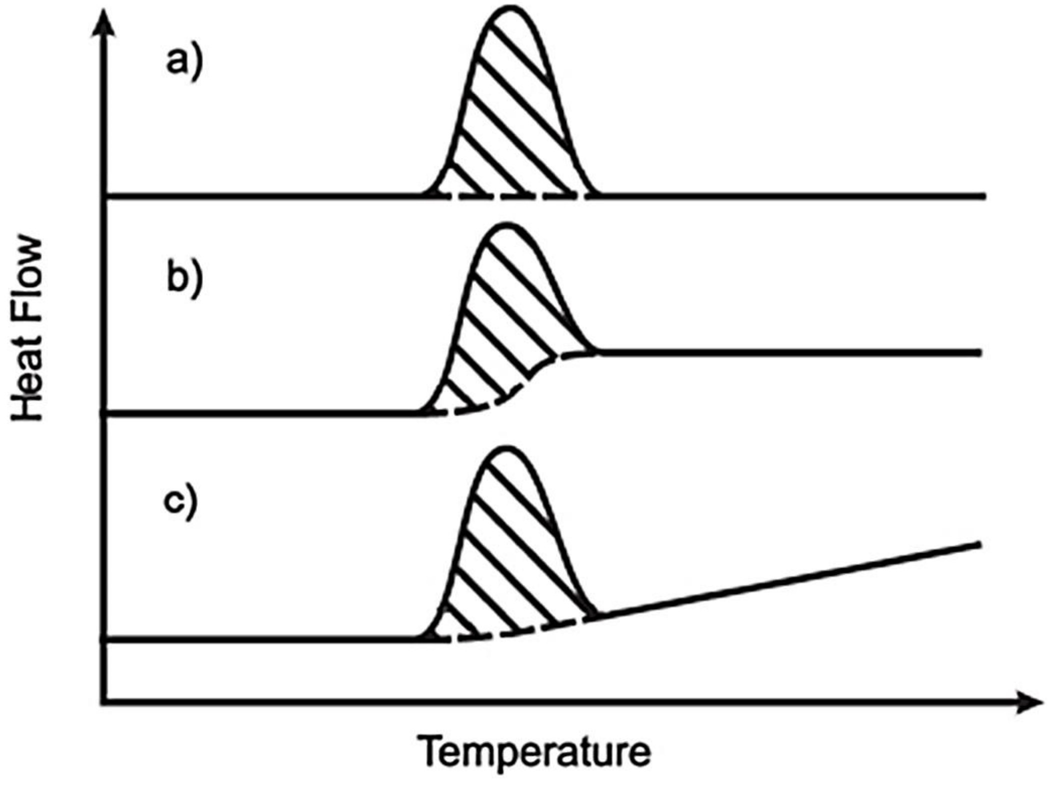

Figure 3.3 - Schematic of Baseline Corrections during Peak Measurements Modified from Kuntz Showing a) Linear; b) Sigmoidal and; c) Bezier Functions [22]

diffusion into the base metal, or due to intermetallic formation, then there will be a noted change in the baseline upon returning from the enthalpy peak. The DSC is still correctly recording a smooth baseline following the change in specific heat and here a sigmoidal baseline correction is applied, see Figure 3.3b. Finally, if there a concurrent event onsetting during the recording of the peak of interest (where it is assumed that this concurrent peak is gradual and over a large temperature range), then a Bezier fit can be used to correctly trace this secondary event. In the current work, all of these baseline correction methods were adopted based on the appropriate correction of the baseline shown in Figure 3.3.

3.2.1 Experimental Methods using DSC

Thermal events due to the interaction between the titanium sheet and copper foil (e.g. intermetallic formation, eutectic melting/solidification, etc.) were measured using a DSC. During brazing of Ti-Cu, a titanium-rich copper liquid would form and react with the alumina crucible making DSC measurements impossible [65]. To avoid this, titanium samples weighing 123.7 ± 1.2 mg were placed in a crucible first with a punched copper foil, placed on the top surface of the titanium slug. In this initial configuration, Ti-rich liquid spread over the sides of the base metal and reacted with both the alumina crucible and lid. In a second configuration (Figure 3.4) a 3.205 ± 0.110 mg Cu foil was undersized to diameter of 0.3175 cm and placed on top of the 0.47625 cm diameter faying surface of the titanium sheet. During brazing, the Ti rich liquid was contained in a spherical cap shape in the center of the titanium faying surface. This unique configuration avoided reaction with the alumina crucible making DSC measurements possible.

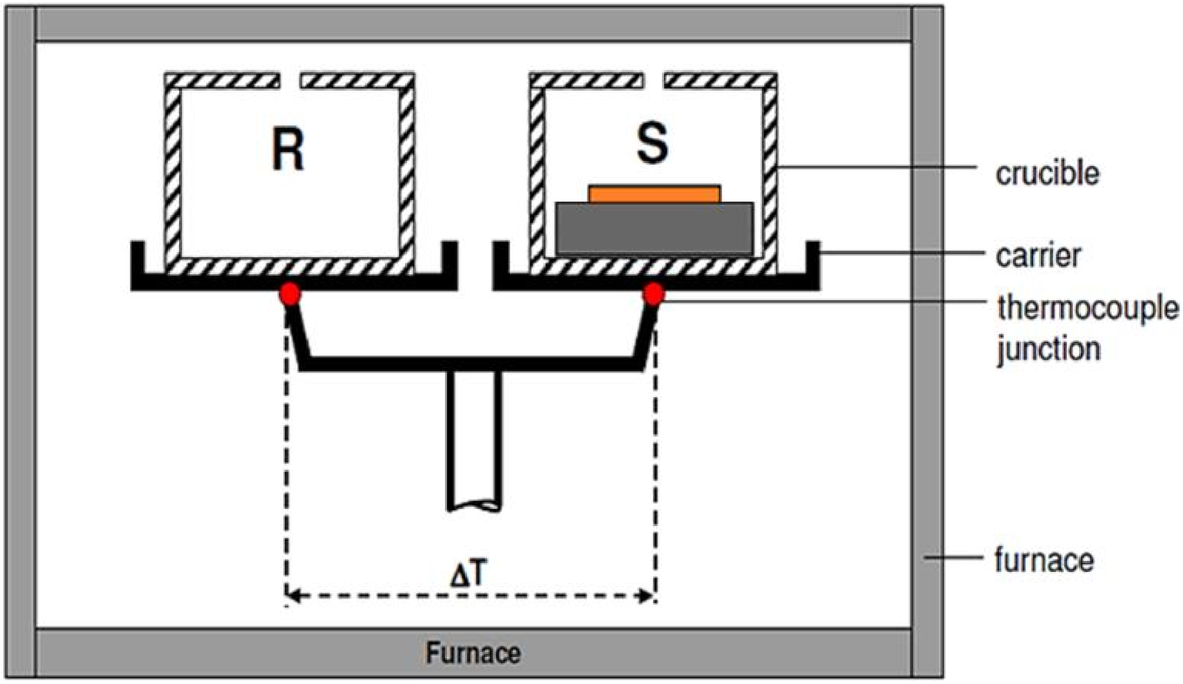

Figure 3.4 - Schematic of DSC Testing of Titanium Copper and Nickel Samples in an Alumina Crucible. Note that the Foil is Placed on Top of the Base Metal

Prior to heating, the chamber was twice evacuated to ~ 10^{-5} mbar using a turbo pump and then backfilled with argon. All testing in the DSC was done in an argon atmosphere with a flow rate of 50 mL/min.

Profile 1 and Profile 2 (Figure 3.5 a and b, respectively) shows two temperature-time profiles used in this study. Both profiles had a 20°C/min (Kpm) heating and cooling rate with a maximum temperature of 1050°C. The maximum temperature was chosen to be above the α→β transus temperature of pure titanium (indicated by red dots in Figure 3.5) to allow for higher rates of solute transport due to a lower atomic packing factor in the bcc crystal structure. This also avoided the formation of stable intermetallic compounds at the faying surface that would be predicted by the Ti-Cu phase diagram below 989°C and 984°C for the Ti-Ni system.

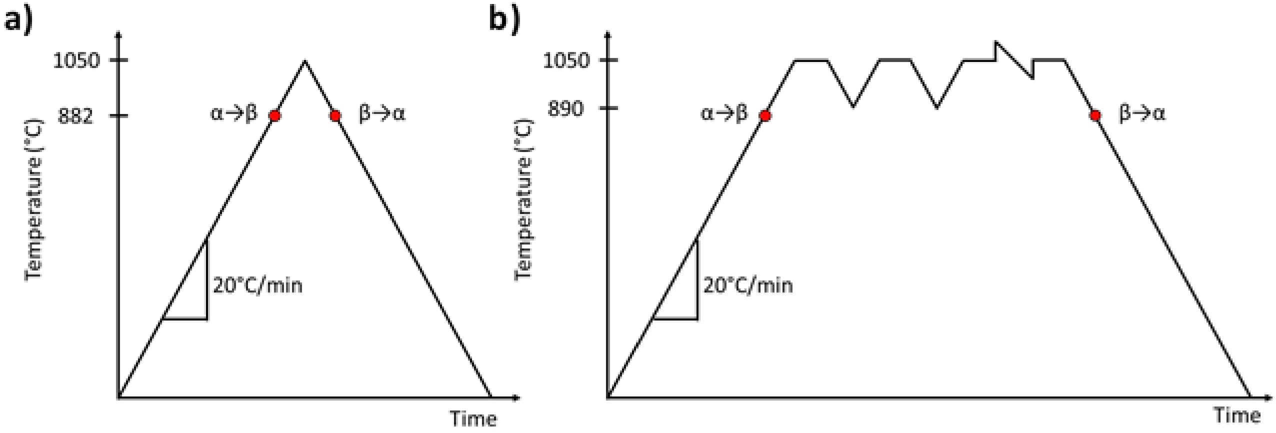

Figure 3.5 - DSC Thermal Profiles Used in Testing (a) Ramp to 1050°C and Cool; (b) Cyclic Testing between 890°C and 1050°C. All Heating and Cooling was Conducted at 20 Kpm Unless Otherwise Specified.

DSC measurements of exothermic and endothermic events were recorded during heating, cooling, and isothermal segments of the temperature profiles. Profile 1 (Figure 3.5a) was designed to characterize the brazing couples upon initial melting, examine the degree of base metal dissolution, and observe solid state interactions. Profile 2 (Figure 3.5b) is a cyclical heating test where the copper or nickel interlayer was melted and solidified several times after short isothermal holds at 1050°C to monitor the liquid fraction (L_f) over liquid duration. Liquid duration in this study is defined as the time between the onset of the melting peak and end of the freezing peak.

Multiple tests were conducted heating to temperatures below 1050°C to examine microstructural development and solid-liquid interactions. These included samples heated to 965, 975, 1000, and 1025°C at a constant rate of heating/cooling (20°C /min). Finally, several samples were heated to 1050°C and held for various times and then cooled. These were termed isothermal hold samples.

Microstructural examination of these samples allowed the evolution of isothermal solidification to be determined with braze time.

During each heating and cooling segment, the enthalpy of melting and solidification of the liquid phase was measured. According to [60], these enthalpy measurements allow a determination of the liquid fraction present as a function of braze time and a determination of the rate of isothermal solidification.

3.2.2 Joints and Tack Welding

The half joints examined within the DSC provided a method of control and consistency when analyzing the detailed mechanisms and kinetics of TLPB for the various titanium systems but did not provide much information concerning braze efficacy. Issues of wetting and porosity between two joining surfaces could not be observed in the microstructure. Several methods were attempted to create full isothermally solidified joints of two titanium pieces. Initially it was thought possible to perform in the DSC so that kinetic information of the liquid could be acquired while joining the samples. Figure 3.6 shows two successfully joined titanium DSC sized slugs joined with a punched undersized nickel foil. The sizes were all similar to previous testing.

While some of these experiments proved successful, there were several problems in the experimental design. The width of the braze gap could not be exactly set, the titanium slugs would shift in the presence of excess liquid, liquid would spread over the sides, and the effects of gravity could not be accounted for. It became necessary to fixture titanium pieces together and to have a defined gap width that was consistent.

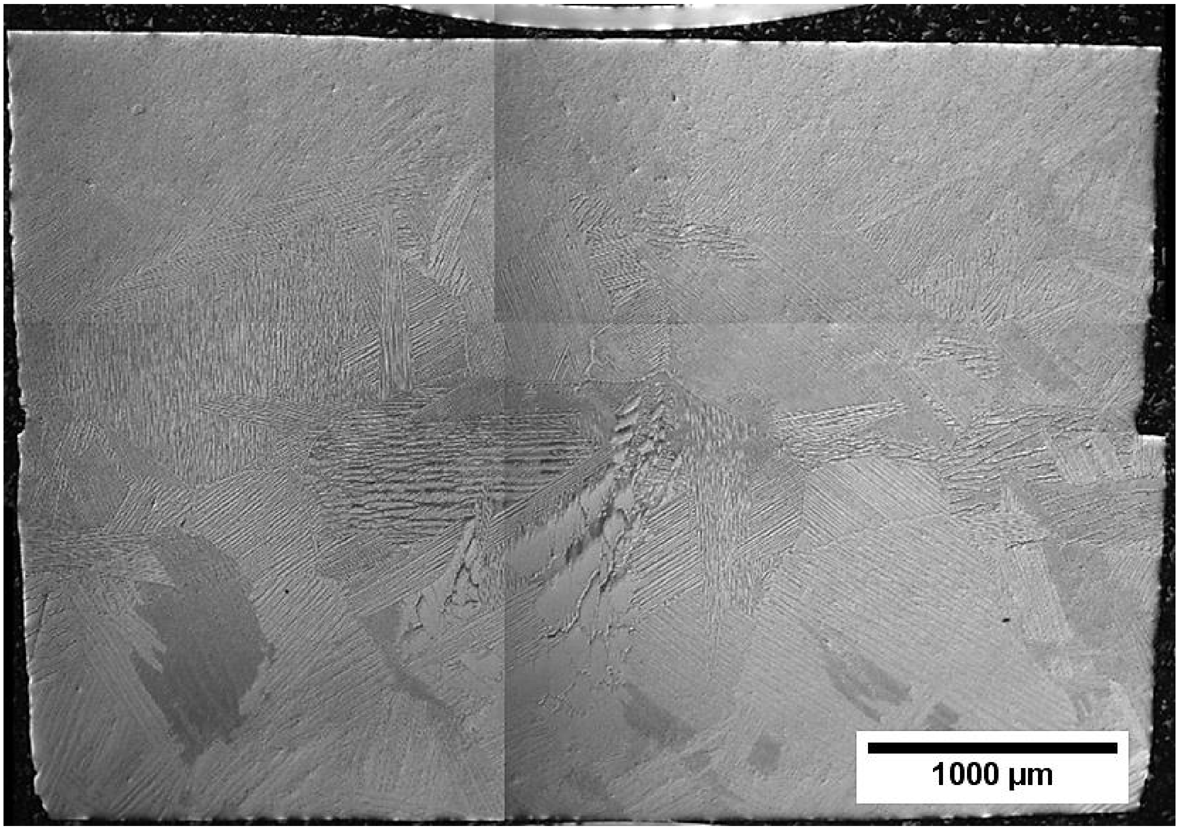

Figure 3.6 - Ti-Ni-Ti Joint Formed in the DSC using 4.76 mm Sized Coupons at 1050°C for 150 min

Using a Hot Spot TC welder (where TC stands for thermocouple), stainless steel balls were tack welded to miniature titanium plates. Figure 3.7 shows the experimental setup. A series of vises were used to hold the two plates together with the foil in between. The anode was attached to the vise holding the sample and the cathode was attached to a copper probe. Prior to clamping these samples were cleaned in acetone, the titanium plates were treated lightly in Kroll's reagent, and the nickel and copper foils were treated with concentrated nitric acid to remove any oxide layers. The foil was placed between the titanium plates and were pressed in a Carver press to one metric ton. This increased metallurgical contact but also helped define a consistent braze gap.

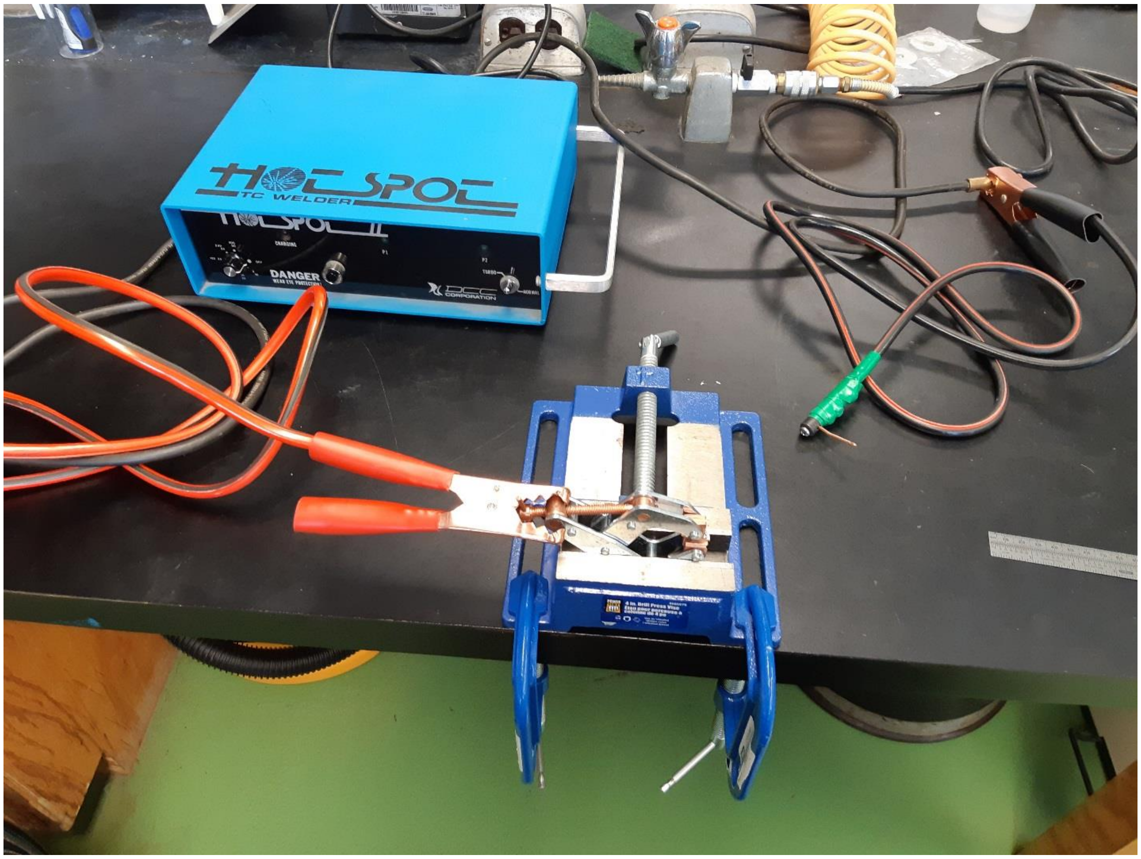

Figure 3.7 - Experimental Setup for Tack Welding Showing Thermocouple Welding Equipment and an Assembly of Vises for Fixturing

Figure 3.8a shows the fixtured plate prior to clamping. The sample dimensions of the top/bottom plate were 10 x 5 x 1.6 mm and were clamped between two copper blocks of the vise. Figure 3.8b shows the experimental setup when tack welding where the copper probe is held firmly against the stainless-steel ball and 120 W·s of energy was applied. This was enough to melt the stainless steel ball and titanium plate interface without melting the entire ball. Four stainless-steel balls were fixtured on the top and bottom of the samples.

Samples were made to the above specifications so that they could be brazed in the dilatometer (DIL). The push rod of the dilatometer was obstructed and the DIL was used as a controlled atmosphere furnace. Samples were painted with StopOff® to prevent spreading of the liquid over the sides. A flow rate of 120 mL/min of Argon was used for all experiments.

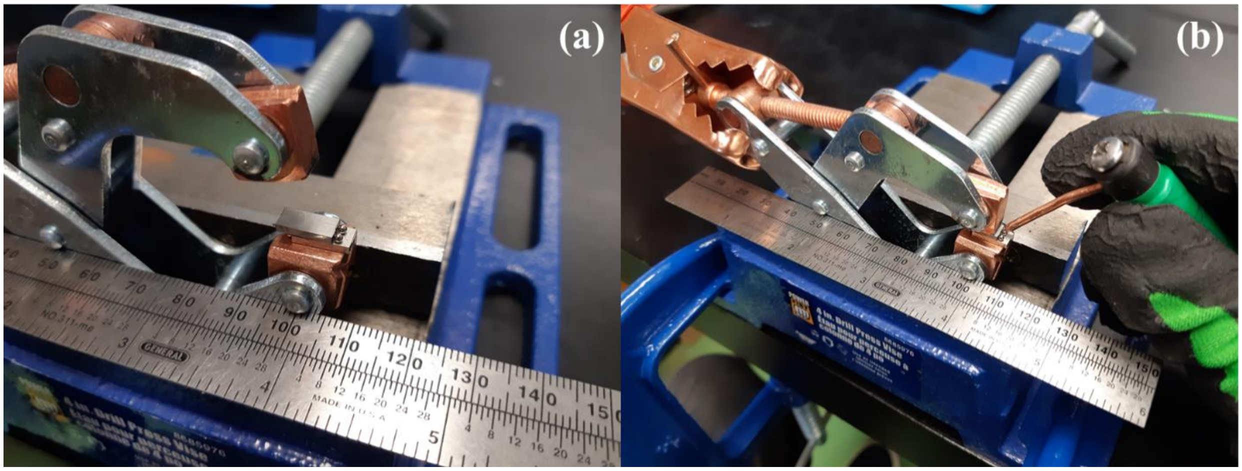

Figure 3.8 - Full Joint DIL Sized Sample in Vise (a) Prior to Welding; (b) During Welding

3.2.3 Dilatometry

For samples too large to fit in the DSC, a Netzsch DIL 402C was used to heat and cool samples in a controlled argon atmosphere similar to DSC testing. Normally this equipment would be for measuring the expansion or shrinkage of a metal part such as sintering applications or examining the coefficient of thermal expansion. Figure 3.9a shows the instrument open with the furnace element moved to the right. Samples are placed in a hollow alumina tube where various alumina supports were used to orient the specimen, see Figure 3.9b. The pushrod for these experiments is pressed against the supports which holds it in place for the duration of testing. The thermocouple is directly adjacent to the sample and piece of titanium foil is wrapped around the inside of the tube as a getter. The sample shown was a full braze joint made with specifications such that it could be placed inside the DIL for experimentation.

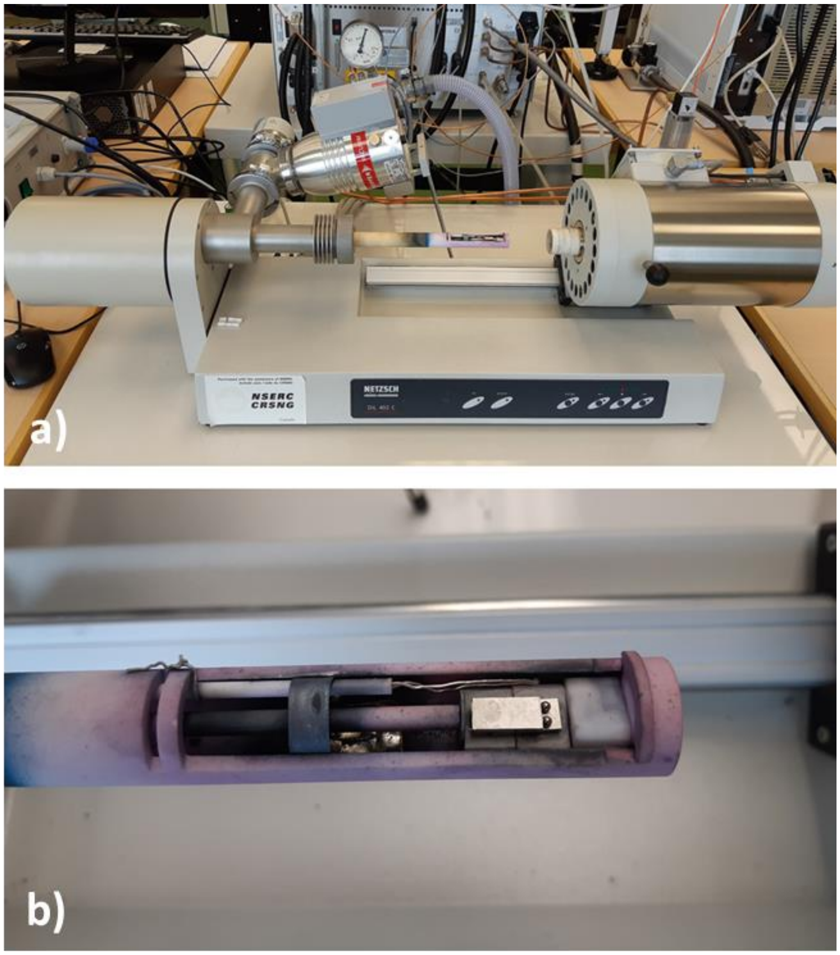

Figure 3.9 - Netzsch DIL 402C at HTTAL Laboratory (a) Open Furnace Chamber and; (b) Imaging of Alumina Tube and Sample

3.3 Microscopy and EDS

Following DSC/DIL testing samples were imaged under a Zeiss 5:1 stereoscope. Images were taken at 2.0X for DSC half joints and 1.0X for full DIL joints to characterize the surfaces. Samples were subsequently mounted in conductive bakelite (Struers Polyfast). DSC half joints were ground using 220 grit until the roughly halfway into the specimen whereas DIL full joints were sectioned in half before mounting using a slow speed diamond saw. Following grinding with 500 grit, both samples were polished using Struers Allegro (9 µm abrasive) and colloidal silica (1 µm abrasive). All samples were etched in Kroll's reagent.

3.3.1 Optical Imaging

Samples were cut and mounted in a conductive epoxy resin prior to grinding and polishing. Specimens were then imaged and subsequently etched using Kroll's reagent. The polished cross sections were viewed under optical microscopy using a Zeiss Axiotech HD 100 microscope. Images were captured using a digital camera at magnifications ranging from 100-1000X.

3.3.2 Sample Orientation and Measurement

Sample orientation became important due to the adjustments made in the experimental methodology as well as in properly characterizing the dissolution process. It was discovered early in the work that titanium copper will not only wet the surface of the titanium slug but is a known filler for ceramic components such as alumina [65]. In one experiment, an excess of liquid wet the entire interior of an alumina crucible but fortunately did not spread around the outside to contact the thermocouples. Experiments following were done with an undersized foil with the foil placed on top of the slug allowing no contact with the alumina walls. This added an extra layer of thermal resistance that had to be accounted for by a correction of the base metal.

Figure 3.10 shows the arrangement of half joint specimens for all experiments with copper and nickel. Foils were punched with a 1/8” (3.175 mm) die set and placed as close as possible to the center of the 4.76 mm titanium slug. With such a small amount of foil (~3.2 mg), the liquid that forms had little time to spread and dissolution occurred rapidly for all specimens. This consumed all of the foil and formed a bowed interface with the titanium base metal. In terms of modelling this formation, the ideal shape was found to be a spherical cap. Measurements taken from the cross section included the max height, width, and angle of the spherical cap.

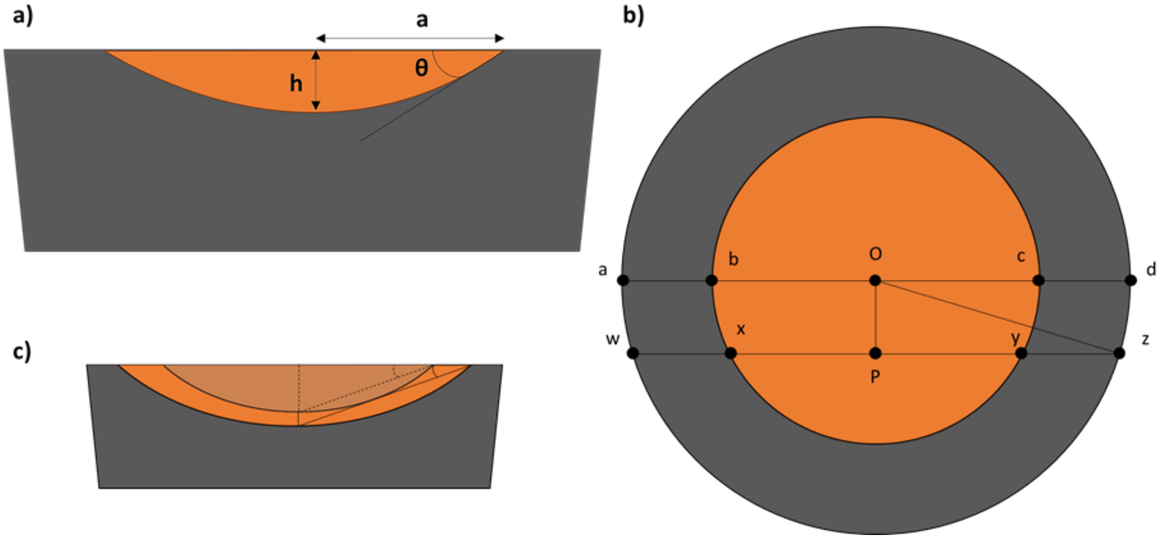

Figure 3.10 - Schematic of Microstructural Projections to Measure the Height at the Sample Middle (a) Schematic of Spherical Cap and Parameters; (b) Top of Sample Surface and Projection (ad); (c) Justification of Constant Width to Height Ratio

Accurate modelling of a spherical cap requires the absolute maximum height to be known for proper volume calculations. Unfortunately, it is very difficult to grind/polish samples to the exact center of a sample. Mathematical approximations were implemented using trigonometry and the known distances in the sample, see Figure 3.10b. For example, if the sample was only polished to wz, the distance oz is the radius of the slug and the value for OP can be found. This is the distance away from the center of the sample. Using this value, an approximation of values such as Oc can be made. Figure 3.10c demonstrates that the angle of the interface remains the same grinding further into the sample such that the ratio of Oc/Py can be used to determine the height at the center. To determine the microstructural morphology from a three-dimensional perspective, samples were also polished from the surface inwards such as the orientation in Figure 4.5.

The volume of the spherical cap can be used to determine the amount of liquid remaining and is calculated using:

$$\boldsymbol{V_{cap} = \frac{\pi h}{6}\left(3a^2 + h^2\right)} \tag{3.1}$$

Note that the angle θ is not necessary in these calculations. Using these measurements and volumes, the maximum depth of dissolution as well as liquid and volume fractions could be found.

The layout of the full joints is shown in Figure 3.11. With the presence of two brazing surfaces, dissolution would result in half of the maximum width of dissolution (W_{max}) above and below the joint centerline such that wetting of the liquid along the sides of the sample was not an issue. Foils were placed in the center and stainless steel balls were tack welded such that the assembly was rigid with a defined braze gap. A planar geometry was possible with these samples though there was heterogeneity across the joint when an excess of liquid was present. Samples to be used in optical and SEM characterization were sectioned in half between the stainless steel balls shown in the bottom two figures of the schematic. Since the foil was uniformly spread throughout the braze gap, there was no need to polish directly into the centerline for these specimens.

Two contrasting tests were selected to examine the efficacy of full titanium joints, shown in Figure 3.11. To examine the validity of the $2W_{ISZ}$ curve in predicting the remaining widths of the isothermally solidified zone (ISZ) and athermally solidified zone (ASZ), a pre-sandwiched assembly with two foils was heated to 1050°C and immediately cooled at 80 Kpm. The ASZ is the remaining liquid which solidifies upon freezing and the ISZ is the layer of solidified base metal resulting from isothermal solidification. It should be noted that the DIL was not capable of cooling at 80 Kpm and a heating rate closer to 40 Kpm was observed when testing. In a second experiment, a capillary action assembly was created with one foil, heated to 1050°C holding for 75 minutes, and subsequently cooled at 20 Kpm (see Figure 3.11b). This was done to examine the effects of homogenization and quantifying the extent of wetting and capillary action.

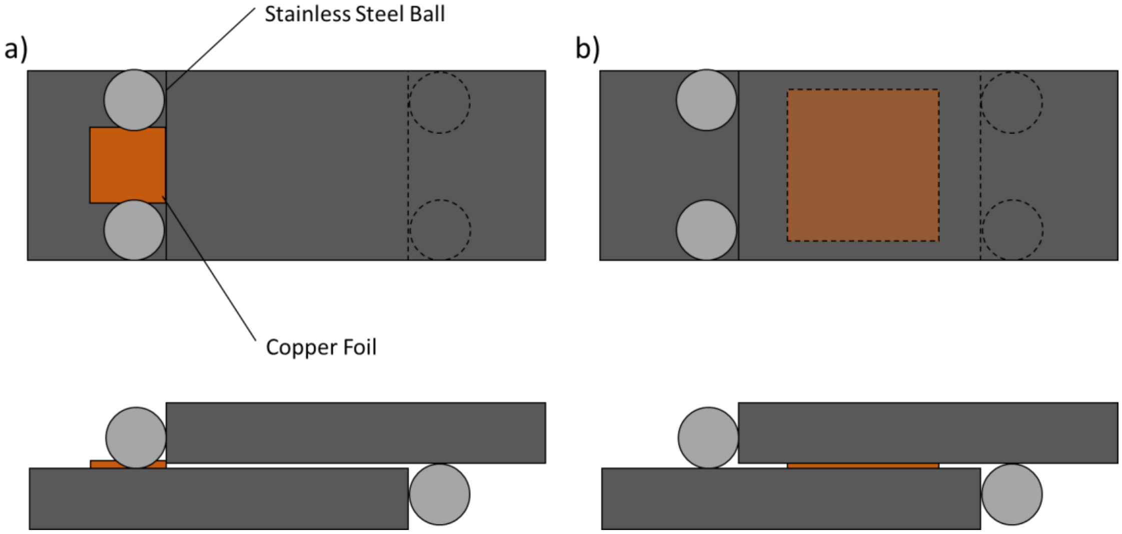

Figure 3.11 - Experimental Setup for Full Joint Assemblies using (a) Capillary Action Assembly and; (b) Pre-Sandwiched Assembly

3.3.3 Scanning Electron Microscopy

A Hitachi Cold-Field Emission S4700 scanning electron microscope (SEM) was used for high magnification metallographic examination of specimens. A 20 keV acceleration voltage was used. Samples used in optical microscopy were also used during SEM examination. Secondary electron imaging was used to interpret the morphology and topographical contrast of the sections. A JEOL 8200 Super Probe was used for all EDS data. All values were measured in wt% and the resolution of the probe was ±1 wt% [66].

Compositional profiles were constructed from EDS measurements beginning at the sample surface and completing when the interlayer solute could no longer be detected. Individual point scans lead to inconsistent results due to local fluctuations in composition caused by varying densities of precipitates in the sample. Instead, box scans at a given depth were taken when measuring the ASZ, ISZ, and into the base metal.

The depth of the box scan was measured from the sample surface to the middle of each individual box scan. These box scans were taken in areas of homogenous microstructure and were made short in height so that the middle of the scan best represented the given depth. Figure 3.12 provides an example of this for a titanium nickel sample which has been cycled. Measurements are taken along the ASZ around the dendrites to measure the eutectic composition and then box scans continue into the ISZ. The measurement of the depth for spectrum nine is demonstrated in the figure.

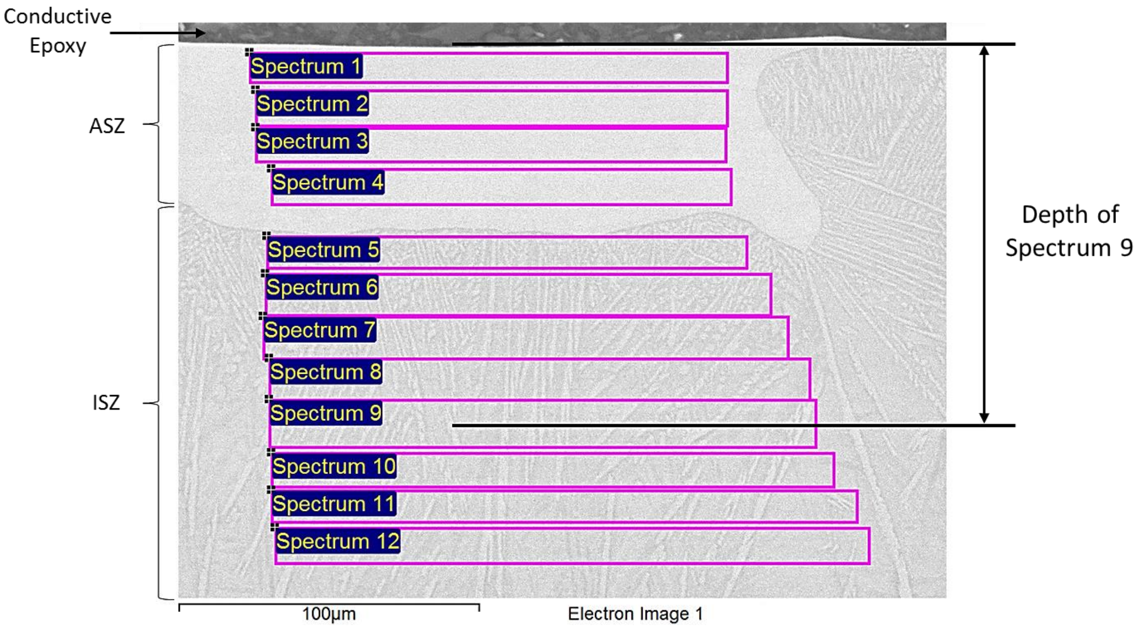

Figure 3.12 – Example of EDS Measurements in a Titanium Nickel Sample Cycled Eight Times

3.4 Microhardness Testing

Full joint samples were tested using two foils creating a braze gap of 100 µm which created enough liquid to leave an ASZ remaining upon cooling after 0 min. These full joints were heated in the DIL to 1050°C and immediately cooled at 20 Kpm. A single sample was created for each material system and foil, Grade 2 and 5 titanium coupled with copper and nickel. These samples were sent to Material Property Assessment Laboratory (MPAL) located at McMaster University under Dr. Veldhuis and Dr. Bose. Two linear hardness profiles were taken such that indentations were taken in the base metal, the ISZ, and the ASZ.

Figure 3.13 shows the hardness profiles across a Ti-6-4 full joint using copper as a filler metal courtesy of the MPAL laboratory. Microindentations were taken using a MicroMaterials NanoTest Platform 3. Indents were taken using a 50 mN load creating triangular indents which were roughly

10 μm in size. Twenty data points were taken for each line with a spacing of 25 μm between indents.

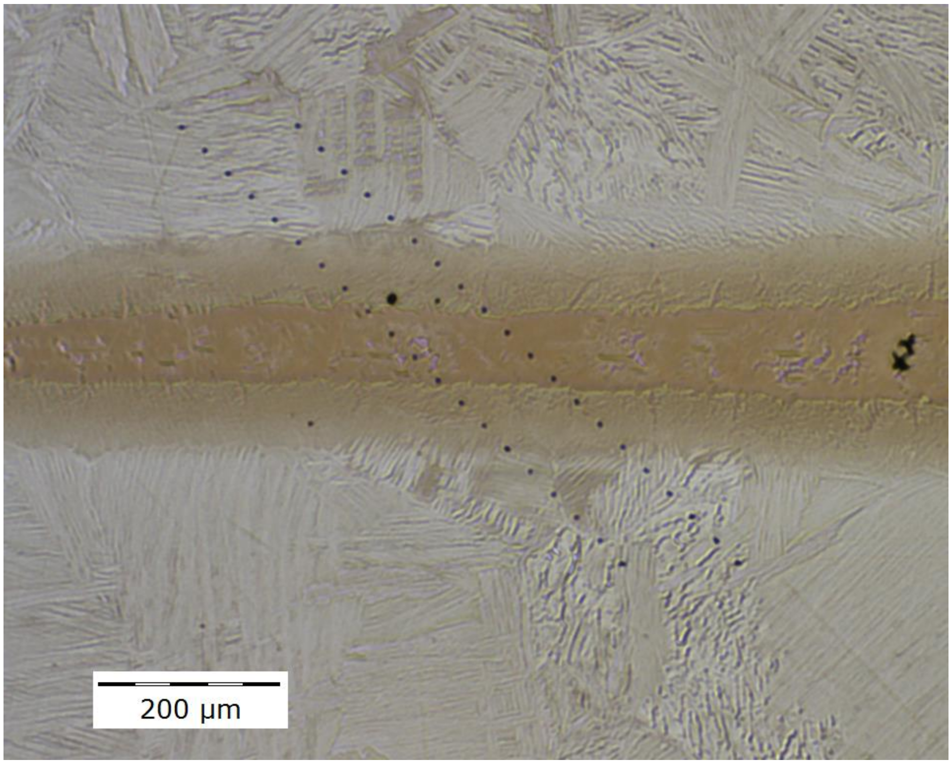

Figure 3.13 - Hardness Profiles Across a Ti-6Al-4V and Copper Sandwich Full Joint Using Two Foils, Heated to 1050°C, and Cooled at 20 Kpm

4.0 Commercially Pure Titanium and Copper

4.1 Initial Heating and Dissolution

Figure 4.1 shows the DSC results of Ti-Cu half braze joints heated and cooled from 975, 1000, and 1025°C. In all tests, the titanium undergoes the α→β transformation in the same manner. Since the presence of copper in titanium alters this phase transformation temperature, minimal amounts of long-range diffusion into the base metal occurred during heating since the β→α transition remains unchanged.

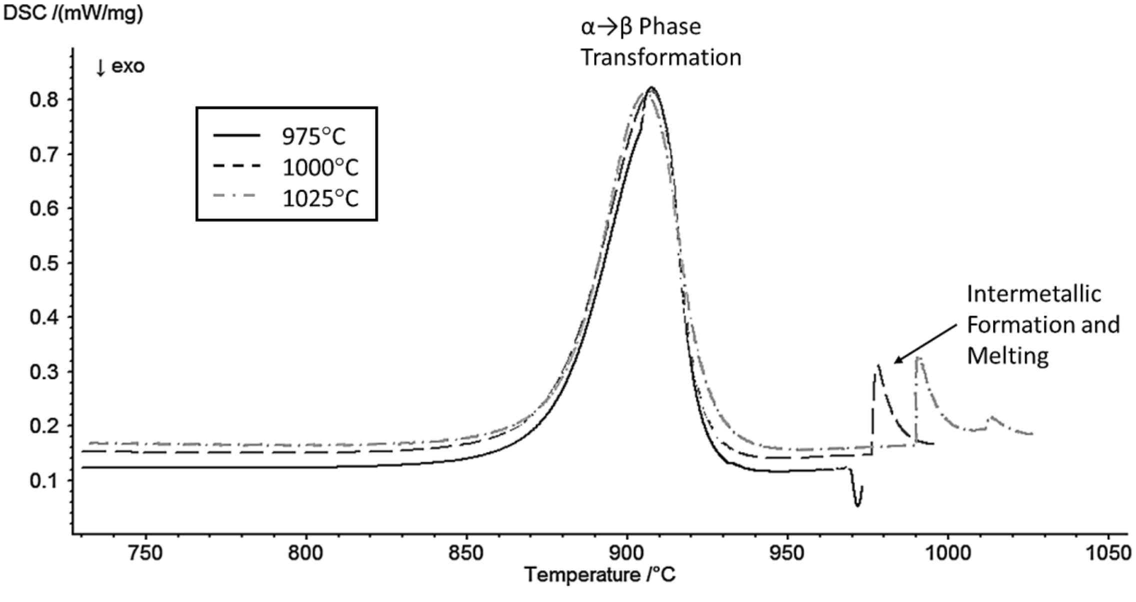

Figure 4.1 - DSC Heating Trace for Titanium Copper Half Joints Heated to 975, 1000, 1025°C

During heating, an exothermic peak indicating intermetallic formation was observed in the 975°C sample close to the TiCu -Ti_2Cu eutectic temperature of 960°C. The 1000°C and 1025°C exhibited endothermic peaks beginning at 975°C and 990°C respectively indicating melt formation, with no exothermic signal present. These are indicative of the L→TiCu reaction (985°C ± 10°C) according to Murray *et al.* [56]. For all samples, the copper foil interacts with the titanium surface, forms intermetallics, and rapidly dissolves the base metal incorporating large amounts of titanium. This will involve the nucleation and melting of TiCu as the liquid becomes increasingly titanium rich in composition.

Upon cooling, see Figure 4.2, all samples indicated eutectic formation (L→TiCu+Ti_2Cu) evident by the presence of an exothermic peak observed just below 960°C with varying degrees of undercooling. The 1000°C and 1025°C samples also indicate a smaller and broader higher temperature exothermic peak which likely corresponds to the peritectic reaction (L + (β-Ti) = Ti_2Cu). All samples showed a small exotherm around 803°C which corresponds to the eutectoid reaction ((β-Ti) = (α-Ti) + Ti_2Cu). This indicates some short-range diffusion of Cu into the titanium base metal near the faying surface.

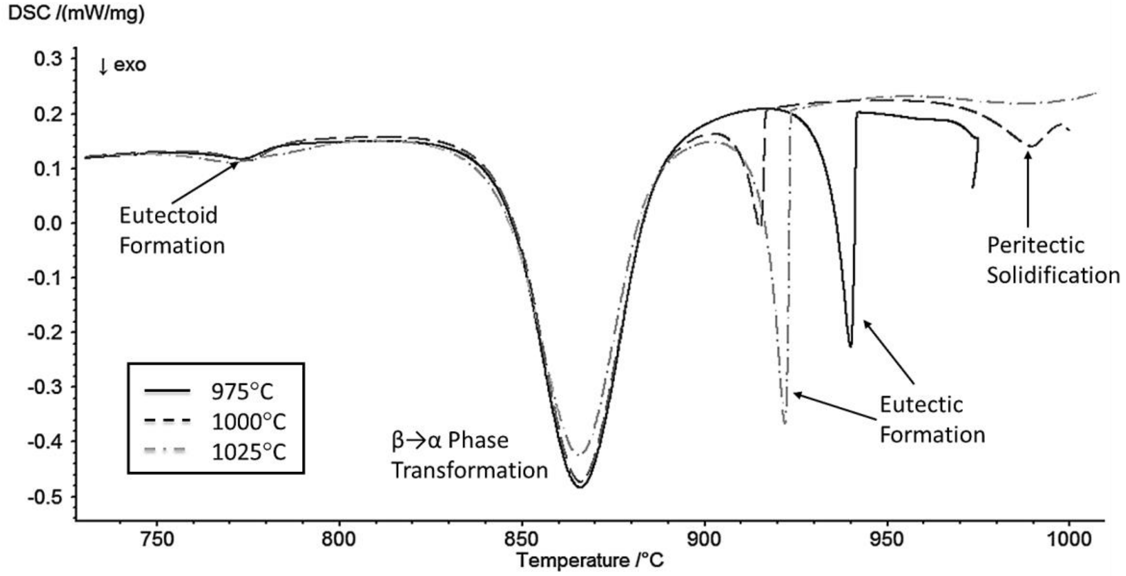

Figure 4.2 - DSC Cooling Trace for Titanium Copper Half Joints Heated to 975, 1000, 1025°C

The temperature difference between the eutectic and peritectic is small and the freezing event for most DSC samples presented later showed a single peak upon cooling. It is likely that the eutectic is occurring concurrently, or immediately following, the peritectic transformation.

Figure 4.3 shows the resultant microstructures of these DSC tests. All phases were confirmed using EDS, see Table 4.1. Large differences in microstructure are due to the temperatures chosen which are below, on, and above the line demarcating the peritectic phase transition at 989°C. However, independent of the temperature chosen, a layer of the diffusionally affected zone (DAZ) with a composition of approximately Ti-8 wt% Cu is present in each sample. Based on the Ti-Cu phase diagram, this region would have been undissolved, solid base metal with a (β-Ti) structure at the braze temperature. Upon cooling, much of this region would undergo the solid-state eutectoid reaction at 803°C, which is evident from the DSC cooling traces. Some of these regions may have remained as retained (β-Ti).

Examining the 975°C microstructure in the top of Figure 4.3, an initial interaction of the pure copper and titanium lead to a molten zone formed by dissolution of the base metal. No evidence of the starting pure Cu, or unmelted Cu rich intermetallic compounds including Ti_2Cu_3, Ti_5Cu_6 etc. (associated with the original location of the Cu foil) were found. At the braze temperature following dissolution, a diffusion couple of β-Ti/Ti_2Cu/L was established. This was evidenced by a thin, continuous layer of Ti_2Cu which has formed prior to solidification.

As the liquid cools from 975°C, the Ti_2Cu layer begins to exhibit dendritic solidification. Excess solute is rejected from this dendritic growth until cooling below the eutectic temperature of 960°C.

At this point, the remaining liquid forms an interdentritic eutectic mixture of TiCu + Ti_2Cu. The curved interface of the liquid demarcates the solid-liquid interface location and was characterized as the athermally solidified zone (ASZ).

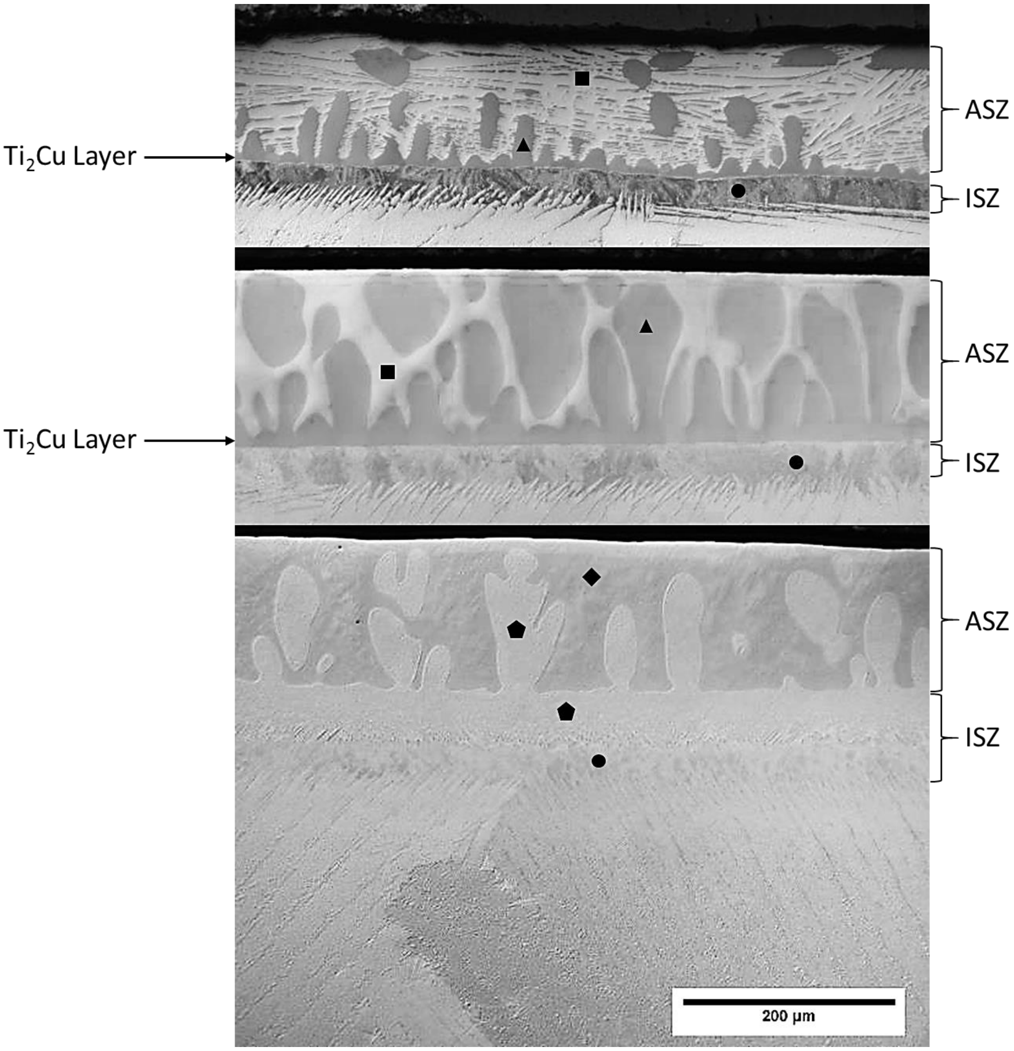

Figure 4.3 - Optical Imaging of Microstructural Cross Sections of Titanium Copper Samples Heated to Top: 975°C; Middle: 1000°C; and Bottom: 1025°C. Symbols Found in Table 4.1.

The 1000°C (middle figure) remained below the peritectic temperature as evidenced by a similar microstructure to that observed in the 975°C sample. Continued Ti_2Cu dendritic growth occurred coupled with the formation of interdendritic eutectic structure. The fraction of solidification that occurred through the eutectic reaction decreased when compared to the 975°C sample. This is evidence of increasing dissolution of the base metal and an enriched titanium composition.

The 1025°C (bottom figure) lies above the peritectic temperature and a marked change is observed in the solidification structure. The liquid is now above the peritectic temperature (989°C) such that any Ti_2Cu which had formed melts and upon cooling the ASZ now undergoes the peritectic reaction. Dendrites of (β-Ti) grow into the liquid with a composition in the range of 27 wt% Cu. In the interdendritic spaces, an initial layer of Ti_2Cu is observed followed by the formation of a eutectic structure with small amounts of TiCu. This microstructure matches classic peritectic solidification [67].

Upon further cooling in the solid state the (β-Ti) dendrites within the ASZ precipitate Ti_2Cu by solid state reaction which can be described as hypereutectoid according to the Ti-Cu phase diagram. The DAZ region also contains a high volume faction of Ti_2Cu precipitation through the hypereutectoid reaction. The volume fraction of these precipitates reduces along the Cu concentration gradient with no more large precipitates observed below the eutectoid composition (~8 wt% Cu). Below 803°C all remaining (β-Ti) undergoes the eutectoid reaction resulting in a

Table 4.1 - EDS Compositions of Phases Observed in Initial Heating Samples

Symbol	Conc. Ti (wt%)	Conc. Cu (wt%)	Phase
■	50.93 ± 0.71	49.07 ± 0.71	Eutectic
◆	55.90 ± 1.39	44.10 ± 1.39	Hypo-Eutectic (Ti_2Cu-rich)
▲	60.70 ± 0.79	39.30 ± 0.79	Ti_2Cu-rich Peritectic
★	72.07 ± 0.46	27.93 ± 0.46	Eutectoid + Ti_2Cu
⬟	80.60 ± 2.74	19.40 ± 2.74	Eutectoid + Ti_2Cu
●	91.99 ± 0.45	8.01 ± 0.45	Eutectoid

finely divided eutectoid microstructure. All microstructural regions measured using EDS are labelled on Figures 4.3 with the values included in Table 4.1.

Samples heated to the braze temperature of 1050°C were examined at a typical 20 Kpm cooling rate. In an effort to preserve the microstructure immediately developed at 1050°C and more accurately measure the maximum amount of dissolution another sample was ‘fast’ cooled from 1050°C using an 80 Kpm cooling rate. Figure 4.4a shows the typical 1050°C microstructure with the ASZ and DAZ labelled. The compositions and microstructure are similar to the 1025°C sample. (β-Ti) dendritic growth is observed with a composition close to that of the DAZ close to the solid-liquid interface (19 to 21 wt% Cu). Interdendritic Ti_2Cu forms as well as a eutectic structure in the last liquid to freeze. The exception to the previous microstructures would be the formation of a lamellar hypoeutectic of TiCu and Ti_2Cu which forms in the interdendritic regions (designated by the ♦ symbol).

In comparison, the sample cooled at 80 Kpm has a larger ASZ and also lower Cu diffusion into the base metal, as evidence by the thinner DAZ layer seen in Figure 4.4b. This was as close an approximation as possible to a microstructural measurement of the maximum depth of dissolution developed while heating to 1050°C. Secondary arms are visible on the dendrites from the increased level of undercooling and again the formation of solid-state Ti_2Cu precipitates is observed in the dendrites and into the DAZ. This sample will later be used to assist in the confirmation of the maximum depth of dissolution.

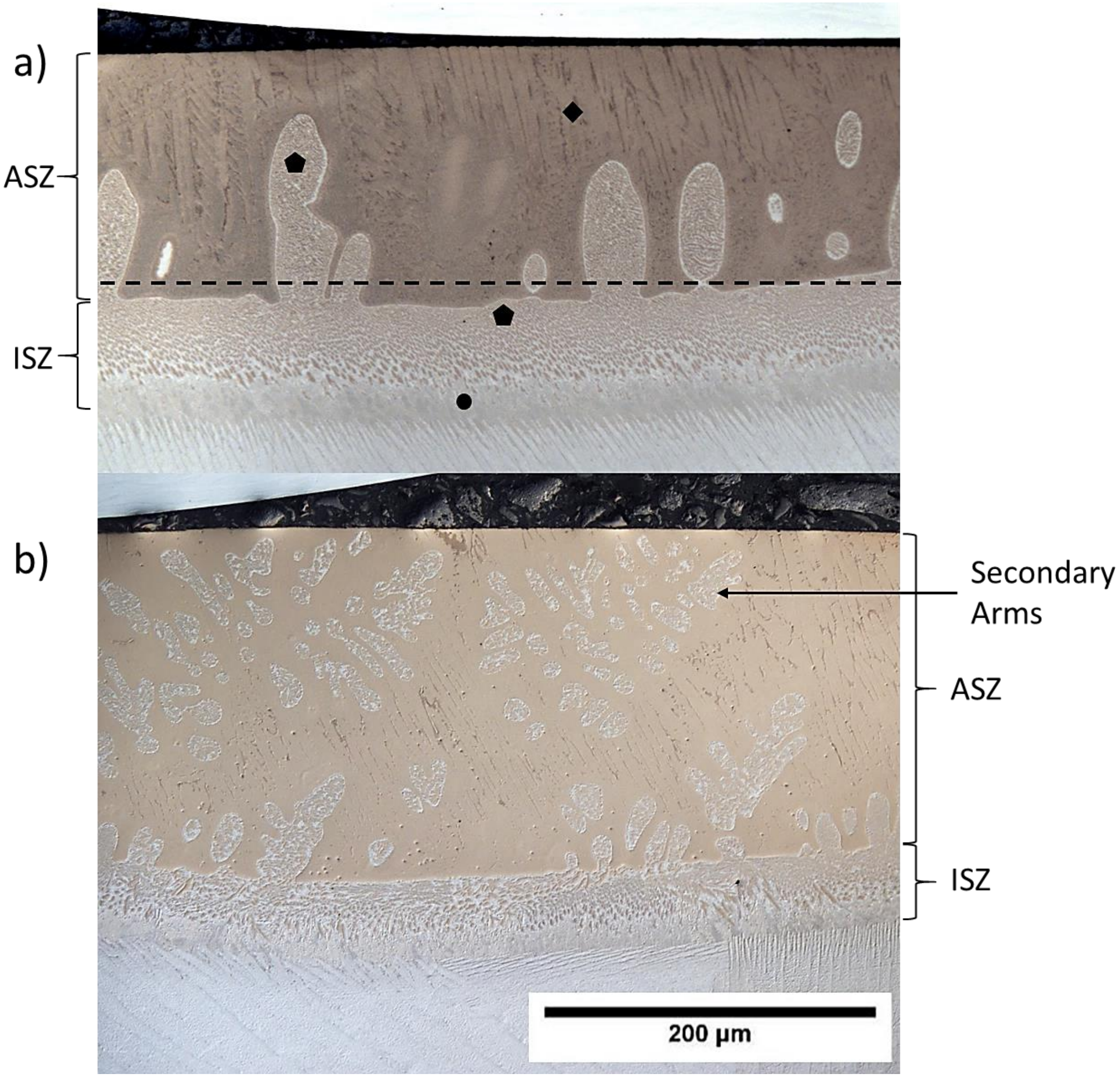

Figure 4.4 – Optical Imaging of Microstructural Cross Sections of Titanium Copper Samples Heated to 1050°C and Cooled at (a) 20 Kpm; (b) 80 Kpm. Symbols Found in Table 4.1. The Dashed Line in the 20 Kpm Sample Represents Distance of Grinding/Polishing in Figure 4.5.

To confirm that the peritectic transformation and microstructure were consistent, a sample processed under identical conditions to that of Figure 4.4a was mounted with the faying surface facing out such that the braze area could be ground in from the surface. The dashed line in Figure 4.4a denotes the depth to which the sample was polished. Figure 4.5a shows the resultant microstructure where the sample was polished roughly 200 µm into the braze surface. A small amount of ASZ remains surrounded by DAZ microstructure. Figures 4.5b and 4.5c confirms that (β-Ti) dendritic solidification along with interdendritic Ti_2Cu. Solid-state hypereutectoid Ti_2Cu precipitates within the dendrites are clearly visible.

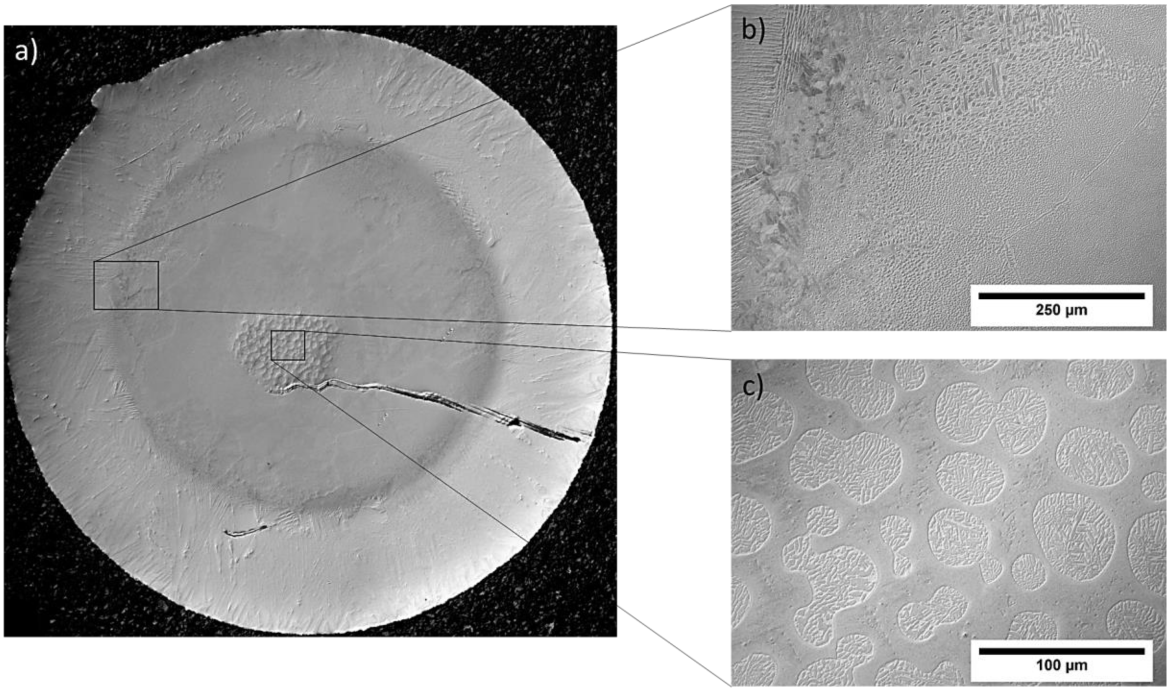

Figure 4.5 – Optical Imaging of Topographical Microstructure of Ti-Cu Sample Heated to 1050°C and Cooled at 20 Kpm

4.2 Isothermal Solidification

Isothermal solidification was examined using the cyclical DSC techniques discussed in section 3.2.2. Figures 4.6 and 4.7 show the DSC trace of a titanium sample with copper foil repeatedly heated to 1050°C, held for three minutes and cooled to 890°C. Individual heat and cool segments are shown in greyscale with dashed lines, whereas the initial heating segment is solid. Using

Netzsch software the start of melting during heating and the end time of solidification during cooling was documented. From these values a total time of liquid duration for the braze foil was estimated. For each successive run, the total amount of liquid duration is noted beside the peak.

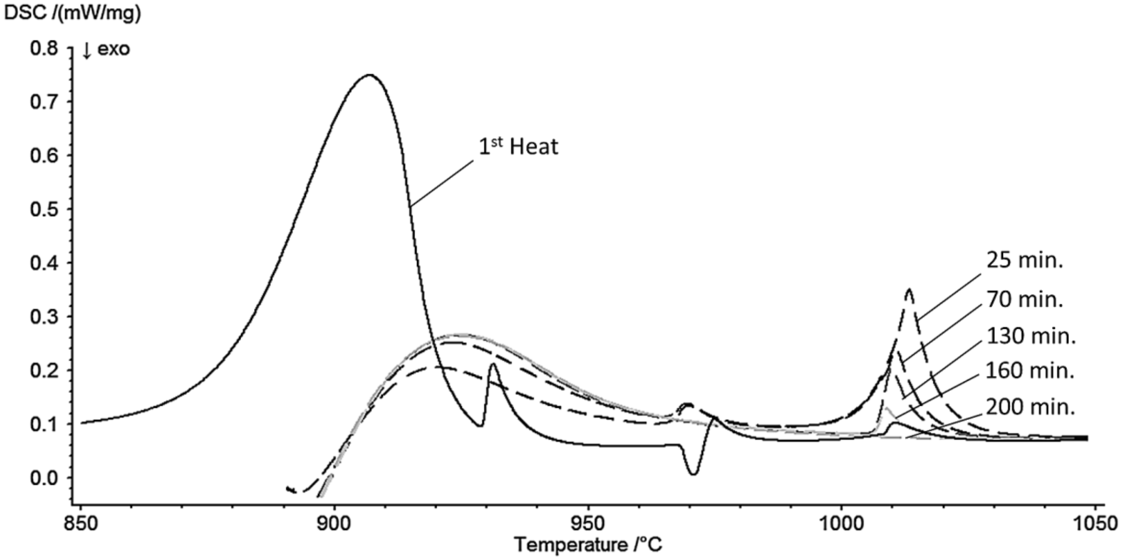

Figure 4.6 - Heating Traces for Titanium Copper Sample Heated Cyclically for 18 Cycles

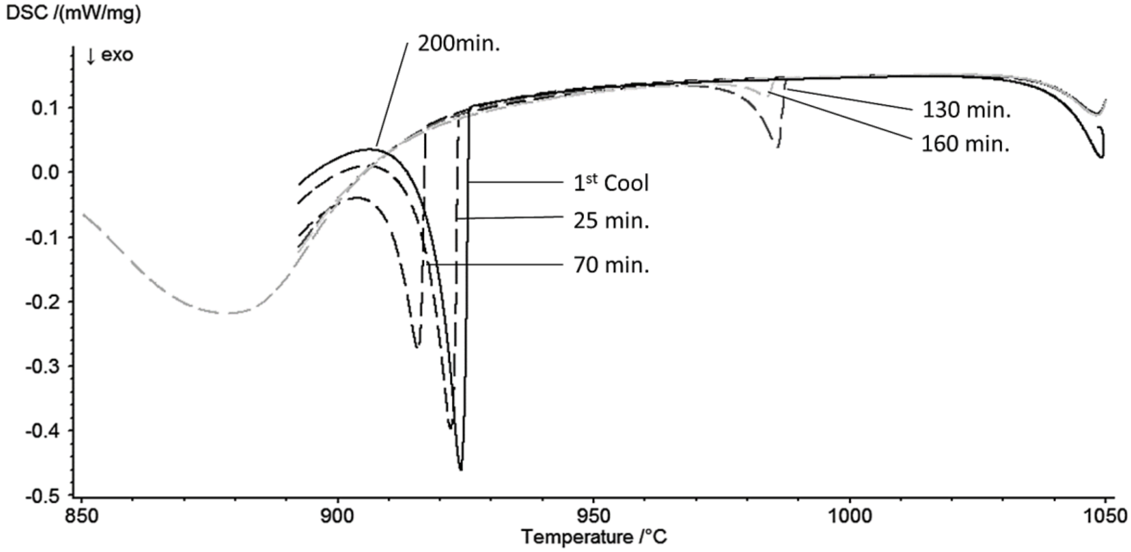

Figure 4.7 - Cooling Traces for Titanium Copper Sample Heated Cyclically for 18 Cycles

The initial heating traces exhibit two endothermic peaks, one onsetting at 965°C which corresponds to the reverse eutectic reaction (TiCu + Ti_2Cu = L), and the second onsetting near 989°C corresponding to the reverse peritectic reaction (Ti_2Cu = L + β-Ti). This melting sequence is consistent with the solidified microstructure reported for the 1050°C 20 Kpm and 80 Kpm cooled samples reported above. Overall, the magnitude of the peritectic endotherm is much larger than the eutectic. Both peaks depreciate in magnitude with increasing time in a manner consistent with isothermal solidification. After 220 minutes of liquid duration, no melting peaks were observed, indicating complete IS. The eutectic peak reduces to zero while the peritectic remains to longer cycling times. The left-hand shoulder of the peritectic peak shifts to a higher temperature and sharpens after the 70-minute peak, corresponding to when the eutectic peak disappears. This sharp onset at 989°C indicates that a precise peritectic reaction is the only melting event occurring after roughly 100-150 minutes. This will be discussed in more detail with Figure 4.9.

Figure 4.7 shows the associated cooling curves for the same cyclical experiment. A degree of undercooling is observed such that the freezing of both the peritectic and eutectic occur well below 965°C. This particular sample coincides with the data of the cyclic test used to generate the data of Figure 4.9. The eutectic reaction persists for roughly 150 minutes where a marked change in the freezing peak onset is observed as noted above. Subsequently only the formation of the peritectic is observed until no solidification peak appears and all liquid is removed after 220 minutes, consistent with the melting traces.

Figure 4.8 contrasts the DSC trace for a sample heated to 1050°C, and immediately cooled, with the cyclically heated specimen that has undergone complete isothermal solidification, corresponding to a brazing time of 220 minutes. The cooling phase transformation of the titanium base metal is significantly influenced by the brazing process. The transition from β→α is observed with a noticeable shift in temperature and a broadening temperature range. The eutectoid reaction peak observed at 803°C is more prominent on the cyclical specimen in terms of a wider compositional range and overall abundance. Both these changes are consistent with an increase Cu content and increased long-range diffusion of copper into the base metal during isothermal solidification.

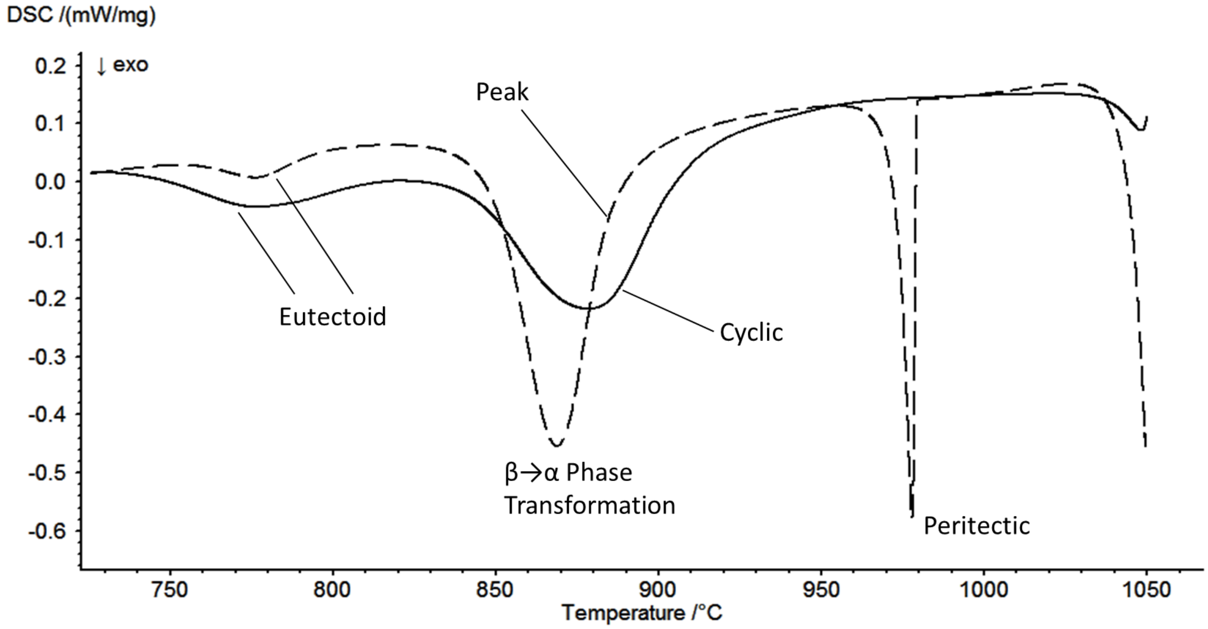

Figure 4.8 - Comparing 1050°C 20 Kpm Peak Sample and Last Cooling Cycle of 18 Cycle Sample

Figure 4.9 shows the melting enthalpies of the eutectic and peritectic reactions observed for three separate cyclical samples which achieved complete isothermal solidification. Note that the enthalpy is expressed as a function of the initial weight of the Cu foil used.

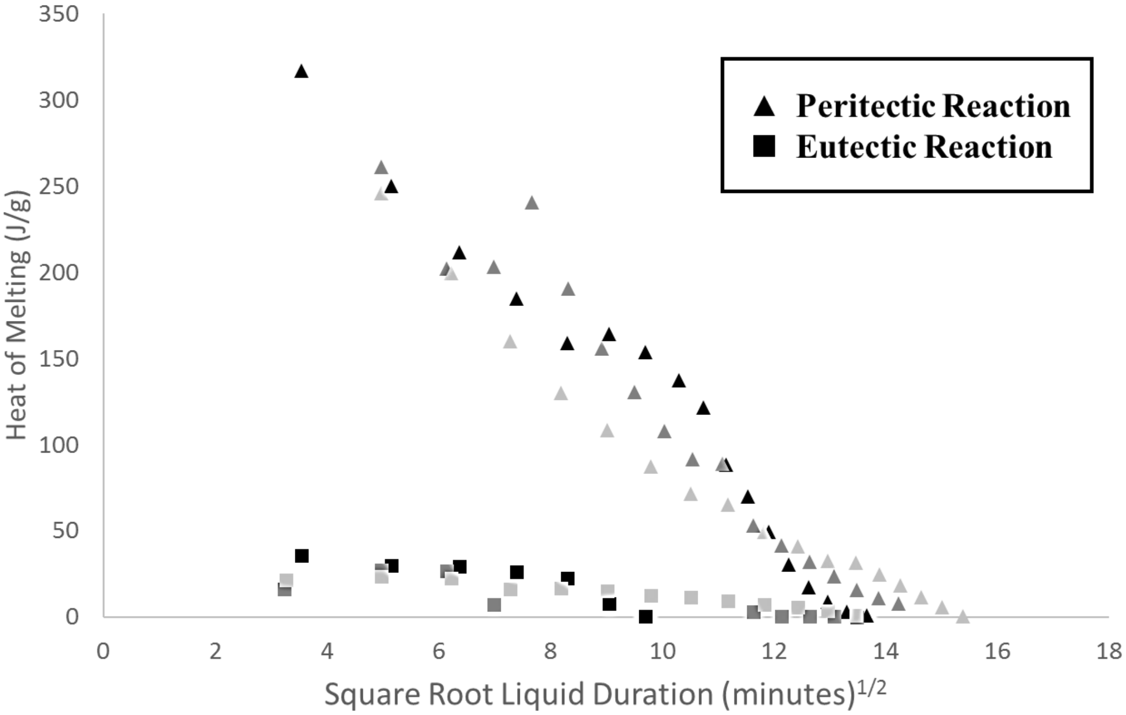

Figure 4.9 - Cyclical Heating Trace Data for Individual Eutectic and Peritectic Melting Peaks

The eutectic reaction is observed for the approximately 150 minutes of liquid duration. A notable shift occurred in the slope of these cyclical samples undergoing isothermal solidification in Figure 4.9. This shift was thought to occur as a result of the eutectic reaction no longer remaining to freeze concurrently with the peritectic reaction. Examining the onset of the cooling exotherm (see Figure 4.7), a noted shift in the temperature onset from 915-940°C to 985°C was found at the same cycle as when this shift occurs. This alters the liquid duration length per cycle and shows up as a 'kink' in the DSC cyclic testing.

As seen in Corbin *et al.*, similar isothermal solidification trends were observed in the melting of the eutectic phase during solidification with a decreasing trend in their respective enthalpies [60]. This shows that liquid is continuously isothermally solidifying during the process which can be plotted versus the square root of time. It has been shown elsewhere that isothermal solidification is a parabolic relationship of melting/solidifying enthalpies with time [60][68]. Figure 4.10 shows that this relation holds for the Ti-Cu system subjected to multiple experiments including three complete isothermal solidification cycles (18x), halted cycles (2x, 8x), as well as isothermal holds of 15, 30, 60 and 120 minutes.

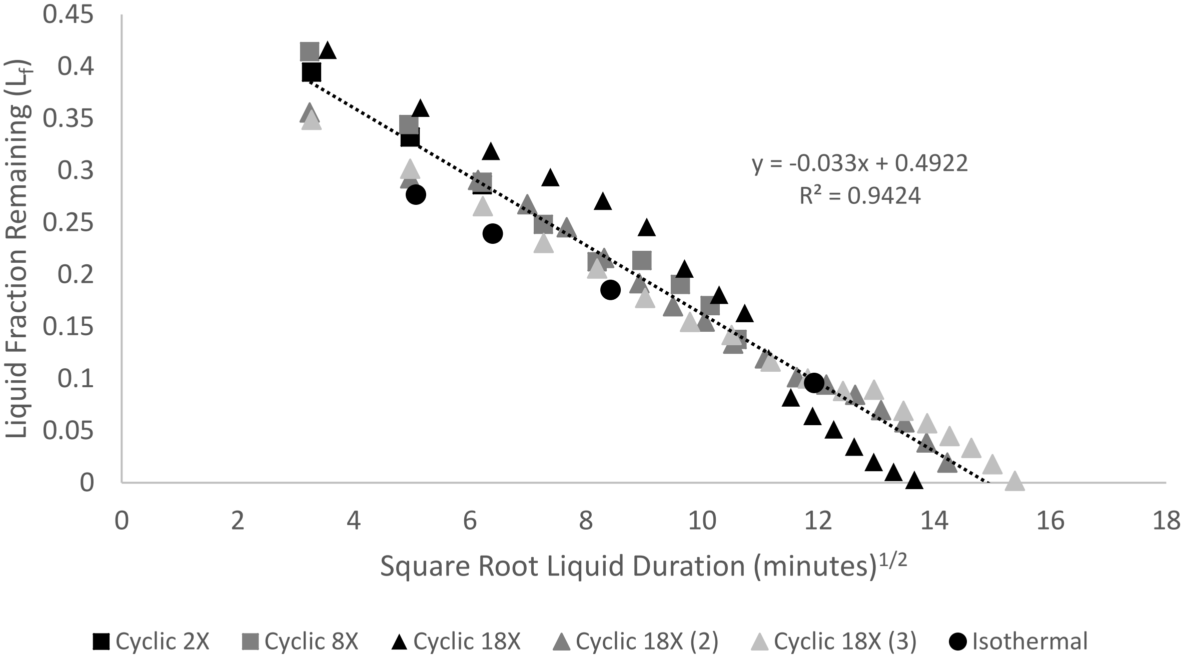

Figure 4.10 - Enthalpy of Solidification Data from Cyclical Testing of Copper and Commercially Pure Titanium

4.3 Determining Liquid Fraction from DSC Enthalpy Measurements

Isothermal solidification behaviour is most commonly interpreted and analyzed based on a gap dimension in microns. A number of steps are required to convert an enthalpy of melting (or solidification) measurement to a gap dimension including a determination of liquid fraction. A theoretical initial enthalpy for the filler metal, is needed in isothermal solidification studies using DSC, to calculate the remaining liquid fraction [69]. Since the filler metal in this case is formed in-situ during dissolution, it was not possible to experimentally measure a filler metal enthalpy directly. The previous section demonstrated that the liquid solidifies predominantly through the peritectic reaction, forming Ti_2Cu. Therefore, it was assumed that the appropriate initial enthalpy for this solidification reaction could be represented by the Ti_2Cu solidification enthalpy of formation, 423.8 J/g, stated in reference [70].

To determine the liquid metal mass, it was assumed that all the copper foil would homogenize to the liquidus composition at 1050°C. As an example, the average copper foil weight was 3.2 mg and the liquidus concentration was 41.5 wt% Cu according to the binary Ti-Cu phase diagram. However, a measured value of 39.3 wt% represents the average of three EDS bulk scans (both the eutectic and the primary dendrites) taken in the 80 Kpm sample ASZ. This value was used instead of 41.5 wt% to more accurately describe experimental observations. Thus, at melting there would be a maximum of 8.14 mg of liquid filler since over forty percent of the entire filler would be copper. Using this value, the respective weights of samples were corrected to only reflect the weight of the filler formed through dissolution.

Together, the above parameters allowed a corrected liquid fraction to be calculated based on the raw enthalpy measurement ΔH_m plotted in Figure 4.10 as;

$$\boldsymbol{L_f = \frac{\Delta H^c{}_m}{\Delta H_{theo}} = \frac{0.393 * 1.188 * \Delta H_m}{423.8}} \tag{4.1}$$

Where 0.393 corrects for dissolution and 1.188 corrects for the presence of the titanium base metal as previously explained in Section 3.2. The terms ΔH^c_m represents the corrected measured enthalpy and the ΔH_m is the direct measured enthalpy from the DSC.

Figure 4.11 plots this calculated liquid fraction versus the square root of braze time. From these calculated values the initial liquid upon melting and cooling was already below 50% suggesting a high degree of liquid reduction during initial heating to the braze temperature through diffusional solidification. This is consistent with the microstructures of Figure 4.4. The liquid duration of the 80 Kpm and 20 Kpm samples are 6.4 and 8 minutes respectively. In the short time frame, a significant reduction in the thickness of the ASZ has already occurred. A significant amount of Cu has diffused into the base metal as well, evidenced by the measurable DAZ thickness. A linear regression analysis of data from three Cyclic 18X samples was performed and is included in Figure

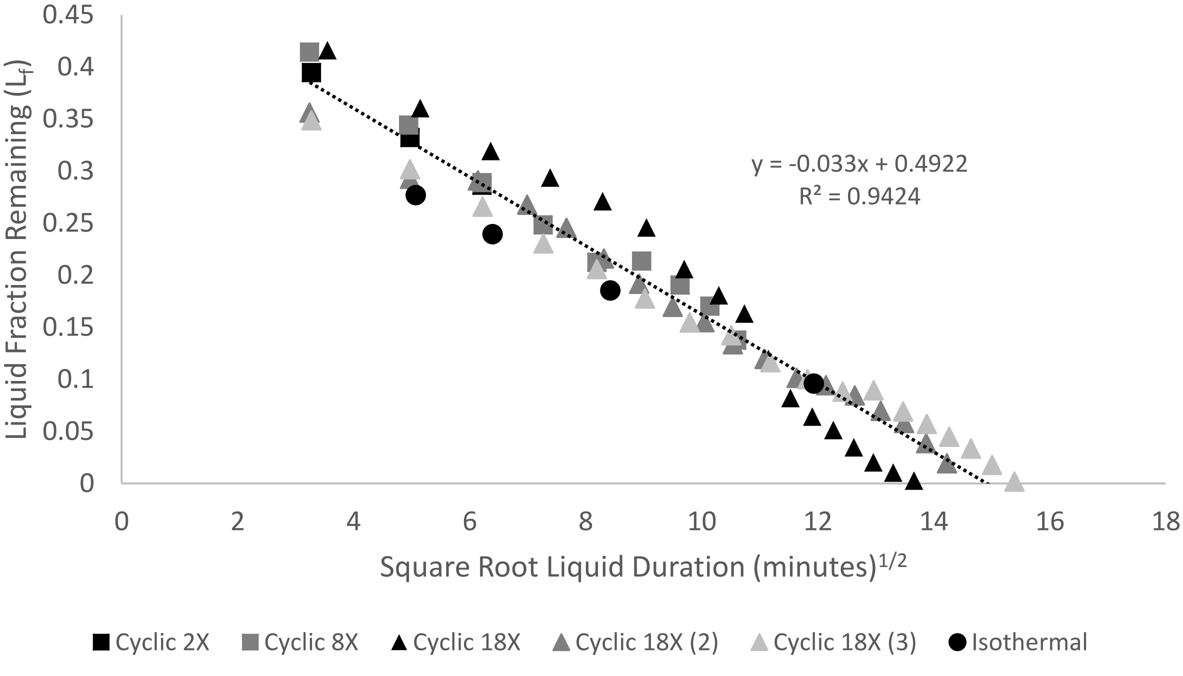

Figure 4.11 - Liquid Fraction Remaining (L_f) Data in Cyclical DSC Samples of Copper and Commercially Pure Titanium

4.11. The estimated time to isothermal solidification was derived from this regression and found to be 222.5 minutes.

Figures 4.12 includes microstructural cross sections of samples isothermally held for 15, 30 and 120 minutes at 1050°C. The ASZ has a similar morphology to the samples of Figure 4.4 with a continued depletion of liquid with increased hold time. The ASZ continues to display a peritectic structure with primary (β-Ti) dendrites and interdendritic Ti_2Cu, characteristic of the peritectic solidification structure in this alloy. In the bottom image of Figure 4.12 a small amount of ASZ or liquid remained after the 120 minute hold (i.e. 142.4 minutes of liquid duration) which is consistent with the DSC measurement plotted in Figure 4.11, which report a liquid fraction of 10.1%.

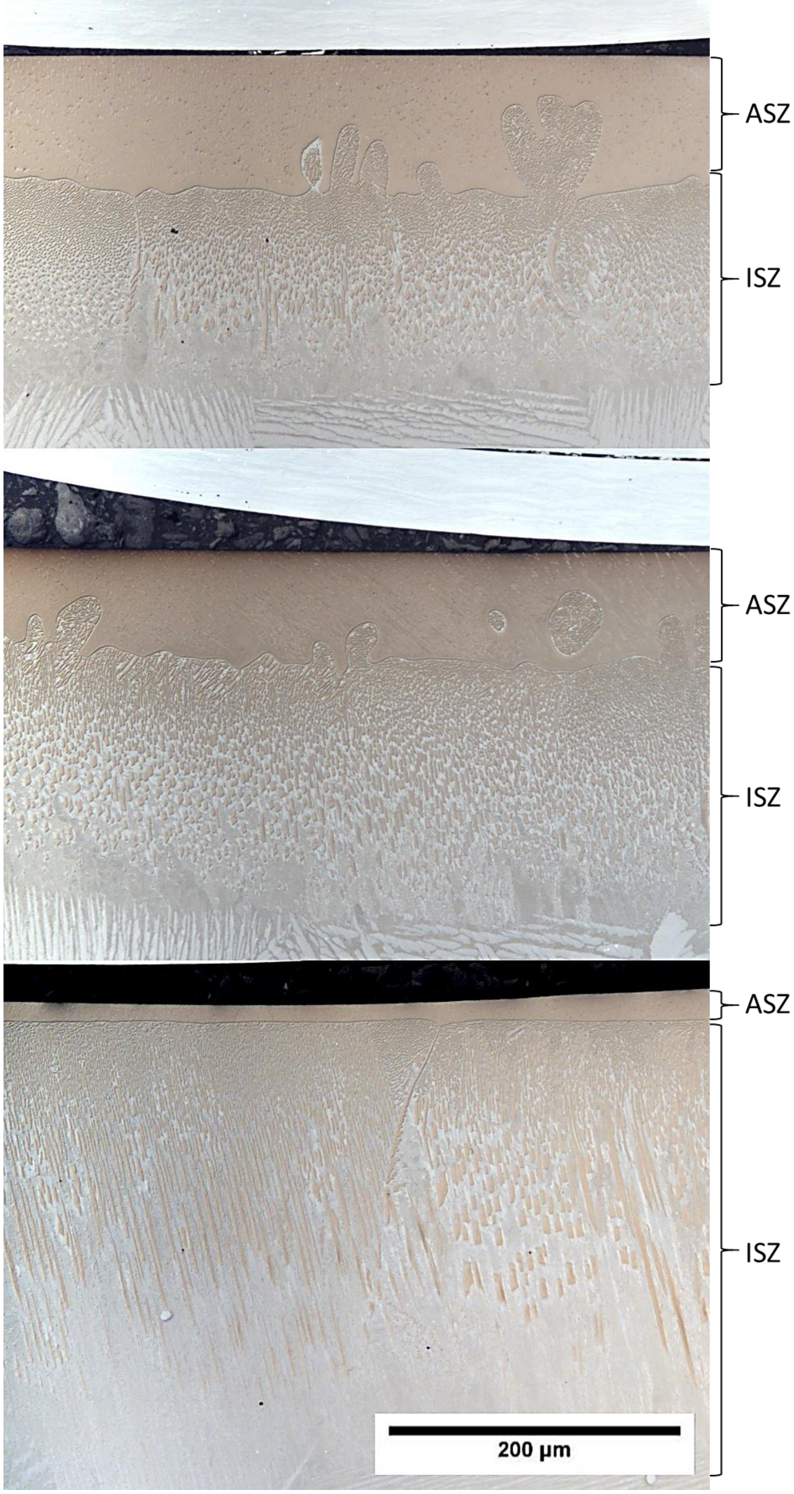

Figure 4.12 – Optical Imaging of Microstructural Cross Sections of Samples Held Isothermally at 1050°C for Top: 15; Middle: 30; Bottom: 120 minutes

4.4 Microstructural Validation of DSC Measurements

As mentioned in the experimental section, precautions were taken to prevent wetting of the alumina crucibles to avoid impacting results or coating the instrumentation in the DSC [71]. Use of an undersized foil lead to a curved solid/liquid interface and created issues in calculating the volume of liquid to determine the rate of isothermal solidification in terms of a gap dimension in micrometers (the width of the isothermally solidified zone, W_{ISZ}). Figure 4.13 shows a sample isothermally held for 15 minutes and the resultant pool of liquid.

Figure 4.13 – Optical Imaging of Microstructural Cross Section of Ti-Cu Sample Heated to 1050°C and Cooled at 20 Kpm Showing Entire Width

A spherical cap was adopted to best represent this pool geometrically where the volume can be calculated by:

$$V_{cap} = \frac{\pi h}{6}\left(3\left(\frac{D}{2}\right)^2 + h^2\right) \tag{4.2}$$

Where D is the width of the liquid pool at the surface and h is the maximum depth (or height) into the base metal.

Previous work in Corbin *et al.* has shown that, when the braze layer is the same diameter as the faying surface, the solid-liquid interface undergoes planar dissolution and solidification [61][69]. For a cylindrical sample, this would be the equivalent liquid volume of a cylinder. Figure 4.14a illustrates how dissolution and gap widening would occur for a cylindrical base metal with a starting Cu foil thickness and diameter W_{Cu} and d_{Cu}. In this work, it is assumed that the spherical cap volume created by the undersized foil on top of the base metal, is equivalent to the same dissolved volume of a cylinder (see Figure 4.14b). It is also assumed that the original liquid pool diameter D, is the diameter of the Cu foil used (d_{Cu}). This assumption was validated by stereo images of the top surface of the braze joint. The W_{max} term will be discussed later in this section.

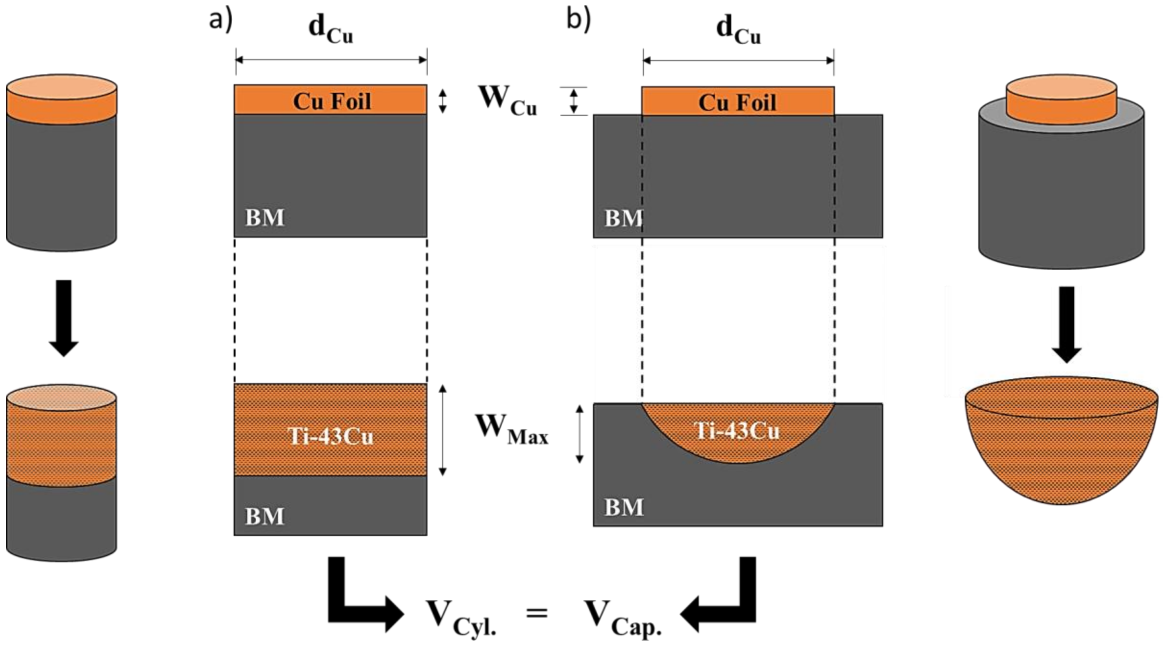

Figure 4.14 - Schematic of Dissolution Models for (a) Cylindrical Geometry and; (b) Spherical Cap Geometry. Note that both Geometries Create an Equivalent Volume of Liquid

If the interaction volume formed from dissolution is assumed to be a cylinder with a defined diameter of the foil width, then a volume can be calculated knowing the composition of the liquid and its respective density. The density of the liquid was calculated by a rule of mixtures from the liquid densities of pure Cu and Ti and was found to be 5.108 g/cm^3. The composition of the liquid was assumed to form a homogenous mixture of the liquidus composition (~39.3 wt%) at 1050°C. The volume of liquid was found using:

$$\boldsymbol{V_L = \frac{m_L\left(\frac{100}{39.3}\right)}{\rho_L}} \tag{4.3}$$

Where m_L is the mass of a copper foil, typically 3.2 mg, and ρ_L is the density of liquid. The calculated maximum dissolution volume V_{max} of liquid becomes 1.594 mm^3 and the height of the cylinder can be found from this volume using Equation 4.3 and d_{Cu}. The maximum height of the interaction volume, W_{max}, was calculated to be 201.3 μm and this height can be converted into the expected height of a spherical cap, 395 μm (see Section 3.3.2). This is the maximum depth of the ASZ at the centre of the spherical cap interaction volume which occurs at the end of the dissolution stage. It assumes that all the Cu is in the liquid phase with no diffusion into the Ti base metal.

To verify this value, a sample was heated to 1050°C at 20 Kpm, typical of the previous ramp samples, but was cooled at the fastest rate possible in the DSC (80 Kpm) (previously shown in Figure 4.4). The measured maximum height of the ASZ was found to be 298 μm, lower than the theoretical maximum of 395 μm. This indicates that during initial melting, some Cu has diffused into the BM and is not replaced into the liquid during dissolution up to 1050°C. This is confirmed by the optical microstructure of Figure 4.4 where a distinct band of altered eutectoid microstructure below the solid/liquid interface with a bulk composition ranging from 8 to 22-wt% Cu is visible.

Additionally, Tuah-Poku *et al.* defined the maximum dissolution height of a cylinder to be calculated using:

$$\boldsymbol{W_{max} = W_o \left[1 + \frac{c_B - c_{L\alpha}}{c_{L\alpha}}\left(\frac{\rho_B}{\rho_A}\right)\right]} \tag{4.4}$$

Where W_o is the initial foil thickness in microns, c_B is the composition of the base metal, $c_{L\alpha}$ is the liquidus composition, ρ_A is the density of the base metal, and ρ_B is the density of the interlayer. Calculating the value of W_{max} when the copper foil is solid (Tuah-Poku ignore volumetric changes in the liquid), the maximum dissolution height is found to be 190.15 μm which is in good agreement with the calculations in this study using Equation 4.3. This demonstrates that the ASZ defined in the microstructures of the above figures has the dimensions expected and predicted by known dissolution laws. Therefore, the depth and volume measurement of the furthest section of the ASZ/ISZ interface from the surface is a validation of the amount of liquid present at a given braze time.

Microstructural measurements were made for post DSC ramp, cyclic, and isothermal samples, whose enthalpies of melting and liquid fraction were included in Figures 4.10 and 4.11 respectively. Since the foil was roughly centered for all samples, the maximum depth and width of the ASZ and spherical cap dimensions could be projected using trigonometry regardless of the grinding depth when polishing into the cross section (see Section 3.3.2). Table 4.2 outlines these measurements assuming a spherical cap. From these measurements, the volume of the peritectic microstructure or ASZ was calculated. Using the V_{max} calculated previously (1.594 mm^3), The liquid fraction was then determined using the individual ASZ volume measurements (i.e. $L_f = V_{ASZ}/V_{max}$). This dimensional and microstructurally based liquid fraction remaining can be compared to the DSC based measurement made from the last cooling segment of each of the samples in Table 4.2. The ASZ liquid fraction, with the DSC values included, are plotted versus the square root of liquid duration in Figure 4.15. Agreement between the two methods is very good, particularly in terms of the linear regression (LR) analysis for both data sets, validating the DSC measurements and the associated method of calculating L_f.

Table 4.2 -Progression of Isothermal Solidification in Grade Two Titanium and Copper Half Joints

Sample	Projected ASZ Width (mm)	Projected ASZ Height (mm)	Volume of ASZ (mm^3)	Calc. Liq. Fraction	DSC Liq. Fraction	Root Liquid Duration ($min.^{1/2}$)
Cyclic 2X	2.894	0.147	0.486	0.305	0.286	6.21
Cyclic 5X	3.344	0.052	0.228	0.143	0.155	8.37
Cyclic 8X	3.043	0.066	0.240	0.151	0.138	11.06
Cyclic 10X	2.609	0.035	0.095	0.059	0.103	12.11
Cyclic 18X	0.000	0.000	0.000	0.000	0.000	14.91
Iso 15 min.	2.826	0.128	0.403	0.252	0.277	4.80
Iso 30 min.	2.925	0.129	0.435	0.272	0.236	6.16
Iso 120 min.	2.520	0.028	0.070	0.044	0.185	11.93

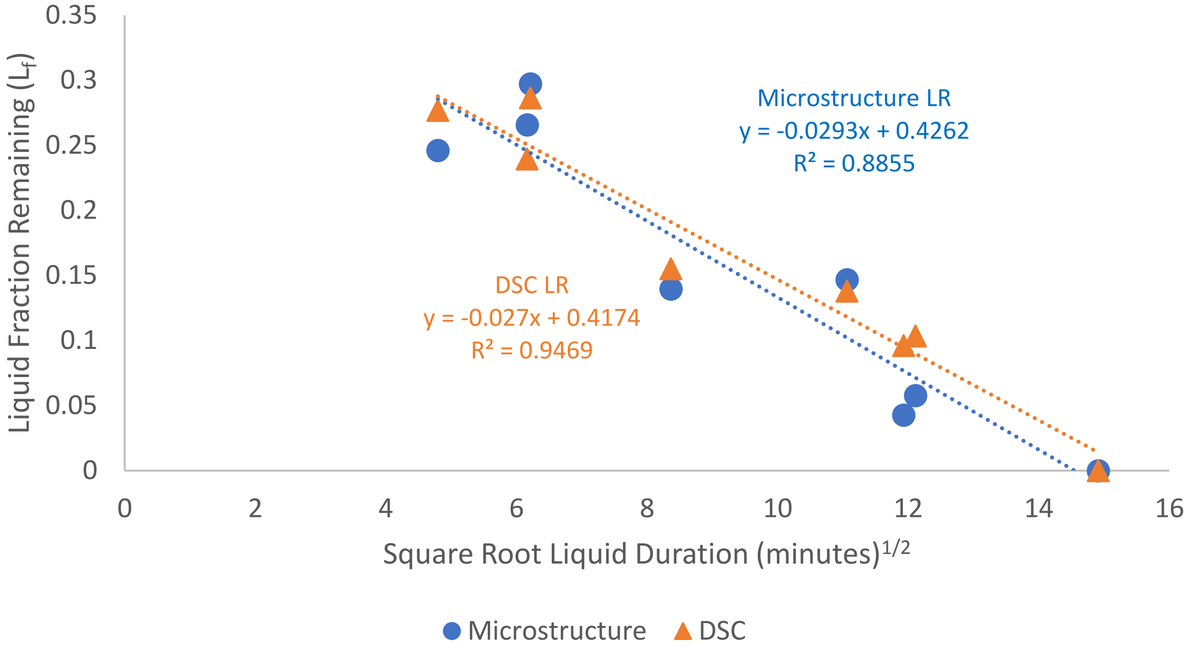

Figure 4.15 - Comparing DSC and Calculated Microstructural Liquid Fractions of Copper and Commercially Pure Titanium

The linear regression for the smaller subset of data in Figure 4.15 is slightly different than the equation arrived at using the full data set of Figure 4.11. It should be noted that the linear regression applied in Figure 4.11 is the more accurate of the two data sets.

4.5 The Rate of Isothermal Solidification and the $2W_{ISZ}$ Curve

From the validated DSC liquid fraction measurements, both the liquid width W_t and the width of the isothermally solidified zone W_{ISZ} as a function of time can be calculated. It is first considered that the liquid fraction can be obtained by a ratio of the liquid volume at any braze time over the theoretical maximum volume due to dissolution;

$$\boldsymbol{L_f = \frac{V_t}{V_o} = \frac{W_t}{W_o} = 1 - \frac{W_{ISZ}}{W_o}} \qquad \textbf{(4.5)}$$

If the volume is considered as a spherical cap, both D and h from equation 4.3 would have to be known as a function of braze time. However, industrial brazing is best described by the cylindrical volume of Figure 4.14a). In this case it is applicable to a one dimensional IS process where the area cross section A_o and A_t are constant or unchanged. Since $A_o = A_t$, the ratio of volumes is equal to the ratio of liquid widths (W_t/W_o). Since the fraction of solid (ISZ) $L_s = 1\text{-}L_f$, the right-hand side of Equation 4.5 can be expressed. The initial gap width, W_o is the maximum depth of dissolution for a cylindrical volume which was calculated above using Equation 4.3 and a cylindrical volume. However, as explained in the introductory chapter, TLPB is described as a symmetrical problem with reference to a joint centreline. The full gap width is expressed as $2W_o$. In this regard the experimental studies were investigating half joints. Making this change and rearranging Equation 4.5 gives;

$$\boldsymbol{2W_t = 2W_oL_f \quad and \quad 2W_{ISZ} = 2W_o(1 - L_f)} \qquad \textbf{(4.6)}$$

Therefore, both the full liquid width and full width of the isothermally solidified zone can be directly calculated from DSC liquid fraction measurements. A plot of $2W_{ISZ}$ versus the square root of time is shown in Figure 4.16 using data from the three 18 cycle braze samples and a $2W_o$ value equal to twice the maximum cylindrical height (402.6 μm).

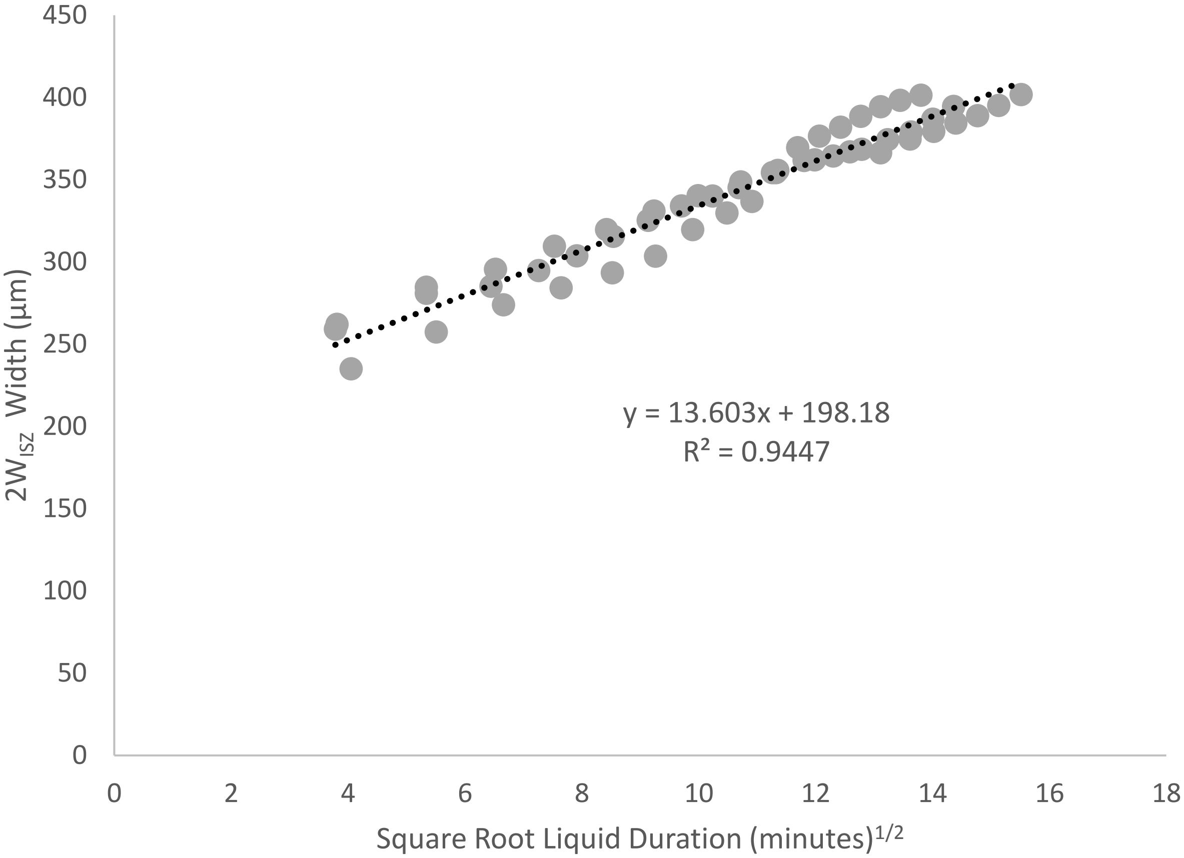

Figure 4.16 - $2W_{ISZ}$ Curve Using Cyclical DSC Data of Copper and Commercially Pure Titanium

The $2W_{ISZ}$ curve maps the development of the ISZ region in a double-sided specimen for the entire duration of isotheral solidification. A notable feature of the ISZ curve is that the y-intercept is non-zero. Moreau *et al.* identified a similar non-zero y-intercept when examining TLPB of nickel superalloys using boron containing filler metals [61]. This was attributed to rapid diffusion of boron into the base metal while heating to the braze temperature. This led to diffusional solidification prior to reaching the isothermal hold stage, creating a $2W_{ISZ}$ layer as a y-intercept. The $2W_{ISZ}$ curve for Ti-Cu also indicates that a significant initial copper uptake into the base metal occurs prior to reaching the braze temperature. Linear regression applied to the data set of all three samples indicates that the y-intercept for the braze joint is $2W_{ISZ}$ = 198.2 µm for a full joint, or

99.1 μm on a half joint basis. This is qualitatively consistent with the microstructural evidence of Figures 4.3 and 4.4.

The slope of the $2W_{ISZ}$ curve is a measure of the rate of isothermal solidification and relates to the ability of copper to diffuse past the solid-liquid interface and further into the base metal. From the linear regression analysis this slope is 13.60 μm /min$^{1/2}$.

4.6 Examination of the Isothermally Solidified and Diffusionally Affected Zones

Given the importance of Cu diffusion into the base metal on the kinetics of IS, the ISZ and DAZ regions were examined more closely. Figure 4.17 shows an example of the microstructural

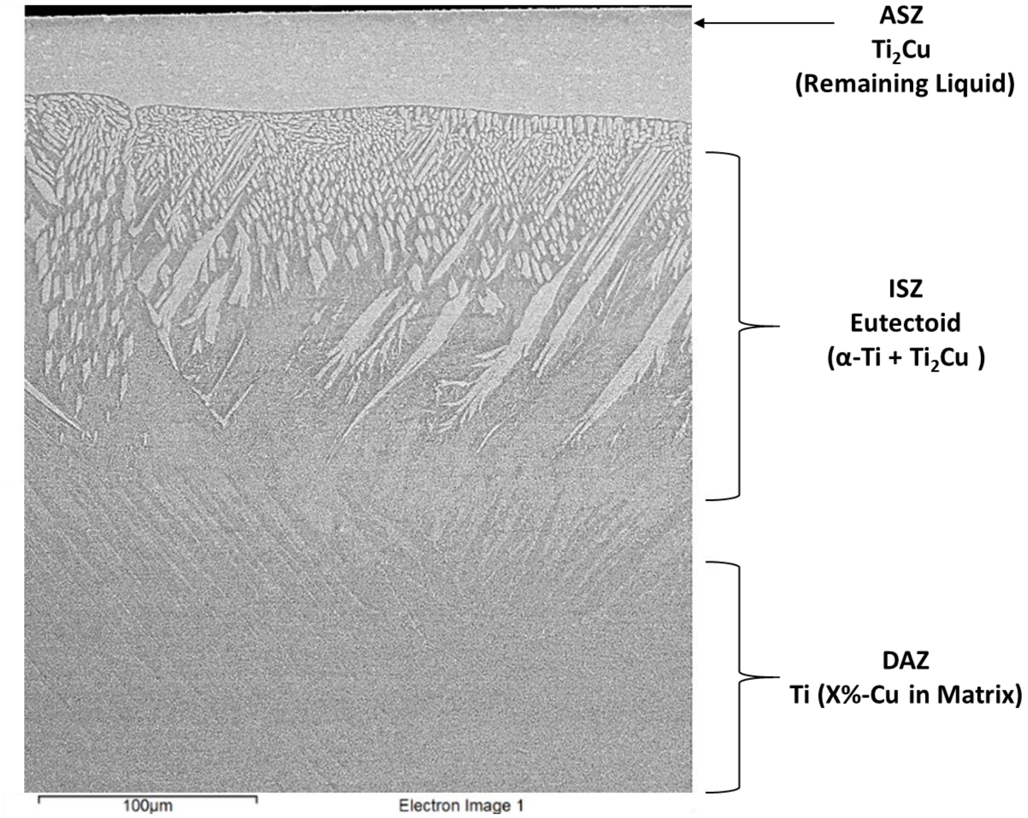

Figure 4.17 – SEM Imaging of a Ti-Cu Cyclically Heated Between 1050°C and 890°C Five Times

variation which occurs as a function of depth into the ISZ/DAZ region. As will be demonstrated later, there is a systematic decrease in the copper concentration with increasing depth.

In the ASZ the composition is close to that of Ti_2Cu and this is also the predominant phase present in this region. Very fine deposits of TiCu were found in the Ti_2Cu ASZ layer demonstrating that even after approximately 70 minutes in the liquid state that Ti_2Cu-TiCu eutectic forms to some extent on cooling. This is consistent with the DSC results which shows evidence of eutectic melting up to at least 150 minutes of braze time.

Below the solid/liquid interface in the ISZ, the Cu concentration starts at 21 wt%. This region is characterised by a high density of Ti_2Cu precipitates in a Ti-rich matrix. The volume fraction of precipitates and the bulk Cu concentration reduces with further distance into the base metal. With reference to the Ti-Cu binary phase diagram, this region would be expected to be single phase solid solution (β-Ti) at the braze temperature of 1050°C. Upon cooling, the (β-Ti) would undergo a hypereutectoid phase transformation producing the Ti_2Cu precipitates. As the bulk composition reduces from 21 wt% to the eutectoid composition (i.e. 8 wt% Cu), the lever rule would dictate the reduction in the hypereutectoid Ti_2Cu volume fraction that is observed in the microstructure.

Below approximately 10 wt% Cu, the coarse Ti_2Cu precipitates no longer form. Instead, a fine dispersion of Ti_2Cu and (α-Ti) exists in the microstructure, which is indicative of a eutectoid phase transformation [72]. A higher magnification image of this structure is shown in Figure 4.18a. This microstructure also exists within the 'matrix' of the hypereutectoid region where (β-Ti) would have remained as part of the hypereutectoid reaction. Once cooling below the eutectoid temperature any (β-Ti) with a composition above the eutectoid (8 wt% Cu) will undergo the reaction (β-Ti) = Ti_2Cu + (α-Ti). This significant region of eutectoid microstructure is consistent with the DSC results, which show a distinct eutectoid transformation peak during cooling of the

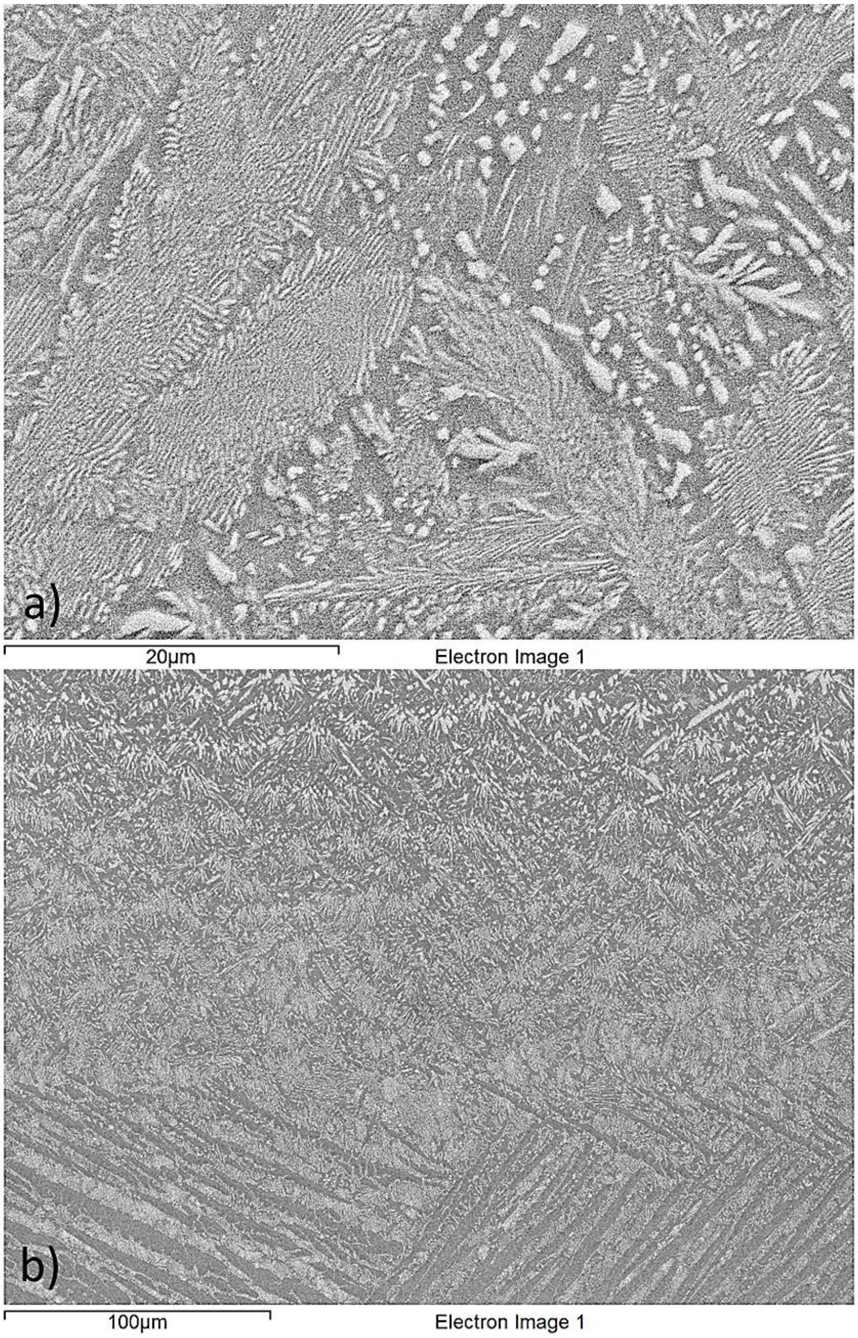

Figure 4.18 - SEM Imaging of Eutectoid Microstructure in the ISZ of a Sandwich Assembly Heated in the DIL for 1.25 hours shown at (a) 2500X Magnification and; (b) 400X Magnification

brazed joints. In the region between 10 and 5 wt% Cu, the microstructure transitions from eutectoid to hypoeutectoid. Plates of (α-Ti) form separated by eutectoid regions (see Figure 4.18b). Further below this region a microstructure expected for pure CP-Ti forms.

All cyclical and isothermal samples had bulk scans taken from the surface of the ASZ to the DAZ to create compositional profiles, see Figure 4.19. As with the data in Table 4.2, a correction was made to the distance (or height) since each sample under SEM was polished to a different depth into the melt pool. As isothermal solidification continues, the peritectic ASZ layer, begins to reduce in thickness as more Cu diffuses away into the base metal. It should be noted that measurements in the ASZ included only the peritectic/eutectic regions and not the primary dendrites. Therefore, the ASZ Cu compositions in Figure 4.19 are somewhat higher than the bulk composition of 39.3 wt% Cu which included primary dendrites, as outlined in Section 4.3.

All samples show a sharp discontinuity in copper concentration in a location corresponding to the solid/liquid (or ISZ/ASZ) interface. The ISZ near the interface has a maximum Cu composition between 19 and 21 wt% Cu depending on the braze time. This value is close to the maximum solubility of the (β-Ti) predicted from the phase diagram of Figure 2.13 (20.05 wt% Cu).

Eleven EDS measurements in the ISZ layer taken within 25 μm of the solid/liquid (S/L) interface exhibited elevated Cu levels. This was judged to be due to the curved and wavy nature of the spherical cap shaped ASZ and the S/L interface. The interaction volume of the electron beam was likely sampling the ASZ region underneath the polished surface. For this reason, EDS data with 25 μm of the S/L interface were omitted from the plots in Figure 4.20.

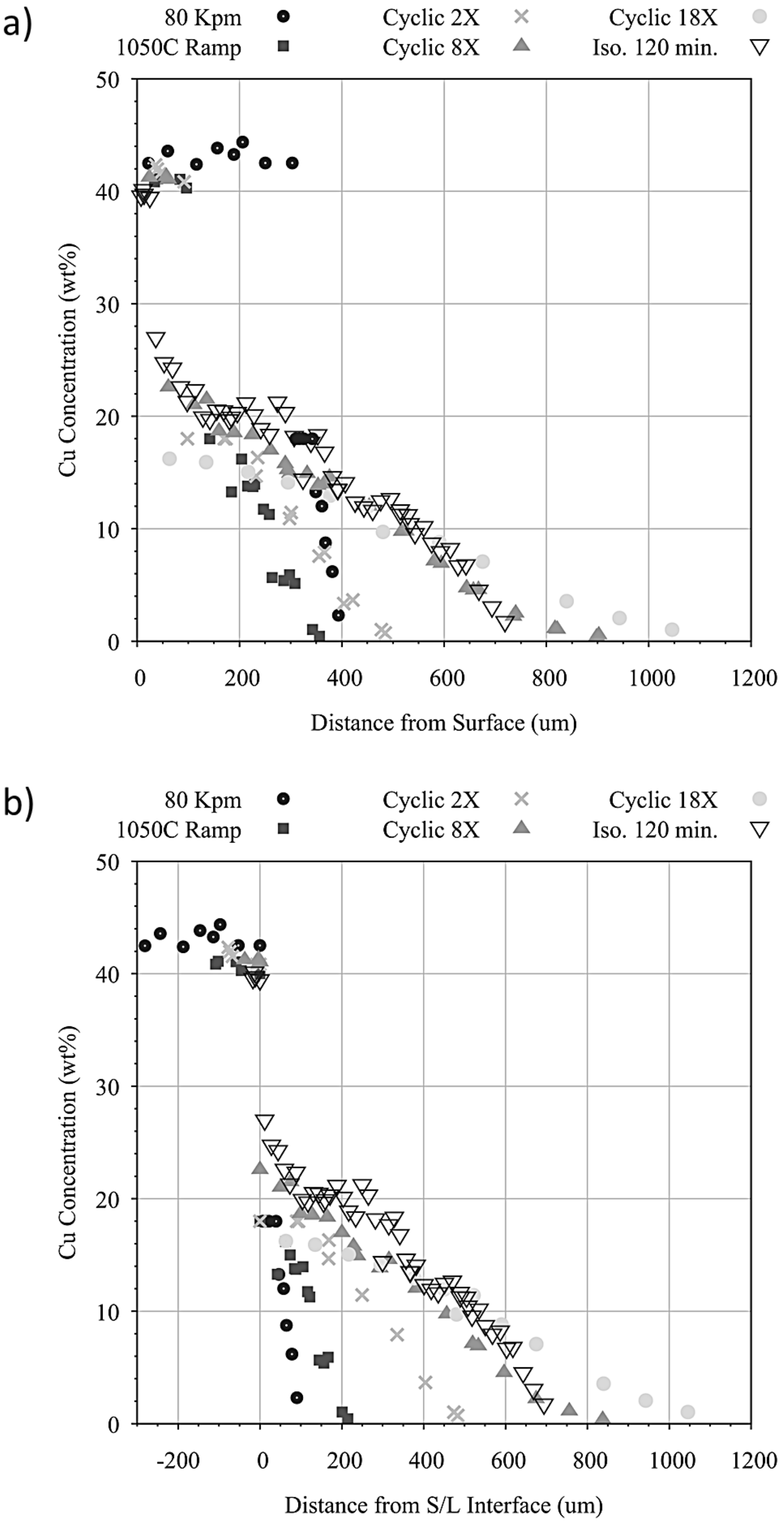

Figure 4.19 - Compositional Profiles of DSC Samples Plotted as (a) Distance from the Sample Surface; (b) Distance from S/L Interface

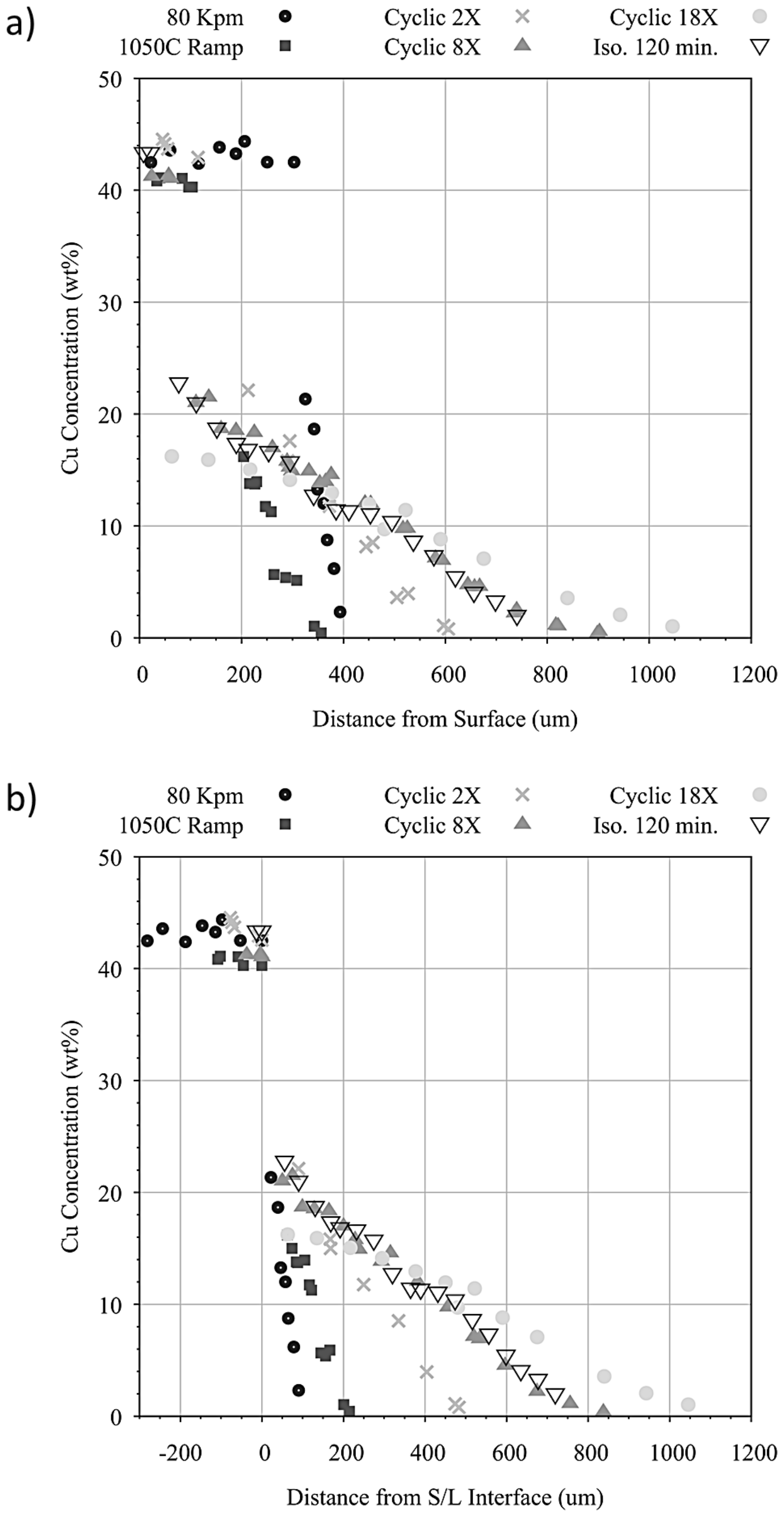

Figure 4.20 - Corrected Compositional Profiles of DSC Samples Plotted as (a) Distance from the Sample Surface; (b) Distance from S/L Interface

The composition further away from the ASZ/ISZ interface fits the expected diffusion mode where the concentration gradient is non-uniform and the surface concentration is assumed fixed. This is more easily seen in Figure 4.20 where the profiles were plotted with reference to a ‘zero distance’ for the solid/liquid position. The diffusion of Cu into the base metal is significant even in the 1050°C 80 Kpm quench sample, with a Cu penetration distance of 100 μm. As braze time progresses, the Cu penetration increases with a diffusion distance over 1000 μm developed after 222 minutes and complete isothermal solidification. Note that all the samples in Figures 4.19 had a similar microstructural progression through the Cu compositional profile to that described in Figure 4.17. The microstructure of the base metal progressed from hypereutectoid, to eutectoid, to hypoeutectoid.

4.7 Application of Analysis to Maximum Brazing Clearance and IS Time

When the DSC analysis is plotted as $2W_{ISZ}$ versus the square root of liquid duration (i.e. Figure 4.16) it should be capable of predicting the Maximum Brazing Clearance (MBC) of a joint with any starting gap. To verify this capability, both the microstructural evolution and the isothermal solidification behaviour of titanium and copper were examined under the conditions of a full sandwiched assembly, Ti-Cu-Ti. The liquid duration was set to examine the predictability of the $2W_{ISZ}$ curve when using full joints and to examine the effects of homogenization. All assemblies were brazed in the DIL.

Two contrasting tests were selected to examine the efficacy of full titanium copper joints, which were discussed and shown in Figure 3.11. To examine the validity of the $2W_{ISZ}$ curve in predicting the remaining widths of the ISZ and ASZ, a pre-sandwiched assembly with two foils was heated to 1050°C and immediately cooled at 80 Kpm (shown in Figure 3.11a). It should be noted that the DIL was not capable of cooling at 80 Kpm and a cooling rate closer to 40 Kpm was observed when testing. In a second experiment, a capillary action assembly was created with one foil, heated to 1050°C holding for 75 minutes, and subsequently cooled at 20 Kpm (see Figure 3.11a). This was done to examine the effects of homogenization and allowed examination of isothermal solidification using the $2W_{ISZ}$ curve for prealloyed titanium copper liquid.

Figure 4.21 shows the results of the first experiment with a pre-sandwiched assembly. Two copper foils were stacked and compacted to a braze gap of roughly 100 μm. Post analysis of the actual gap is possible by examining the distance between the free surfaces of the titanium plates outside the overlap area. For the specimen of the figure, this gap was determined to be 110 μm. Two foils were used to create sufficient liquid for observing the ASZ upon cooling. In addition, it provided an analog of the half joint specimens using a single foil. Stereoscope imaging showed minimal wetting outside the joint or along the sides of the assembly. In this experiment, undersized foils were used to minimize wetting or dissolution of the joint sides outside the gap. Copper foils were roughly 4 mm by 4mm and were placed in a joint with an overlap length of roughly 6 mm. Optical imaging was implemented after the sample was cut lengthwise and shows the centre of the joint.

The width of the full joint in Figure 4.21 varies significantly across the overlap region. This is most evident through a measurement of the ASZ width in the marked regions A and B. B regions

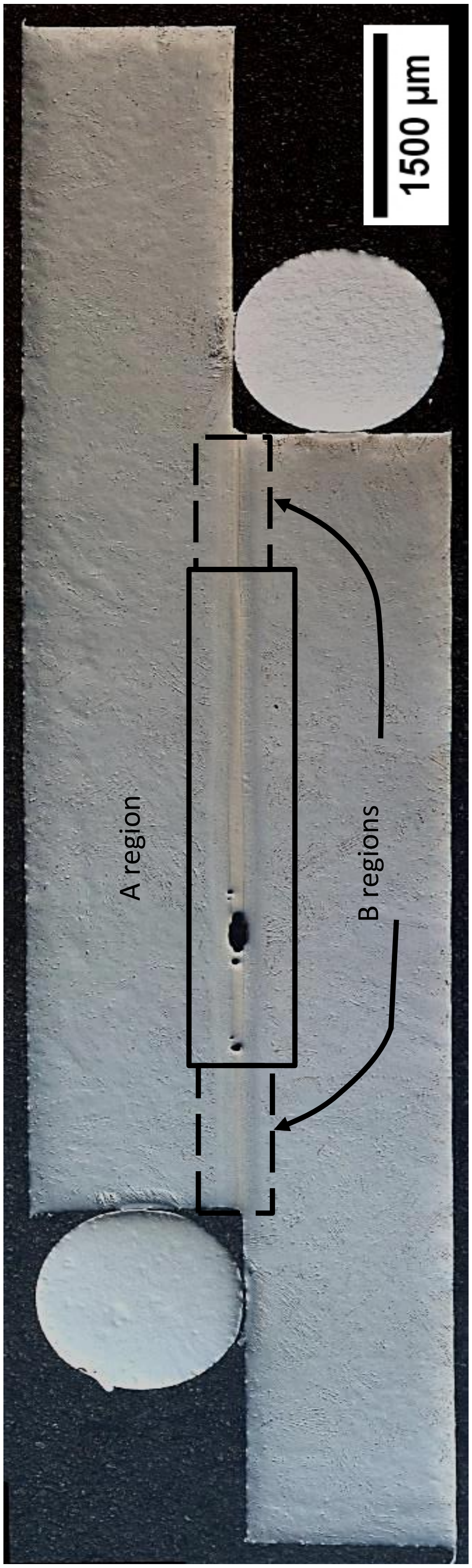

Figure 4.21 – Optical Imaging of DIL Ti/Cu/Ti Sandwich Full Joint Heated to 1050°C and Cooled at 40 Kpm with Two Cu Foils

on the left and right edges, had $2W_{ASZ}$ of 25 μm thick and the central A region was 115 μm. A large pore in the centre of the joint has a maximum width of 173 μm.

The structure of this joint can be explained with reference to the schematic of Figure 4.22. Potential joint formations include Type A:Stage A and Type B:Stage B. In Stage A it is assumed that the Cu foil remains in place until the peak braze temperature is reached, allowing for full base metal

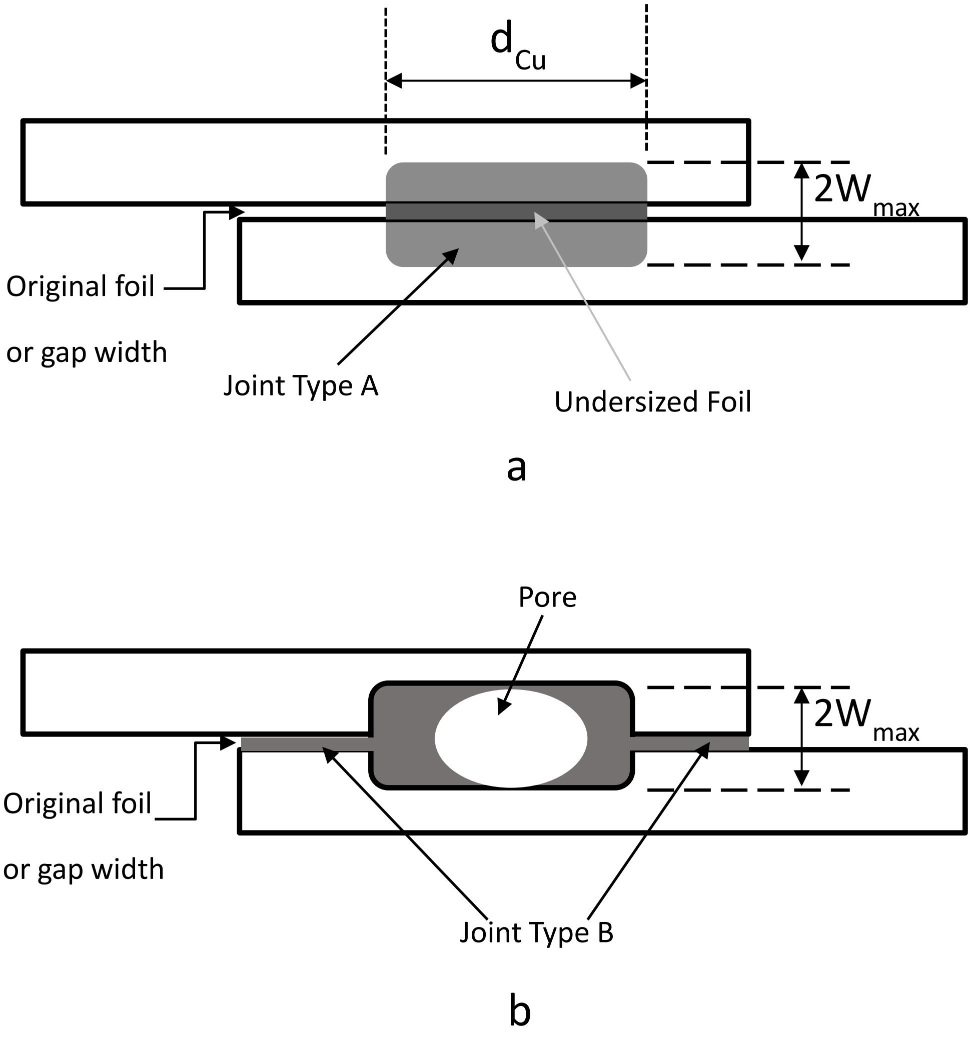

Figure 4.22 - Schematic of Full Joint Formation with a Fixed Gap and Undersized Foil Outlining (a) Stage A and Joint Type A; (b) Stage B and Joint Type B

dissolution to occur. In this case the $2W_{max}$ calculated from equation 4.3 and using the measured gap width of 110 μm would be 443 μm.

Figure 4.23 illustrates how the MBC curve could be used to predict the thickness of the ASZ for this case. Knowing the time of brazing t_1 the isothermally solidified width $2W_{ISZ}$ can be predicted from the linear regression curve. For the experiment of Figure 4.21 the liquid duration time (assuming a cooling rate of 40 KPM) was estimated at 9.3 minutes (i.e. 3.04 $min^{1/2}$). Using the LR data of Figure 4.16, this would result in a 2Wisz thickness of 240 μm. Subtracting this value from $2W_1$ in Figure 4.23 gives the $2W_{ASZ}$ as 203 μm for the Type A joint, which is greater than the 115 μm measured in the sample centre. This discrepancy will be discussed further below.

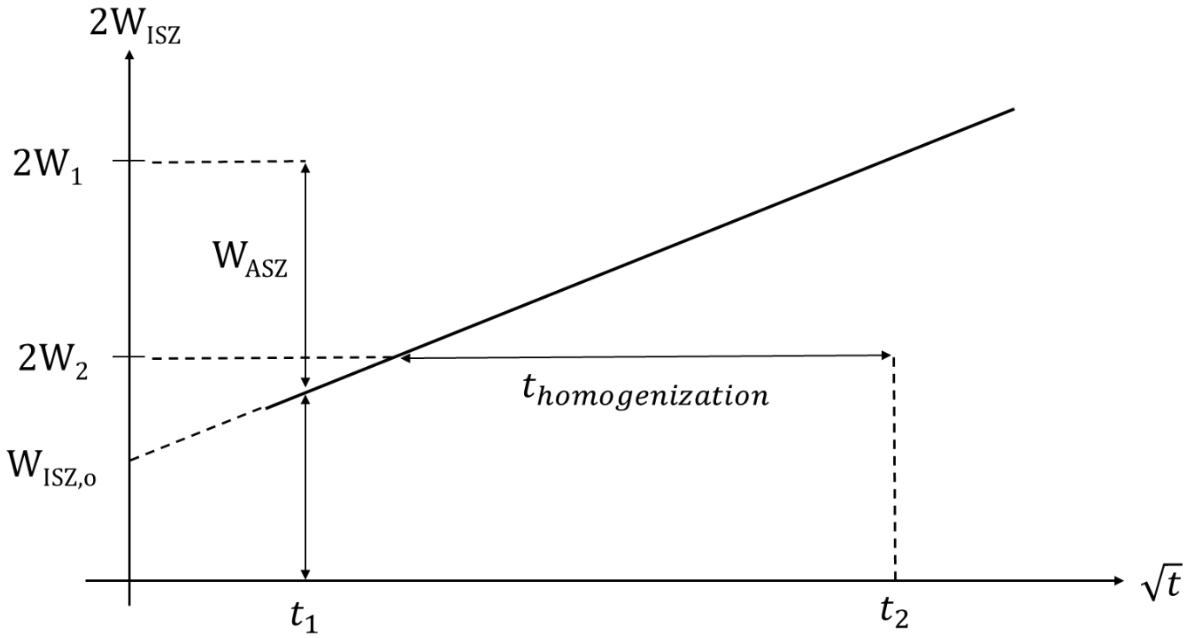

Figure 4.23 - Schematic Showing Useful Terms Derived from the $2W_{ISZ}$ Curve

Stage B is assumed to start when the braze temperature is reached and full dissolution has occurred in Region A. At this stage, the liquid near the edge of the diluted area is drawn into the smaller unfilled gaps to the left and right by capillary action (see Figure 4.24b). This quickly fills the gap forming a Type B joint. The movement of this finite amount of liquid would create a corresponding void in the original Type A region of the joint.

Under the conditions of joint Type B the liquid is already at the liquidus composition such that no dissolution in region B would occur. The liquid also comes into contact with the faying surface under isothermal conditions. In this case the growth of the $2W_{ISZ}$ layer can be estimated by the simplified equation of $2Wisz = 13.603(t)^{1/2}$ (i.e. removing the y-intercept from the LR equation of Figure 4.16. With the current assumption that the gap of region B does not fill until 1050°C is reached (melting observed at 970°C), the liquid duration time would be 4 minutes (i.e. 2.0 $min^{1/2}$), resulting in an IS growth layer of 27.2 μm. Using the initial set gap of 110 μm, gives a W_{ASZ} = 82.8 μm for a type B joint for a Type B joint region. This is larger than the measured value of 25 μm.

The discrepancies in the measured (i.e. 115 and 25 μm) and predicted (i.e. 203 and 87 μm) $2W_{ASZ}$ thickness in the Type A and B joints are related to the assumptions that Stages A and B are separate and sequential events. More realistically, once some liquid forms in Region A, it may begin to flow into Region B during heating to the braze temperature. Removal of some liquid from Region A would tend to reduce the ongoing gap widening and dissolution in this area. With less gap widening, the overall width of the ASZ present after the brazing time would be less than the prediction, which matches the experimental observation. Since liquid would be introduced into

Region B sooner than in the original assumption it would have longer to undergo diffusional solidification. Therefore, the ASZ width in this region would be less than predicted which also matches the experimental observation.

The assumption described in Figure 4.22 would result in the largest joint thickness variation between regions A and B. The extent to which capillary flow overlaps with the dissolution process would reduce the thickness variation making it more uniform, which was observed experimentally.

A cross section for the sample brazed with the second arrangement of capillary flow is presented in Figure 4.24. No ASZ region was observed at the joint centerline indicating complete IS, which would be expected for the 75 minute braze time used. The maximum Cu concentration at the centre of the joint was measured to be 3 wt%, indicating significant homogenization in this sample. It was assumed that full dissolution occurred for this sample outside the gap, where the Cu foil was placed, and the liquid flowed into the gap having obtained the liquidus composition. Therefore, no dissolution or gap widening is expected and the equilibrium liquid is in contact with the faying surface under isothermal conditions. Therefore, the same approach can be used to determine IS kinetics as that described above for a Type B joint. Assuming a 50 μm braze gap was maintained, dissolution would reach the maximum cylindrical height (201.3 μm) and the expected completion of isothermal solidification was 0.23 min.$^{1/2}$, or roughly 3 seconds. This means that the sample homogenized ($t_{\text{homogeniztion}}$) for 75 minutes.

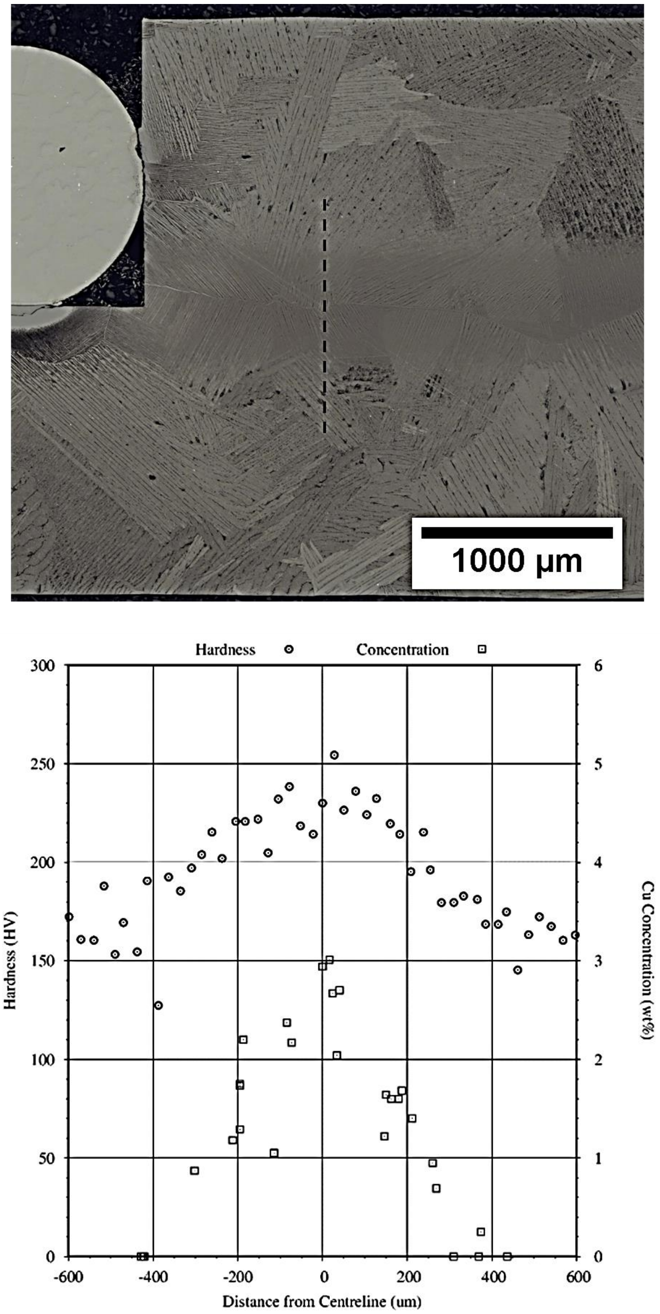

Figure 4.24 – Optical Imaging and Hardness/Compositional Profiles for a Ti/Cu/Ti Capillary Action Sample Heated to 1050°C and Held for 75 Minutes

SEM EDS scans and microhardness measurements were taken perpendicular to the joint interface for both the capillary action, single foil, 75 minute and the pre-sandwich joint with two Cu foils held for 0 minutes at 1050°C (Figures 4.24 and 4.25 respectively). Microhardness measurements for the capillary action sample were taken at Dalhousie University and were calculated from optical images using the measured diagonal width. The hardness profile shows that away from the copper rich joint the average Vickers hardness approached 200 HV.

According to Oh *et al.*, this value corresponds to an oxygen concentration in the base metal just over 1500 ppm or 0.15 wt% which is within the specification of commercially pure titanium (<0.25 wt% O) [73]. EDS area scans along the centreline were also taken and their compositions and relative locations are included in the figure. The increase in hardness across the joint was attributed to solid solution strengthening since no second phase Ti_2Cu or TiCu precipitates were found.

For the pre-sandwich sample, the composition profile across the joint is typical of previous profiles in Figure 4.19 and 4.20 with the a peritectic ASZ (40-42 wt% Cu) and a hypereutectoid composition tapering off from 18 wt% Cu. Hardness measurements were taken perpendicular to the joint centreline using two diagonal profiles. Each consisted of twenty indentations beginning and ending from the base metal below the eutectoid microstructure. These results are compared to the EDS measurements in Figure 4.25.

Hardness measurements across the interface showed no increase at the ASZ with a few peaks in hardness in the ISZ. These values above 325 HV were found in the eutectoid and hypoeutectoid region and were likely statistical anomalies as values this high were not found in other hardness measurements of the hypoeutectoid. The base metal away from the ISZ was found to be around 180-280 HV and average hardness over the entire interface was 275 HV. There was no observable spike in hardness for indentations in the Ti_2Cu in the ASZ.

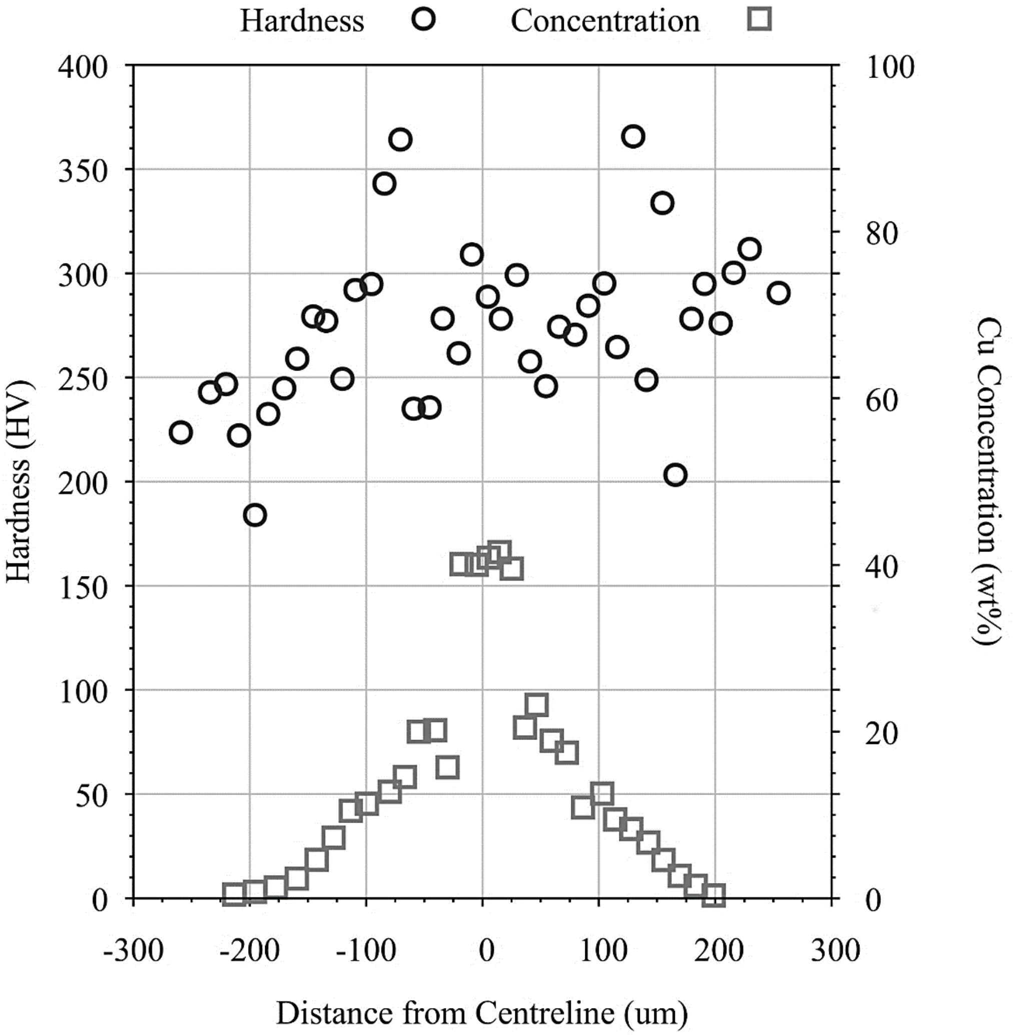

Figure 4.25 - Hardness and Compositional Profiles across the Joint Centerline of a Ti/Cu/Ti Two Foil Experiment Brazed at 1050°C and Cooled at 20 Kpm

5.0 Commercially Pure Titanium and Nickel

5.1 Initial Heating and Dissolution

Figure 5.1 shows the DSC heating traces for Ti-Ni samples heated to 975, 1000, and 1025°C. The transition of the base metal from α→β is observed consistently for all samples with an expected onset of 882°C. All samples undergo a similar broad exothermic event which onsets at 967.4 ± 2.9°C. A small endothermic peak close to 984°C corresponds to the peritectic temperature and reaction, $Ti_2Ni = L + TiNi$. This creates the look of a double exothermic peak. However, it is expected that intermetallic formation and melting are both occurring along the liquidus surfaces between the eutectic (942°C) and peritectic temperatures. This behaviour differs from the Ti-Cu system where melting was the predominant peak observed during initial heating with only a minor exothermic peak that was not always observed.

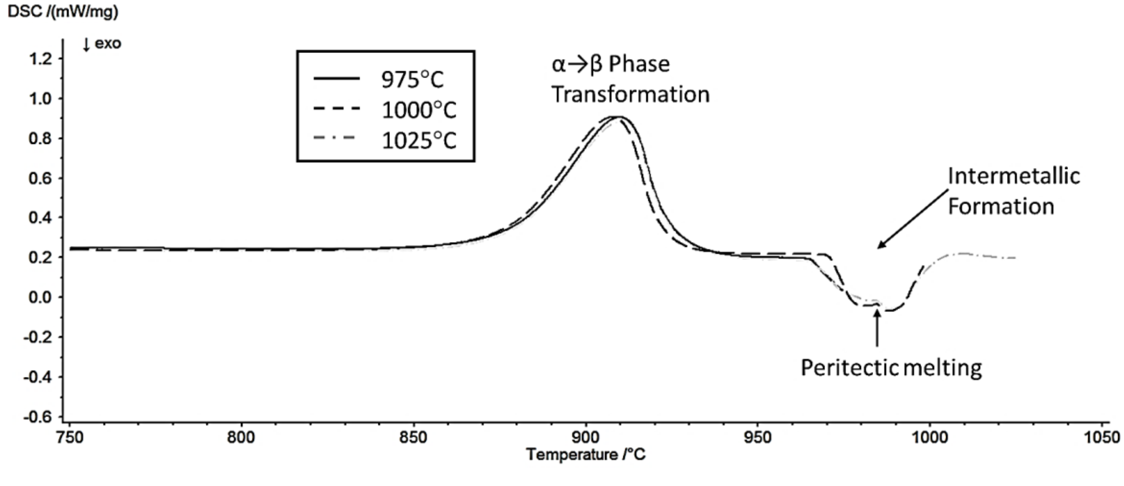

Figure 5.1 - DSC Heating Trace for Titanium Nickel Half Joints Heated to 975, 1000, 1025°C

On cooling the base metal undergoes the same allotropic transformation back into the α phase with minimal signs of change in the peak shape, see Figure 5.2. This indicates minimal long-range solid-state diffusion of nickel into the base metal. All samples display an onset of an exothermic solidification peak at 941.5 ± 1.06°C which corresponds closely to the eutectic temperature. The eutectoid transformation for all samples occurs consistently at 722.3 ± 1.47°C. This suggests some undercooling from the eutectoid temperature (765°C). The sharpness and magnitude of this peak is more significant than was observed for the Ti-Cu system. This indicates that short range diffusion of Ni into the base metal near the solid/liquid interface may be more significant than Cu.

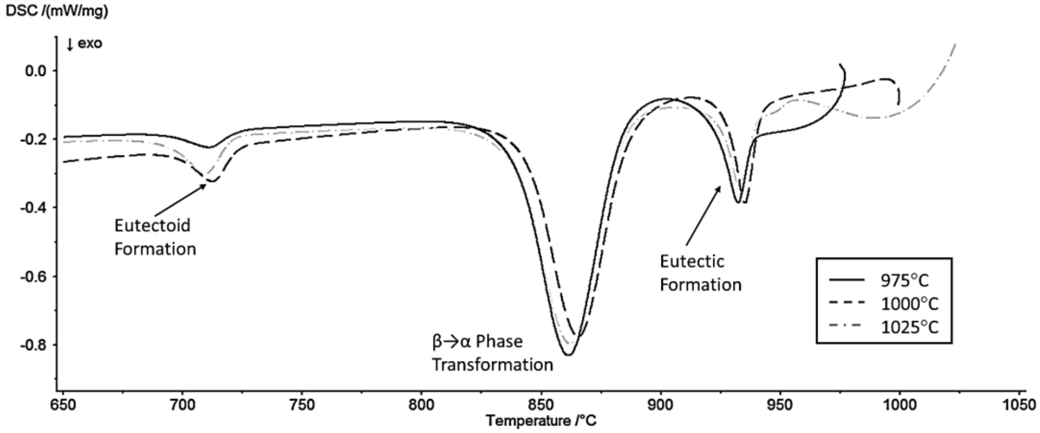

Figure 5.2 - DSC Cooling Trace for Titanium Nickel Half Joints Heated to 975, 1000, 1025°C

In order to determine the microstructural origins of the exothermic peaks observed during heating, Figure 5.3 shows an SEM image of a sample heated to 965°C and cooled. A band of intermetallic layers can be observed spanning the titanium-nickel phase diagram as a diffusion couple is created between pure titanium and nickel. This includes a region that has a microstructure consistent with solidified eutectic, which would have been liquid at 965°C. Below the solidified eutectic layer is a region of microstructure containing Ti_2Ni precipitates similar to the hypereutectoid region observed in the Ti-Cu system. This region follows a compositional gradient to the eutectoid composition (5 wt% Ni). Beyond which a hypoeutectoid region consisting of eutectoid and α-Ti needles growing from the base metal is observed. Most of the region would have been (β-Ti) at 1050°C, undergoing phase transformation during cooling. It is interesting to note that 20.7 μm of the original 50 μm Ni foil remains undissolved after heating to 965°C.

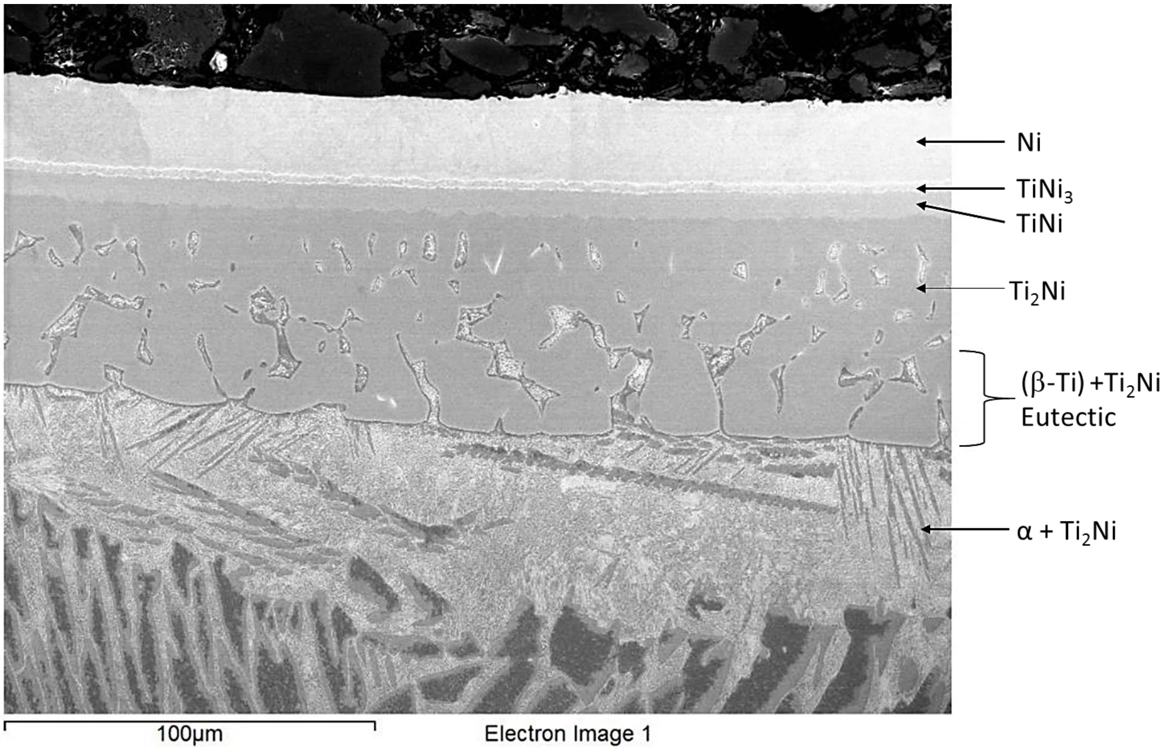

Figure 5.3 – SEM Imaging of a Half Joint Sample Heated to 965°C and Cooled at 20 Kpm Showing the Formation of Intermetallic Layers from the Nickel Foil

Figure 5.4 shows the microstructures of samples heated to 975°C, 1000°C, and 1025°C. Phases present when joining grade two titanium and pure nickel were consistent with the formation of white Ti_2Ni dendrites (37.10 ± 1.22 wt% Ni) in the ASZ with pockets of dark grey transformed primary (β-Ti) (12.14 ± 0.64 wt% Ni) in the interdendritic spaces. The same composition is found in eutectoid just below the ISZ where solid state diffusion continues into the base metal. At 975°C this dark grey area would have been (β-Ti), transforming through the eutectoid transformation during cooling. It is evident from the 965°C, and even the 975°C (top of the figure), sample that the microstructure has just completed its transition from Ni-rich intermetallic layers to a transient eutectic structure. This enforces a compositional gradient through the ASZ producing the complex microstructures evident in Figure 5.4. Later in this section it can be seen that the 1050°C sample eventually resolves into a simple hypoeutectic layer when heated for longer liquid durations.

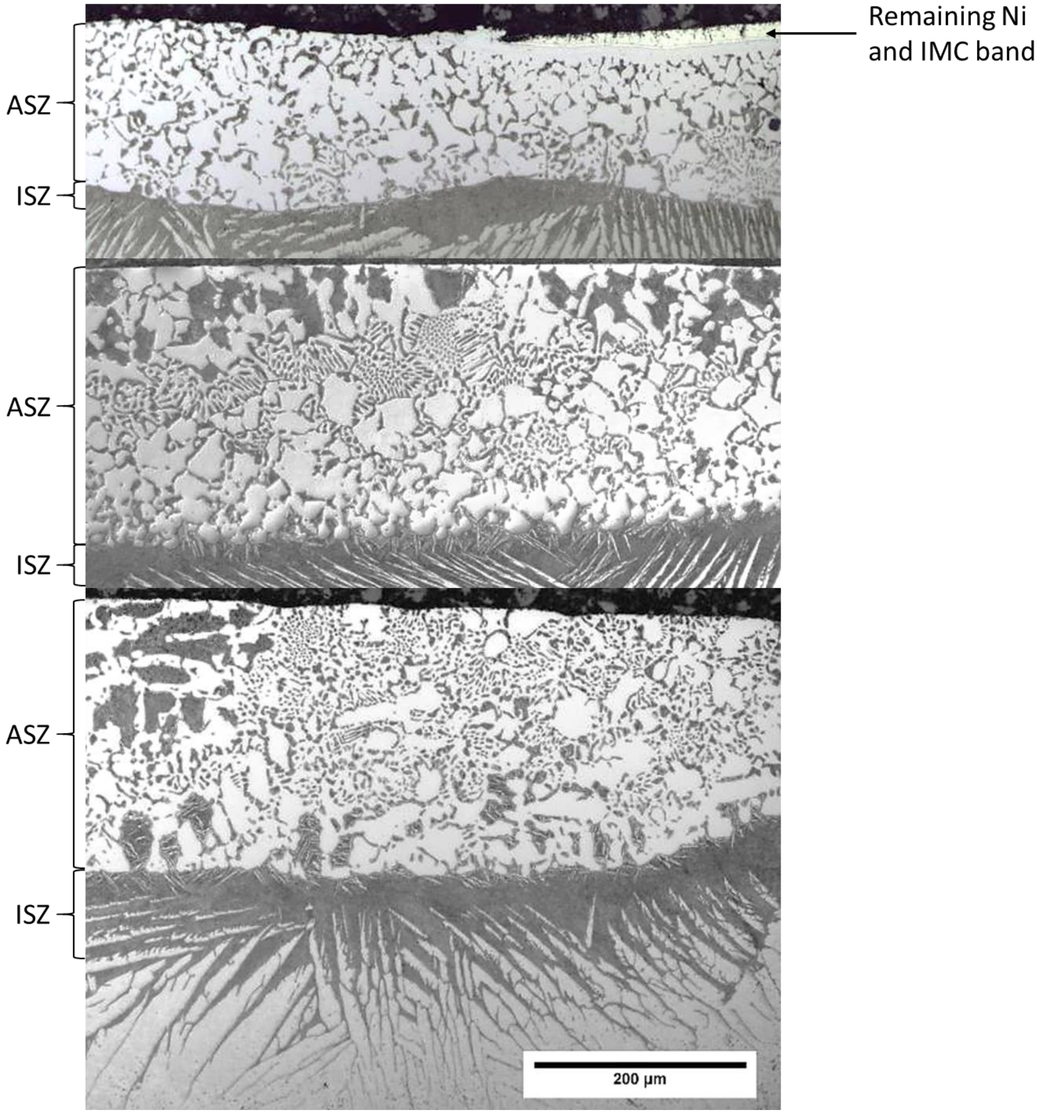

Figure 5.4 - Optical Imaging of Microstructural Cross Sections of Titanium Nickel Samples Heated to Top: 975°C; Middle: 1000°C; and Bottom: 1025°C

Minimal growth of the eutectoid layer is seen in the 975°C sample due to the low amount of time the liquid was present.

With increasing temperature, dissolution and gap widening become more evident by a thicker ASZ layer. From the DSC results in the heating curves of Figure 5.1, only an exothermic event is observed which means it is predominantly governed by intermetallic formation despite exceeding the melting temperature of 984°C. As a result, there is a composition gradient into the liquid layer which becomes more homogenous with increasing temperature. Dendritic growth of beta titanium is observed into the ASZ as the liquid becomes a more stable composition.

Upon reaching the braze temperature of 1050°C, the ASZ reaches a slightly hypoeutectic microstructure, see Figure 5.5a. Primary dendrites of (β-Ti) grow epitaxially from the solid/liquid interface followed by eutectic microstructure. Similar to the Ti-Cu system, a hypereutectoid microstructure is noted in previously (β-Ti) dendrites and near the ASZ/ISZ interface. When cooled at 80 Kpm secondary arms are observed on the dendrites with an otherwise similar microstructure, see Figure 5.5b. This sample was used later in finding the maximum depth of dissolution.

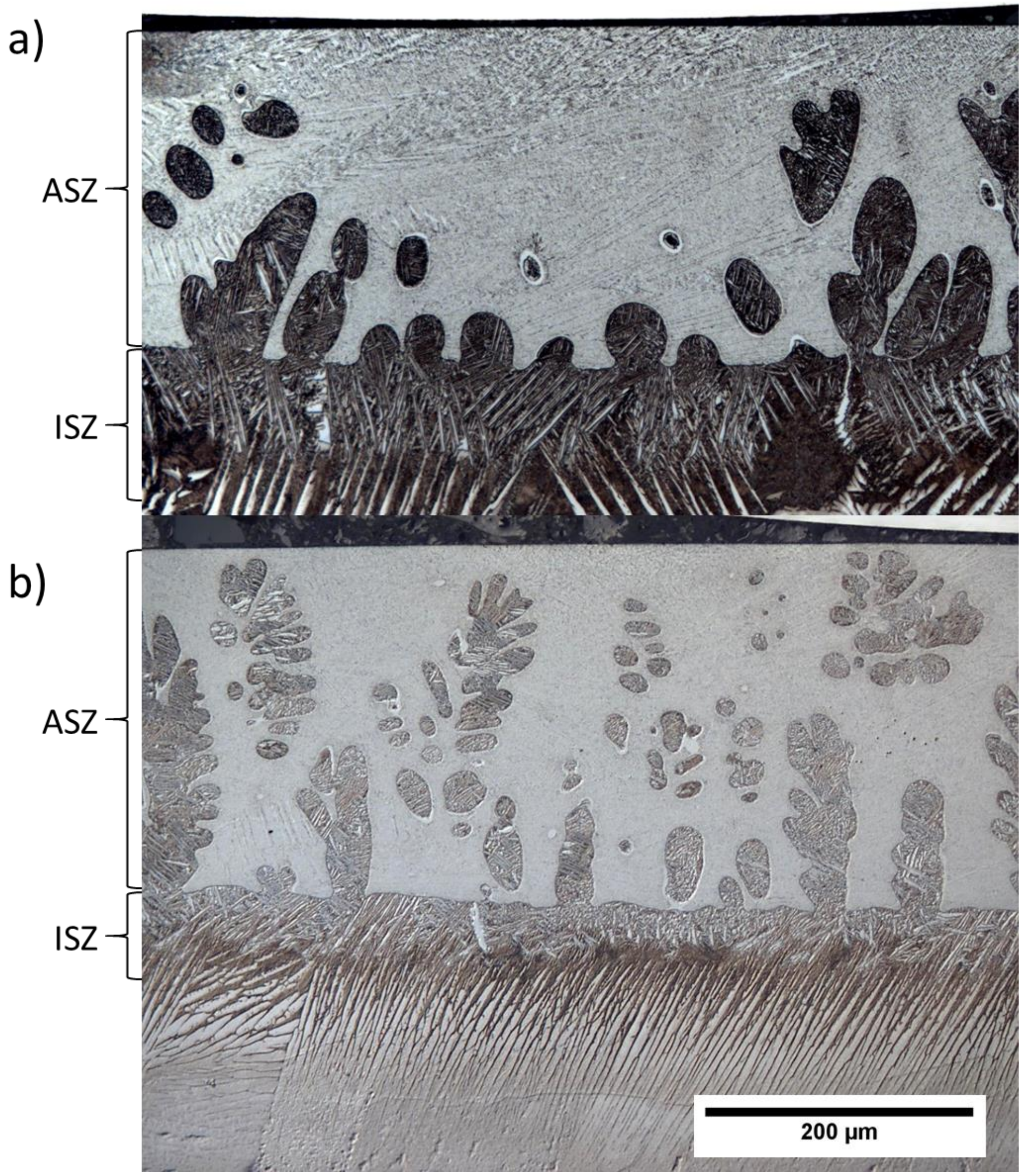

Figure 5.5 - Optical Imaging of Microstructural Cross Sections of Titanium Copper Samples Heated to 1050°C and Cooled at (a) 20 Kpm; (b) 80 Kpm

5.2 Isothermal Solidification

Isothermal solidification was examined using the cyclical DSC techniques discussed in section 2.3. Figures 5.6 and 5.7 shows the DSC trace of a titanium sample with nickel foil repeatedly heated to 1050°C, held for three minutes and cooled to 890°C. Individual heat and cool segments are shown in greyscale with dashed lines whereas the initial heating segment is solid. Using Netzsch software the start and end time of melting was documented and from these measurements, a total time of liquid duration for the braze foil was estimated. For each successive run, the total amount of liquid duration is noted beside the peak.

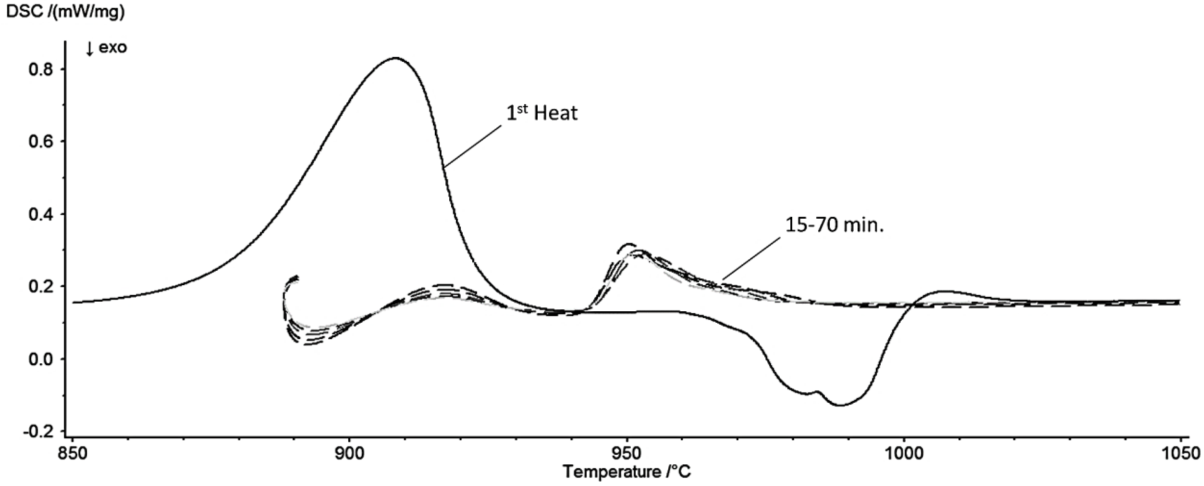

Figure 5.6 - Heating Traces for Titanium Nickel Sample Heated for Five Cycles

In some cases, the DSC traces for the Ti-Ni system exhibit inconsistent behaviour. This is best described with reference to the cooling traces of Figure 5.7. As cycles proceed solidification events progressively undercool. In some cycles and samples undercooling was such that solidification did not occur when cooling to 890°C. Consequently, upon reheating no melting peak could be measured. This led to gaps in the cyclic data points since solidification did not take place during the cooling cycle. This would result in an associated lack of re-melting during the heating cycle.

For these samples, liquid remained over several cycles and solidification peaks were only detected during the final cooling segment to room temperature.

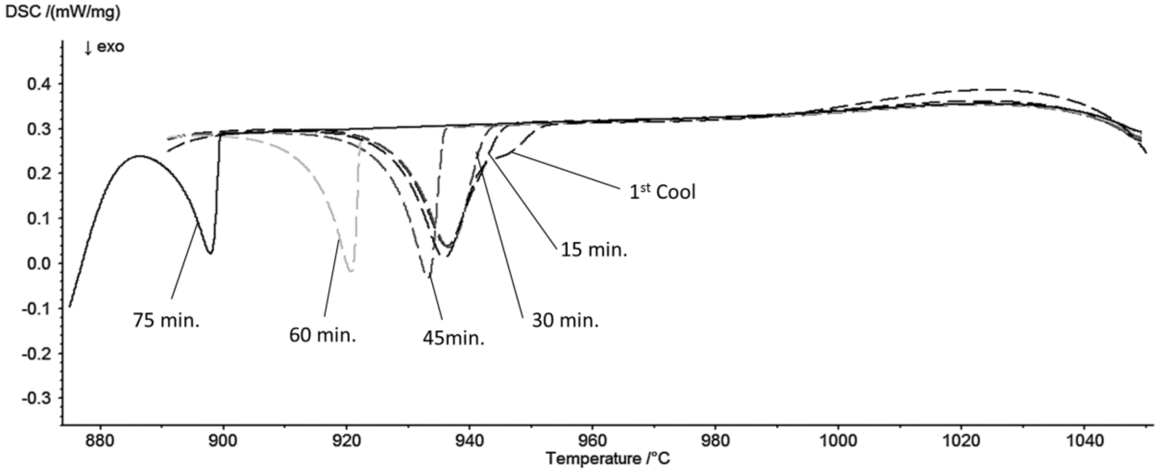

Figure 5.7 - Cooling Traces for Titanium Nickel Sample Heated for Five Cycles

An example of the ASZ microstructure for samples exhibiting high degrees of undercooling, is shown in the 1000°C sample (middle of Figure 5.4). In several locations (β-Ti) dendrites have nucleated at the liquid/gas interface rather than epitaxially at the solid/liquid interface below. This is strong evidence that nucleation of the solid phase during cooling is difficult in the Ti-Ni system. Despite this recurring issue certain samples displayed a full, or near full, set of melting and solidification events which were used to create isothermal solidification curves. Figure 5.6, 5.7, and 5.8 shows a 5X cycle sample where the events were all present and recorded. During heating and reheating, a single event is observed which onsets at 943.92 ± 0.465°C roughly beginning at the eutectic temperature.

Figure 5.7 shows the solidification peaks for the eutectic reaction. It is apparent that there is an increasing degree of undercooling occurring with increased liquid duration. Initially, the sample froze at the eutectic temperature (942°C) but by 70 minutes the sample began to undercool and instead would initiate at 899.4°C.

Figure 5.8 compares the final solidification trace of an eighteen cycle sample (labelled ‘cyclic’ in the figure) with one heated to 1050°C and cooled (labelled ‘peak’ in the figure). Despite the cyclic specimen repeatedly undercooling, such that several freezing peaks went unrecorded, it is evident that isothermal solidification has completed. Additionally, the β→α transformation peak has widened and initiates earlier in the cyclic sample due to extended diffusion of nickel into the solid. Nickel is a beta phase stabilizer so there is an extension of the right shoulder of the peak into higher temperatures. The longer LD time also increases the eutectoid peak area as more (β-Ti) transitions to α + Ti_2Ni. As mentioned in the previous section, the need for α-Ti to nucleate leads to a delayed onset of the eutectoid transformation in the peak sample.

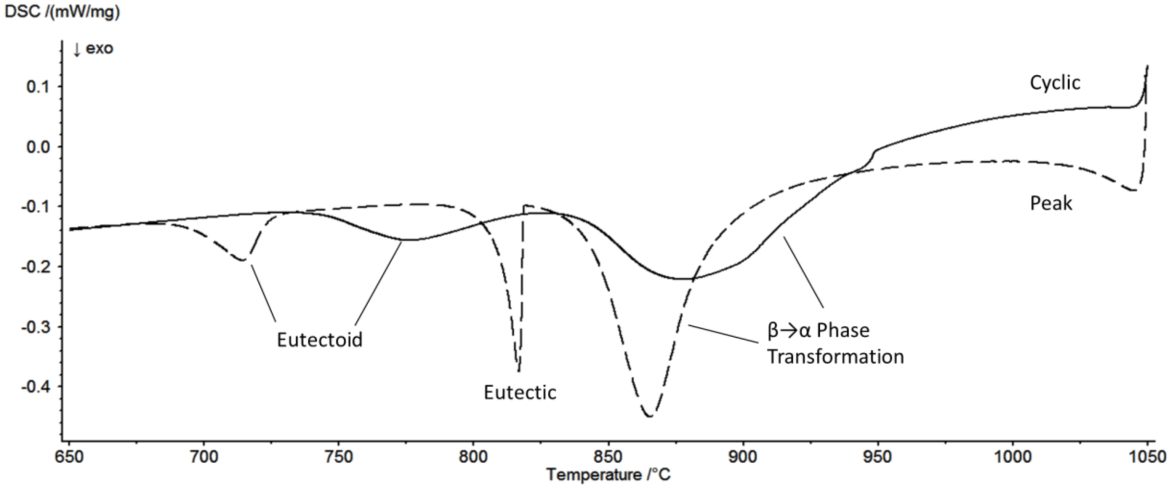

Figure 5.8 - Comparing 1050°C Peak Sample and Last Cooling Cycle of an Eighteen Cycle Sample

Figure 5.9 plots the enthalpy of solidification for samples where solidification peak values could be measured. Consistent with the data for the Ti-Cu system the enthalpy reduces in a linear way with the square root of liquid duration time. Again, enthalpy measurements were expressed based on the original mass of the Ni foil.

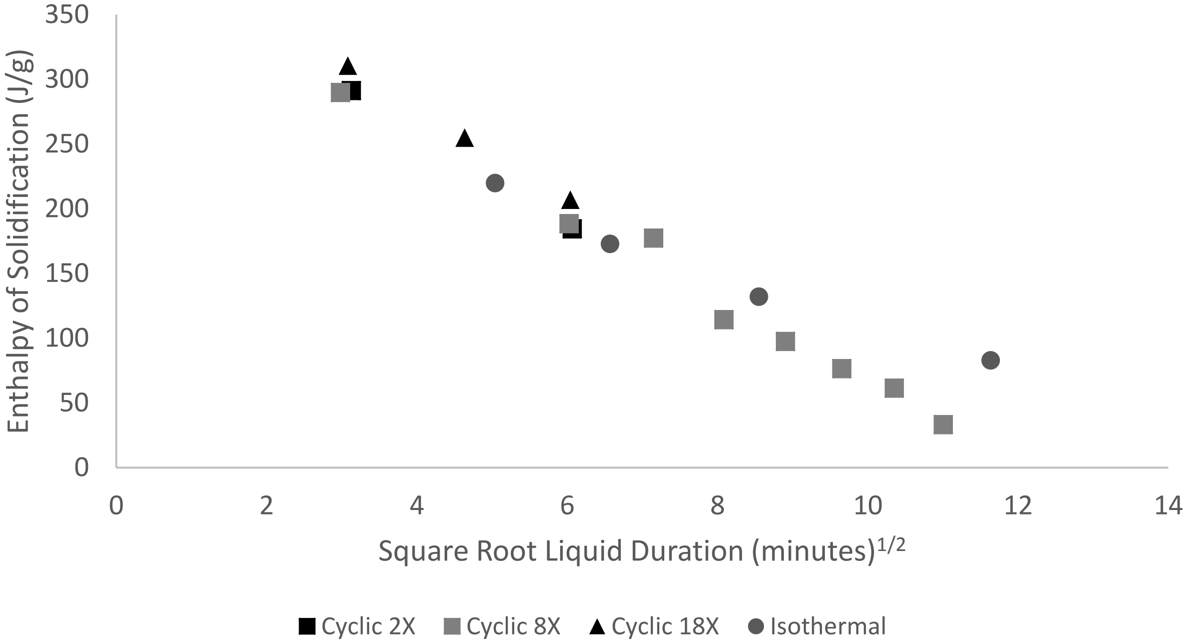

Figure 5.9 - Enthalpy of Solidification Data from Cyclical Testing of Nickel and Commercially Pure Titanium

5.3 Determining Liquid Fraction from DSC Enthalpy Measurements

The previous section demonstrated that the liquid solidifies predominantly through the eutectic reaction, involving Ti_2Ni + (β-Ti). Therefore, it was assumed that the appropriate enthalpy for this solidification reaction could be represented by the Ti_2Ni solidification enthalpy of formation, 220.16 J/g, stated in reference [74]. This is significantly lower than the theoretical enthalpy of 423.8 J/g used in the Ti-Cu system.

In a similar approach to the Ti-Cu system it was assumed that all the nickel foil homogenizing to the liquidus composition at 1050°C, would result in the maximum dissolution possible. As an example, the average nickel foil weight was also 3.2 mg and the liquidus concentration was measured from the 1050°C 80 Kpm sample to be 28.41 wt% Ni using EDS analysis. Thus, at melting there would be a maximum of 11.26 mg of liquid filler since twenty five percent of the entire filler would be nickel. In comparison, the Ti-Cu system represented a lower level of base metal dissolution, with a liquidus composition of 39.3 wt% Cu and a diluted filler mass increasing from the 3.2 mg Cu foil to 8.14 mg. Therefore, the Ti-Ni system should undergo significantly higher base metal dissolution compare to the Ti-Cu system. This is consistent with the microstructural analysis for the 1050°C 80 KPM samples for both systems. The ASZ width for these samples were measured to be 298 and 317 μm for the Ti-Cu and Ti-Ni samples respectively.

Together, the above parameters allowed a corrected liquid fraction to be calculated based on the raw enthalpy measurement ΔH_m plotted in Figure 5.10 as;

$$\boldsymbol{L_f = \frac{\Delta H^c{}_m}{\Delta H_{theo}} = \frac{0.2841 * 1.188 * \Delta H_m}{220.16}} \qquad \textbf{(5.1)}$$

Where 0.2841 corrects for dissolution (similar to section 4.3 by measuring the bulk ASZ in the 80 Kpm sample) and 1.188 corrects for the presence of the titanium base metal as outlined in section 3.2.

Figure 5.10 plots this calculated liquid fraction versus the square root of braze time. From these calculated values, the initial liquid upon melting and cooling (i.e. LD = 3 min.$^{1/2}$) was already below 45% suggesting a high degree of liquid reduction during initial heating to the braze temperature through diffusional solidification. Similar to titanium copper, there is an initial nickel uptake by the base metal which decreases the available nickel during melting. Within 30 minutes of hold time (i.e. LD = 6 min.$^{1/2}$), less than 30% of the liquid remained with complete isothermal solidification achieved in roughly 145 minutes as determined from the linear regression.

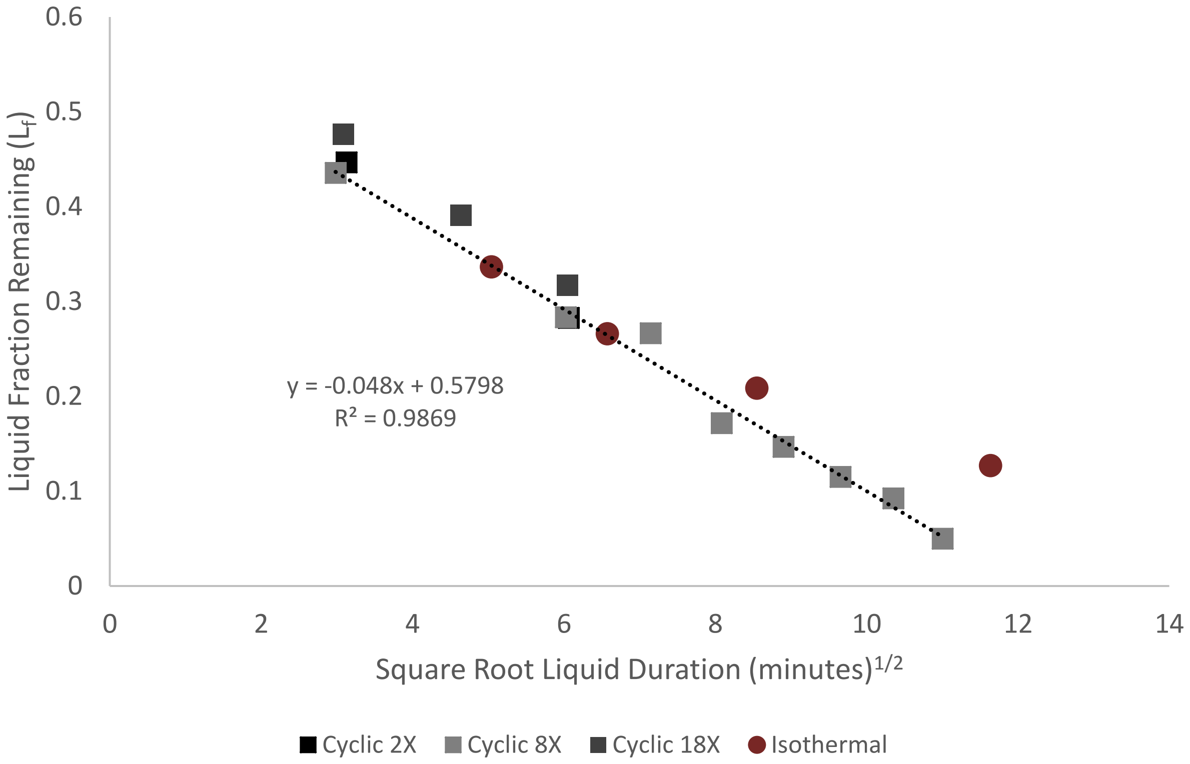

Figure 5.10 - Liquid Fraction Remaining Data in Cyclical DSC Samples of Nickel and Commercially Pure Titanium

Figures 5.11 includes microstructural cross sections of isothermal samples held at 1050°C for 15, 30, and 120 minutes. The microstructures resemble the 1050°C 20 and 80 KPM samples of Figure

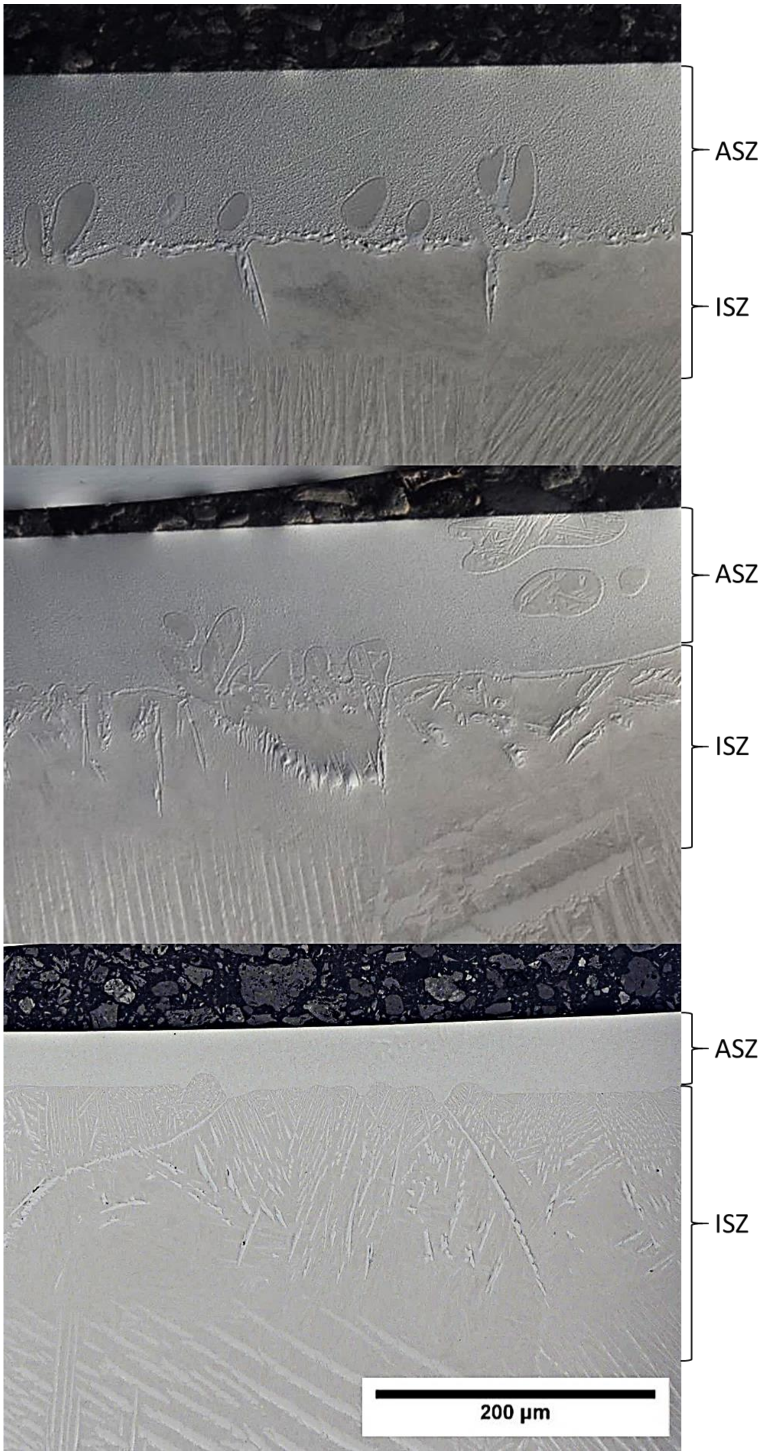

Figure 5.11 – Optical Imaging of Microstructural Cross Sections of Samples Held Isothermally at 1050°C for Top: 15; Middle: 30; Bottom: 120 minutes

5.5 with a hypoeutectic ASZ of primary (β-Ti) dendrites and eutectic and hypereutectoid that shifts to hypoeutectoid ISZ with Ti_2Ni growing from the base metal grain boundaries near the ASZ/ISZ interface. The width of the ASZ reduces and the hypereutectoid ISZ region grows with continued liquid duration. By 120 minutes of liquid duration (bottom figure), there is only 10.8% liquid remaining in the sample according to the DSC measurements.

The eutectic ASZ transitions to a finer structure and are shown in Figure 5.12 a and b under SEM for the 15 and 120 minute isothermal samples at the same magnification. The fine eutectic microstructure under EDS showed a composition respectively of 29.78 ± 0.46 wt% and 32.51 ± 0.31 wt% which is still a hypereutectic composition. However, bulk scans of the entire ASZ returned values of 28.41 ± 0.70 wt% which is the eutectic composition given from the phase diagram. The dendritic (β-Ti) discussed previously is evident Figure 5.11 (top image).

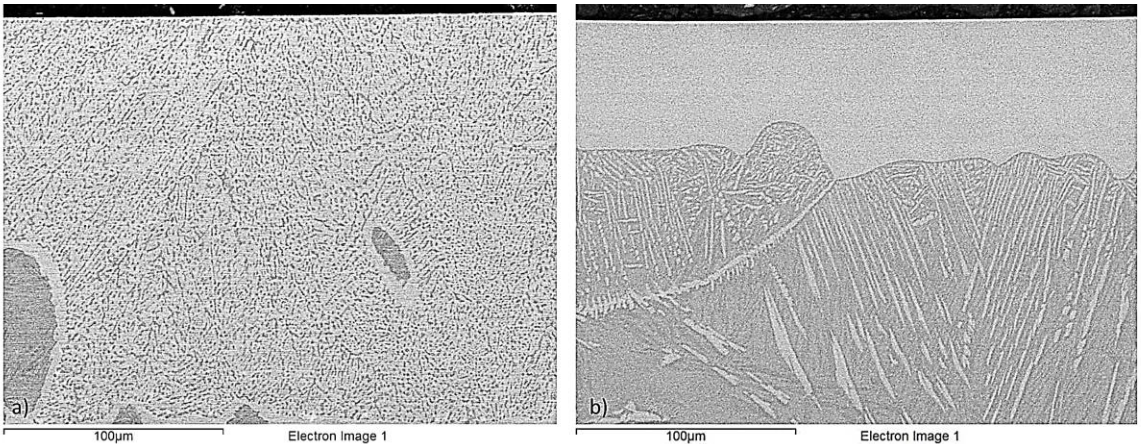

Figure 5.12 - SEM Imaging of Fine Eutectic Structure of the ASZ at 1050°C (a) Isothermally Holding for 15 minutes and; (b) for 120 minutes

5.4 Microstructural Validation of DSC Measurements

Similar to titanium copper studies, the titanium nickel interaction zone can best be defined by the geometry of a spherical cap, shown in Figure 4.14. Figure 5.13 demonstrates this geometry with a Ti-Ni sample heated to 1050°C and cooled. To characterize the dissolution process and understand the maximum volume of liquid, it was again assumed that the foil becomes a Ti-Ni liquid of cylindrical volume. For these calculations, the density of liquid was determined from a rule of mixtures to be 4.78 g/cm^3. The sample mass of 3.2 mg remained similar to the work discussed in Chapter 4 and Equations 4.3 and 4.4 were applied to find the equivalent cylindrical and spherical cap volumes. Assuming that all the Ni is contained in the liquid that develops a liquidus concentration of 28.41 wt%, the height of the cylinder was found to be 297.6 μm with a volume of 2.356 mm^3. A spherical cap with an equivalent volume would have a maximum height of 572.7 μm.

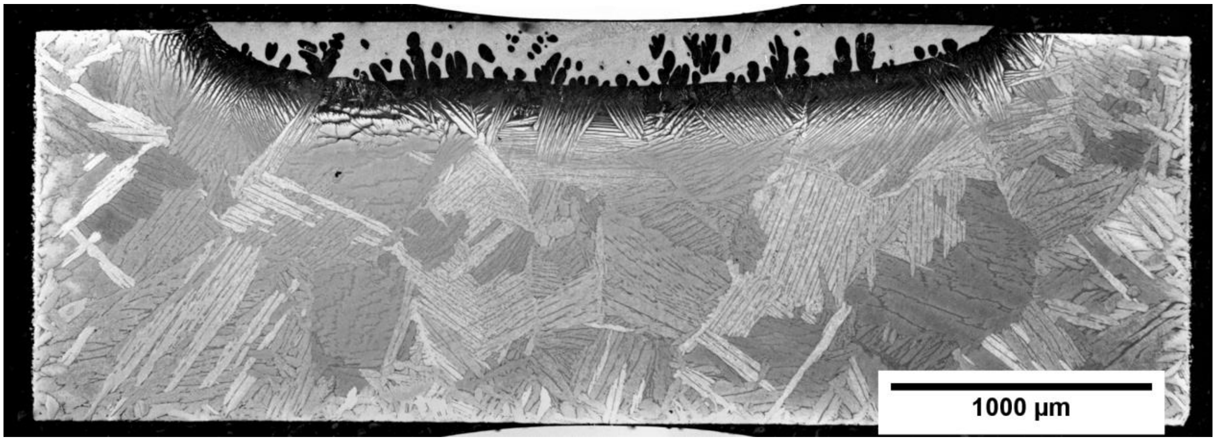

Figure 5.13 - Optical Imaging of Microstructural Cross Section of Ti-Ni Sample Heated to 1050°C and Cooled at 20 Kpm Showing Entire Width

This is a larger value than the spherical cap width of 395 μm calculated for the Ti-Cu which is consistent with the higher degree of dissolution in Ti-Ni predicted by the phase diagram. The measured spherical cap height of the 1050°C 80 KPM sample was 317 μm. Therefore, like the Ti-

Cu system the assumption that all the Ni is within the liquid phase following dissolution is incorrect. Some Ni has diffused into the base metal during heating to the braze temperature resulting in an initial Ni uptake once 1050°C is reached.

Microstructural measurements of post-brazed specimens are included in Table 5.1 along with calculated volumes of the ASZ and the liquid fraction remaining. This was calculated using the volume of the ASZ as a fraction of the maximum theoretical spherical cap volume discussed above. These values are contrasted with calculated liquid fractions from DSC cooling enthalpies. Figure 5.14 compares these values against the square root of liquid duration. As with the Ti-Cu system, microstructural and DSC measurements are in very good agreement. The linear regression (LR) of Figure 5.10 was taken to be the most accurate given the larger body of data used to obtain it.

Table 5.1 - Progression of Isothermal Solidification in Grade Two Titanium and Nickel Half Joints

Sample	Projected ASZ Width (mm)	Projected ASZ Height (mm)	Volume of ASZ (mm^3)	Calc. Liq. Fraction	DSC Liq. Fraction	Root Liquid Duration ($min.^{1/2}$)
Cyclic 2X	**2.366**	**0.130**	**0.528**	**0.224**	**0.241**	**6.07**
Cyclic 5X	**2.803**	**0.126**	**0.501**	**0.213**	**0.175**	**9.22**
Cyclic 8X	**2.805**	**0.084**	**0.277**	**0.118**	**0.042**	**11.23**
Cyclic 18X	**0.000**	**0.000**	**0.000**	**0.000**	**0.000**	**12.08**
Iso 15 min.	**2.795**	**0.192**	**0.716**	**0.304**	**0.287**	**5.04**
Iso 30 min.	**2.991**	**0.215**	**0.640**	**0.272**	**0.226**	**6.57**
Iso 60 min.	**2.523**	**0.111**	**0.375**	**0.159**	**0.178**	**8.55**
Iso 120 min.	**2.549**	**0.054**	**0.183**	**0.078**	**0.108**	**11.64**

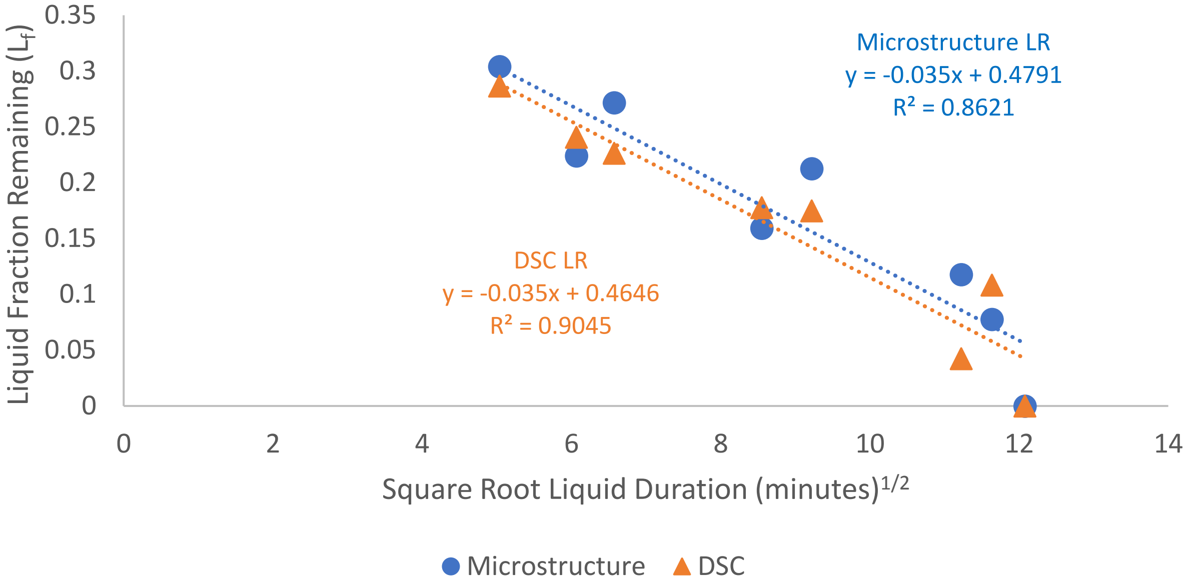

Figure 5.14 - Comparing DSC and Calculated Microstructural Liquid Fractions of Nickel and Commercially Pure Titanium

5.5 The Rate of Isothermal Solidification and the $2W_{ISZ}$ Curve

Using the analysis techniques outline in the Ti-Cu chapter from pages 69 to 79 and Equation 4.6, the $2W_{ISZ}$ value was determined as a function of the square root of liquid duration time, see Figure 5.15. The data from titanium copper has been added for a comparison in the figure and the rates of isothermal solidification (from Figure 4.16 and 5.15) have been included in Table 5.2. Recall that the y-intercept of the $2W_{ISZ}$ curve represents the initial uptake of solute prior to isothermal solidification. Interestingly, both copper and nickel show comparable amounts of initial uptake when extrapolating the initial $2W_{ISZ}$ y-intercept. (i.e. 250.1 vs. 198.2 μm). This was a surprising result given a much higher degree of dissolution expected in the Ti-Ni system. This phenomenon was also observed in the 80 Kpm samples of the copper and nickel systems where nickel showed only a minor increase in ASZ height compared to theoretical expectations. This will be discussed further in Chapter 8.

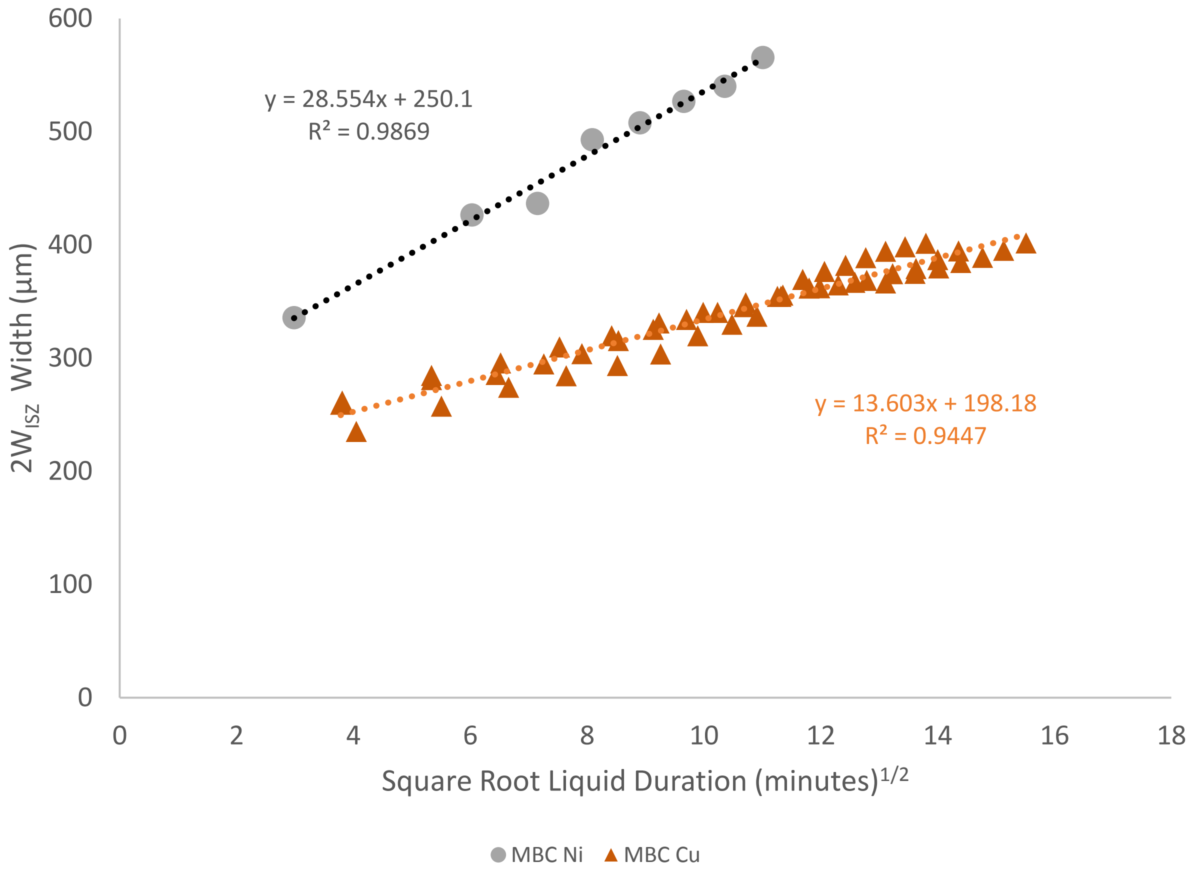

Figure 5.15 - $2W_{ISZ}$ Curves for Nickel and Copper in Commercially Pure Titanium

Table 2.5 outlines the diffusion rates of copper and nickel in β titanium and confirms that the rate of diffusion of nickel in beta titanium is around 2.5 times faster than copper. Comparing the rates of isothermal solidification (µm/√min.), this seems to be in good agreement with nickel displaying a rate of IS that is 2.2 times faster than copper. The rate of liquid fraction removal and the initial liquid fraction in Table 5.2 are derived from Figures 4.10 and 5.10. The implications of these values in terms of TLPB behaviour will be further discussed in Section 8.2.

Table 5.2 - Comparing Rates of Liquid Removal and Isothermal Solidification in Ti-Cu and Ti-Ni Systems

Diffusing Species	Rate of L_f Removal ($L_f/\sqrt{\text{min.}}$)	Initial Liquid Fraction (L_f)	Rate of IS ($\mu m/\sqrt{\text{min.}}$)	Initial $2W_{ISZ}$ Width (µm)
Nickel	**-0.048**	**0.5798**	**28.554**	**250.1**
Copper	**-0.033**	**0.4922**	**13.603**	**198.2**

5.6 Examination of the Isothermally Solidified and Diffusionally Affected Zones

Figure 5.16 provides a detailed microstructural image of the ASZ and the ISZ/DAZ region of a 5X cycle Ti-Ni half joint. The ASZ remains as a fine eutectic composition of 31.5 wt%. Precipitation

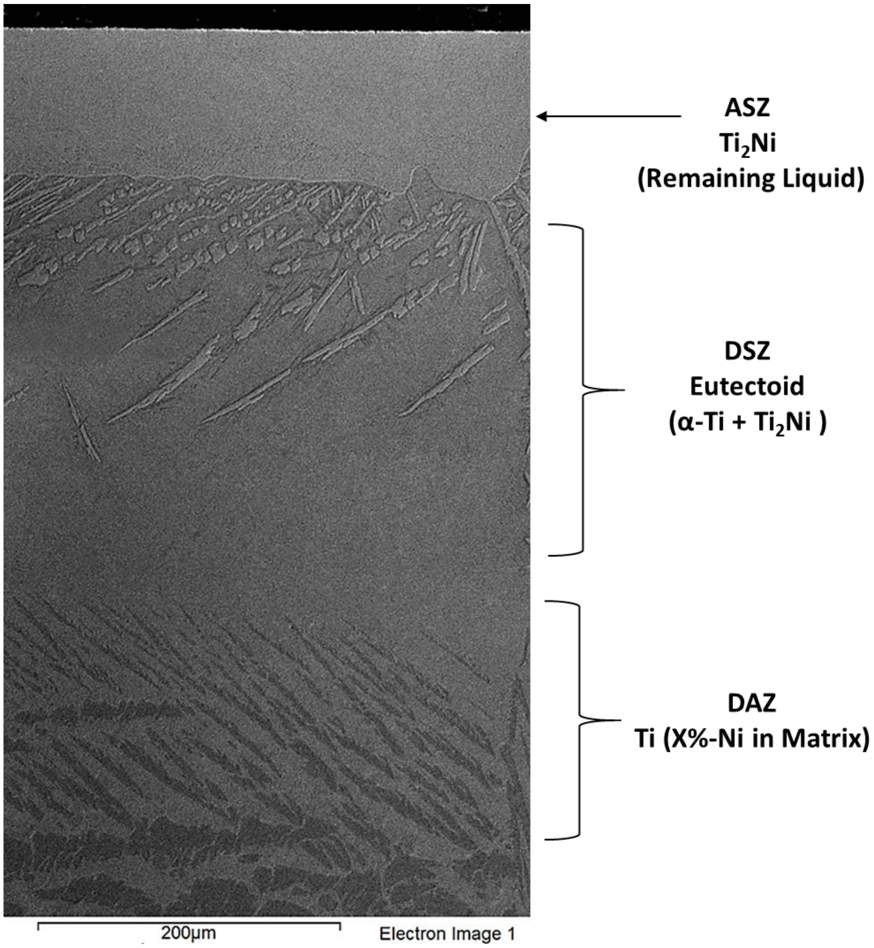

Figure 5.16 – SEM Imaging of a Ti-Ni Cyclically Heated Between 1050°C and 890°C Five Times

of needles of Ti_2Ni have grown into the ISZ as part of the hypereutectoid transformation that occurs in the solid-state during cooling. This transitions into the eutectoid structure at a depth of roughly 200 µm below the ASZ/ISZ interface.

Figure 5.17 shows the coarse Ti_2Ni precipitates just below the ASZ/ISZ interface that grew as part of the hypereutectoid reaction. In between these precipitates is a fine eutectoid structure that would have transformed from (β-Ti) during cooling below 730°C for early liquid duration samples.

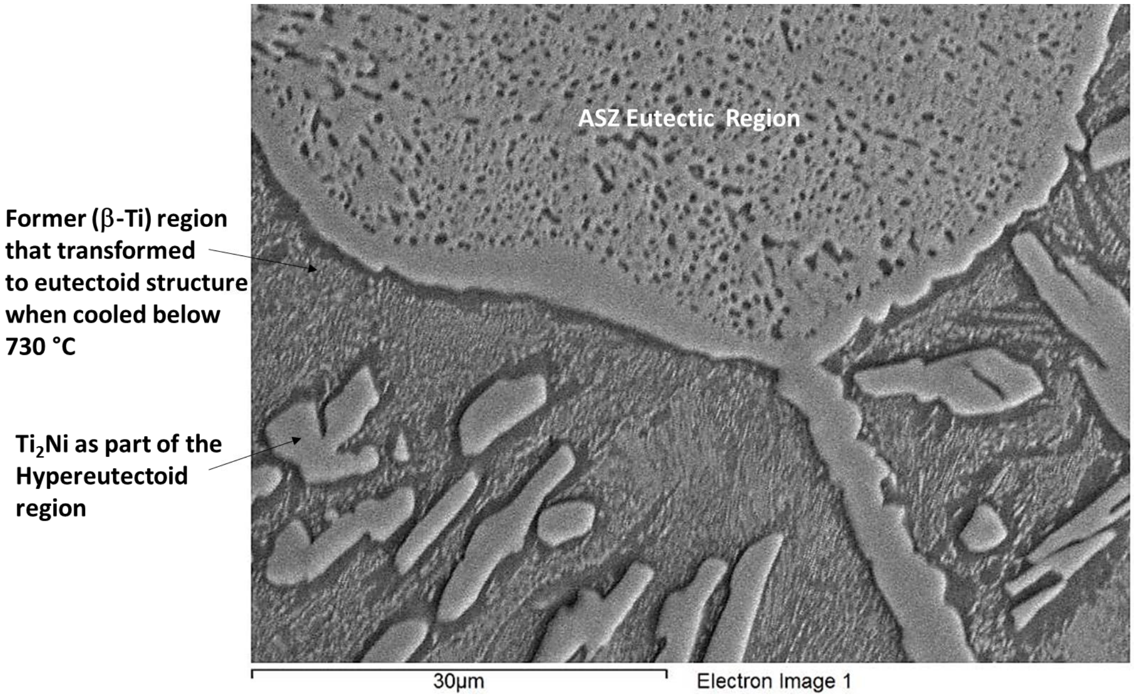

Figure 5.17 - SEM Imaging of the ASZ/ISZ Interface showing the Fine Eutectoid Microstructure Formed in a Ti-Ni Five Cyclic Sample

EDS scans were performed on a selection of half joint samples that captured the range of liquid duration time observed to create composition profiles with respect to depth from the ASZ surface. Figure 5.18 shows these compositional profiles. It should be noted that measurements in the ASZ

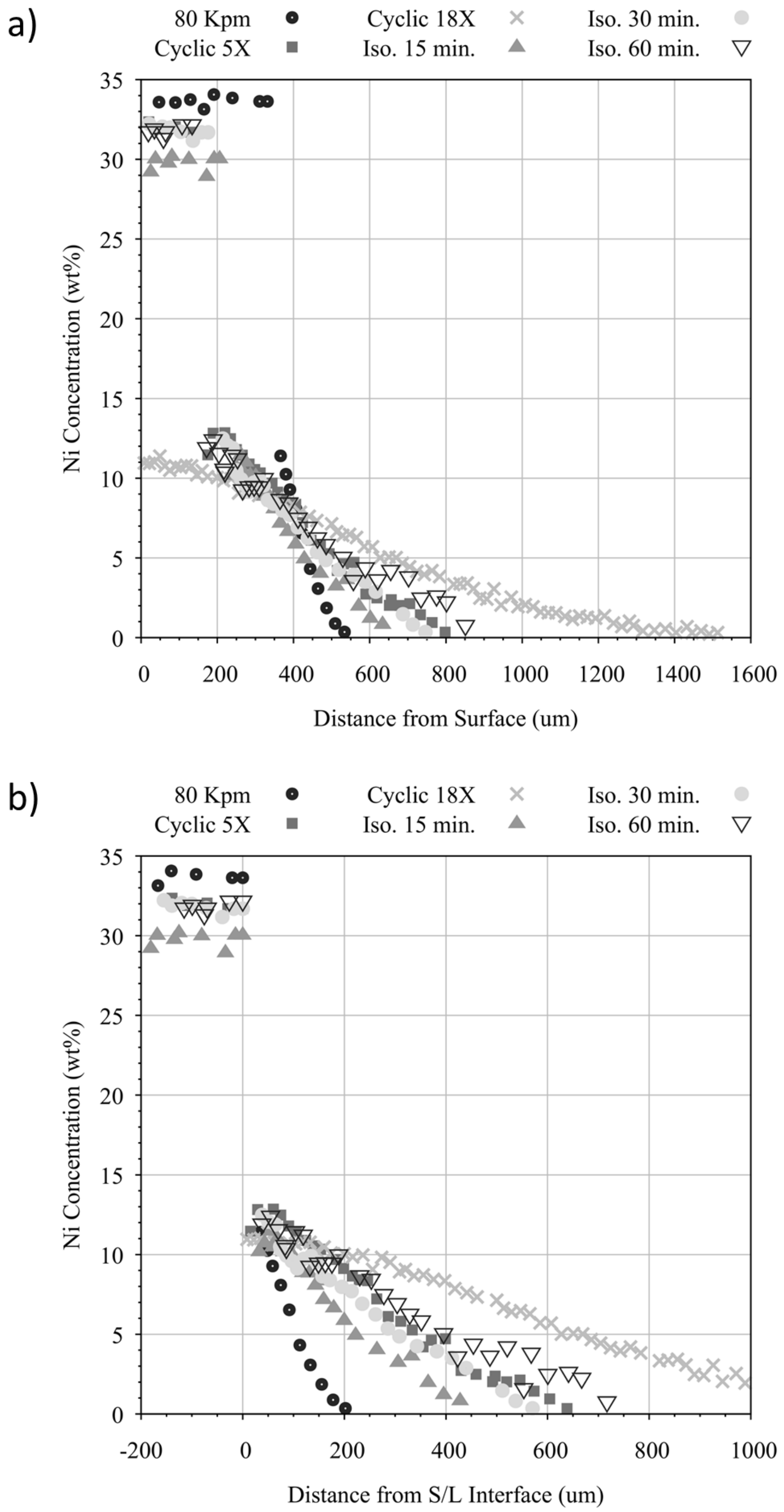

Figure 5.18 - Corrected Compositional Profiles of DSC Samples Plotted as (a) Distance from the Sample Surface; (b) Distance from S/L Interface

were scans of the eutectic phase. Similar to the Ti-Cu work, it was necessary to normalize all curves to the solid-liquid interface to properly characterize the diffusional distances of nickel for each sample. The solidus concentration of 13.2 wt% Ni was used as a maximum concentration in the base metal which was determined from a recent study of the Ti-Ni binary system [77].

It is worth noting that the titanium plate measured 1.6 mm and in the 18-cycle sample nickel was detected in concentrations of 0.5 wt% Ni at diffusion distances as high as 1500 μm away from the surface. In comparison, the maximum diffusion distance was 1100 μm for the 18-cycle sample in the titanium copper system. Of interest is the 80 Kpm sample which shows a diffusional distance of 510 μm which is in agreement with predictions of the maximum height of a spherical cap (572.7 μm) in Section 5.4.

5.7 Application of Analysis to Maximum Brazing Clearance and IS Time

Full joint assemblies, as outlined in Figure 3.11, were fixtured using nickel as an interlayer. Capillary action samples were attempted but titanium nickel liquid was found to not preferentially wet into the joint gap. Previous experimentation seemed to indicate that the contact angle of the liquid is higher than in titanium copper when wetting titanium as a substrate which was in agreement with literature [71]. Another added complication was interaction of Ti-Ni liquid with the stainless steel balls fixturing the assembly creating a liquid rich in iron and chromium. As a result, no further capillary action samples were created and sandwich assemblies with either one or two foils were used instead. Titanium nickel completed isothermal solidification in 145 minutes compared to 222 minutes for copper but, for consistency, the same liquid durations were used in full joint testing of nickel as discussed in section 4.7.

Figure 5.19 shows the results of a two foil sandwich assembly heated to 1050°C in the DIL and cooled at 80 Kpm (recall this is closer to 40 Kpm). Overall the experimental joint structure matches very well with the theoretical prediction previously described in Figure 4.22. A large pore exists right at the center of the sample surrounded by a wide $2W_{ASZ}$, corresponding to the Stage A:Type A description. The left side of the joint exhibits a smaller $2W_{ASZ,}$ from a Stage B:Type B joint. The nickel foil was undersized and judging from the joint structure was in a position to the right of centre of the gap, leading to no significant Type B joint on the right side. Note that maximum dissolution is observed to the right of the pore and is larger than the pore dimension. This suggests that liquid flowed into the left side of the joint prior to reaching 1050°C and full dissolution. This is evident by the smaller but continued dissolution to left of the pore, which would only be expected if liquid was present prior to 1050°C. The very narrow ASZ to the far left is an indication of a gap filled by liquid close to the liquidus composition and braze temperature. The liquid on the far left side reached 28.41 wt% nickel and dissolution ceased so that only isothermal solidification was occurring in this area.

As in the Ti-Cu case, the joint of Figure 5.19 can be analyzed with the $2W_{ISZ}$ curve of Figure 5.15 and in the context of Figure 4.22. The original gap width was found to be 158 μm by tracing the surfaces of the titanium plates and measuring the difference. Recall that dissolution, for a 50 μm foil, results in an equivalent cylindrical height of 297.6 μm for the Ti-Ni case. Applying this ratio to the existing gap width resulted in an expected gap width of 940 μm.

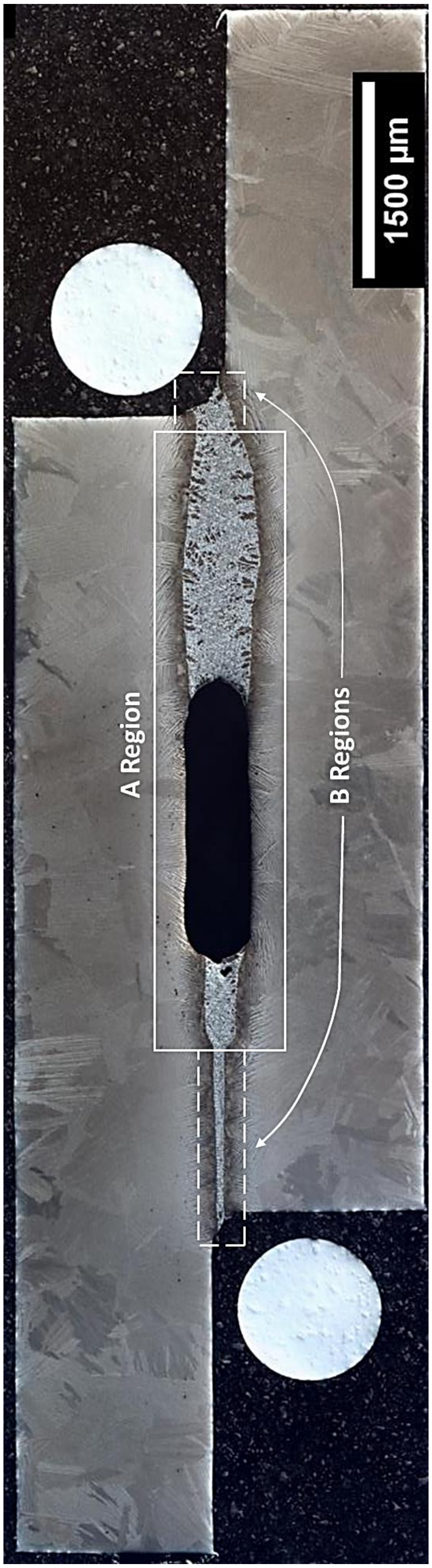

Figure 5.19 – Optical Imaging of DIL Ti/Ni/Ti Sandwich Full Joint Heated to 1050°C and Cooled at 40 Kpm with Two Ni Foils

From the $2W_{ISZ}$ curve and using a calculated liquid duration for 40 Kpm of 3.69 $min^{1/2}$ for the DIL processed sample, a value for $2W_{ISZ}$ was found to be 355 μm. Subtracting the values of $2W_{ISZ}$ from the maximum dissolution expected leads to a prediction for the width of the ASZ of 585 μm which was very close to measurement of 597.3 μm in the Type A joint just right of the pore in Figure 5.19.

Under the conditions of joint Type B to the far left of the joint, the growth of the $2W_{ISZ}$ layer can be estimated as before by the simplified equation of $2Wisz = 28.554(t)^{1/2}$ for the Ti-Ni system. With the current assumption that the gap of region B does not fill until 1050°C is reached, the liquid duration time would be 3.1 minutes (i.e. 1.76 $min^{1/2}$), resulting in an IS growth layer of 50.3 μm. Using the initial set gap of 158 μm, gives a $W_{ASZ} = 107.7$ μm for a type B joint. Averaged values across the uniform ASZ of the far left side showed values of 47.0 ± 3.2 μm. This discrepancy between the predicted and measure $2W_{ASZ}$ for this region indicates that the gap was filled before 1050°C was reached.

Compositional and hardness profiles were taken across the joint centreline and the results are included in Figure 5.20. The ASZ concentration was 29.7 ± 2.3 wt% Ni with similar concentration profiles to those in Figure 5.18. The maximum hardness (859 HV) was observed at the ASZ which shows agreement with previous literature [75][76][78]. Hardness values in the ISZ and the base metal were similar (~350 HV) suggesting the eutectoid is not detrimental to overall mechanical integrity of the joint. Near the centre line a maximum value of 32.37 wt% Ni is observed in the ASZ eutectic as seen in previous sections. Near the ASZ/ISZ interface a value of 10.50 wt% was found which is under the solidus concentrations noted in Section 5.6. Due to the flat interface of the base metal and the foil, there was no artificially heightened values to correct for as noted in Section 4.6 which were applied for Figures 4.20 and 5.18.

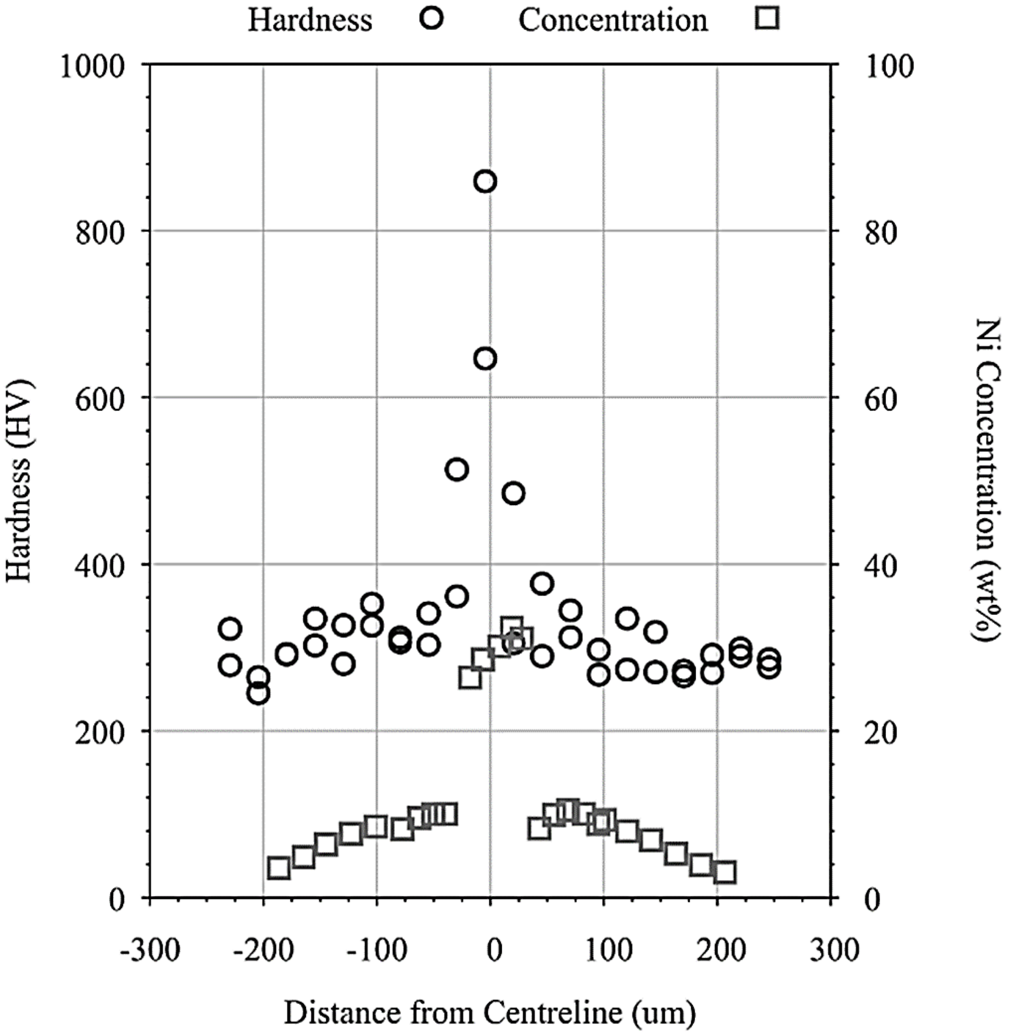

Figure 5.20 - Hardness and Compositional Profiles across the Joint Centerline of a Ti/Ni/Ti Two Foil Experiment Brazed at 1050°C and Cooled at 20 Kpm

As mentioned previously, capillary action testing proved difficult and a single foil sandwich assembly was joined instead. This sample was heated to 1050°C and held for 75 minutes followed by cooling at 20 Kpm. The results of this experiment are show in Figure 5.21. Similar to the double foil experiment both an A and B region are still visible and included in the figure. With only a single foil and a braze gap of 50 µm, dissolution would be expected to reach a maximum at the calculated cylindrical height of 297.6 µm. From the $2W_{ISZ}$ curve, isothermal solidification would complete in 6.8 minutes and the sample homogenized for the remaining 68 minutes.

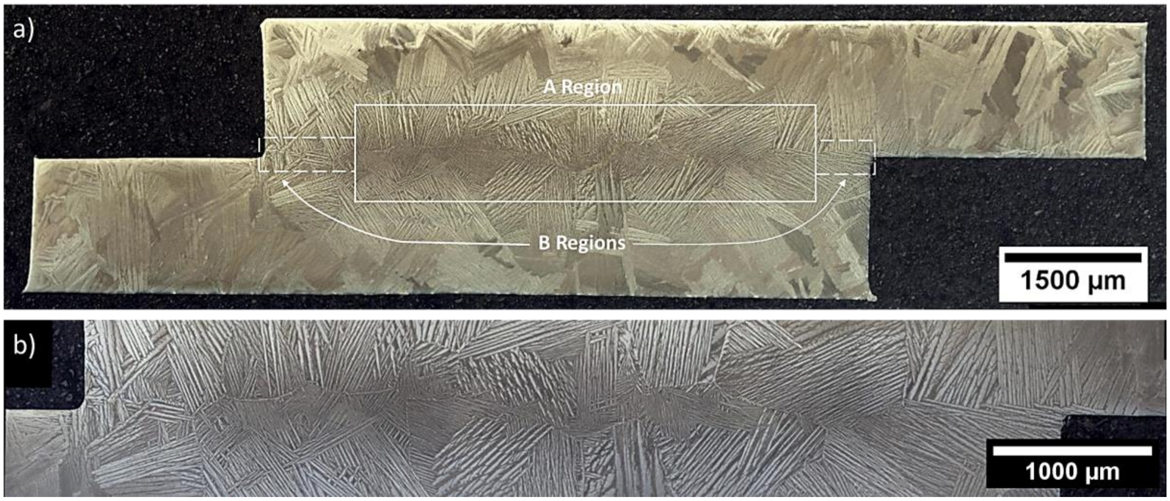

Figure 5.21 - Single Foil Sandwich Assembly Heated to 1050°C and Held for 75 Minutes at (a) 5X Magnification and; (b) 10X Magnification. Cooled at 20Kpm.

Complete removal of the ASZ is evident and the joint gap is no longer visible. The maximum composition at the centre of the sample was measured to be 4-5 wt% Ni. The resultant microstructure is eutectoid and hypoeutectoid and uniform along the joint centerline suggesting an even wetting of liquid considering an undersized foil was used. The compositional profile is likely comparable to the CP5d compositional profile in Figure 2.6.

6.0 Ti-6Al-4V and Copper

6.1 Initial Heating and Dissolution

Half joint samples of Ti-6Al-4V were heated with pure copper foil on the top surface to 975°C, 1000°C, and 1025°C in the DSC similar to studies involving commercially pure titanium. Figure 6.1 shows the heating traces and the resultant events. Initial heating exhibited melting events similar to results observed in Figure 4.1 where two endothermic peaks are observed. However, the onset temperatures of these peaks are lower than the 975°C temperatures observed in binary Ti-Cu.

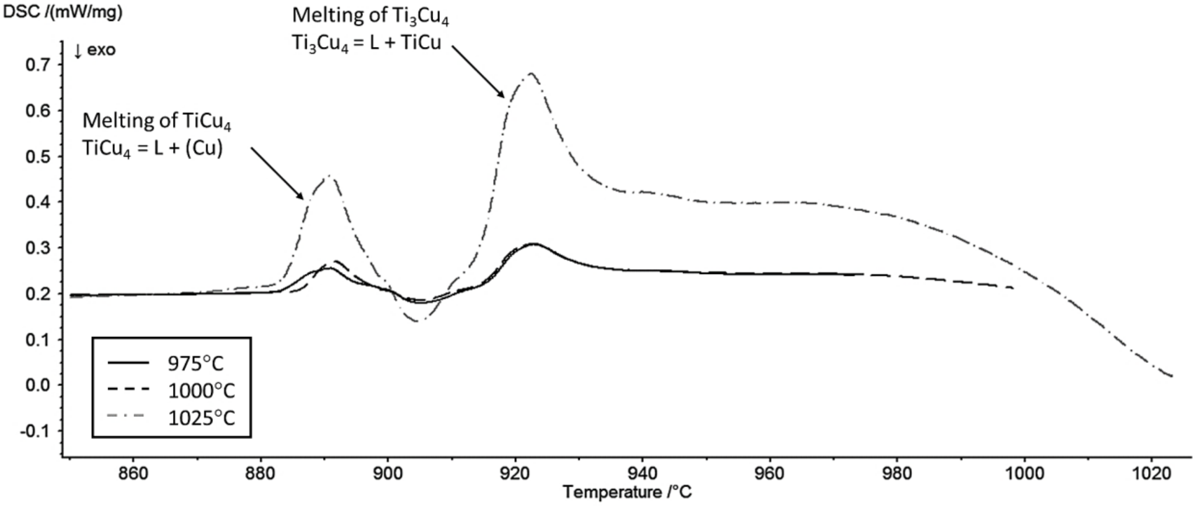

Figure 6.1 - DSC Heating Trace for Ti-6Al-4V Copper Half Joints Heated to 975, 1000, 1025°C

Two unique melting events occur at 884.3 ± 1.5°C and 914.1 ± 0.4°C. Assuming that the binary phase diagram can be applied for grade five titanium (later confirmed using EDS and previous literature), these events would be expected to be copper-rich phases outlined in the work by Murray *et al*. [56]. As Figure 6.1 shows, these phases were attributed to the formation and melting of $TiCu_4$ and Ti_3Cu_4 phases. This was confirmed when examining microstructures in Section 8.1.

Sample cooling traces are shown in Figure 6.2. Samples heated to 975°C and 1000°C behaved similarly showing an initial event at 927.9 ± 0.3°C and then a dual peak event initiating at 883.2 ± 1.4°C. This dual peak structure had peak values at 880°C and 865°C. For samples heated to 1025°C, and above, this initial peak undercools and the previous dual peak resolves to a single peak at 874.5°C. The undercooled peak onsets at 904.6°C and in all samples is believed to be the peritectic (L + β-Ti = Ti_2Cu) which was observed in the work with grade two titanium. The remainder of the copper-rich liquid solidifies into copper-rich eutectic which will be discussed next.

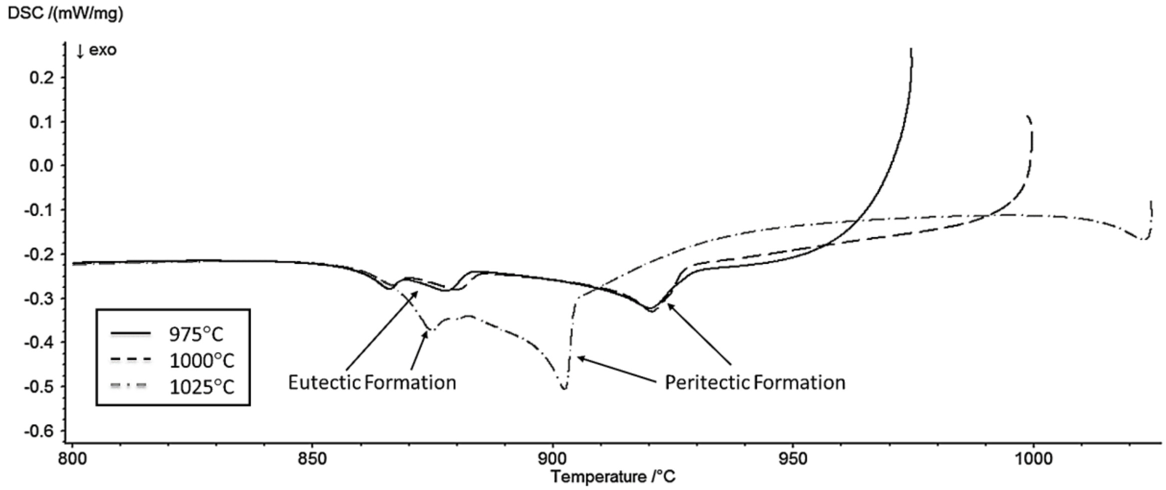

Figure 6.2 - DSC Cooling Trace for Ti-6Al-4V Copper Half Joints Heated to 975, 1000, 1025°C

Work published by Kundu *et al.* examined diffusion brazing of duplex stainless steel to Ti-6Al-4V using a pure Ni|Cu interlayer [44]. Individual layers of nickel and copper were placed such that pure copper was in contact with Ti-6Al-4V and when examined at 875°C formed a binary diffusion couple. This diffusion couple is shown in Figure 6.3a under SEM. All intermetallics discussed in Section 2.6.3 are present with more titanium-rich phases including Ti_3Cu_4, TiCu, and Ti_2Cu followed by the eutectoid, (β-Ti) = (α-Ti) + Ti_2Cu. This work confirms that the Cu rich layer on Ti-6Al-4V develops a Ti-Cu binary interdiffusion zone in the solid state (see the compositional profile is included in Figure 6.3b). A similar microstructure is expected to develop in the current samples upon heating in the DSC and explains the initial melting and solidification traces. A recurring phenomenon when using Ti-6Al-4V as the base metal was a slower observed interaction with the base metal and the foil, using either copper or nickel (discussed further in Chapter 7). In the case of copper, this is supported by the fact that Cu-rich intermetallics are not seen when using commercially pure titanium as a base metal. This suggests copper has already alloyed with CP-Ti to more Ti-rich intermetallics (Ti_2Cu and TiCu) even at the earliest observed temperature of 975°C.

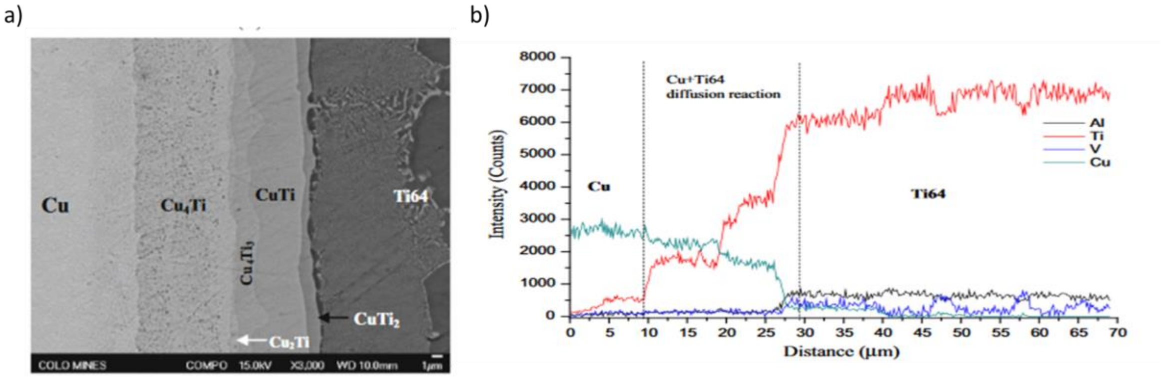

Figure 6.3 - Ti-6Al-4V and Copper Diffusion Couple Heated to 875°C and Held for 60 min. [44]

Figures 6.4 show the resultant microstructures post DSC with the ASZ and ISZ marked accordingly. A transient microstructure is observed though there is agreement with DSC results as a peritectic microstructure of β-Ti dendrites is seen growing into Ti_2Cu microstructure near the

ASZ/ISZ interface. This interface is mainly planar and is well defined for samples heated to 975°C (top figure) and 1000°C (middle figure). Recall that above 989°C both TiCu and Ti_2Cu will remelt such that the interface is less defined in 1025°C (bottom figure) [31]. In addition, there is a reduction in copper-rich intermetallics (the darker phase) in the 1025°C sample in accordance with

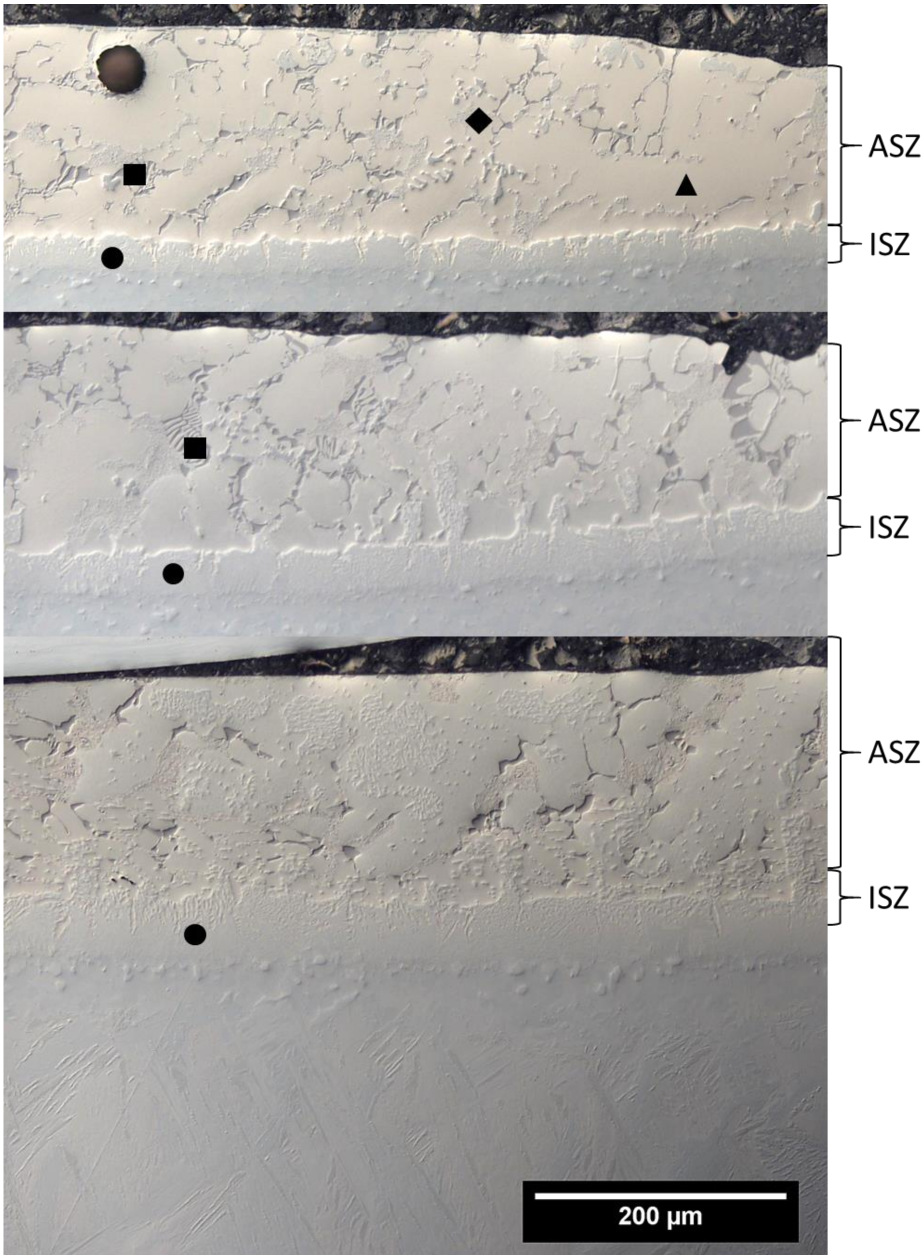

Figure 6.4 – Optical Imaging of Microstructural Cross Sections of Ti64/Cu Samples Heated to Top: 975°C; Middle: 1000°C; and Bottom: 1025°C

the change in the cooling trace to a single peak in Figure 6.2 Further into the ASZ a transient eutectic microstructure is visible and EDS identification became necessary which is included in Table 6.1.

SEM images of the 975°C microstructure discussed are shown in Figure 6.5 and Figure 6.6 which were included to contrast with the optical image of Figure 6.4. Examining these images with the aid of Table 6.1, the previous discussion of the peritectic formation is confirmed with minor additions of Al and V. The base metal composition (6 Al and 4 V) can be seen in the eutectoid phase. In addition, there are two phases which form in the interdendritic spaces (eutectic TiCu + Ti_2Cu, and Ti_3Cu_4). These phases have been confirmed in previous studies joining α + β alloys with pure copper filler metals [42][44].

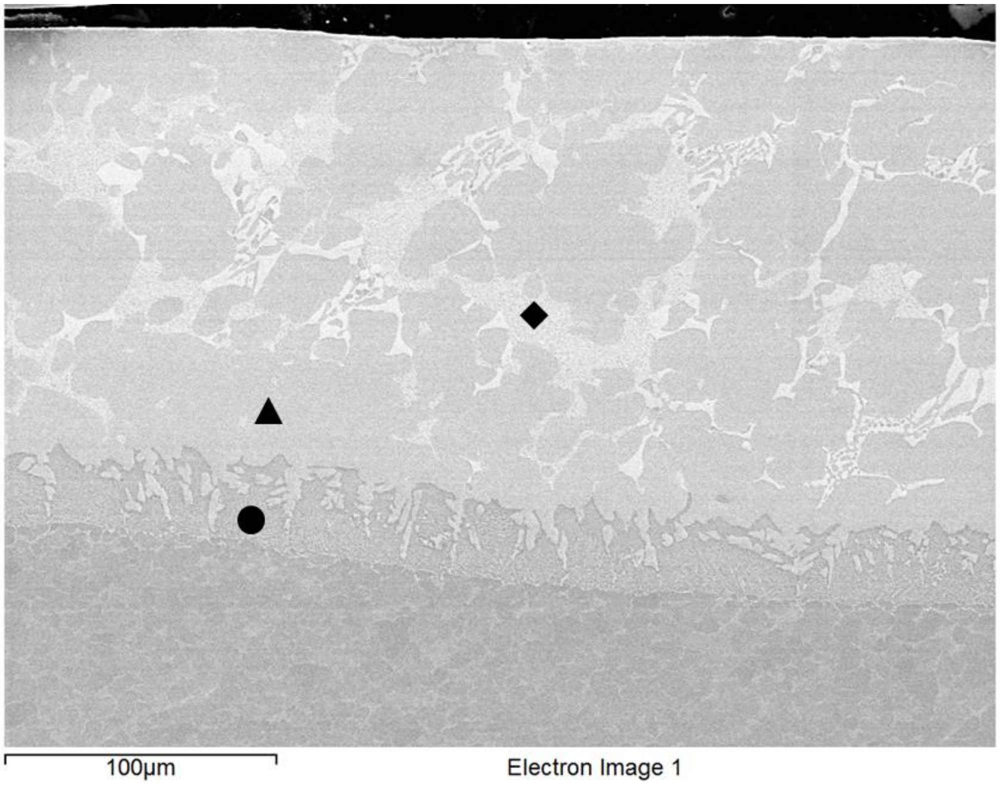

Figure 6.5 - SEM Imaging of 975°C Ti64/Cu Microstructure. EDS Results Provided in Table 6.1

Table 6.1 - EDS Compositions of Phases Observed in Initial Heating Samples

Symbol	Conc. Ti (wt%)	Conc. Cu (wt%)	Conc. Al (wt%)	Conc. V (wt%)	Phase
■	24.14 ± 0.21	67.10 ± 0.74	8.55 ± 0.55	0.21 ± 0.03	Ti_3Cu_4
◆	42.53 ± 0.75	50.66 ± 0.51	2.76 ± 0.45	4.05 ± 0.16	Eutectic TiCu + Ti_2Cu
▲	56.96 ± 0.49	39.75 ± 0.71	2.21 ± 0.28	1.07 ± 0.28	Ti_2Cu
●	74.40 ± 0.77	15.90 ± 0.48	5.37 ± 0.40	4.33 ± 0.16	Eutectoid + Ti_2Cu

Figures 6.6 a and b are taken at higher magnification in the 975°C to provide better detail of these phases. Figure 6.6a shows a fine eutectic of TiCu + Ti_2Cu was observed in pockets throughout the ASZ. The copper rich Ti_3Cu_4 incorporates a much higher amount of aluminum while rejecting vanadium which becomes incorporated in the binary eutectic. In Figure 6.6b, a layer of Ti_2Cu has grown from the solid-liquid interface into the ASZ and below the interface a fine lamellar eutectoid structure is observed.

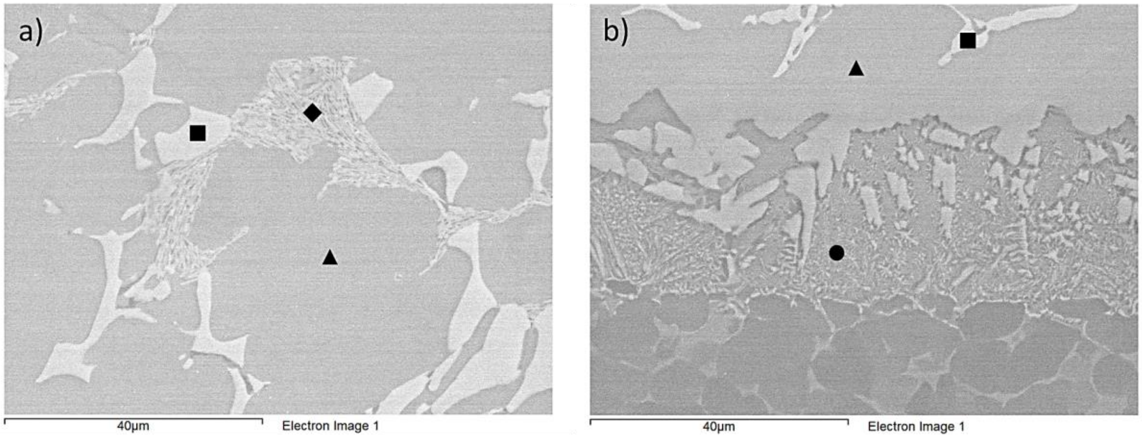

Figure 6.6 - SEM Imaging of Microstructure in the 975°C Sample (a) Phases in the ASZ; (b) At the ASZ/ISZ Interface

Figures 6.7 a and b shows samples heated to 1050°C and cooled at 20 Kpm and 80 Kpm respectively. Dendrites of β-Ti are more prevalent in both samples with secondary arms visible in the 80 Kpm sample. The interdendritic Ti_2Cu regions are visible with the bulk of the ASZ exhibiting a peritectic structure. It would appear that additions of aluminum and vanadium do not alter the primary mode of solidification observed in the Ti-Cu binary systems; peritectic and subsequent eutectic freezing. As a result, Figure 6.7 shares many similar characteristics to Figure 4.4, (β-Ti) dendritic solidification along with the formation of an interdendritic Ti_2Cu matrix which contains TiCu (and initially more Cu-rich intermetallic) precipitates. The presence of TiCu was observed in low liquid duration samples of Chapter 4 and can be seen precipitating in a similar fashion in Figure 4.4.

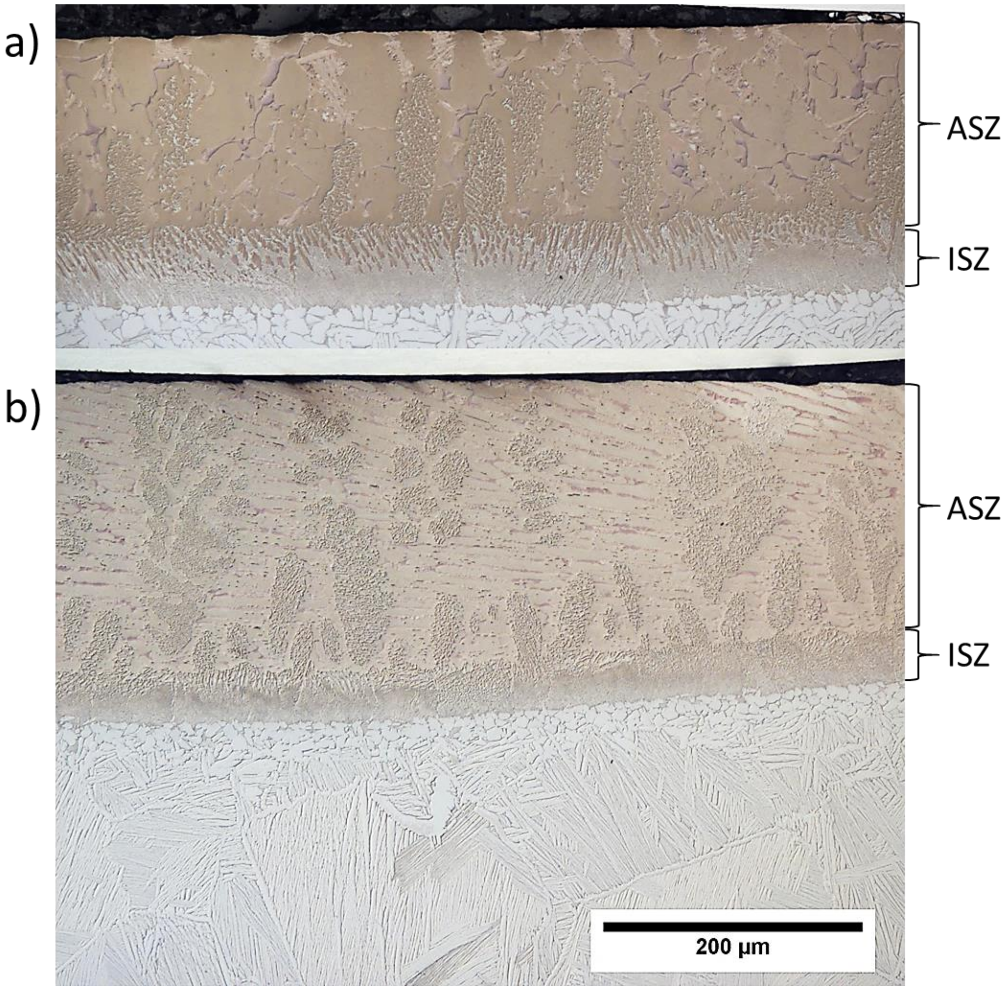

Figure 6.7 – Optical Imaging of Microstructural Cross Sections of Ti64/Cu Samples Heated to 1050°C and Cooled at (a) 20 Kpm; (b) 80 Kpm

6.2 Isothermal Solidification

To avoid the formation of intermetallics in the Ti-6Al-4V and copper system, the same brazing temperature of 1050°C was selected for cyclical studies. For consistency across studies, the same cyclic temperature range (1050-890°C) was selected for simpler comparison. However, this created difficulties when later examining liquid fraction and $2W_{ISZ}$ curves as the liquid remaining was consistently underestimated compared to L_f measurements made from metallography. This was determined to be the result of larger degrees of undercooling in Ti-6Al-4V such that portions of the freezing event were not captured before reheating from 890°C. This will be addressed following a discussion of early cyclic testing results presented below.

The heating traces for a cyclic 24X DSC experiment are shown in Figure 6.8. A similar initial heating trace is observed comparable to those in Figure 6.1. Following initial heating, there is a single consolidated peak with an onset at 941.4 ± 3.8°C. This was in stark contrast with observations in Figure 4.6 where a double peak melting event was seen (attributed to the melting

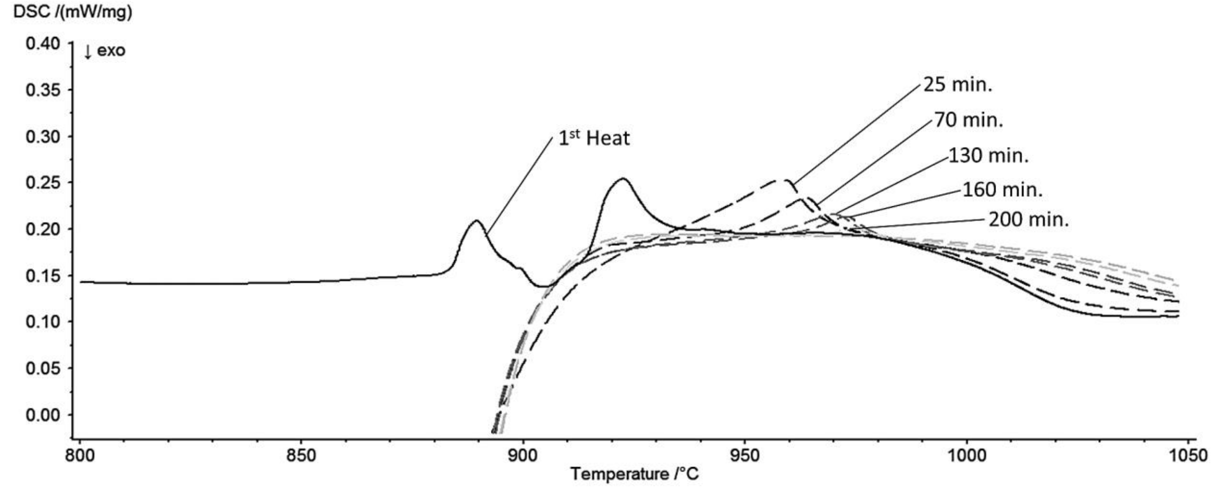

Figure 6.8 - Heating Traces for Ti-6Al-4V Copper Sample Heated Cyclically for 24 Cycles

of the eutectic and the peritectic). Based on microstructural observations in the previous section, this peak was presumed to be the repeated melting of the peritectic ASZ.

Cooling traces are included in Figure 6.9 where a single event is present for the duration of testing. Figure 6.9 indicates that the peritectic solidification event occurs over the same temperature range as the β to α phase transformation in the Ti-6Al-4V base metal. This is also true for the remelting peak in Figure 6.8. In comparison, the DSC traces for the binary Ti-Cu couples (see Figures 4.6 and 4.7) show that the ASZ freezing and melting events do not overlap with the β to α phase transformation of the pure titanium. The β to α transformation occurs at lower temperatures compared to the Ti64 alloy. As a consequence, it was more challenging in the Ti64/Cu couple to define a baseline for accurate enthalpy measurements of the melting/solidification ASZ event.

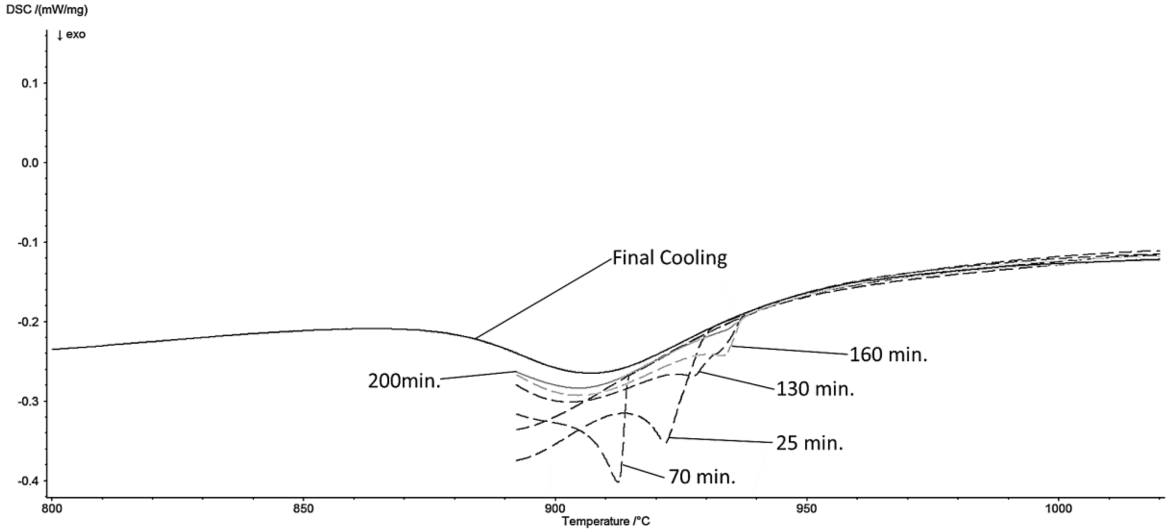

Figure 6.9 - Cooling Traces for Ti-6Al-4V Copper Sample Heated Cyclically for 24 Cycles

The freezing peaks show a large degree of undercooling initially followed by a gradual shift in onset to higher temperatures. During cyclical testing for 24 cycles, this shift would begin from

915°C and end at 940°C. This shift was not unusual and was prevalent in the commercially pure titanium and copper system, discussed in Chapter 4, where the range was from 925°C to 940°C.

The final cooling curve of a cyclic 3X sample was contrasted with a 24X cycle that underwent complete isothermal solidification, see Figure 6.10. Complete isothermal solidification is evident in the 24X sample where no solidification peak was observed. A noticeable eutectoid phase transformation is present, indicating significant diffusion of copper into the base metal. The undercooling of the 3X sample and its overlap with the base metal β to α phase transformation is evident. The final cooling curve reveals the secondary eutectic peak which was expected in cyclical testing. The 3X sample shows that in earlier cyclic steps (where cooling only goes to 890°C before reheating) this solidification event would not be properly measured or occur at all.

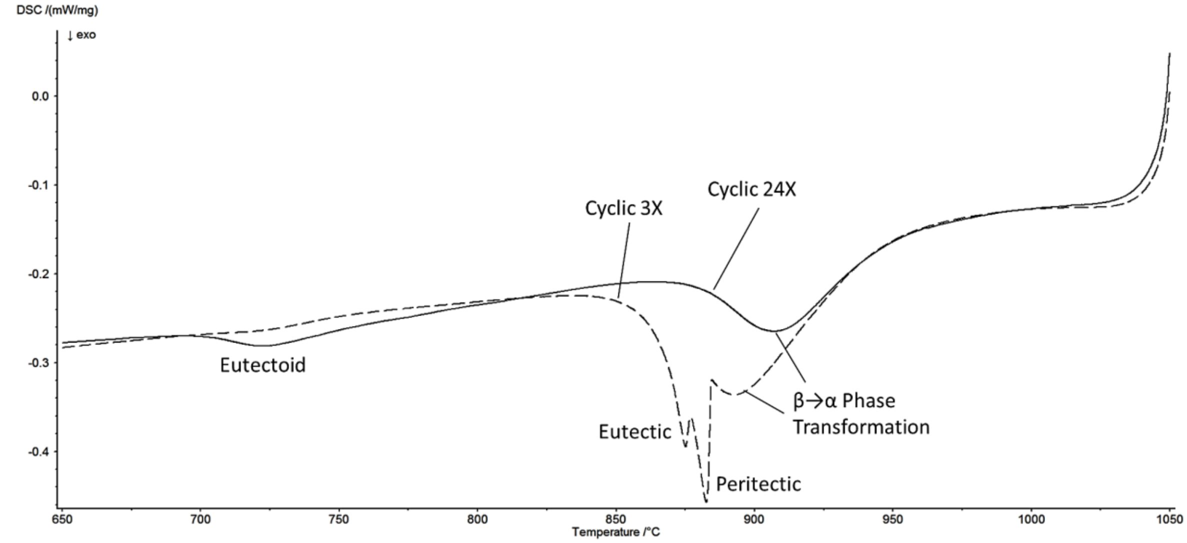

Figure 6.10 – Comparing Last Cooling Curve of Cu Cyclic 3X Sample and Cycle of 24 Cycle Sample

DSC traces from Figure 6.10 made it evident that some, or in some cases all, of the enthalpy data was not being accounted for in cyclical testing. This was especially true for early liquid durations. Since there was a more severe case of undercooling in Ti-6Al-4V, a new cyclical temperature program was created to capture the entire melting/solidification process. Section 2.7.1 outlined that the degree of undercooling for a particular event will increase with increasing cooling rate. To minimize undercooling, a cooling rate of 10 Kpm was used for this temperature program and the heating rate was maintained at 20 Kpm for consistency. In addition, the temperature range was extended to 1050-850°C to capture all solidification events from the liquid. Finally, an isothermal hold time of ten minutes was used. The heating traces are included in Figure 6.11.

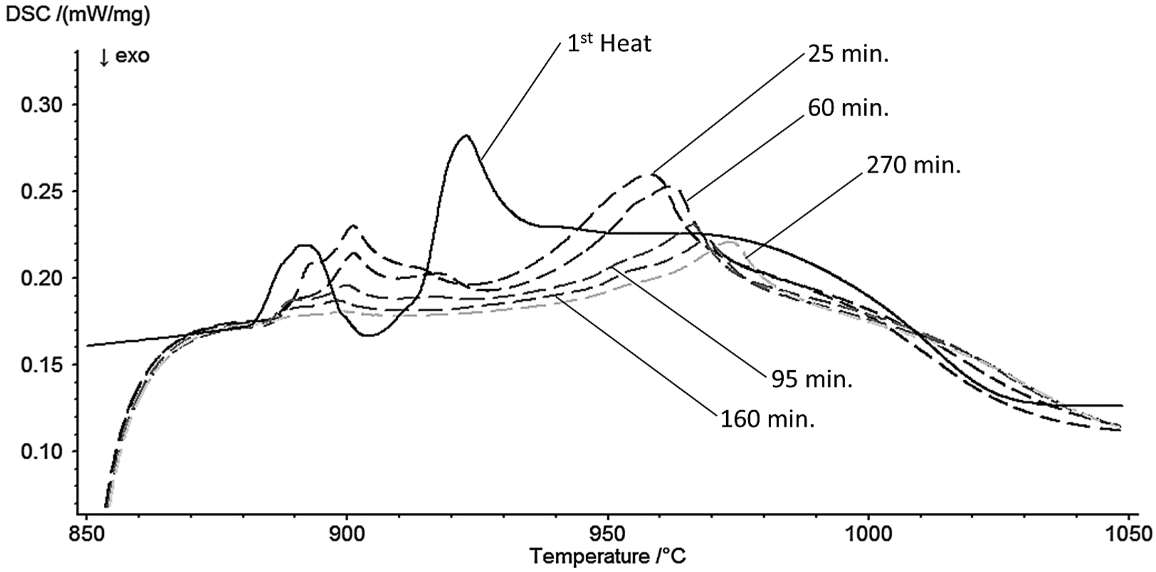

Figure 6.11 - Heating Traces for a Ti-6Al-4V Copper Sample Heated Cyclically for 8 Cycles from 1050-850°C Cooling at 10 Kpm

Figure 6.11 shows the return of the double peak structure found in Figure 4.6 where there is a eutectic melting peak (onsets at 884.97 ± 2.02°C) and a later peritectic melting peak (onsets at 950.15 ± 10.11°C). These likely correspond to the formation of Cu-rich intermetallics, which subsequently melt, and eutectic melting (Ti_2Cu + TiCu → L) [56]. In early liquid durations, the eutectic shows additional minor peaks which may represent the melting of incorporated of Cu-rich intermetallics ($TiCu_4$, etc.). Again, similar to binary Ti-Cu system, the additional eutectic peak disappears only after the last cycle of 270 minutes. This is nearly twice the time observed when using commercially pure titanium where the eutectic disappeared in only 150 minutes suggesting slower kinetics. This also implies that the Cu-rich intermetallics are never fully removed, but remain as minor additions, until complete isothermal solidification.

Figure 6.12 shows the cooling traces for the same cyclical test. It is evident that the entire β to α phase transformation and the early liquid duration peaks have been fully captured. Initially, the peritectic is heavily undercooled such that the eutectic onsets very shortly after. Similar to the first heating segment, the first cooling segment shows an additional peak between the peritectic and the eutectic which is again due to the presence of Cu-rich intermetallics. Following an hour of liquid duration, the peritectic shifts to the other side of the transus transformation peak where it onsets at 938.87 ± 1.80°C. This is consistent with earlier testing where the peritectic peak was found to shift eventually to 940°C at longer hold times.

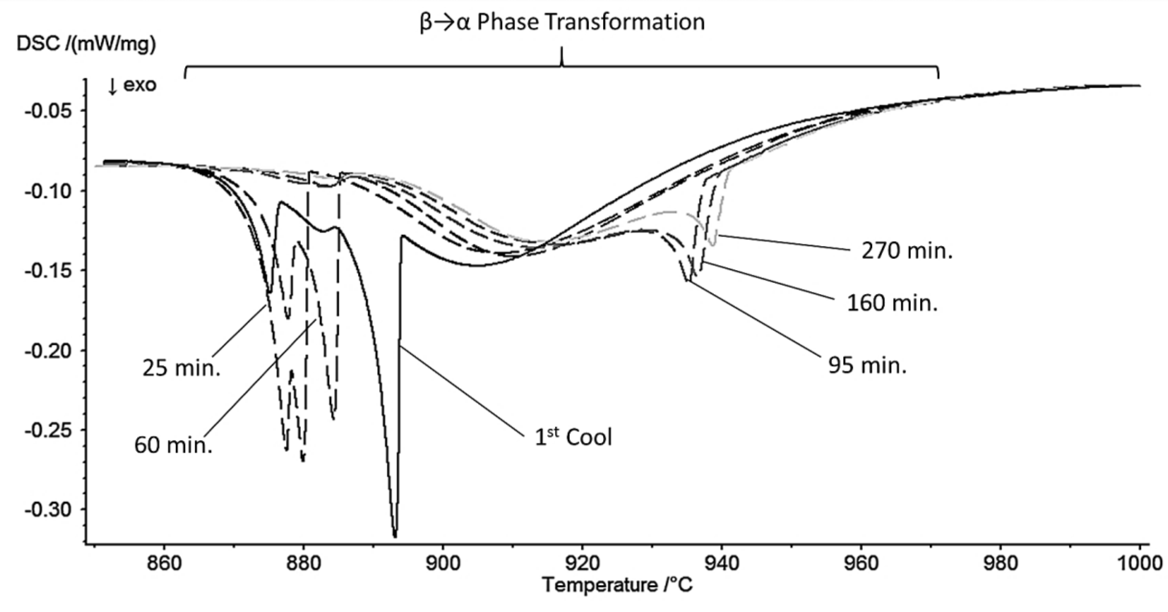

Figure 6.12 - Cooling Traces for a Ti-6Al-4V Copper Sample Heated Cyclically for 8 Cycles from 1050-850°C Cooling at 10 Kpm

Figure 6.13 illustrates selected cooling traces from Figure 6.12 in order to explain the baseline construction used for these more complicated DSC curves. The selected curves indicate the different ways in which the solidification peaks overlap with the broader β to α phase transformation of the Ti64 base metal. The first solidification peak occurs in the second half of the BM transformation with a baseline curvature that was best captured by a Bezier (B) construction method (see Section 3.2 for more detail on baseline construction methods). The 2nd through 5th cooling curves (95 to 200 minutes liquid duration) occur near the end of the BM transformation such that a Linear (L) baseline construction could be used.

Figure 6.13 - Measurements of Cyclically Tested Sample Denoting Appropriate Use of Bezier (B) and Linear (L) Baseline Corrections

The 4th and 5th cooling trace solidification peaks occurred over different temperatures such that both were measured separately. The high temperature peak of this cycle occurred near the peak of the β to α transformation with high curvature. Using the baseline shape of the previous cooling segment as a guide, constructing an accurate baseline was possible using the Bezier construction technique. All other peaks were in locations where a linear baseline construction was appropriate.

DSC samples that underwent an isothermal hold segment required a different baseline construction due to the unique position of the solidification peak (see Figure 6.14). For all isothermal cooling traces, the solidification peaks onset close to the BM β to α transformation peak temperature and extended near to the end of the transformation. Linear, Bezier and Sigmoidal baseline constructions were all attempted to simulate the shape of the underlying baseline. Visual inspection shows that the Linear and Bezier constructions underestimate the area under the solidification peak. The Sigmoidal construction reflects the baseline well, although may slightly overestimate the enthalpy of solidification.

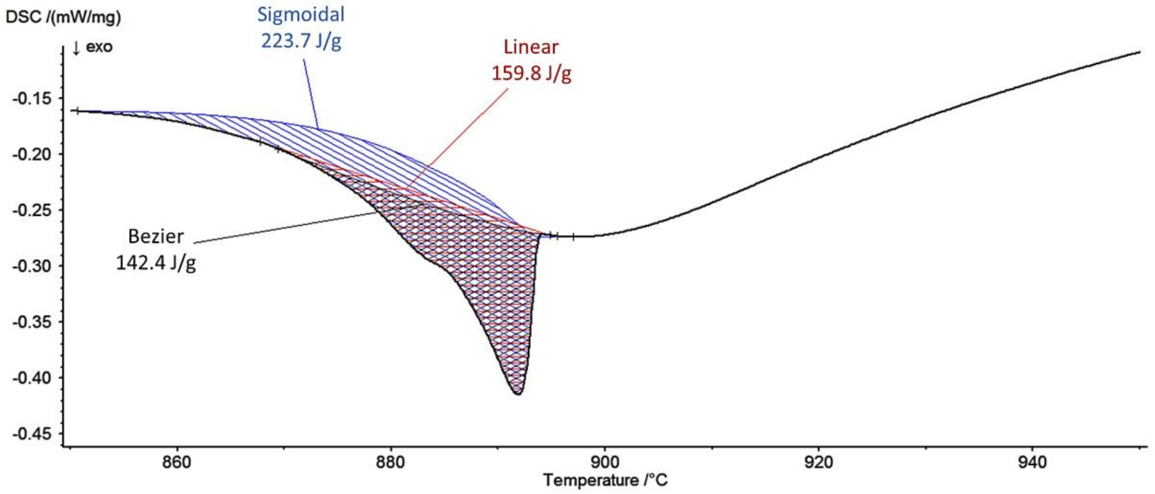

Figure 6.14 - Measurement of Sample Held Isothermally for 60 min. and Cooled Showing Difference in Peak Enthalpies Between Linear, Sigmoidal, and Bezier Baseline Corrections

Figure 6.15 shows the 10 KPM modified cyclical data and isothermal data plotted for the Ti-6Al-4V and copper system. The Sigmoidal baseline derived solidification enthalpy for the isothermal samples are included in the plot and agree very well with the enthalpies determined from the two 10 Kpm cyclic samples. Isothermal solidification was observed to complete in 364 minutes, or 19.07 min.$^{1/2}$ (CP-Ti competed in 222 minutes).

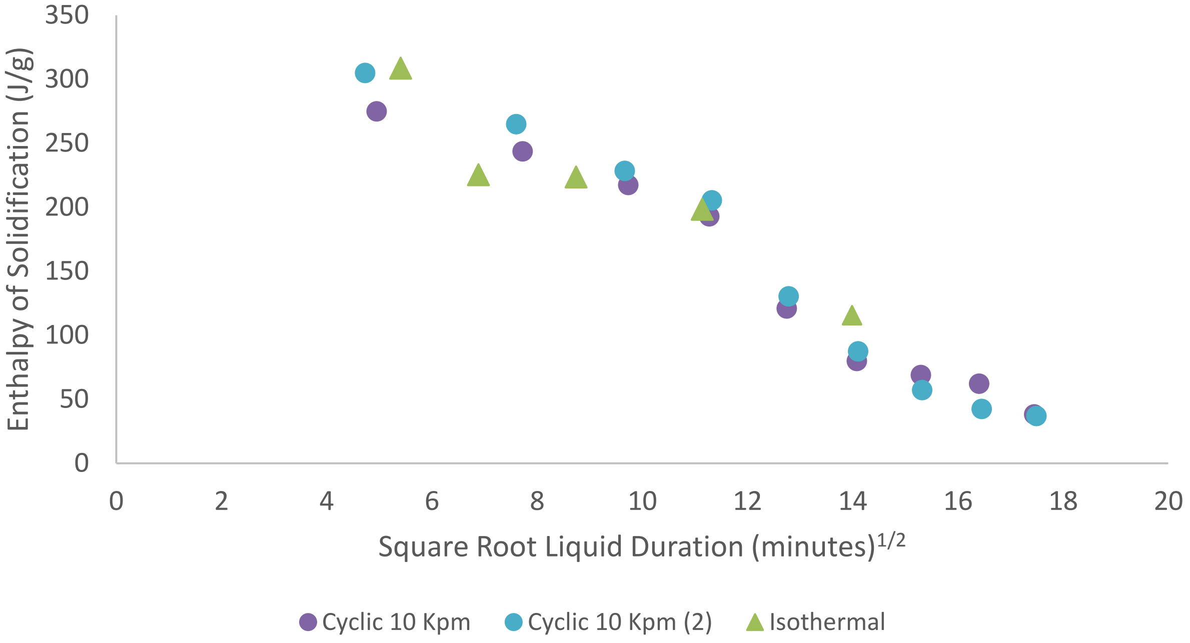

Figure 6.15 - Enthalpy of Solidification Data from Isothermal and 10 Kpm Cyclical Testing of Copper and Ti-6Al-4V

6.3 Determining Liquid Fraction from DSC Enthalpy Measurements

Bulk EDS scans of the copper concentration of the ASZ of samples heated to 1050°C and cooled at 80 Kpm showed near matching values when compared to grade two titanium and copper. In the case of commercially pure titanium, the bulk ASZ (eutectic and dendrites measured together) was averaged to 39.31 ± 0.79 wt% Cu. For Ti-6Al-4V the EDS values averaged to 40.94 ± 0.67 wt% Cu. The balance of the ASZ was 53.42 wt% Ti, 3.46 wt% Al and 2.18 wt% V, where the ratio of Ti, Al and V is very close to that for Ti-6Al-4V. These compositions indicate that there is a uniform dissolution of the base metal elements into the ASZ in such as way that it creates a similar Cu dilution experienced in the Ti-Cu binary case. This confirmed assumptions of the ASZ behaving according to the Ti-Cu binary phase diagram and further calculations and modelling of this system were conducted in the exact same manner as Chapter 4. Therefore, it was assumed that the appropriate enthalpy for this solidification reaction could be represented by the Ti_2Cu solidification enthalpy of formation, 423.8 J/g, stated in reference [70].

Liquid fractions were calculated in a similar fashion to the titanium copper system with the exception that the base metal correction differed slightly. The average foil weight was the same since pure copper was used in both studies. The liquidus concentration was modelled as 40.94 wt% Cu with a maximum of 7.81 mg of liquid filler similar to data outlined in Section 4.3. From these values the liquid fraction was calculated using:

$$\boldsymbol{L_f = \frac{\Delta H^c{}_m}{\Delta H_{theo}} = \frac{0.4094 * 1.156 * \Delta H_m}{423.8}} \tag{6.1}$$

Where 0.4094 corrects for dissolution and 1.156 corrects for the presence of the titanium alloy base metal.

Liquid fractions derived from Equation 6.1 are shown in Figure 6.16 with the same samples discussed in Figure 6.15. Comparing these values against the commercially pure titanium discussed in Chapter 4, the rate of isothermal solidification is 0.033 in terms of liquid fraction, L_f in grade two and 0.0241 in grade five. The initial liquid fraction in grade two and grade five titanium is 0.4922 and 0.4596 respectively. Later microstructural work showed strong agreement with the cyclical work. The difference in the rate of isothermal solidification can be attributed to a lower diffusivity coefficient which will be discussed in Chapter 8. The similar liquid fraction is due to similar dissolution behaviour in the two systems.

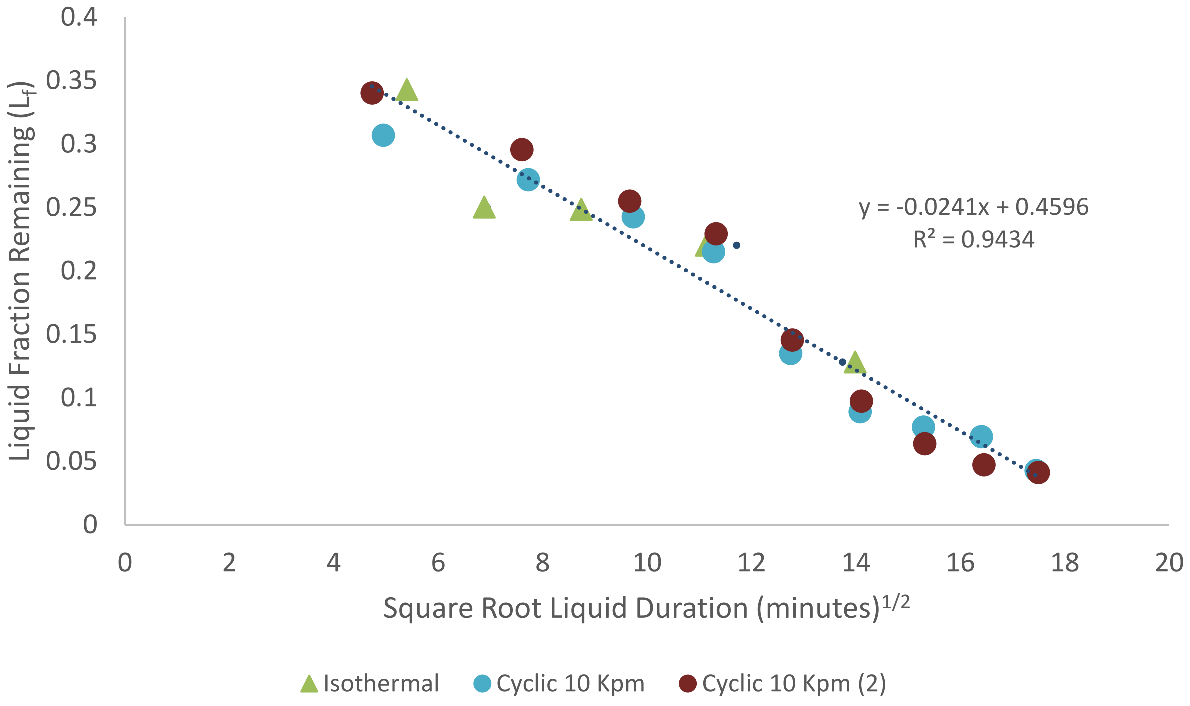

Figure 6.16 - Isothermal Solidification Data from Isothermal and 10 Kpm Cyclical Testing of Copper and Ti-6Al-4V

The microstructural cross sections of samples held isothermally are shown in Figure 6.17. In both cyclical and isothermal samples there was an observed delay in retraction of the ASZ. Isothermal 15 and 30 minute samples (top and middle figures) had a maximum ASZ height of 161 µm and 118 um respectively when properly projected. The ASZ maintains the peritectic microstructure with a lamellar eutectic of alternating TiCu and Ti_2Cu. As the EDS analysis of Table 6.1 indicates, Al and V form solid solutions with the primary phases of β-Ti, TiCu and Ti_2Cu but do not change the basic solidification behavior of the ASZ in any significant way. The ASZ of the 60 minute sample has been reduced to almost half of the height of the 15 minute sample (89 µm). The ISZ is

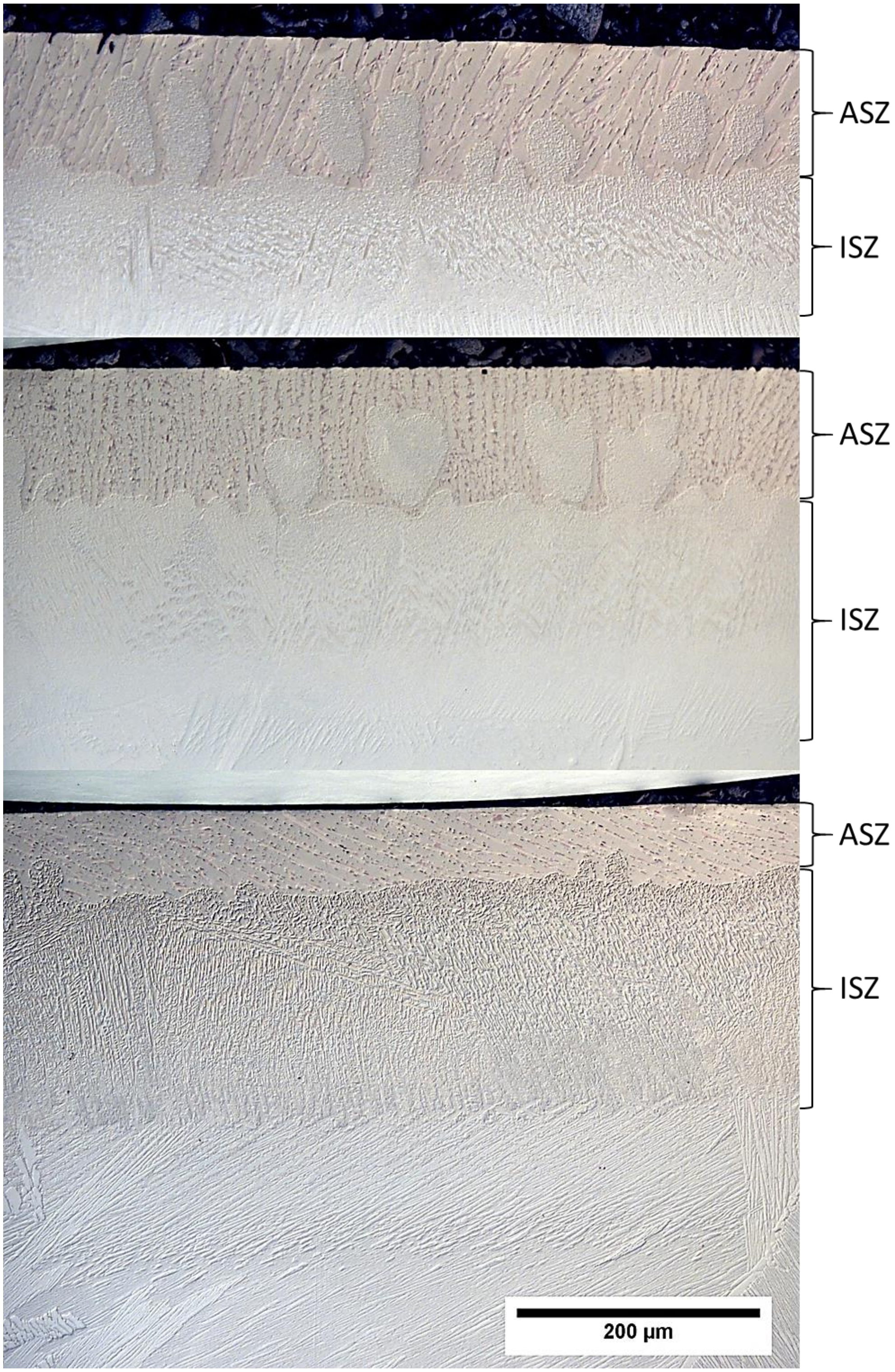

Figure 6.17 – Optical Imaging of Microstructural Cross Sections of Copper and Ti-6Al-4V Samples Held Isothermally at 1050°C for Top: 15; Middle: 30; Bottom: 60 minutes

reminiscent of microstructures observed in Chapter 4 with a hypereutectoid microstructure leading into a eutectoid composition and finally the base metal.

6.4 Microstructural Validation of DSC Measurements

Figure 6.18 shows a cross section of a Ti64/Cu sample heated to 1050°C and cooled at 20 Kpm. Again, the assumption of a spherical cap was appropriate to model the area of interaction with the foil. Previous data had shown support for the continued assumption that the interaction could be modelled using the binary phase diagram [56]. An analysis similar to section 4.4 was conducted with a slight variation in the liquid density. With the addition of Aluminum and Vanadium, the recalculated value was 5.02 g/cm^3. The addition of lighter Aluminum and Vanadium (which has a comparable density to titanium) reduces the density from the calculated 5.108 g/cm^3 found in commercially pure titanium.

Figure 6.18 - Optical Imaging of Microstructural Cross Section of Ti64/Cu Sample Heated to 1050°C and Cooled at 20 Kpm Showing Entire Width

Measurement of the 80 Kpm ASZ had shown a minimal difference in composition when comparing to grade two titanium. As stated previously, this value was found to be 40.94 wt% which is the liquidus concentration dictated by the phase diagram. Assuming that all Cu is contained in the liquid that develops a liquidus concentration of 40.94 wt%, the height of the cylinder was found to be 196.6 µm with a volume of 1.56 mm^3. A spherical cap with an equivalent volume would have a maximum height of 386.4 µm. These values were almost the same as the commercially pure system, with a cylinder height of 201.3 µm and a spherical cap height of 395.2 µm, owing to a similar density and liquid composition.

Microstructural cross sections of isothermal and cyclical samples were measured, and the results are included in Table 6.2. Projections and the resultant volumes were calculated similar to those discussed in Section 4.4. The liquid fraction was then calculated from microstructural measurements by assuming that the sample underwent dissolution to the maximum volume discussed above (1.56 mm^3).

Figure 6.19 shows the DSC and calculated liquid fractions on a plot over square root liquid duration. For the Ti64/Cu system, DSC data was represented by the work of 10 Kpm cyclic testing where the full solidification events could be completely measured and the isothermal samples using the sigmoidal baseline construction. Overall there is good agreement between the DSC and microstructural data which validates that, despite the challenges of overlapping thermal events, the careful use of appropriate baseline constructions can still yield accurate enthalpy results.

Table 6.2 - Progression of Isothermal Solidification in Grade Five Titanium and Copper Half Joints

Sample	Projected ASZ Width (mm)	Projected ASZ Height (mm)	Volume of ASZ (mm^3)	Calc. Liq. Fraction	DSC Liq. Fraction	Root Liquid Duration ($min.^{1/2}$)
Cyclic 10 Kpm	3.222	0.041	0.166	0.106	0.043	17.495
Iso 15 min.	3.422	0.161	0.741	0.475	0.343	5.437
Iso 30 min.	3.328	0.118	0.512	0.328	0.250	6.932
Iso 60 min.	3.491	0.089	0.424	0.272	0.248	8.718
Iso 120 min.	3.451	0.043	0.201	0.129	0.220	11.713
Iso 180 min.	1.901	0.017	0.024	0.015	0.128	13.741

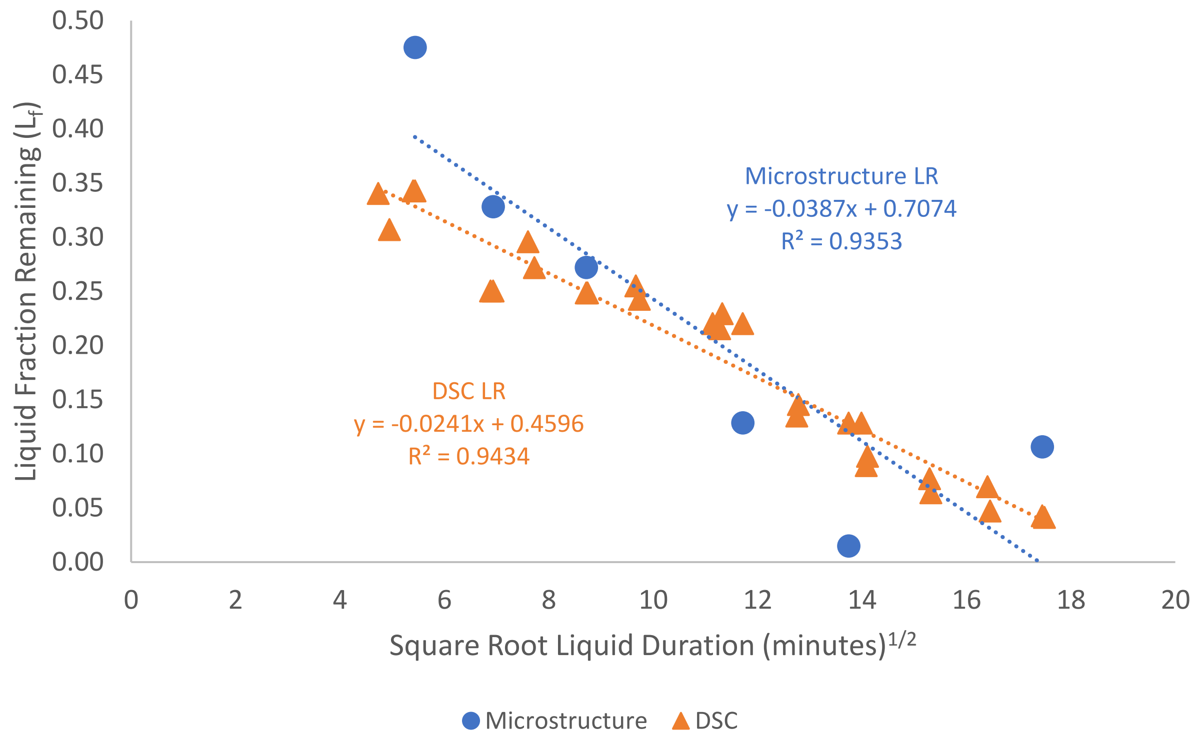

Figure 6.19 - Comparing DSC and Calculated Microstructural Liquid Fractions of Copper and Ti-6Al-4V

6.5 The Rate of Isothermal Solidification and the $2W_{ISZ}$ Curve

The $2W_{ISZ}$ curve is calculated using the analysis outlined in Section 4.4 and compared to the commercially pure work, see Figure 6.20. There is a noticeable difference in the rates of isothermal solidification, where grade two titanium has a rate of 13.603 μm/min.$^{1/2}$ and 9.796 μm/min.$^{1/2}$ for grade five. It is evident that the rate of solid-state diffusion is more sluggish at the solid/liquid interface for Ti-6Al-4V than for commercially pure titanium.

The initial $2W_{ISZ}$ values (y-intercepts) are similar for the Gr.2 and Gr.5 Cu joints. In section 6.3 it was shown that the calculated maximum spherical cap height was very close between grade two and grade five titanium, and dissolution was shown to be comparable, which supports the similarities between the two $2W_{ISZ}$ curves.

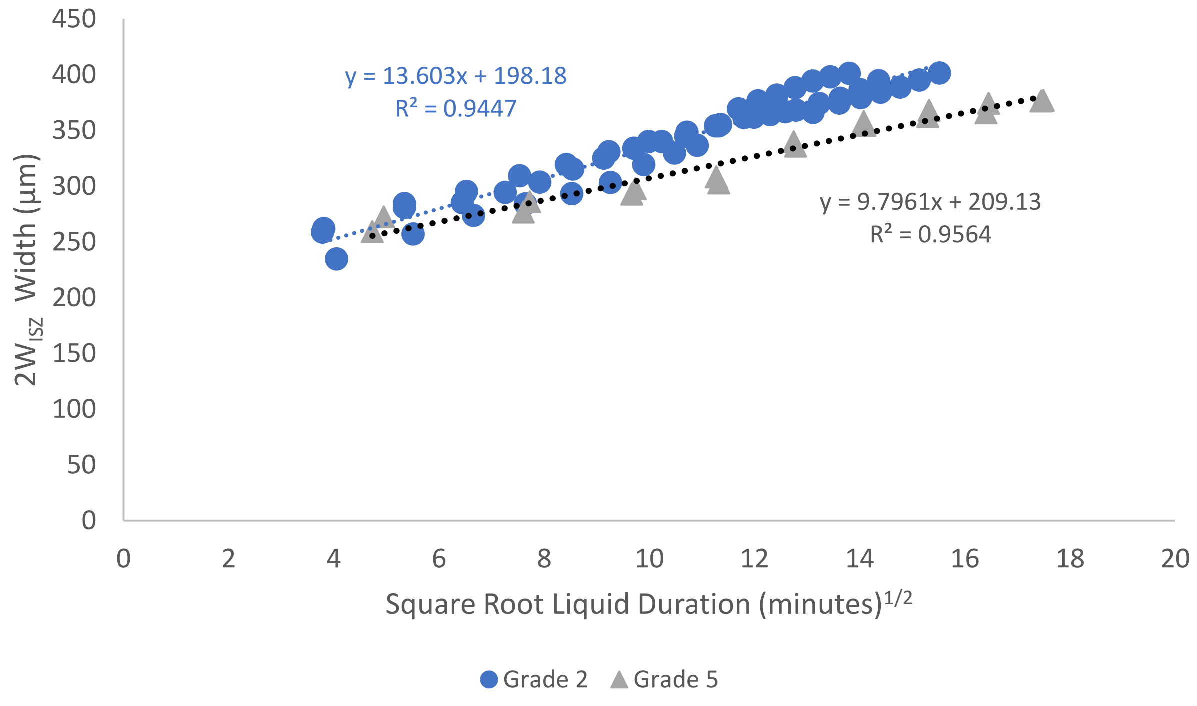

Figure 6.20 - $2W_{ISZ}$ Curves for Copper in Commercially Pure Titanium and Ti-6Al-4V

An example cross section of the ASZ/ISZ region is shown in Figure 6.21 with SEM imaging of a Cyclic 6X sample. The microstructural evolution as a function of Cu concentration within the base metal is similar to that observed in the Ti-Cu case.

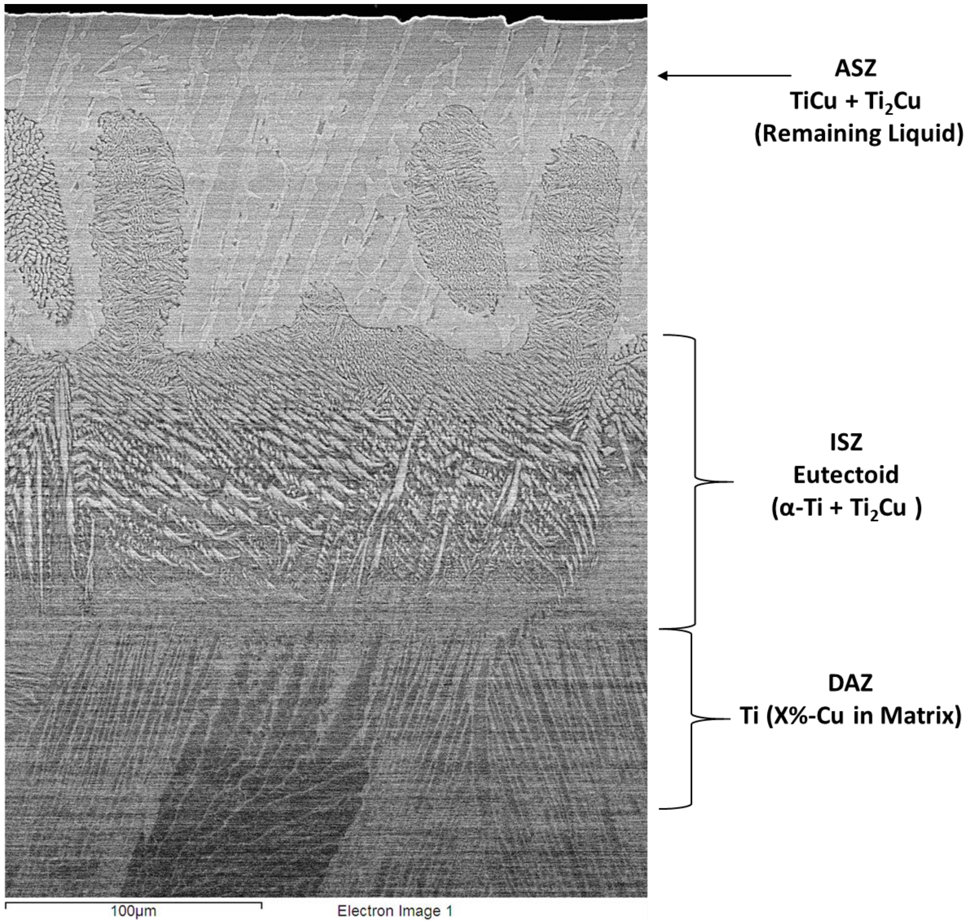

Figure 6.21 – SEM Imaging of a Ti64/Cu Cyclic Sample Heated Between 1050°C and 890°C Six Times

Compositional profiles were mapped and projected for comparison of isothermal and cyclical samples shown in Figures 6.22. This figure is corrected in a similar fashion to the previous two chapters where values within 25 µm of the ASZ/ISZ interface were omitted due to copper

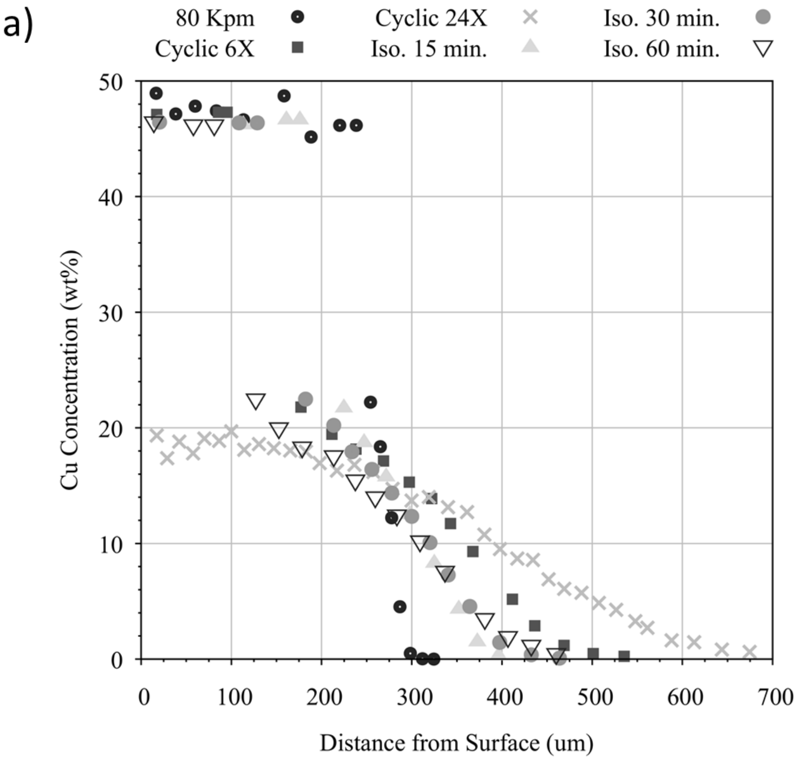

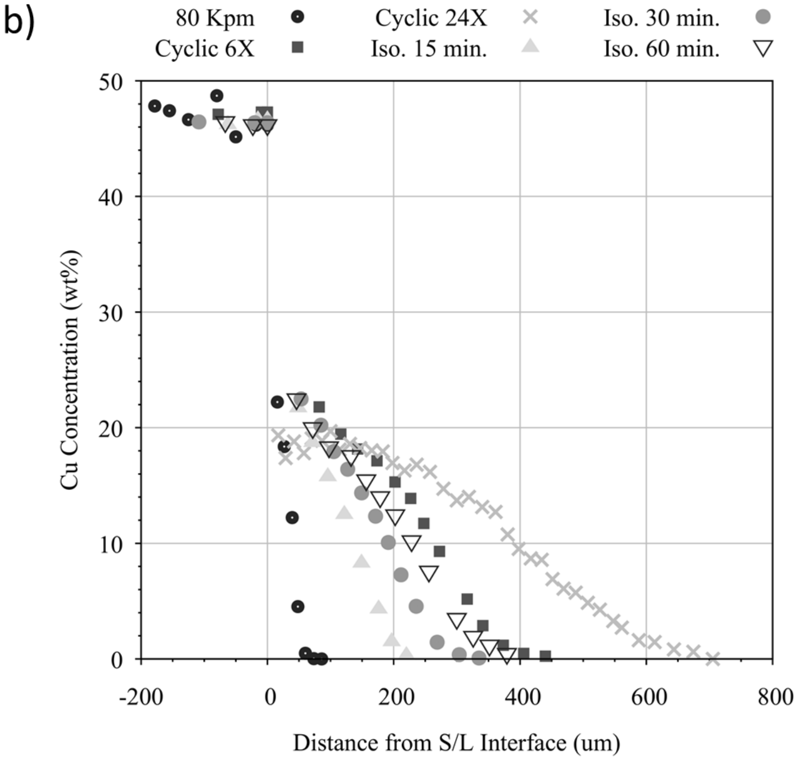

Figure 6.22 - Corrected Compositional Profiles of DSC Samples Plotted as (a) Distance from the Sample Surface; (b) Distance from S/L Interface

concentrations above values possible for the maximum solid solubility. Beyond this range, values were found to reach a maximum of 21-22 wt% as previously seen in Chapter 4. Diffusion distances were shorter than those seen in section 4.6, with a maximum distance of 700 µm for grade five in comparison to 1000 µm in grade two. Again, this supported evidence that diffusion in Ti-6Al-4V was limited in comparison to commercially pure titanium despite similar expected volumes of dissolution/incorporation of copper into each base metal.

6.6 Application of Analysis to Maximum Brazing Clearance and IS Time

Full joint sandwich assemblies were fixtured using the same experimental setup as samples discussed in Sections 5.7. Figure 6.23 shows a two foil sandwiched joint that was heated to 1050°C and cooled at 40 Kpm. From the schematic in Figure 4.22, the joint is uniform in Region A with the exception of a pore close to where liquid was pulled by capillary action into Region B. Overall the appearance of the Gr.2-Cu and Gr.5-Cu full joints (Figures 4.21 and 6.23) are similar. The Gr.5-Cu ASZ width of 107 µm versus the 115 µm measured for the Gr.2-Cu joint is also similar.

An original joint gap of 134.0 µm was measured by extrapolating the original plate surfaces into the centre. Given the ratio of the maximum cylinder height to the original foil thickness (196.6:50 µm), the gap was calculated to widen to 527 µm based on the original gap width. The liquid duration of a 40 Kpm sample was calculated from 20 and 80 Kpm samples and found to be 3.32 min.$^{1/2}$. Using the $2W_{ISZ}$ curve from Figure 6.18, the value for $2W_{ISZ}$ was found to be 242 µm leaving a difference of 285 µm for the expected height of the $2W_{ASZ}$. Measurements along the ASZ

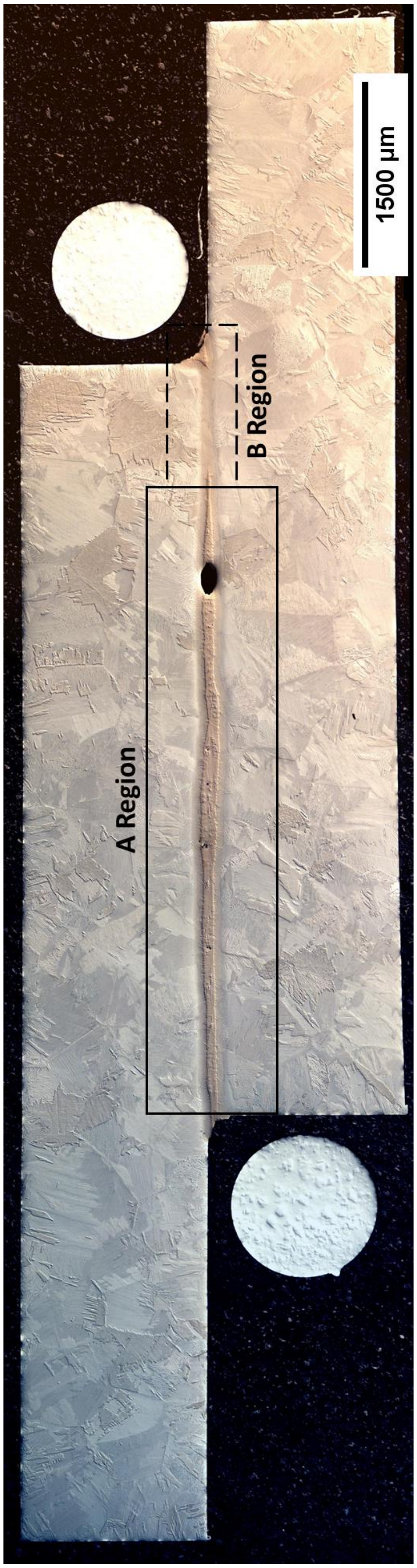

Figure 6.23 - Optical Imaging of Ti64/Cu/Ti64 DIL Sandwich Full Joint Heated to 1050°C and Cooled at 40 Kpm with Two Cu Foils

showed an average height of 107.0 ± 22.5 μm which deviated from calculated values. The pore was measured to be at the original gap width of 134.6 μm indicating minimal dissolution, or interaction, occured before the liquid was displaced.

Assuming liquid at the liquidus composition only enters the joint under Type B conditions, the growth of the $2W_{ISZ}$ layer is simplified to $2W_{ISZ} = 9.796(t)^{1/2}$ for the Ti-6Al-4V and copper system. Under the assumption that no liquid enters the gap in Region B until the braze temperature, the liquid duration time is 8.25 minutes (2.87 $\text{min}^{1/2}$), resulting in an IS growth layer of 28.1 μm. With an original gap width of 134 μm, this would leave 105.9 μm as the W_{ASZ} for a type B joint. However, no ASZ remains in the joint gap of Region B and is only visible in a formed fillet outside of the joint. This indicates that the conditions for a Type B joint were not met and that some level of dissolution has occurred along the joint gap.

Figure 6.24 a and b show closer magnification of microstructure close to the joint centre and the gap entrance. The fillet noted shows excess liquid in Figure 6.24a where the ASZ is still transient

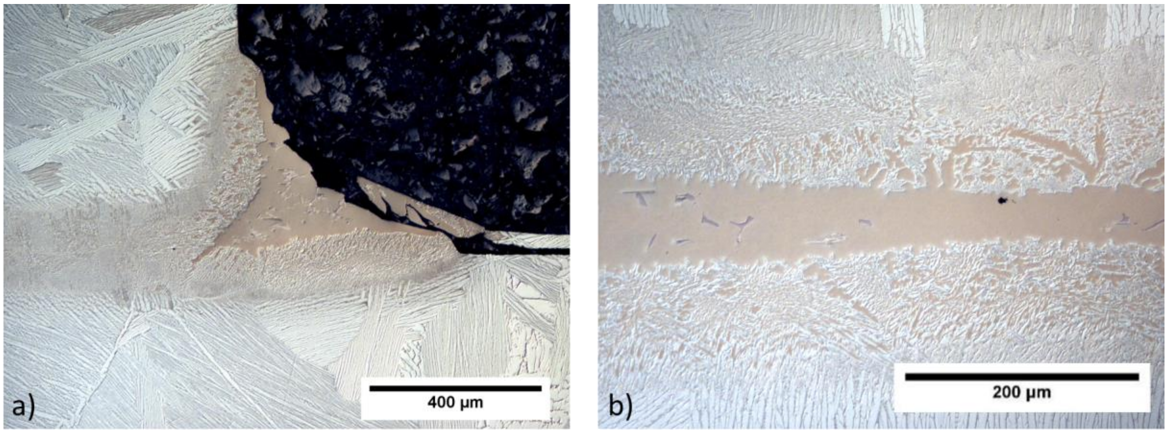

Figure 6.24 – Optical Imaging at Higher Magnification of Joint Microstructure (a) Close to the Joint Centre; (b) The Gap Entrance

where predominantly Ti_2Cu is observed with darker patches of TiCu. The same is seen in liquid close to the centre of the joint, see Figure 6.24b. Across a joint centreline with similar microstructure, hardness and concentration profiles were constructed.

Figure 6.25 a and b show the results of hardness indentations and EDS scans along the joint centreline. The ASZ width is equivalent to what was measured previously and a concentration profile similar to the 80 Kpm sample in Figure 6.22. Similar to hardness profiles in Figure 4.22, there was no increase in hardness observed for the ASZ. In fact, a hardness similar to the base metal was measured. As in Section 4.7, the maximum hardness was observed in the ISZ close to eutectoid region away from Ti_2Cu precipitates suggesting a softening effect from this intermetallic. The base metal displayed hardness values of 400 HV. These values suggested either that the measured hardness had not surpassed all copper present in the base metal, or that the Ti-6Al-4V had becomes enriched with oxygen [73]. Figure 6.25b includes the same hardness with Al and V

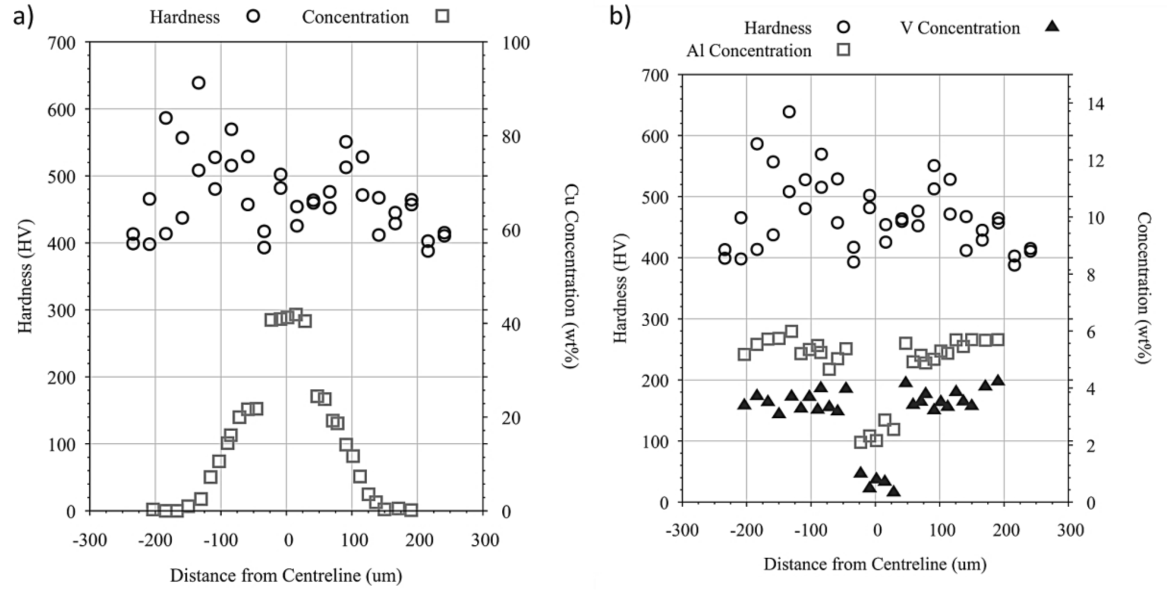

Figure 6.25 - Hardness and Compositional Profiles across the Ti64/Cu/Ti64 Centerline of a Two Cu Foil Experiment Cooled at 20 Kpm Showing (a) Cu Concentration; (b) Al and V Concentration

measurements included. There is less incorporation of Al and V in the ASZ compared to the ISZ and base metal. It is interesting to note that, although the aluminum concentration drops approaching the ASZ, there is no real change in the concentration profile of vanadium (other than the step change into the ASZ).

7.0 Ti-6Al-4V and Nickel

7.1 Initial Heating and Dissolution

Samples of Ti-6Al-4V were heated with pure nickel foil on the top surface to 975°C, 1000°C, and 1025°C in the DSC. Figure 7.1 shows the resultant heating curves for these specimens. No observable thermal event associated with the Ni foil occurs when the samples are heated to, or below, 1000°C. This is also seen in the cooling curves (Figure 7.2) where no liquid phase formation is evident when cooled from 975°C, or 1000°C. An intermetallic reaction similar to that observed for the Ti-Ni samples (Figure 5.1) does occur in the 1025°C. In addition, the 1000°C onset temperature is higher than the 967°C value for binary Ti-Ni.

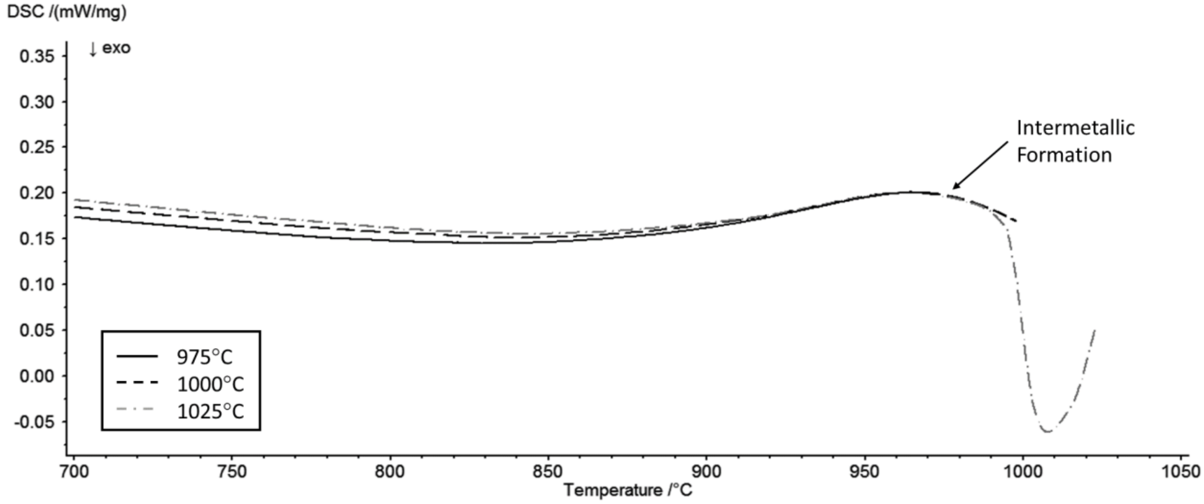

Figure 7.1 - DSC Heating Trace for Ti-6Al-4V Nickel Half Joints Heated to 975, 1000, 1025°C

Cooling traces in Figure 7.2 points to the fact that the intermetallic reaction during heating to 1025°C generates a liquid phase, since a solidification peak is present. This peak onsets in a similar fashion to cooling traces in Figure 5.2.

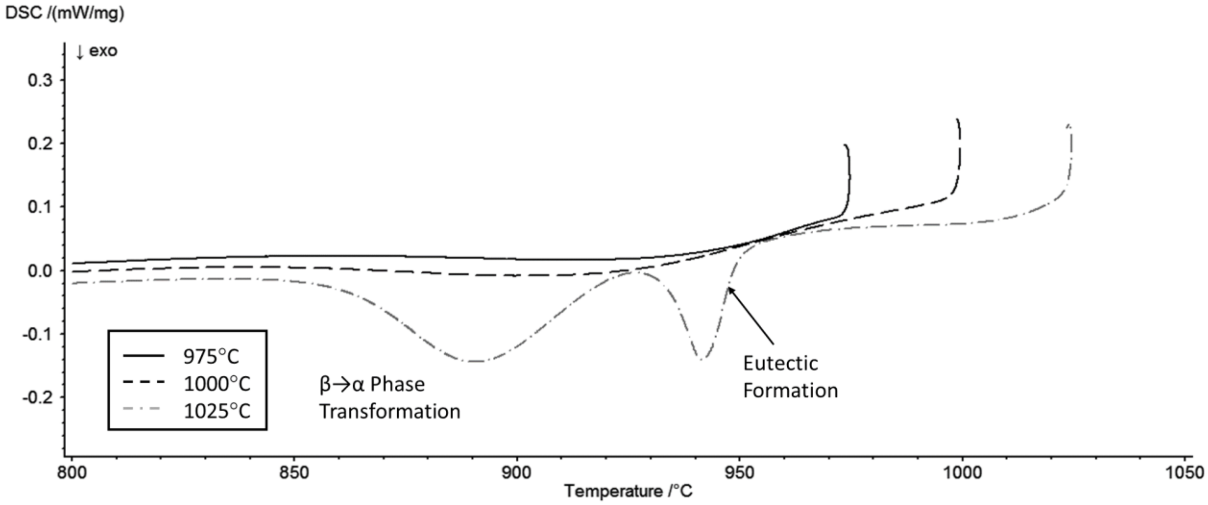

Figure 7.2 - DSC Cooling Trace for Ti-6Al-4V Nickel Half Joints Heated to 975, 1000, 1025°C

The freezing exotherm for the eutectic formation onsets 949.5°C with a peak temperature of 941.7°C. This is in the range of the eutectic temperature of the binary Ti-Ni system. A eutectoid peak is observable but not included in the figure as it onsets at 631°C and had a relatively minor peak enthalpy in comparison. This was much lower than the binary Ti-Ni value of 765°C.

Further evidence of minimal interaction below 1025°C is provided in Figure 7.3 displaying the microstructures of the initial heating samples. The nickel foil had not bonded to the Ti64 base metal after heating to 975°C and was not included in the initial microstructures. The top figure (1000°C) shows that despite strong metallurgical contact there is no observable indication of nickel diffusion into the base metal. As opposed to the titanium nickel samples in Chapter 5, the formation of intermetallic layers during heating was not observed in the 1000°C sample and the formation of a titanium rich liquid was quite rapid between 1000°C and 1025°C.

The 1025°C sample in the middle of Figure 7.3 was the only sample to show interaction in the DSC traces shown in Figures 7.1 and 7.2. The liquid homogenizes quickly to the eutectic

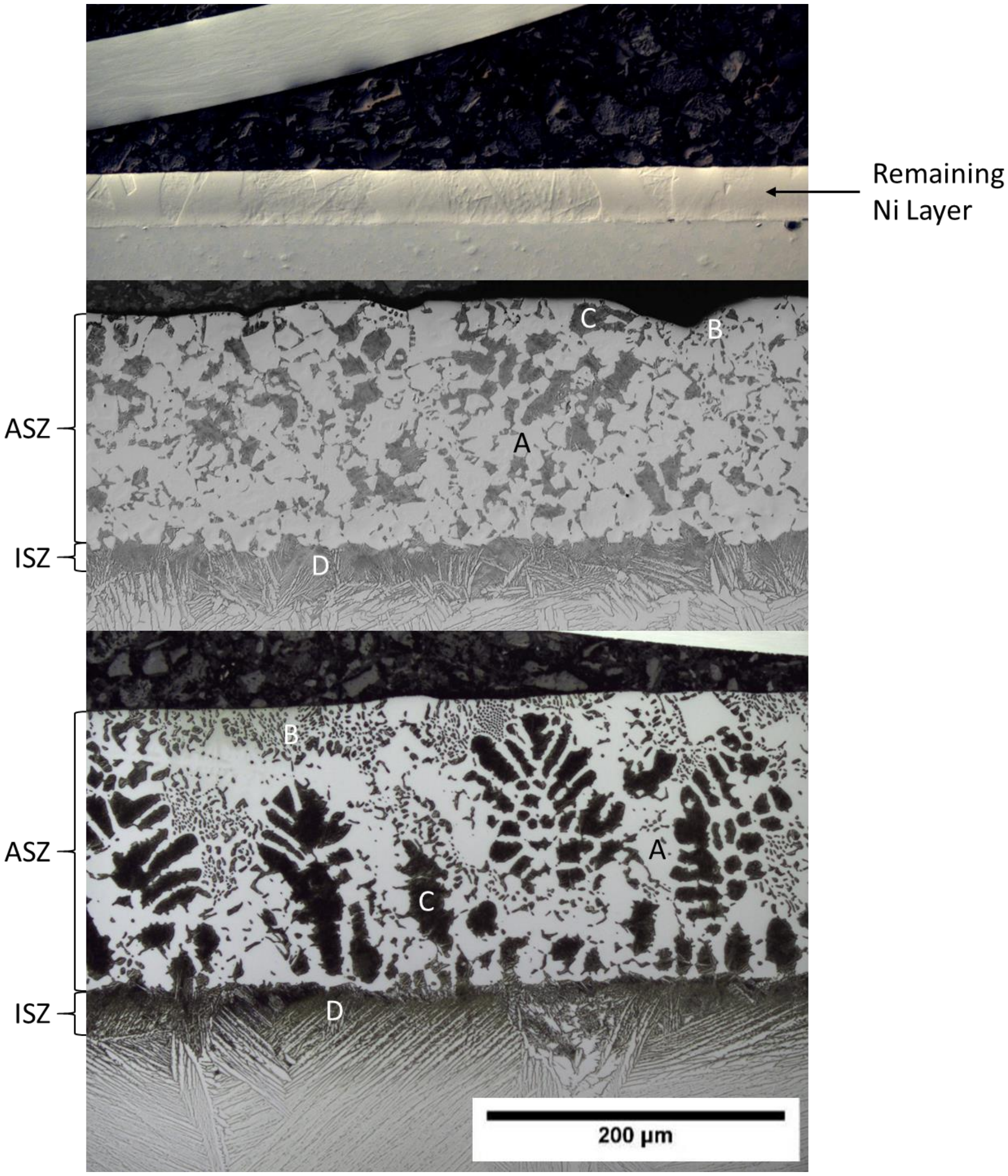

Figure 7.3 – Optical Imaging of Microstructural Cross Sections of Samples Heated to Top: 1000°C; Middle: 1025°C; and Bottom: 1050°C and Cooled at 20 Kpm. Phases in Table 7.1.

composition as evidenced by the exothermic event occurring at 942°C. Initially, no β(Ti) dendrites are observed suggesting a planar interface and a very familiar transient microstructure is observed (similar to Figure 5.4). A minimal amount of solid-state diffusion would have occurred between 1000°C and 1025°C and a thin layer of eutectoid (ISZ) is observed. This is supported by the shallow eutectoid peak observed in the DSC. Gap widening, the development of primary (β-Ti) dendrites, and an overall hypoeutectic ASZ microstructure are displayed in the bottom 1050°C (20 Kpm) sample.

Samples heated to 1025°C and 1050°C show a network of Ti_2Ni dendrites (phase A) with similar morphology to the pure titanium experiments when initially heated. All phases were confirmed using EDS which indicates that the white phase is Ti_2Ni and that no phases richer in nickel were present. Table 7.1 outlines these results including the amount of aluminum and vanadium present in each phase.

As the liquid becomes more titanium rich, pockets of eutectic (phase B) become more prevalent and more Al and V become incorporated. There is a large shift in the stability of the solid liquid interface when differentiating these two samples. Large dendrites with secondary arms appear in the 1050°C. The eutectoid close to the interface and in pockets in the ASZ showed similar composition indicating that these regions are also (β-Ti) dendrites. For reference, the sample heated to 1050°C has been etched for a longer duration which explains the difference in contrast.

Table 7.1 - EDS Compositions of Phases Observed in Initial Heating Samples

Symbol	Conc. Ti (wt%)	Conc. Ni (wt%)	Conc. Al (wt%)	Conc. V (wt%)	Phase
A	59.09	37.28	2.86	0.77	Ti_2Ni
B	62.68	31.17	4.15	2.00	Eutectic (β(Ti) + Ti_2Ni)
C	78.57	9.22	6.35	5.86	(β-Ti) dendrites
D	82.10	7.51	5.95	4.44	ISZ Eutectoid

Examining the difference in cooling rate at 1050°C, Figure 7.4 a-b contrasts samples cooled at a rate of 20 and 80 Kpm respectively. Solid state diffusion appeared to be more sluggish through the Ti-6Al-4V alloy as the difference in heights of the ASZ was 298 μm at 20 Kpm and 301 μm at 80 Kpm. At the very least, there is period of time necessary for the liquid to stabilize prior to reaching an effective diffusion rate into the solid. Dendritic formation of β(Ti) is visible at the solid liquid interface and also near the surface of the liquid. Compositions of phases measured were similar to those discussed in Figure 7.3.

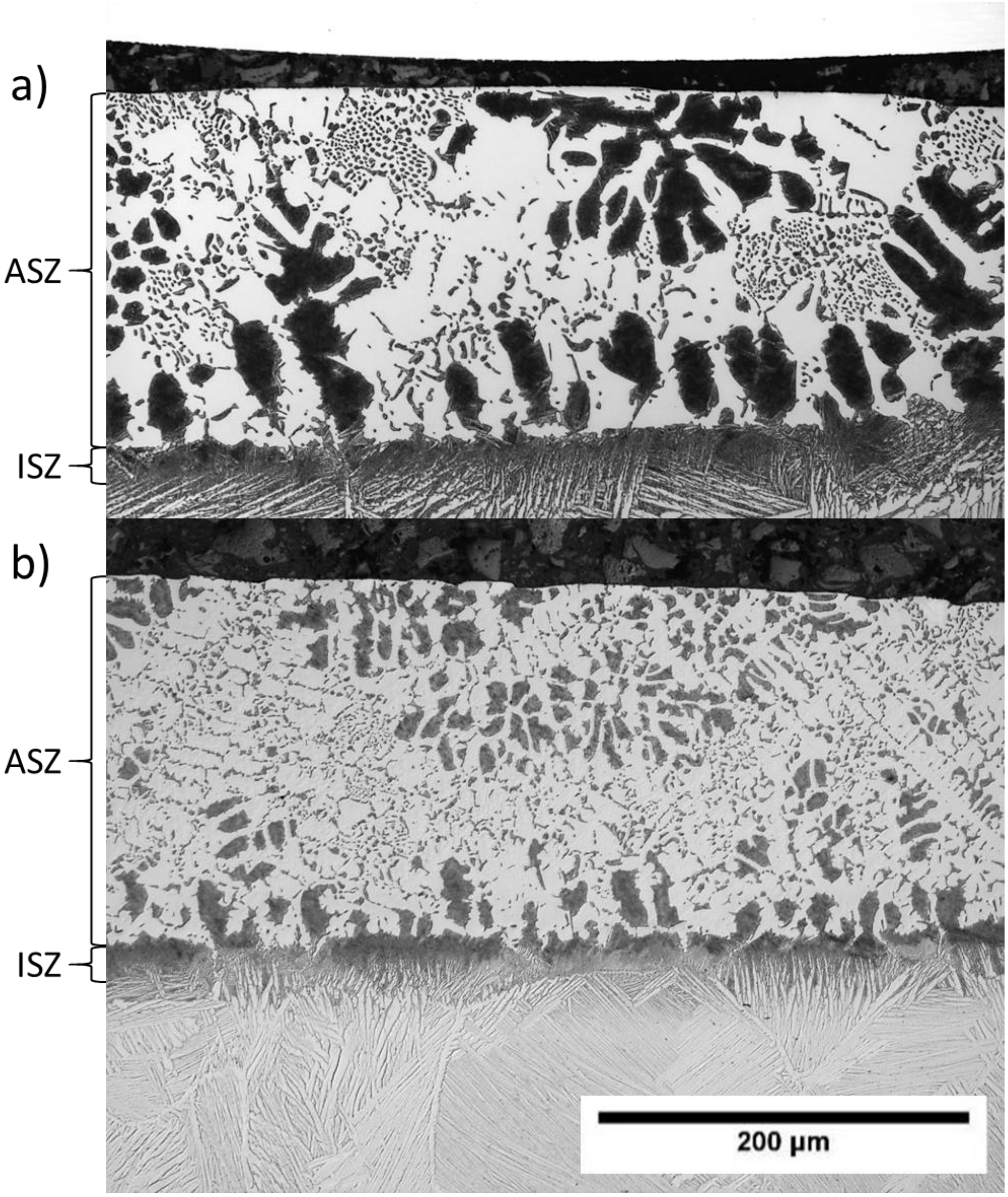

Figure 7.4 - Optical Imaging of Microstructural Cross Sections of Ti64/Ni Samples Heated to 1050°C and Cooled at (a) 20 Kpm and; (b) 80 Kpm

7.2 Isothermal Solidification

Of all systems examined in this study, nickel and grade five titanium were the most consistent in terms of peak onset temperature and liquid duration. This was in stark contrast to nickel and grade two titanium in Chapter 5 where severe undercooling was present and unpredictable. In the study of TiNiAl intermetallics, Xu *et al*. found that the substitution of Al for Ni can reinforce TiNi-based intermetallics through the precipitation of $(Ti,Al)_2Ni$ [79]. Aluminum values are low in composition for Ti_2Ni (see Table 7.1), however, it is possible that aluminum may improve the ability for Ti_2Ni to nucleate from the liquid. Figure 7.5 shows the heating traces for a sample cyclically heated in the DSC for 24 cycles. As higher number of longer cycles were necessary to observe complete isothermal solidification compared to Ti-Cu. The onset of melting events shifts to 954.3°C with a peak temperature of 960°C which is observed consistently for 15 cycles after which measurement became difficult.

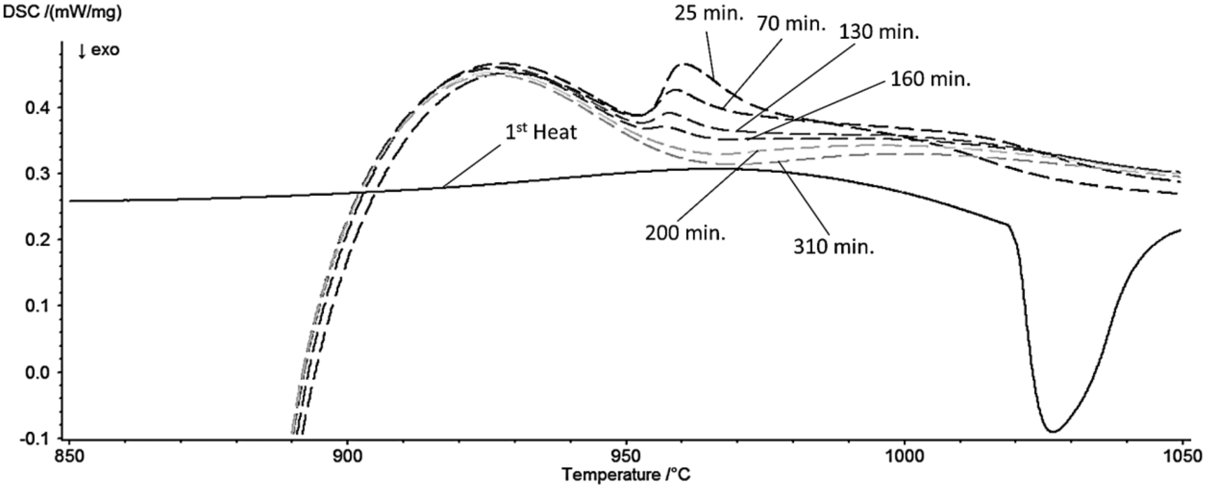

Figure 7.5 - Heating Traces for Ti-6Al-4V Nickel Sample Heated Cyclically for 24 Cycles

The cooling traces are shown in Figure 7.6. During cyclical studies, a secondary peak was observed prior to the main cooling peak associated with the eutectic. The value of this peak never exceeded 10% of the main peak in total enthalpy. This event onset between 985°C and 955°C and was only present for the first ten cycles. This event, though minimal in enthalpy contributions, is likely the formation of (β-Ti) observed in microstructure. The total liquid enthalpy was calculated using the total enthalpy of both events. There is no real shift of the main eutectic peak onsets and temperatures between initial studies and cyclical. The disappearance of the secondary peak does not affect the overall liquid duration of a cycle due to the eutectic peak freezing later during cooling.

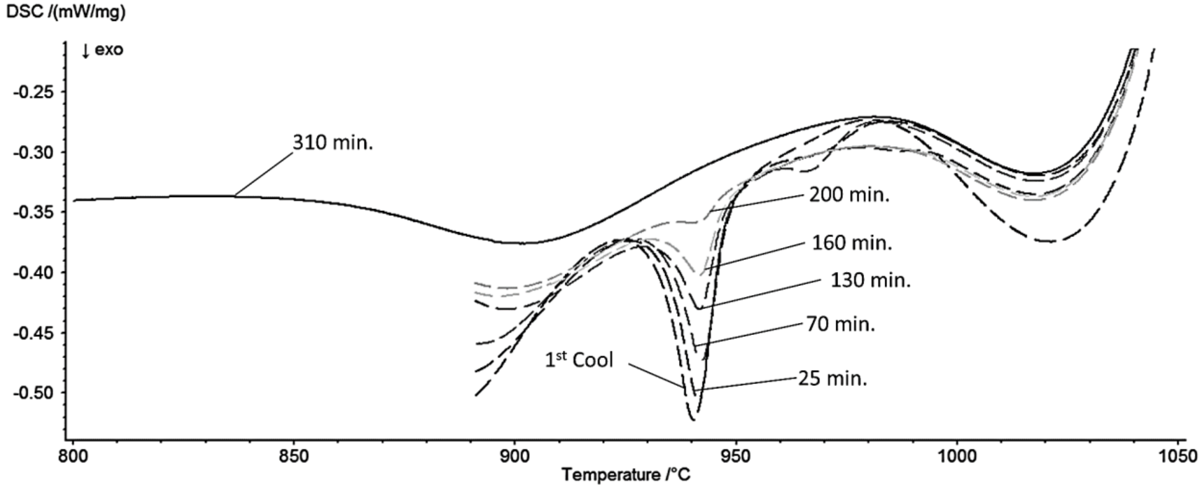

Figure 7.6 - Cooling Traces for Ti-6Al-4V Nickel Sample Heated Cyclically for 24 Cycles

Comparing the final cooling peak in DSC cyclical testing with a sample heated to 1050°C is shown in Figure 7.7. The ASZ solidification peak present with no hold at 1050°C is completely absent in

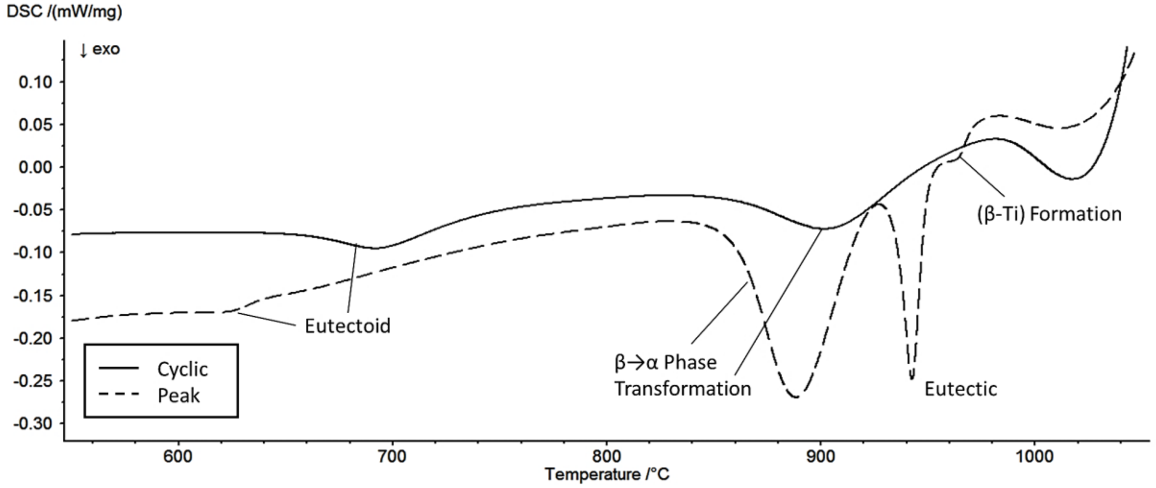

Figure 7.7 - Comparing 1050°C Peak Sample and Last Cooling Cycle of 24 Cycle Sample

the cyclic sample, confirming complete isothermal solidification after 24 cycles. The diffusion of nickel into the base metal broadens the β to α phase transformation and shifts to higher temperatures. Overall this is consistent with similar plots in Chapters 4-6. As in previous chapters, the formation of eutectoid reaction was observed around 700°C.

Compilation of all cyclical data is included in Figure 7.8 and plotted against the square root of liquid duration. All cyclical and isothermal data is plotted using the total cooling peak exotherms using methods described above and, unlike the pure titanium and nickel system, all values were able to be recorded (no undercooling observed). Cyclical and isothermal data were measured using a Bezier fit. Isothermal solidification was measured from the three cyclic 24X samples and observed to complete in 299.7 minutes, or 17.31 min.$^{1/2}$. The disappearance of the smaller secondary peak during cooling shifts the data slightly due to a small decrease in overall freezing enthalpy. This is different from shifts in Figures 4.10 where liquid durations were affected.

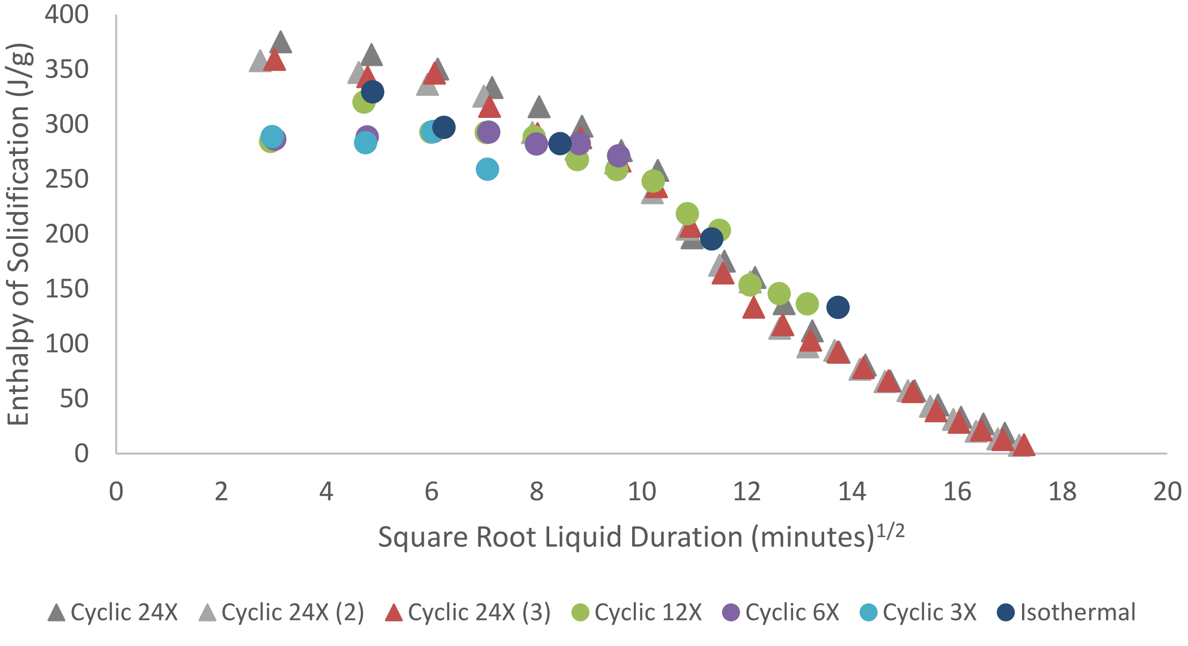

Figure 7.8 - Enthalpy of Solidification Data from Cyclical Testing of Nickel and Ti-6Al-4V

7.3 Determining Liquid Fraction from DSC Enthalpy Measurements

Bulk EDS scans of the ASZ for samples heated to 80 Kpm and cooled showed near matching values when compared to grade two titanium and nickel. In the case of commercially pure titanium, the bulk ASZ composition (eutectic and dendrites measured together) was averaged to 28.41 ± 0.70 wt% Ni. For Ti-6Al-4V, the EDS values averaged to 29.44 ± 0.78 wt% Ni. The balance of the ASZ was 63.64 wt% Ti, 4.27 wt% Al and 2.65 wt% V, where the ratio of Ti, Al and V is again close to that for Ti-6Al-4V. This confirmed assumptions of the ASZ behaving according to the Ti-Ni binary phase diagram in terms of dissolution and further calculations and modelling of this system were conducted in the exact same manner as Chapter 5. Therefore, it was assumed that the appropriate enthalpy for this solidification reaction could be represented by the Ti_2Ni solidification enthalpy of formation, 220.16 J/g, stated in reference [74].

Liquid fractions were calculated in a similar fashion to the titanium nickel. The average foil weight was 3.2 mg as in previous chapters. The liquidus concentration was modelled as 29.44 wt% Ni with a maximum of 10.87 mg of liquid filler as outlined in section 5.3. From these values the liquid fraction was calculated using:

$$L_f = \frac{\Delta H^c{}_m}{\Delta H_{theo}} = \frac{0.2944 * 1.156 * \Delta H_m}{220.16} \tag{1}$$

Where 0.2944 corrects for dissolution and 1.156 corrects for the presence of the titanium alloy base metal.

The liquid fractions for this system are displayed in Figure 7.9 against the square root of liquid duration. Linear regression for this system was applied following the disappearance of the secondary peak to accommodate an offset in enthalpy data (due to delays in the homogenization of the liquid discussed in Chapter 8). Comparing these values against the commercially pure titanium discussed in Chapter 5, the rate of isothermal solidification is 0.048 in grade two and 0.041 in grade five. The initial liquid fraction in grade two and grade five titanium is 0.580 and 0.712 respectively. The difference in the rate of isothermal solidification can be attributed to a lower diffusivity coefficient in Ti-6Al-4V discussed in Chapter 8. The larger liquid fraction is due to differences in dissolution behavior, which will also be discussed in Chapter 8.

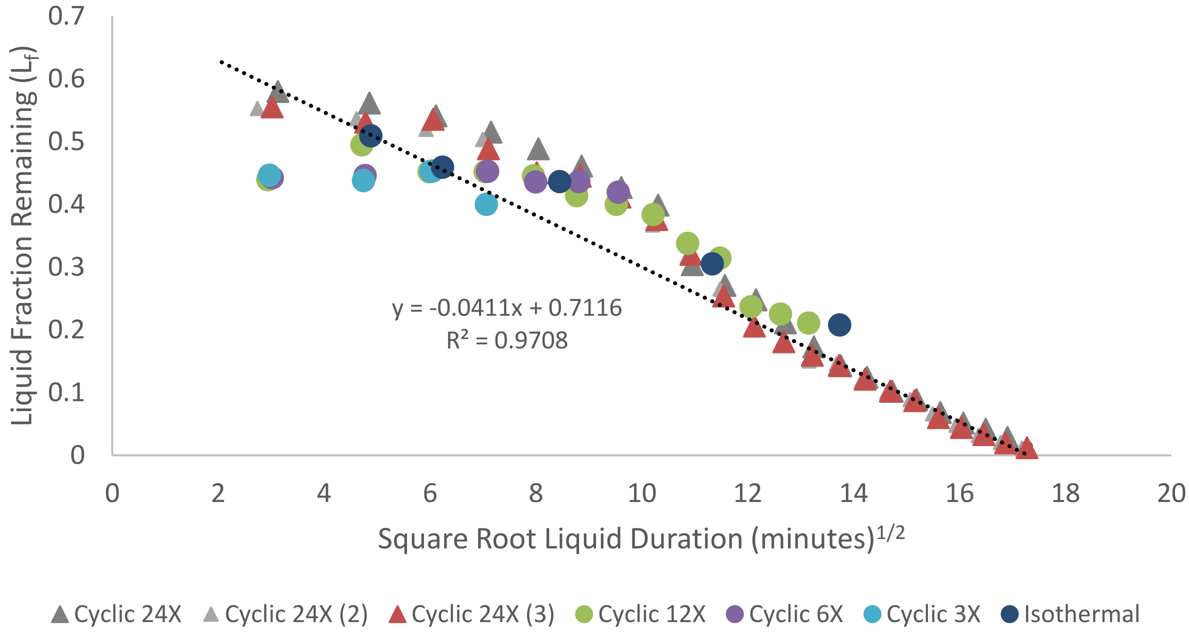

Figure 7.9 - Isothermal Solidification Data from Cyclical Testing of Nickel and Ti-6Al-4V

Figures 7.10 include the microstructural cross sections of samples heated to 1050°C and held for 15, 30, and 60 minutes. The microstructure of the sample held for 15 and 30 minutes (top and middle figure) shows microstructure similar to observations in section 7.1. There is evidence of nucleation from the liquid surface with large pockets of β(Ti) growing into Ti_2Ni dendrites similar to microstructure in Chapter 5.

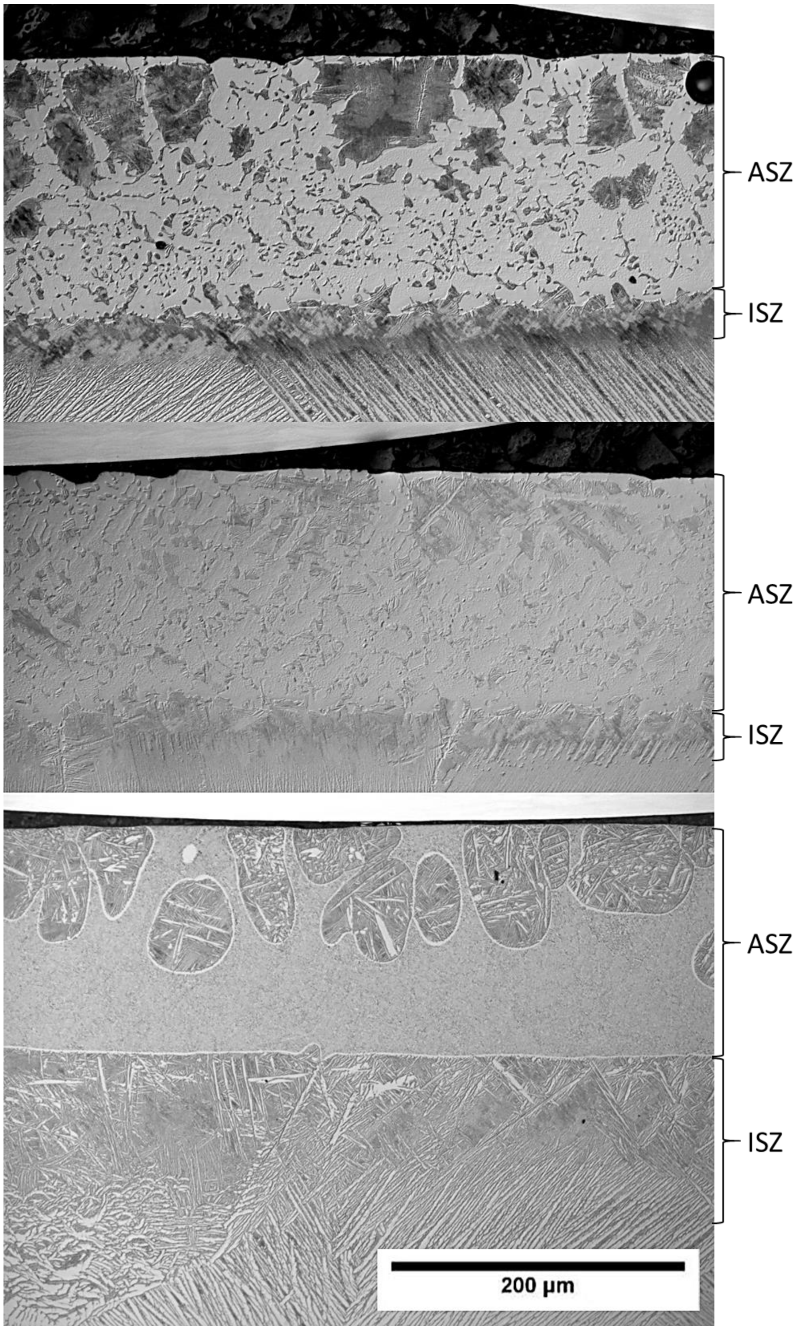

Figure 7.10 – Optical Imaging of Microstructural Cross Sections of Ti64/Ni Samples Held Isothermally at 1050°C for Top: 15; Middle: 30; Bottom: 60 minutes

A marked change was observed in the sample held for 60 minutes (bottom figure) where the ASZ changes to a finer eutectic microstructure observed in the binary titanium nickel system (Chapter 5). The DSC trace verified that this sample had undercooled to 884.9°C reminiscent of work with commercially pure titanium. Few samples of Ti-6Al-4V and Ni showed any undercooling when testing, especially cyclical specimens, but this microstructure was observed whenever it occurred. Nucleation of Ti_2Ni was still impeded at the solid liquid interface such that β(Ti) preferentially grows from the surface.

7.4 Microstructural Validation of DSC Measurements

Figure 7.11 shows the entire cross section of the sample heated to 1050°C and cooled at 80 Kpm. This supported modelling of the liquid as a spherical cap and analysis similar to previous chapters was conducted. Recall that in previous sections it became evident that the reaction between Ti-6Al-4V and Ni did not result in any significant deviation from the binary phase diagram of Ti and

Figure 7.11 - Optical Imaging of Microstructural Cross Section of Ti64/Ni Sample Heated to 1050°C and Cooled at 20 Kpm Showing Entire Width

Ni. Thus, an analysis similar to Section 5.4 was performed with the only difference being the liquid density with a recalculated value of 4.68 g/cm^3. The addition of lighter Aluminum and Vanadium (which has a comparable density to titanium) reduces the density from the calculated 4.78 g/cm^3 found in commercially pure titanium.

Measurement of the 80 Kpm ASZ indicated a minimal difference in composition when comparing to grade two titanium. This yielded a hypereutectic value of 29.44 wt% Ni which was used when calculating the height of a cylinder and a spherical cap. Assuming that all Ni is contained in the liquid that develops a liquidus concentration of 29.44 wt%, the height of the cylinder was found to be 293.3 μm with a volume of 2.32 mm^3. A spherical cap with an equivalent volume would have a maximum height of 565.1 μm. These values were close to the commercially pure system, with a cylinder height of 297.6 μm and a spherical cap height of 572.7 μm, owing to a similar density and liquid composition.

The maximum height and diameter of the ASZ was measured microstructurally for isothermal and cyclically heated samples, as well as those discussed in the Section 7.1. The results of these measurements are included in Table 7.2. From these values, the volume of the ASZ was found and liquid fraction was calculated as outlined by Section 4.4. These values are compared with calculated DSC liquid fractions to validate both measurements.

Liquid fraction data of Table 7.2 are plotted in Figure 7.12 as a function of the square root of liquid duration. Good agreement exists between DSC and microstructural values.

Table 7.2 - Progression of Isothermal Solidification in Grade Five Titanium and Nickel Half Joints

Sample	Projected ASZ Width (mm)	Projected ASZ Height (mm)	Volume of ASZ (mm^3)	Calc. Liq. Fraction	DSC Liq. Fraction	Root Liquid Duration (min.$^{1/2}$)
Cyclic 3X	**3.376**	**0.244**	**1.099**	**0.474**	**0.400**	**7.064**
Cyclic 6X	**3.087**	**0.239**	**0.900**	**0.388**	**0.419**	**9.555**
Cyclic 12X	**3.318**	**0.216**	**0.873**	**0.376**	**0.153**	**13.145**
Cyclic 24X	**0.000**	**0.000**	**0.000**	**0.000**	**0.000**	**17.315**
Iso 15 min.	**3.344**	**0.280**	**1.241**	**0.535**	**0.509**	**4.879**
Iso 30 min.	**3.593**	**0.253**	**1.293**	**0.557**	**0.459**	**6.237**
Iso 60 min.	**3.218**	**0.243**	**0.994**	**0.428**	**0.437**	**8.444**
Iso 120 min.	**3.196**	**0.235**	**0.638**	**0.275**	**0.220**	**11.140**
Iso 180 min.	**3.223**	**0.154**	**0.395**	**0.170**	**0.128**	**13.989**

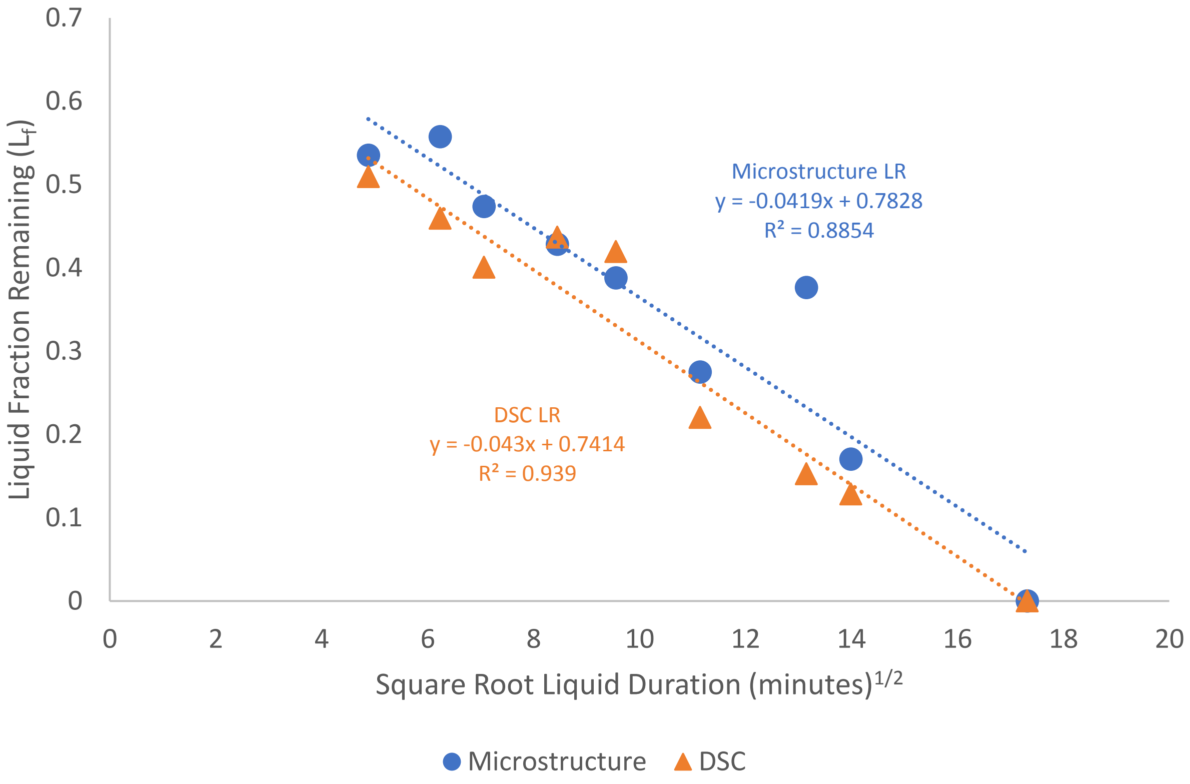

Figure 7.12 - Comparing DSC and Calculated Microstructural Liquid Fractions of Nickel and Ti-6Al-4V

7.5 The Rate of Isothermal Solidification and the $2W_{ISZ}$ Curve

The $2W_{ISZ}$ curve was calculated from the three cyclic 24X samples and is shown in Figure 7.13 and is contrasted with the curve found when using grade two titanium as the base metal. Similar to Figure 7.9, regression of the $2W_{ISZ}$ curve was applied to later liquid fractions. Contrasting Tables 5.1 and 7.2, samples under the same conditions show larger ASZ heights and liquid volumes for grade five samples. This would imply there is more liquid available in Ti-6Al-4V and a higher degree of dissolution. This is evidenced in Figure 7.13 as the $2W_{ISZ}$ of grade five titanium and nickel is always lower than grade two. In Section 7.3, it was already established that the rate of

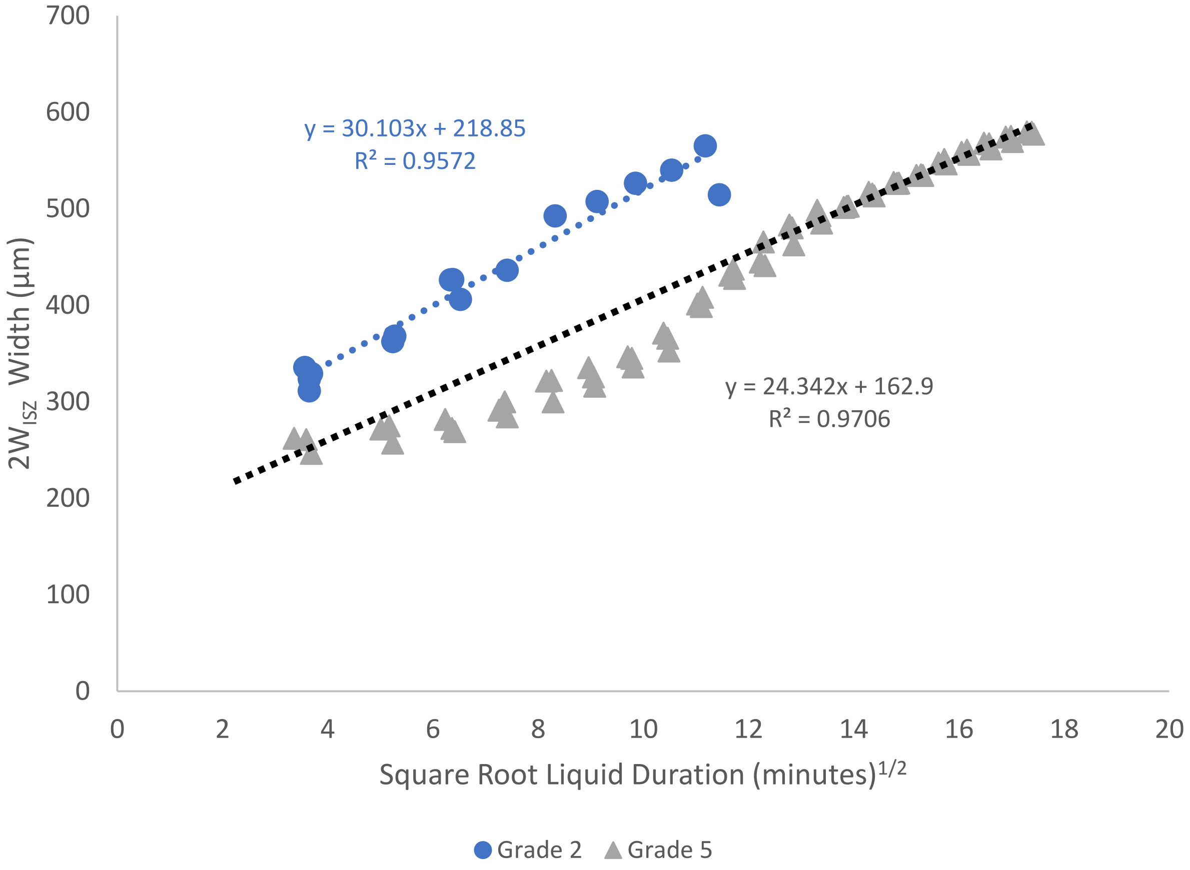

Figure 7.13 - $2W_{ISZ}$ Curves for Nickel in Commercially Pure Titanium and Ti-6Al-4V

liquid fraction removal for grade five was half of that observed in grade two. This will be further discussed in Chapter 8.

Grade five titanium using nickel and copper were also compared regarding the rates of dissolution and are shown in Table 7.3. Similar to Chapter 5, nickel was observed to diffuse much more readily into the base metal when compared with copper. The rate of isothermal solidification was 2.5 times the value observed in copper but the initial $2W_{ISZ}$ is lower than copper suggesting again that more liquid is present in the nickel system. These results can be confirmed when examining the full joints with two foils used in both systems where a much higher degree of dissolution is observed in Ti-6Al-4V and nickel.

Table 7.3 - Comparing Rates of Liquid Removal and Isothermal Solidification in Gr. 5 Ti-Cu and Ti-Ni

Diffusing Species	Rate of L_f Removal (L_f/√min.)	Initial Liquid Fraction (L_f)	Rate of IS (μm/√min.)	Initial $2W_{ISZ}$ Width (μm)
Gr. 5 Nickel	**-0.0411**	**0.712**	**24.342**	**162.90**
Gr. 5 Copper	**-0.0241**	**0.460**	**9.796**	**209.13**

Compositional profiles were created using SEM EDS data taking bulk scans of the composition at a given distance from the surface. An example of this scan is shown with an SEM image of a sample cycled six times in the DSC, see Figure 7.14. In this sample the Ti_2Ni dendritic structure still remains and the ASZ is still quite pronounced. Measurements of the ASZ were taken along the Ti_2Ni dendrites and not the entire liquid layer. The ISZ drops to a concentration starting at 10.5 wt% Ni and remains as eutectoid until roughly 7.5 wt% Ni.

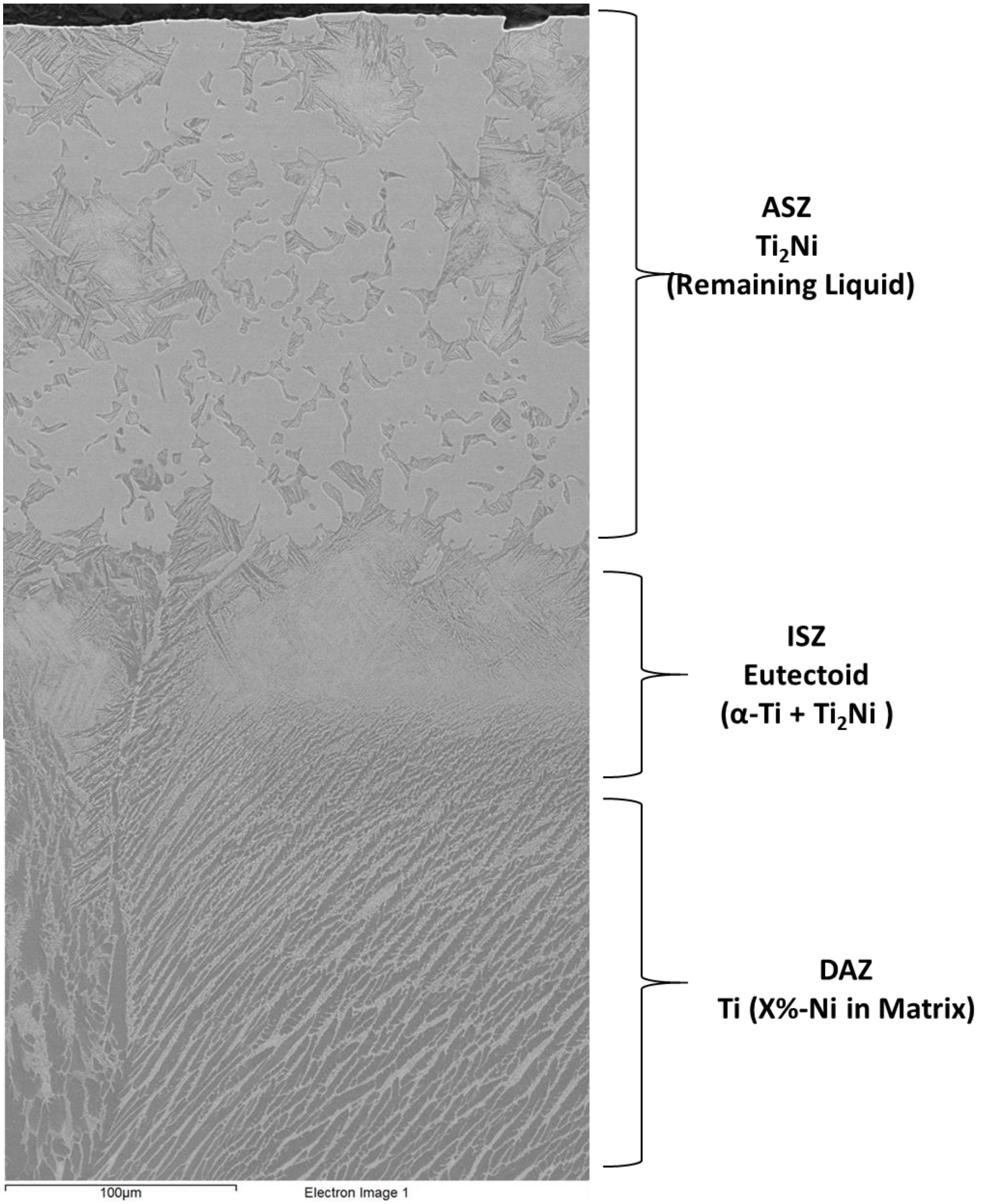

Figure 7.14 – SEM Imaging of a Ti64/Ni Cyclic Sample Heated Between 1050°C and 890°C Six Times

Compositional profiles were measured along all cyclical and isothermal samples and are included in Figure 7.15. Figure 7.15a shows the profiles of cyclical, isothermal, and 80 Kpm samples. Comparing these results back to Chapter 5, the maximum diffusion distance (seen in Cyclic 18X)

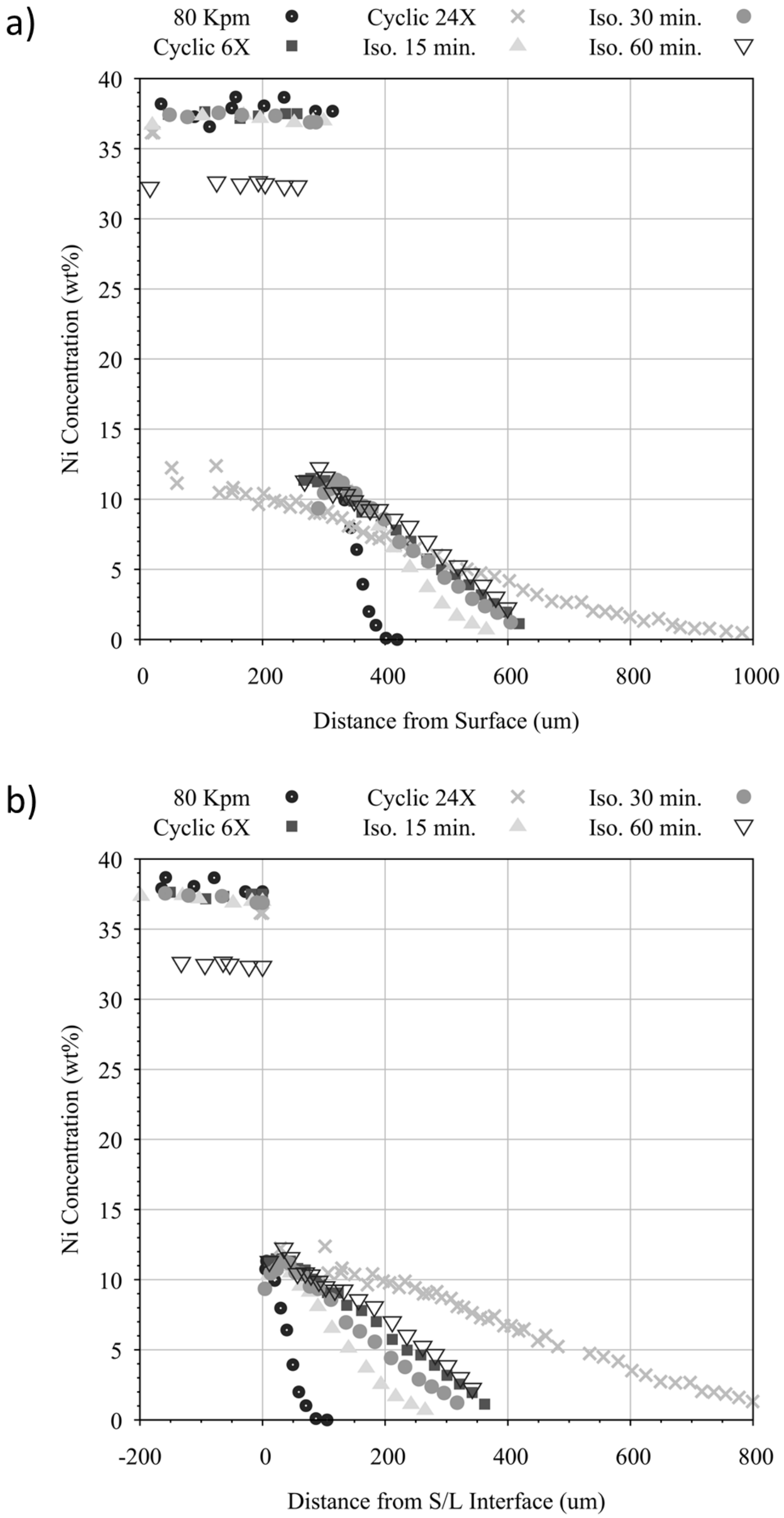

Figure 7.15 - Corrected Compositional Profiles of DSC Samples Plotted as (a) Distance from the Sample Surface; (b) Distance from S/L Interface

is around 1000 μm and lower than in grade two titanium where nickel had diffused through the entire base metal. There is a noted decrease in Ni concentration for the isothermal 60 min. sample which was due to the change in microstructural morphology. Recall this is the sample shown in the bottom of Figure 7.10 where a fine eutectoid ASZ is observed which had a lower measured nickel concentration. This transition was only found in samples that had been held for long liquid durations (isothermal samples held longer than 60 min.) or in samples heated to higher temperatures (1200°C to 1300°C). This is likely the resultant microstructure when the secondary peak disappears in the DSC traces which may inhibit the formation of the fine eutectic. Recall that ASZ measurements were taken from the eutectic region for all samples (i.e. no (β-Ti) dendrites were included in the bulk scans).

7.6 Application of Analysis to Maximum Brazing Clearance and IS Time

Full joint sandwich assemblies were fixtured using the same experimental setup as samples discussed in Sections 5.7 and 6.7. Figure 7.16 shows the complete cross section of a sample sandwiched with two nickel foils, heated to 1050°C, and cooled at 40 Kpm. A high degree of dissolution was observed where the undersized foils had been placed. This dissolution appeared normal on the lower plate, but apparent wetting difficulties caused a sharp step in the solid-liquid interface on the top plate. Similar to the full joint assembly in the grade two system (Figure 5.20), there is a region where partial dissolution occurs before the liquid composition of 29.44 wt% Ni is reached. Once this composition is reached, the liquid layer becomes uniform and consistent along the left side of the joint. There was no Type B joint on the other side suggesting the foil was placed closer to the right side of the joint. No porosity was observed the cross section of this sample.

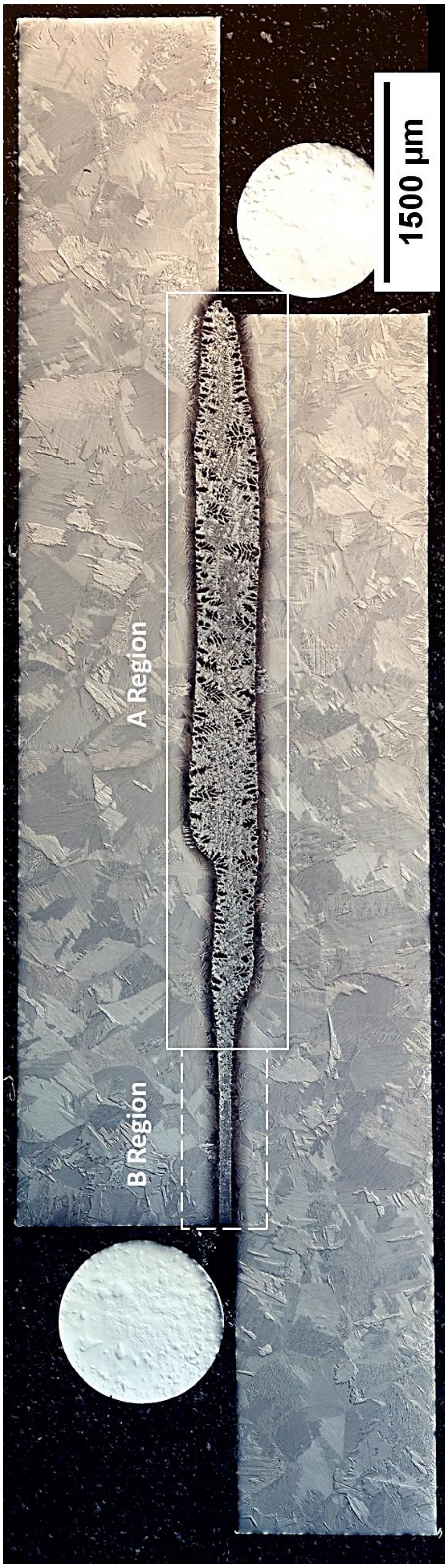

Figure 7.16 – Optical Imaging of Ti64/Ni/Ti64 DIL Sandwich Full Joint Heated to 1050°C and Cooled at 40 Kpm with Two Ni Foils

The original gap width was measured to be 145.2 μm by extrapolating the plate surfaces to the centre and measuring the difference. Using this gap width and the ratio of the maximum cylinder height to the height of a single foil (293.3:50 μm), the gap would be expected to widen to 852 μm. This sample was cooled at 40 Kpm which has a calculated liquid duration from DSC data of 2.83 min.$^{1/2}$. Using the linear regression curve from Figure 7.13, the value for $2W_{ISZ}$ was calculated to be 232 μm. Subtracting this value from the expected gap width after dissolution gives an expected width of the ASZ of 620 μm. Measured values of the ASZ was found to be 469.0 ± 27.6 μm which was in agreement with calculations.

From the $2W_{ISZ}$ curve, the simplified equation in Region B was $2W_{ISZ} = 24.342(t)^{1/2}$ for the Ti-6Al-4V and nickel system. Since the liquid wetting the gap is eutectic composition, there is no dissolution and the gap is filled with the liquid along the centreline. This leaves a liquid duration time of 2.5 minutes (1.58 min$^{1/2}$) which results in an IS growth layer of 38.5 μm. The width of the remaining liquid, W_{ASZ}, expected with an initial gap width of 145.2 μm was 106.7 μm. Measurements of this region of continuous width showed values averaging 52.7 ± 0.7 μm which deviated from predicted values. This difference was attributed to liquid entering the gap prior to the assembly reaching the braze temperature of 1050°C.

Figure 7.17 provides closer magnification images of the ASZ on the far left side of the joint (Figure 7.17a) and near the centre (Figure 7.17b). Figure 7.17b has a very similar microstructure to the sample heated to 1050°C and cooled at 20 Kpm shown in Figure 7.4c. A finer, and largely eutectic, ASZ region was found near the gap entrance where capillary action took place. The gap width is very well defined since no further dissolution occurs during wetting of this area.

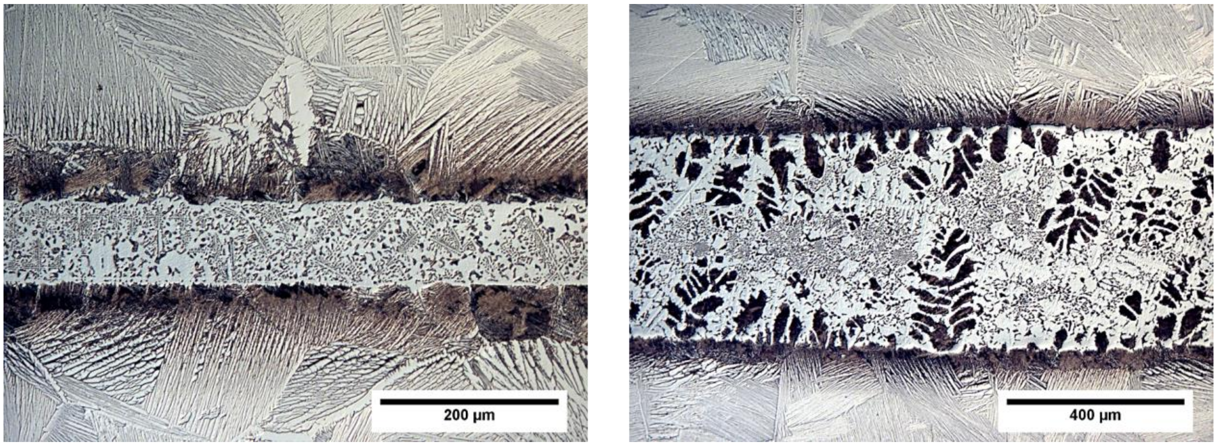

Figure 7.17 - Optical Imaging at Higher Magnification of Joint Microstructure (a) Left Side of the Overlap; (b) The Centre of the Joint

Compositional and hardness profiles were taken across the gap width and are included in Figure 7.18. EDS scans of the ASZ were taken as bulk scans and, as a result, values of composition are lower than in Figure 7.15 (similar to isothermal 60 min. sample). A similar composition profile to those figures is observed in the ISZ with nickel diffusing 200 µm above and below the centreline. Hardness along the centreline showed that the Ti_2Ni-rich ASZ had hardness values in excess of 1000 HV. Further away from the ASZ and ISZ (where Ti_2Ni precipitates are present), the hardness drops to the base metal values of 400 HV. These values suggested either that the measured hardness had not surpassed all nickel present in the base metal, or that the Ti-6Al-4V had become enriched with oxygen [73]. Aluminum and vanadium concentrations were also measured and are included in Figure 7.18b. It is interesting to note that these two elements remain in a consistent ratio and, as less base metal is incorporated in the liquid region, are found in lower concentrations in the ASZ.

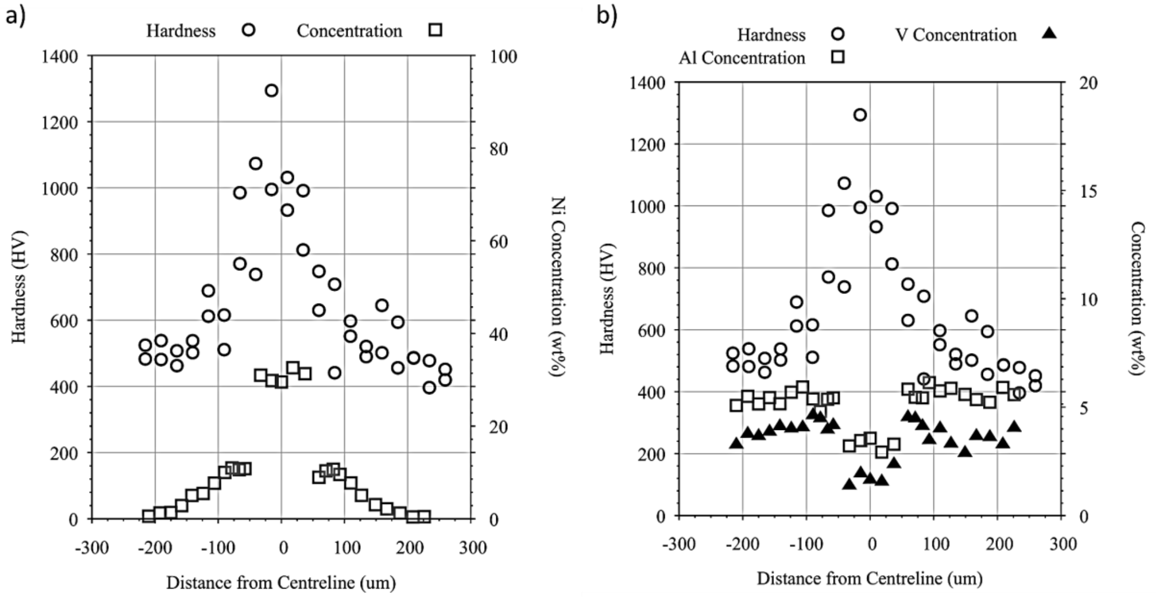

Figure 7.18 - Hardness and Compositional Profiles across the Ti64/Ni/Ti64 Centerline of a Two Ni Foil Experiment Cooled at 20 Kpm Showing (a) Ni Concentration; (b) Al and V Concentration

8.0 Discussions

8.1 Dissolution and Liquid Homogenization

The initial heating and dissolution behavior in the four braze couples studied in Chapters 4 through 7 can be understood with the aid of the conceptual model illustrated in Figure 8.1. Before heating of the sample begins, the initial state is the undersized foil on top of the titanium base metal, see Figure 8.1a. It has been shown that this undersized foil results in dissolution into the shape of a spherical cap but for the purposes of this schematic the layers will be assumed planar. This is a reasonable analog for a higher magnification of the area of dissolution in the middle of a sample. This arrangement remains until the formation of intermetallics between the foil and the base metal occurs. For the titanium nickel system, this process was captured in Figure 5.3 where the individual intermetallic layers expected in a Ti-Ni diffusion couple at 1050°C are observed as well as a liquid layer that had frozen closer to the base metal. This would be the microstructure resultant from Figure 8.1c.

Below 942°C (Figure 8.1b), a solid-state interaction between titanium and nickel similar to diffusion bonding work by Bastin outlined in Section 2.6.3 and in the prior art studies discussed in Section 2.6.1 would be expected. Note that below 880°C this interaction is with the α-Ti phase. With further heating the transformation to β-Ti is complete by 920°C according to the DSC initial heating traces of Chapters 4 and 5. For the Ti-Ni system, the intermetallic compound (IMC) layer would be comprised of $TiNi_3$, TiNi, and Ti_2Ni. These are included in Figure 8.1b. The growth of these layers consumes the pure nickel foil, but some remains in the solid state and even into liquid formation up to at least 965°C.

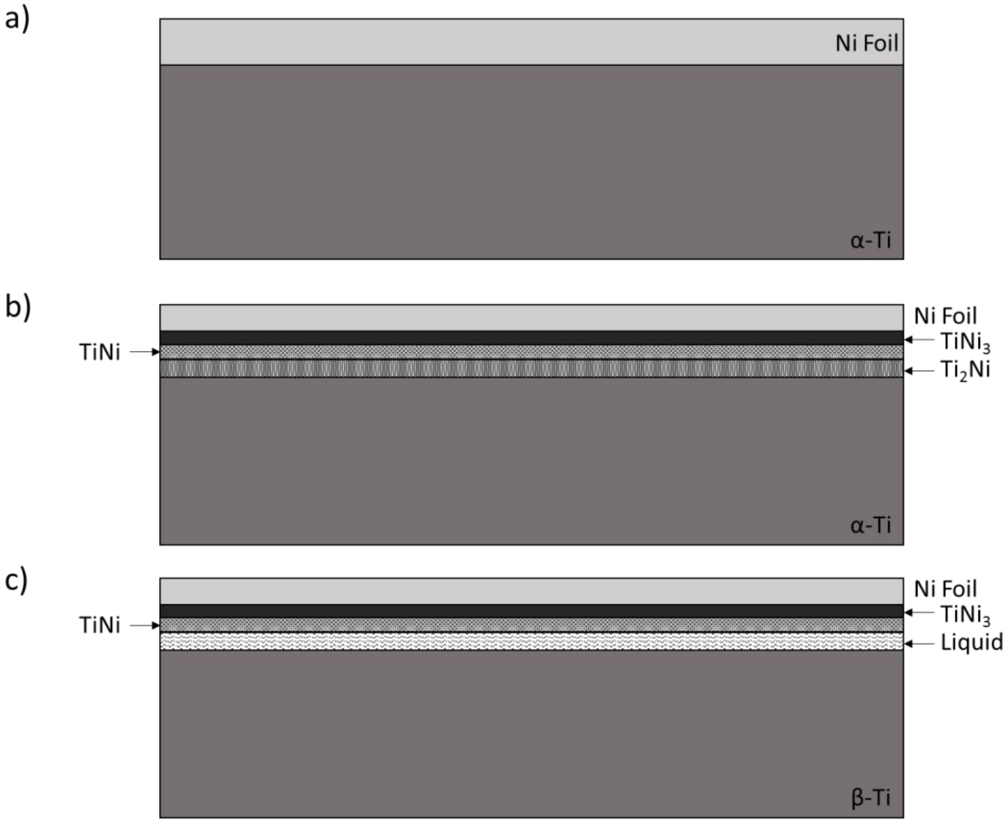

Figure 8.1 - Schematic of the Progression of Dissolution and Homogenization in a Binary Titanium Nickel System at (a) Initial State; (b) Below 880°C and; (c) Above 942°C

At the eutectic temperature (942°C) incipient melting occurs between the β-titanium base metal and Ti_2Ni which creates a liquid layer. Both the base metal and Ti_2Ni are continuously melted back until only the TiNi, $TiNi_3$, and pure Ni foil layers remain. Prior to this point, nickel diffusion was limited and was impeded due to slower diffusion rates through the intermetallic layers. The presence of liquid allows nickel to be transported to the base metal at a rate dictated by the liquid diffusivity (calculated later in this chapter) which is much faster than in solid titanium.

Figure 8.2 shows the schematic above the eutectic temperature but before the braze temperature with a microstructure similar to Figure 5.3. The liquid layer has grown through dissolution of the base metal and of the TiNi layer. Nickel diffusion is now occurring at all points along the solid-liquid interface where it had previously been limited to points of contact in the solid state. The rate of diffusion into the base metal is still dictated by the solid diffusivity of nickel into beta titanium. However, there is also a rate of nickel diffusion associated with the Ni-rich intermetallic layers at the surface. This movement of solute at the surface prevents homogenization of the liquid and requires continued dissolution of the base metal. This competition between the two layers will continue until the Ni-rich surface layers are completely consumed. At this point, homogenization of the liquid can continue to completion. For the binary Ti-Ni system this occurs somewhere between 965°C and 1000°C, as the Ni-rich layer is still observed in the 975°C sample.

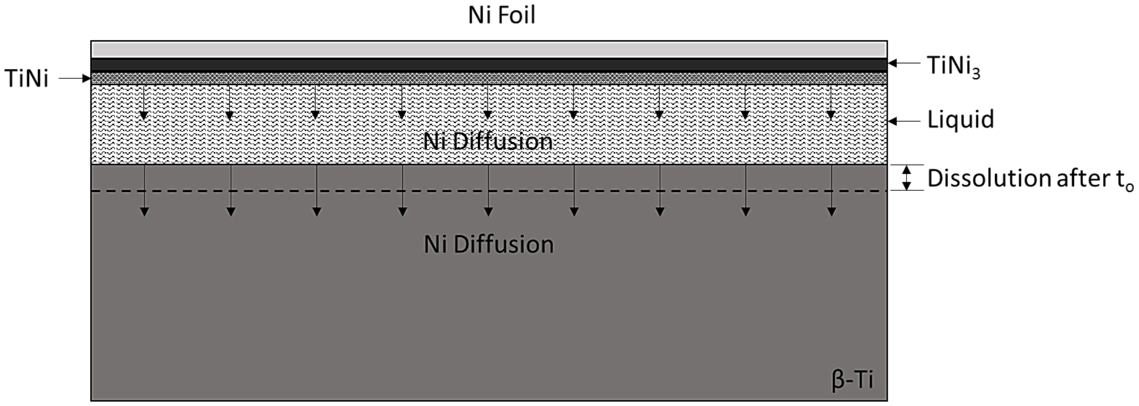

Figure 8.2 - Schematic of the Competition of Dissolution and Homogenization in a Binary Titanium Nickel System Above 942°C

This competition is between the two initial stages of isothermal solidification outlined by Tuah Poku [21]. First, the pure interlayer must dissolve into a liquid necessary for TLPB and following this dissolution the resultant liquid must homogenize to the liquidus composition. Normally stage one, the dissolution of the interlayer, is quite rapid and occurs on the order of seconds [21]. However, in the titanium nickel system, this stage has been inhibited by the presence of the IMC layer close to the remaining nickel foil. Thus, the competition of stage one and two is a relavent phenomenon in these experiments and must be considered.

Unlike the Ti-Ni system, the first melting events expected in the Ti-Cu system involve Cu rich intermetallics such as Ti_3Cu_4, $TiCu_4$, with melting expected as low as 875°C. The copper systems have the ability to melt all intermetallics at the braze temperature selected in this work (highest intermetallic melting point is 1005°C for Ti_2Cu). However, melting peaks corresponding to the temperature range of Cu-rich intermetallics (which would be expected to form) are only observed to a degree in the DSC traces of Ti-6Al-4V/Cu couples. Despite a lower eutectic point on the Cu-rich side of the phase diagram (875°C) in comparison to nickel, there is no event observed in the DSC close to this temperature for grade two titanium. Both grade two copper and nickel onset during heating at around 970°C as evidenced in Figures 4.1 and 5.1.

Figure 8.3 provides a similar analysis of the competition of dissolution and homogenization in the Ti-Cu system as seen in Figure 8.2. Since lower temperature melting events associated with the more Cu rich intermetallics were not observed in the grade two Ti-Cu DSC traces, the diffusion couple is described above 960°C, where the eutectic ($TiCu + Ti_2Cu \rightarrow L$) melting event was observed. The lower melting point Cu-rich IMC layer is assumed to have formed a liquid layer between more Ti rich intermetallics and the Cu foil. Limited copper diffusion passes through the remaining TiCu and Ti_2Cu and as a result solute uptake in the base metal is minimal. Instead, IMC growth occurs into the base metal at the TiCu and Ti_2Cu layers continue to grow. This layer is eventually consumed above 1000°C with the melting of Ti_2Cu as evidenced by Figure 4.3.

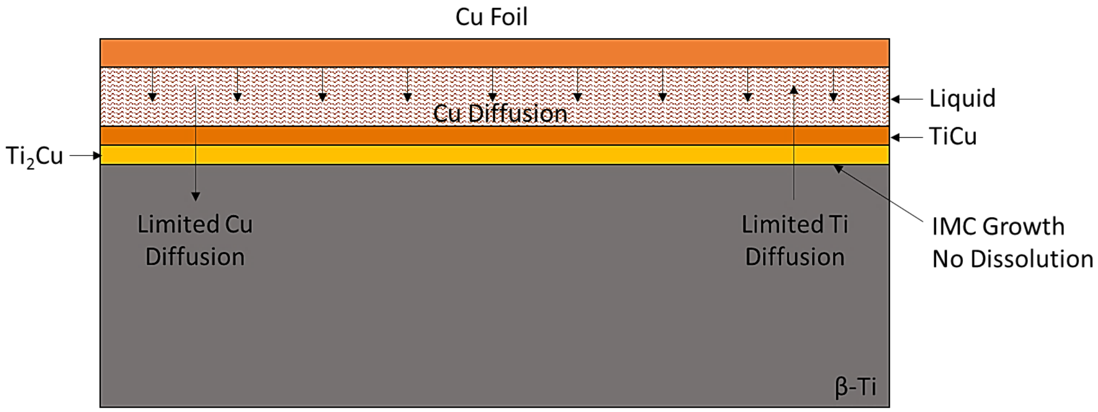

Figure 8.3 - Schematic of the Competition of Dissolution and Liquid Homogenization in a Binary Titanium Copper System Above 960°C

The first layer to melt in the titanium nickel IMC layer is Ti_2Ni which is the closest layer to the titanium base metal. Thus, the opportunity for nickel diffusion into the base metal (solute uptake) is high in the Ti-Ni binary system during heat up. In contrast, the first layer to melt in the Ti-Cu binary system would be a Cu-rich intermetallic close to the copper foil which would limit copper diffusion into the base metal. This would also lead to rapid dissolution of the Cu layer with increasing temperature as all low melting intermetallics are on the Cu-rich side of the phase diagram. The higher melting point Ti-rich intermetallics Ti_2Cu and TiCu would act as diffusion barriers into the base metal since diffusion is limited through these layers. The Ti_2Cu layer remains a diffusion barrier until melting around 1000°C.

From these findings, upon dissolution the copper dissolves rapidly and forms a liquid layer with minimal diffusion into the base metal. However, dissolution of the nickel layer is slowed by the

IMC layer which limits diffusion and incorporation of nickel into the liquid. Despite this limited dissolution and homogenization of the liquid, there is a large amount of nickel diffusion occurring locally at the solid-liquid interface into the base metal. Thus, in the competition discussed in Figure 8.2 between dissolution and solute uptake into the base metal, copper shows favored dissolution over uptake which would result in larger initial liquid fractions. Nickel shows increased solute uptake with a slower time to dissolution of the interlayer which would result in lower initial liquid fractions during the dissolution stage.

Figure 5.3 is worth revisiting at this point to describe in more detail the resultant microstructure (shown again in Figure 8.4). As discussed with Figure 8.2, there is a diffusion barrier between the nickel foil and the formed liquid below the IMC layer. The liquid when cooled results in the (β-

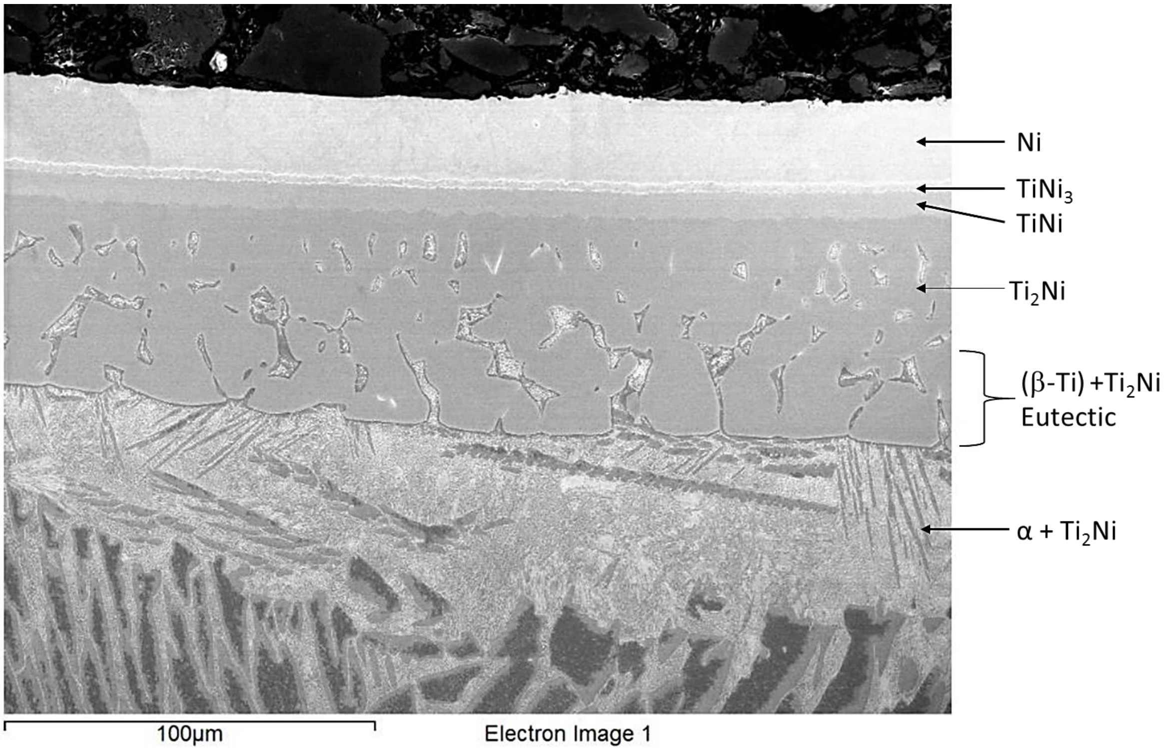

Figure 8.4 - SEM Imaging of a Half Joint Sample Heated to 965°C and Cooled at 20 Kpm Showing the Formation of Intermetallic Layers from the Nickel Foil

Ti) + Ti_2Ni eutectic and the base metal below the S/L interface, which has seen a large degree of solute uptake, forms (α-Ti) + Ti_2Ni eutectoid. The IMC layer does not appear to grow but instead is slowly consumed by the liquid as it forms.

Similar results were found in experimentation of the titanium copper system. Figure 8.5 shows the results of a Ti-Cu half joint heated to 885°C and held for five minutes. The sample was held isothermally due to the lack of interaction observed in DSC prior to 965°C. The results proved that intimate contact is necessary between the foil and the base metal prior to reaction. The temperature difference of 80°C at 20 Kpm requires four minutes to reach the temperature where reaction was observed. EDS results show the reacted sample has a Cu-rich ASZ with $TiCu_4$ in the interdendritic spaces between dendrites of Ti_2Cu_3 and $TiCu_4$. More importantly a continuous layer of TiCu and

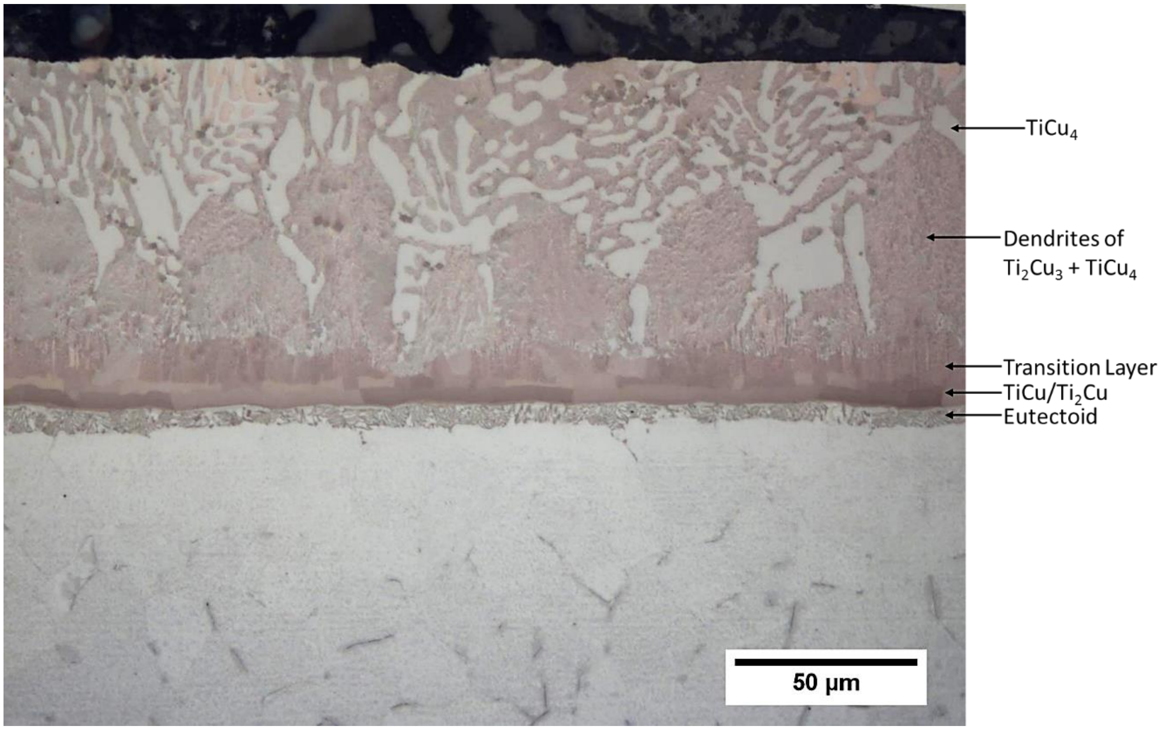

Figure 8.5 - Optical Imaging of a CP-Ti Half Joint Sample Heated to 885°C, Held for 5 min., and Cooled at 20 Kpm Showing the Formation of Intermetallic Layers from the Copper Foil

Ti_2Cu form and separate the Cu-rich liquid layer from the base metal. A thin eutectoid forms on the other side where minimal diffusion is observed beyond this region (less than 20 µm).

Figure 8.6 shows the same sample at another area of the cross section. The remainder of the copper foil is captured before dissolution can complete. The formation of $TiCu_4$ around the layer suggests localized melting of $TiCu_4$ which forms at the copper foil. From Figure 8.5 and 8.6 it is clear that diffusion is limited into the base metal as a result of the IMC layer. This confirms that dissolution in the binary Ti-Cu system is favored over solute uptake.

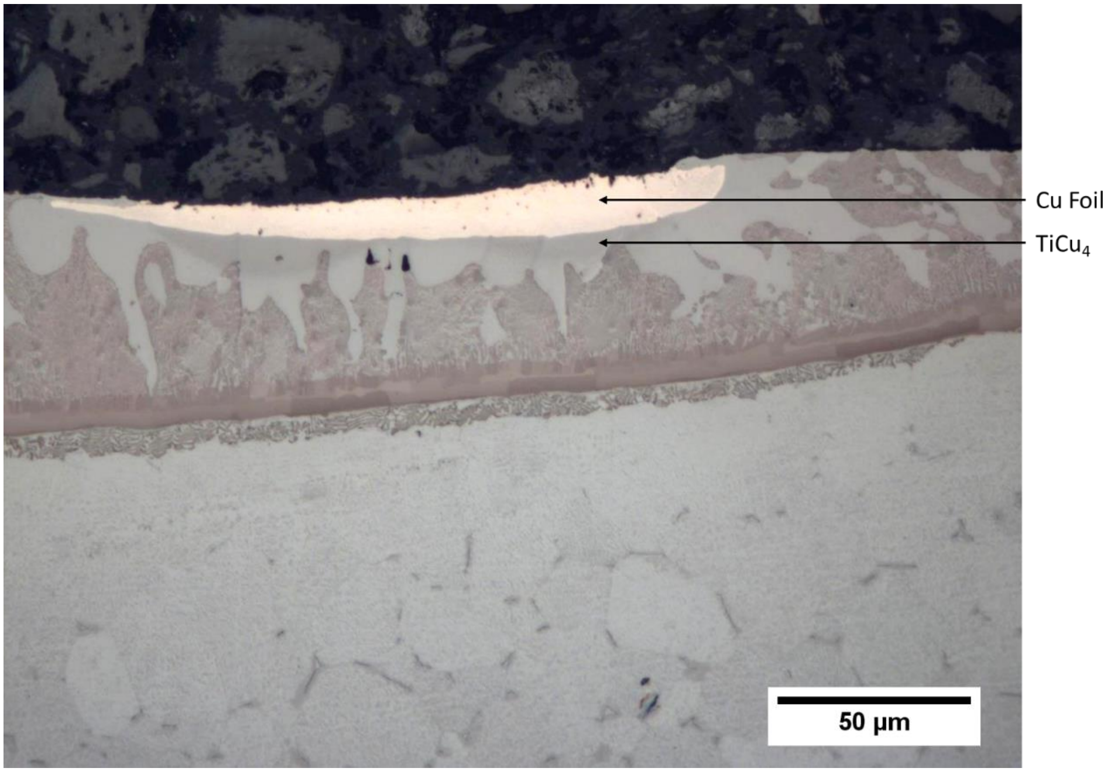

Figure 8.6 - Optical Imaging of a CP-Ti Half Joint Sample Heated to 885°C, Held for 5 min., and Cooled at 20 Kpm Showing Remaining Copper Foil Prior to Complete Dissolution

Figure 8.7 shows a commercially pure titanium base metal brazed with pure copper foil where the sample was heated to 950°C at 20 Kpm then heated to 960°C at 2 Kpm and cooled in a symmetrical fashion. There are minor additions of Cu-rich intermetallics which can be seen in the TiCu layer, but the Cu-rich IMC layer has completely melted. The intermetallic layer in Figure 8.7 is still a diffusion barrier to the direct injection of copper into the base metal (i.e. solute uptake). This microstructure looks similar to Figure 2.19b.

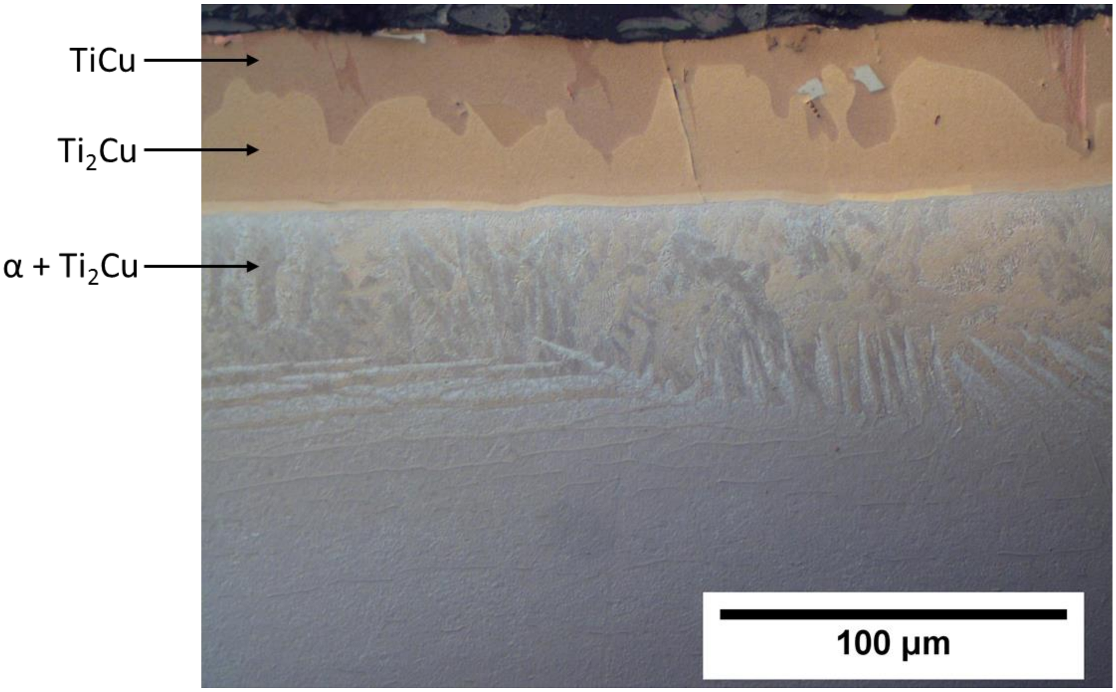

Figure 8.7 - Optical Imaging of a Half Joint Sample Heated to 950°C at 20 Kpm and then to 960°C at 2 Kpm and Cooled at 2 Kpm to 950°C and Subsequently Cooled at 20 Kpm

DSC experimentation showed that a minimum temperature of 960°C was necessary for intermetallic formation in both binary Ti-Cu and Ti-Ni when heating at 20 Kpm. However, subsequent testing showed that a necessary prerequisite was intimate contact between the foil and the base metal. There are other factors which can affect the interaction of base metal and foil which will be discussed in the next section. Reactions in Ti-6Al-4V were more unpredictable with copper onsetting at 885°C and nickel onsetting at 1000°C. The onset and formation of intermetallic reaction at exactly the eutectic temperature in the Ti-6Al-4V and copper was a surprising result.

This early interaction was investigated and is included in Figure 8.8 which shows a Ti-6Al-4V and copper sample heated to 885°C and immediately cooled at 20 Kpm. The resultant microstructure is a transient mixture of Cu-rich intermetallics ($TiCu_4$, Ti_2Cu_3, etc.). A thin layer of Ti-rich intermetallics (TiCu and Ti_2Cu) forms near the base metal. Below this a eutectoid layer is observed leading into the base metal which shows a mixture of equiaxed α-Ti and intergranular β-Ti. From this microstructure, it is evident that the first peak observed during DSC is the melting and dissolution of the copper foil. This occurs rapidly as no copper foil remained in the sample.

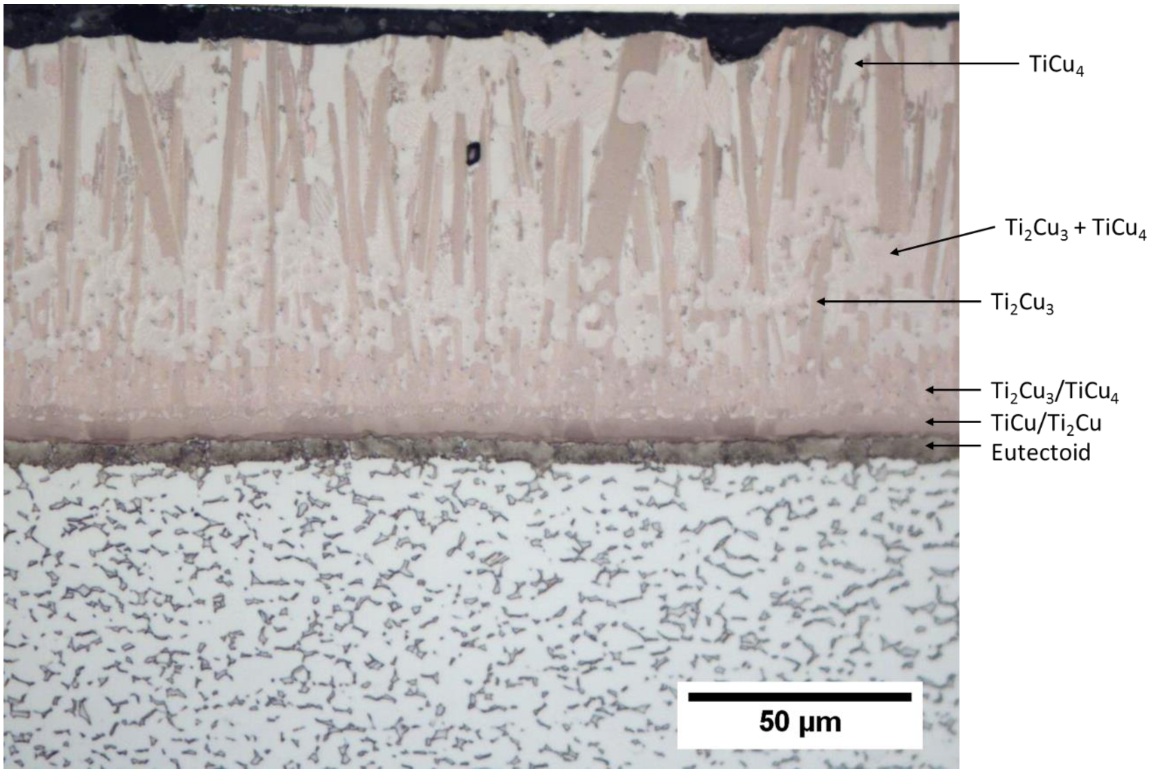

Figure 8.8 - Optical Imaging of a Ti-6Al-4V Half Joint Sample Heated to 885°C and Cooled at 20 Kpm Showing the Formation of Intermetallic Layers from the Copper Foil

Figure 8.9 shows a Ti-6Al-4V and copper sample heated to 900°C and immediately cooled at 20 Kpm. Similar to Figure 8.8 a Cu-rich intermetallic ASZ can be seen. Near the center of the figure, there is a region where incipient melting of Cu-rich intermetallics is occurring. This was observed to happen local to the TiCu layer and growing outwards into the ASZ. From Figure 8.9, the second peak in heating is likely the melting of Cu-rich intermetallics. This seems to continue until complete melting of all Ti_3Cu_4 which melts at 925°C ± 10°C as outlined by Murray *et al*. [56].

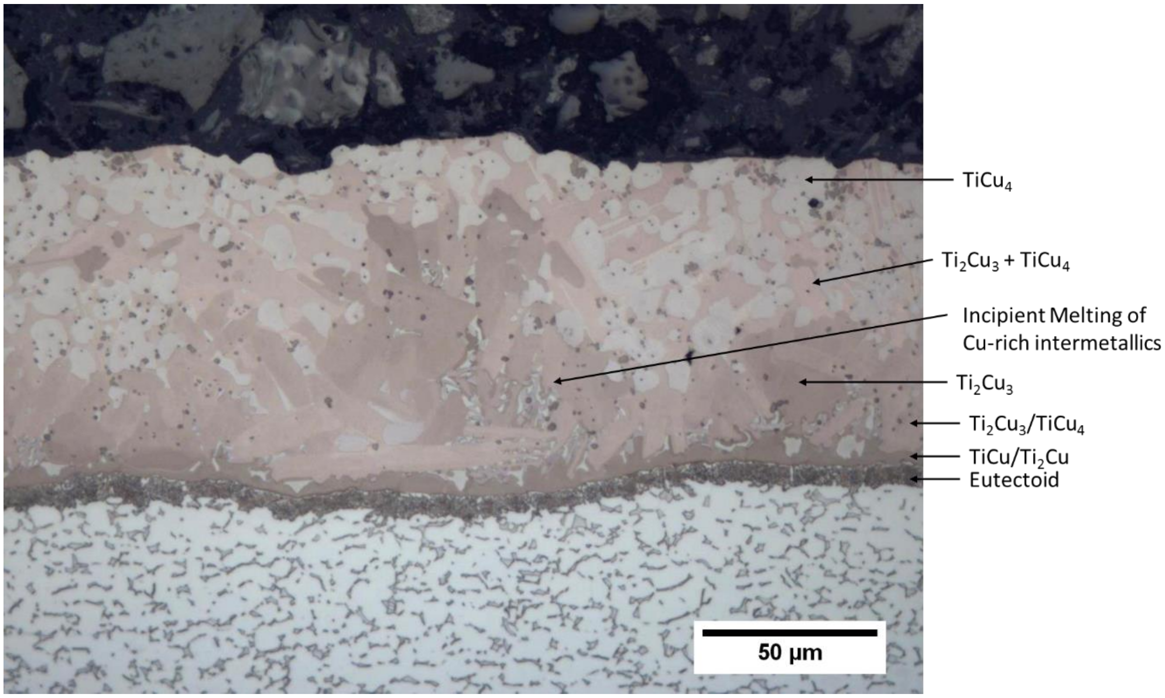

Figure 8.9 - Optical Imaging of a Ti-6Al-4V Half Joint Sample Heated to 900°C and Cooled at 20 Kpm Showing the Formation of Intermetallic Layers from the Copper Foil

8.1.1 Delays in Foil and Base Metal Interaction

The formation of the IMC layer is necessary for liquid formation which is needed for TLPB to continue. There are several factors to consider when explaining the delayed formation/nucleation of intermetallics observed mostly in Chapter 5. These include oxidation and the dissolution of oxygen in titanium and the allotropic α to β transformation. It is probable that each of these factors have some effect on the delayed (or lack of delayed) reaction of intermetallics necessary for dissolution. In addition, these delays in foil and base metal interaction can offset the homogenization stage which affects when isothermal solidification can initiate.

Titanium and titanium alloys will grow an oxide at a parabolic rate when heated to higher temperatures, which is common for thermal oxidation of metals [80]. In the case of titanium nickel, it has been shown that intermetallic formation can be impeded until dissolution of the surface oxide at 600°C (for commercially pure titanium) [55]. In Ti-6Al-4V, there is an increase in diffusivity above 850°C where oxygen diffuses into the sample core [81]. In the absence of an adequate supply of oxygen (i.e. a controlled atmosphere of argon), this would lead to a decrease in the surface oxide layer. Often in brazing the removal of the surface oxide layer is necessary for successful joining of assemblies through the use of flux, or chemical treatment. It seems likely that the oxide would pose a barrier to the interaction of the interlayer and base metal. However, given the affinity of titanium for oxygen and the fact that it will reduce both nickel and copper oxide (as dictated by the Ellingham diagram), it is possible that the oxide layer does not affect intermetallic formation, at least in controlled conditions [82]. As stated in Chapters 6 and 7, the absorption of oxygen into the titanium lattice has a hardening effect in both commercially pure titanium and Ti-6Al-4V [73].

With the exception of Cu and Ti-6Al-4V, all other brazing systems onset after the α to β transformation after initial heat up. From the binary phase diagrams, the transus temperature for commercially pure titanium is 882°C [30][31][56]. DSC testing of CP-Ti samples show an onset of 876.3°C with the peak ending at 920.8°C when heating at 20 Kpm. The reason for this longer temperature range is due to the ability of heat to be conducted into the sample in the crucible.

Another reason is likely impurities in the titanium slugs (predominantly iron and oxygen), see Table 3.1. Finally, oxygen is a known α-Ti stabilizer (see Figure 2.10). As stated previously, the earliest samples onset was around 960°C despite the lower melting point eutectic in the binary Ti-Cu system. The transformation of titanium from HCP to BCC would yield a lower atomic packing factor which would increase the rate of substitutional diffusion for both copper and nickel. However, this is not likely a factor as isothermally holding at 885°C allowed the dissolution of the copper foil in Figures 8.6 and 8.7.

Ti-6Al-4V shows a much wider range for this transformation during heating with a peak onset of 849.5°C and end of 1026.5°C (heating without the foil at 20 Kpm). Table 2.3 outlines that the expected transus temperature would be between 975°C and 995°C depending on the level of oxygen. This wide range in the DSC is explained by the fact that aluminum is an α-stabilizer and vanadium is a β-stabilizer such that, across the base metal, the α-phase is transitioning at different temperatures. Recall that in Chapter 7, Ti-6Al-4V and nickel did not see formation of intermetallics until 1000°C. It seemed that the α to β transformation may be having some effect on the onset of reaction between the foil and the base metal.

Homogenization of the liquid plays a role in how quickly isothermal solidification can initiate in both the titanium nickel systems. The rate at which the nickel foil can completely dissolve in the liquid will largely affect the start time of IS. In a more general sense, the liquid layers that form in Ti-Cu and Ti-Ni samples will have concentration gradients across the layer as dissolution continues. To achieve perfect mixing in the ASZ, these samples would be dependent on their respective liquid diffusivities which will now be discussed.

8.1.2 Role of Liquid Diffusivity in Dissolution and Homogenization

As mentioned, initial dissolution is rapid (on the order of seconds), driven by the compositional difference in solidus and liquidus compositions, and controlled by diffusion in the liquid. Prior to isothermal solidification, the homogenization stage must occur due to the liquid being inhomogeneous, or supersaturated. The liquid and solid are not in equilibrium and more dissolution of the solid is required for the solid-liquid interface to stabilize. Solute atoms will diffuse into the titanium base metal until the solidus composition is reached. In addition, titanium will be dissolving into the liquid until the liquidus composition is reached. Tuah Poku mentions the homogenization stage should be on the order of minutes for a binary Ag-Cu system [21]. Both dissolution and the homogenization process are controlled by diffusion in the liquid.

Liquid diffusivities were found for self-diffusion of nickel, copper, and titanium in work by Meyer [83]. These diffusivities at 1323 K were about 2 x 10^{-5} cm^2/s for nickel, 4 x 10^{-5} cm^2/s for copper, and 2.5 x 10^{-5} cm^2/s for titanium. The interdiffusivity of Ti-Cu and Ti-Ni were calculated from these values assuming a linear relationship between the pure metals and using the compositions of their respective ASZ (40 wt% Cu and 30 wt% Ni). From these calculations, the interdiffusivity in the Ti-Cu ASZ was found to be 3.1 x 10^{-5} cm^2/s and 2.35 x 10^{-5} cm^2/s in the Ti-Ni. From these calculated values it can be seen that there is little difference in terms of how quickly the copper and nickel foils can mix (ignoring the IMC layers formed in both couples).

However, Tuah Poku noted that for the homogenization of liquid stage, an effective diffusivity was more appropriate to factor in the cooperative effort of both the liquid and solid to remove solute. This effective diffusivity (D_e), if neither phase was dominant in solute removal, was the simple geometric mean of the liquid (D_L) and solid (D_S) diffusivity [21]. An example calculation for copper is shown:

$$\boldsymbol{D_e = D_S^{1/2} \cdot D_L^{1/2} = (3.12\ x\ 10^{-8})^{1/2} \cdot \left(3.1\ x\ 10^{-5}\right)^{1/2} = 9.83\ x\ 10^{-7}\ cm^2/s} \qquad \textbf{(8.1)}$$

In a similar manner, the effective diffusivity in nickel was calculated to be 1.665 x 10^{-6} cm^2/s. From these results, it appears that nickel is about two times faster in terms of liquid diffusivity which has significance only during the homogenization of the liquid. This is very close to the ratio of D_{Ni}:D_{Cu} in solid β-titanium and one would expect that nickel samples would initiate isothermal solidification first in the absence of the IMC layers.

Since diffusion is limited through the intermetallics, the Ti-Ni system requires more time for nickel to diffuse away from the foil and for the dissolution stage to complete. Following this, homogenization would be faster than the Ti-Cu systems. This slower process is offset by the solute uptake of nickel into the base metal prior to homogenization completing.

8.1.3 Impact of Solute Uptake

The most important factor that comes out of these first two stages of dissolution and liquid homogenization is the amount of solute uptake that occurs. This is a measure of how much solute has diffused into the base metal prior to a homogenized liquid which onsets isothermal solidification. Any amount of solute uptake will lead to a deviation from a theoretical ideal case which has been discussed throughout Chapters 4-7. In calculations of maximum volume, it was assumed that no solute diffuses into the base metal and the same assumption is made when considering investigating Regions A and B in full joints. However, consistently the liquid fraction when projected to the beginning of isothermal solidification (the y-intercept at a liquid duration corresponding to the time needed to reach 1050°C) shows a deviation from the ideal case where the maximum theoretical volume of liquid forms. This is illustrated in Figures 8.10 and 8.11 for the case of a Ti-Ni braze couple.

Figure 8.10 contrasts the ideal case of dissolution/homogenization (all solute in the interlayer forms the maximum volume, $V=V_{max}$) and the actual observations following dissolution/homogenization (where there is a reduction in liquid volume as a result of solute uptake). The schematic uses the binary Ti-Ni system as an example and the compositions are from values discussed in Chapter 5. In the ideal case, all nickel from the foil makes a Ti-Ni liquid that homogenizes to the liquidus composition just before isothermal solidification begins. However, the actual observations see that solute uptake is occurring during dissolution such that nickel has begun to diffuse away from the solid-liquid interface into the base metal. As a result, there is less nickel partitioned to the liquid when isothermal solidification begins, a lower liquid volume and larger diffusional distances are observed in composition profiles. For the Ti-Cu system, where solute uptake is limited, a much steeper composition profile was expected and the diffusional distances in this system were always below that of nickel.

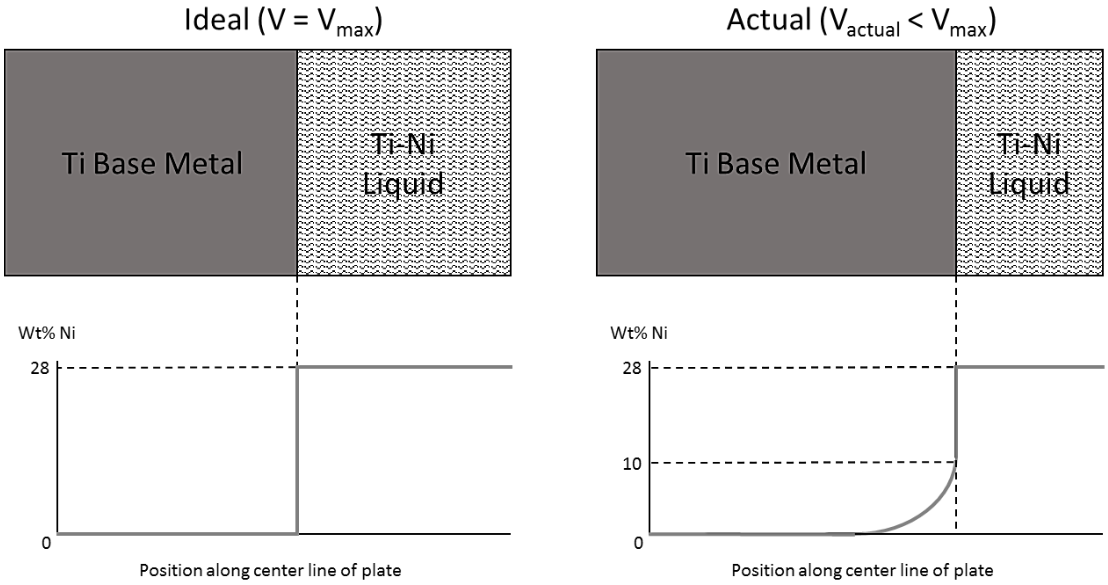

Figure 8.10 - Comparison of Ideal and Actual Volumes of Liquid as a Result of Solute Uptake

Figure 8.11 furthers this demonstration to consider the liquid fractions expected prior to and after isothermal solidification begins. During heat up, there is a period between the temperature where the first liquid forms and the braze temperature. During this period, liquid fraction slowly builds up as incipient melting at the foil-BM interface occurs (in addition to melting of intermetallics) and the liquid layer expands. In the ideal case, this continues until the entire foil is consumed and all solute remains in the liquid to form the maximum volume. This maximum volume denotes a liquid fraction value of one and would be expected to reach the maximum cylindrical (or spherical cap depending on geometry) height outlined the previous chapters.

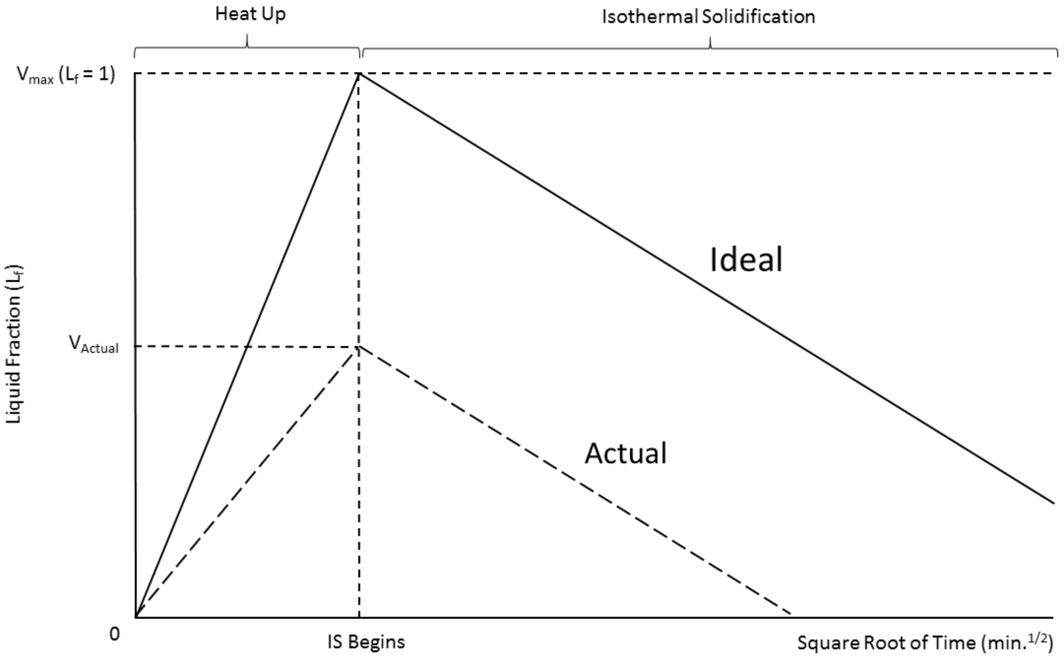

Figure 8.11 - Comparing Ideal and Actual Scenarios in Terms of Liquid Fraction vs. Square Root of Time

The actual sample, which displays some degree of solute uptake, will have less solute available in the liquid and therefore a lower liquid fraction produced during heat-up and dissolution and as isothermal solidification initiates. Note that during isothermal solidification, the rates of the actual and the ideal are the same. Therefore, solute uptake during heating and the associated reduced liquid fraction, has the practical benefit of reducing the time necessary for isothermal solidification to complete.

In Chapters 4 to 7, the liquid fraction was calculated from DSC and microstructural measurements. These measurements omitted initial samples cooled from different peak temperatures below 1050°C since they represent a transient, non-isothermal condition. Figure 8.11 assumes that the liquid fraction of these samples would progressively increase to V_{actual} and decrease from this maximum value as isothermal solidification began. This is in part because homogenization will continue with the changing liquidus composition until the braze temperature is reached. Values of the ASZ volume were determined for these peak samples using microstructural measurements and liquid fractions calculated base on the V_{max} values previously determined for the four systems studied. (see Figure 8.12). Associated DSC measurements were not possible for these samples since a suitable theoretical enthalpy would not be possible to identify. All initial samples were heated to 975°C, 1000°C, 1025°C, and 1050°C for all systems. In addition, samples were heated to 1050°C and cooled at 80 Kpm to capture the initial microstructure at the braze temperature. These samples underwent a faster cooling rate than the 1050°C 20 Kpm sample and were plotted at 1055°C to make this distinction.

Recall that solute uptake is minimized in Ti-Cu due an IMC diffusion barrier and that liquid in the Ti-Ni maximizes the amount of solute uptake due to the proximity to the base metal. Therefore, a larger liquid fraction would be expected in the Ti-Cu systems. However, this was not observed in Figure 8.12 when comparing copper and nickel in both CP-Ti and Ti-6Al-4V. It is possible that this occurs between 1000°C and 1025°C in titanium copper samples. In addition, the values at 1050°C for each system are close to initial liquid fractions determined from plots in each chapter, such as the binary Ti-Cu system in Figure 4.11 where the y-intercept was found to be 0.4922.

Another phenomenon that can be validated with Figure 8.12 is the sluggishness of the Ti-6Al-4V system. During the heat up stage, commercially pure systems show an upward trend in liquid

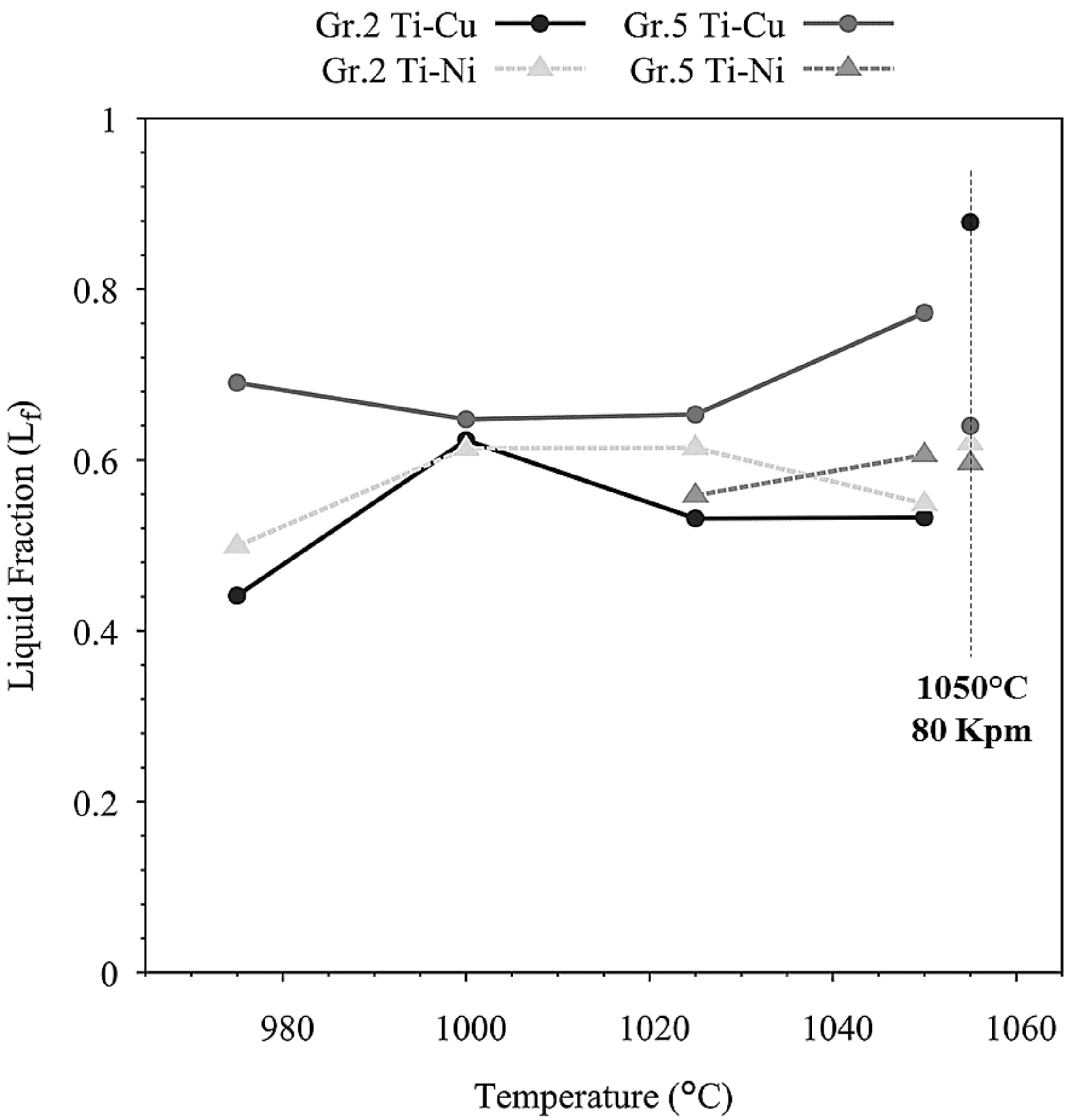

Figure 8.12 - Heat Up Liquid Fractions of Copper and Nickel Half Joints from Halted Temperatures During Initial Testing. Samples Heated to 1050°C are Differentiated Between 20 Kpm and 80 Kpm Cooling Rates

fraction until reaching the braze temperature where a decrease or flattening is observed in the liquid fraction. However, the Ti64 systems show a continued increase even at the braze temperature. This suggests that liquid homogenization is slower in the grade five titanium samples. For the Ti-6Al-4V and nickel system, this can be explained by the short time nickel has in the liquid state prior to reaching the braze temperature. However, the Ti64/copper system onsets earliest of all samples and still struggles with homogenization before transitioning into isothermal solidification.

The 80 Kpm samples provide the closest microstructural evidence to the transition from dissolution and homogenization to isothermal solidification. The compositional profiles for solute below the solid/liquid interface is compared for all four 80 Kpm samples in Figure 8.13. For a given foil (Cu or Ni) solute uptake is more significant in CP-Ti versus Ti64 Ti. This does not correlate very well with liquid fraction, since L_f is higher in CP-Ti couples compared to Ti64 Ti. This is an indication

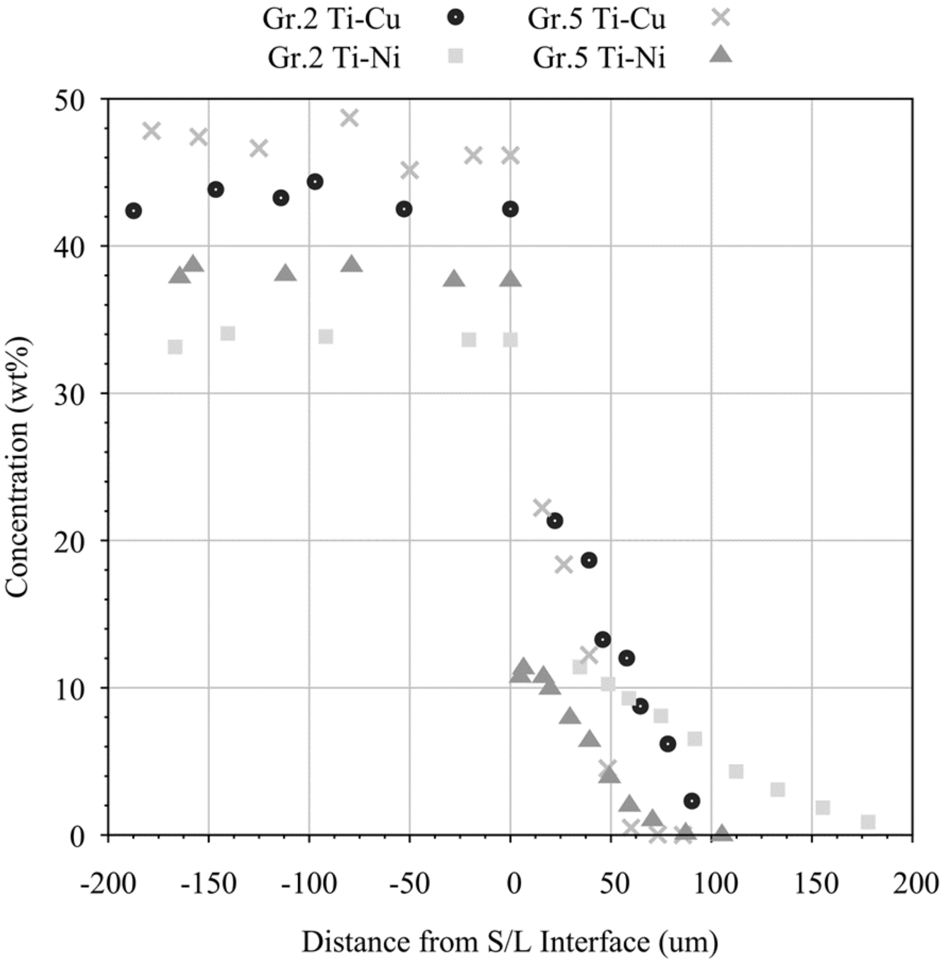

Figure 8.13 - Corrected Compositional Profiles Comparing Concentrations of All 80 Kpm Samples with Distance from the S/L Interface

that the dissolution process depends not only on solute uptake but foil dissolution and liquid homogenization. For a given base metal, Ni penetrates more deeply into the base metal than Cu, particularly for the case of CP-Ti

8.2 Isothermal Solidification

With a firm understanding of dissolution, homogenization and solute uptake, isothermal solidification can now be reviewed for all systems. Section 8.1 outlined the initial conditions of isothermal solidification and explained the differences between nickel and copper interlayers. A brief summary discussion is included for isothermal solidification in each system. Figure 8.14 summarizes all the W_{ISZ} curves determined in studying the joining of CP-Ti and Ti-6Al-4V.

From the figure, it is clear that the grade two titanium nickel samples have the highest amount of solute uptake in terms of the initial layer growth of the $2W_{ISZ}$. In contrast, the other samples displayed very similar growth of the initial layer of the ISZ. This is surprising given the extent of dissolution in titanium nickel systems and it should be noted that a much higher amount of liquid remains in the grade five samples. Ti64/Ni half joints showed the lowest initial growth of solid owing to a delayed onset and slower homogenization of the liquid as a result.

For a given base metal alloy, nickel braze joints indicate a higher rate of isothermal solidification compared to copper. Recall that isothermal solidification is governed by the rate of diffusion into the solid and, from Table 2.5, that nickel has a diffusion rate 2.5 times faster than copper in β-

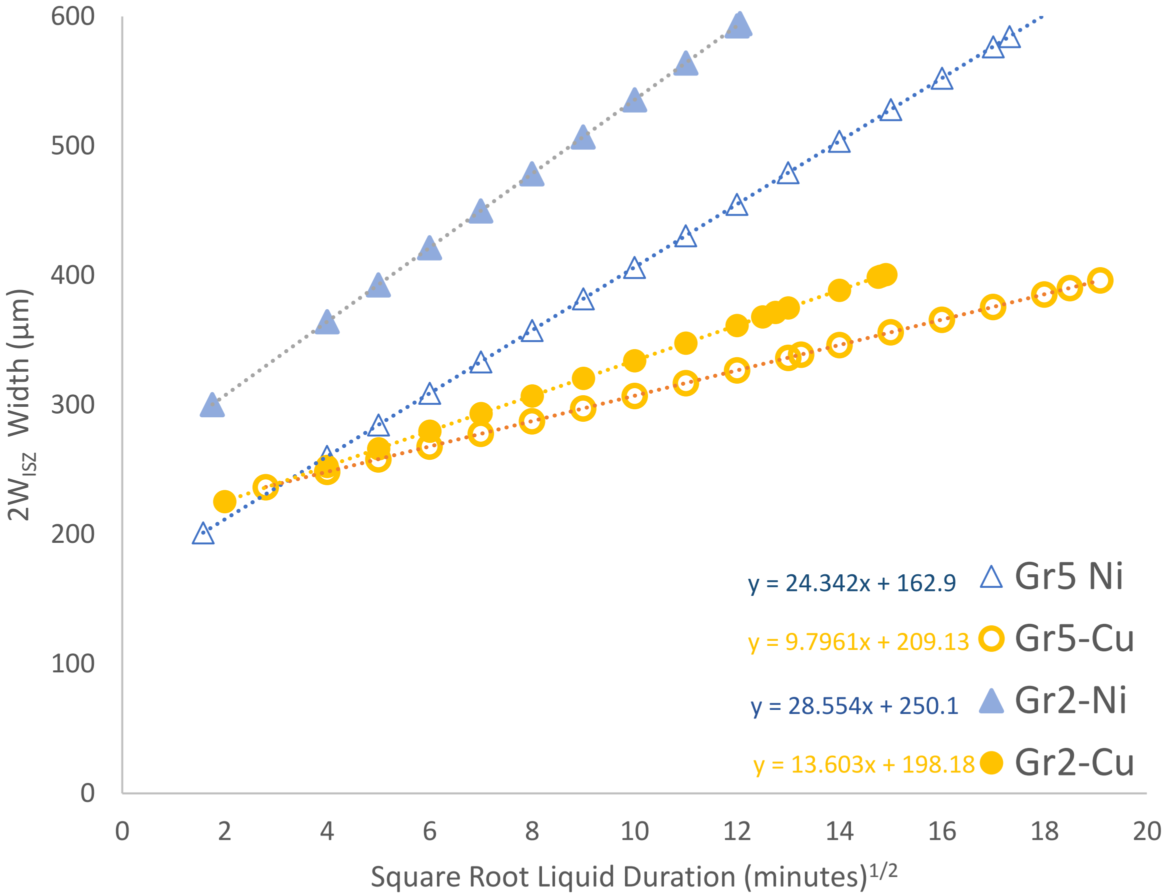

Figure 8.14 - Summary $2W_{ISZ}$ Curves for Copper and Nickel in Commercially Pure Titanium and Ti-6Al-4V

titanium at 1050°C. For a given braze foil type, the rate of isothermal solidification is faster in commercially pure titanium owing to a higher diffusion rate which will be discussed further in Section 8.2.1.

Grade two titanium and nickel exhibits the highest rate of isothermal solidification. This coupled with the highest amount of solute uptake results in the lowest isothermal solidification time for a 50 µm thick starting braze foil. In contrast, grade five and copper displayed the longest solidification time and had the lowest rate of isothermal solidification. Overall, despite higher degrees of dissolution and gap widening potential, higher rates of isothermal solidification in Ni-based filler joints lead to lower isothermal solidification times for a given base metal system.

Figure 8.15 shows the comparison of cyclical samples and isothermal samples for titanium copper using grade two and grade five. For cyclical specimens, early and late cycles were compared since a different number of cycles was used for each base metal. A much more rapid amount of homogenization is apparent from the lower compositions of the ASZ and it can be seen that copper diffuses further in the grade two samples even though (in terms of cyclic testing) they are held for shorter liquid durations.

These were also plotted for the nickel systems and are shown in Figure 8.16. The same trends noted above are present when comparing grade two and grade five titanium. It is clear in Figure 8.16a that the concentration of the solid at the solid-liquid interface drops to the solidus temperature faster when comparing early cycles. This suggests that the grade five cyclic 3X sample may still be somewhat inhomogeneous in the ASZ which will delay the full onset of isothermal solidification. Again, the diffusion distances of nickel are much further into CP-Ti in comparison with Ti-6Al-4V.

This confirms that diffusion in Ti64/Cu and Ti64/Ni samples is slower compared to commercially pure titanium. Since isothermal solidification is governed by the diffusivity of solute into the β-titanium base metal, it is clear that Ti-6Al-4V samples are showing a lower value. This will be discussed in the next section where diffusivity values were calculated for all systems.

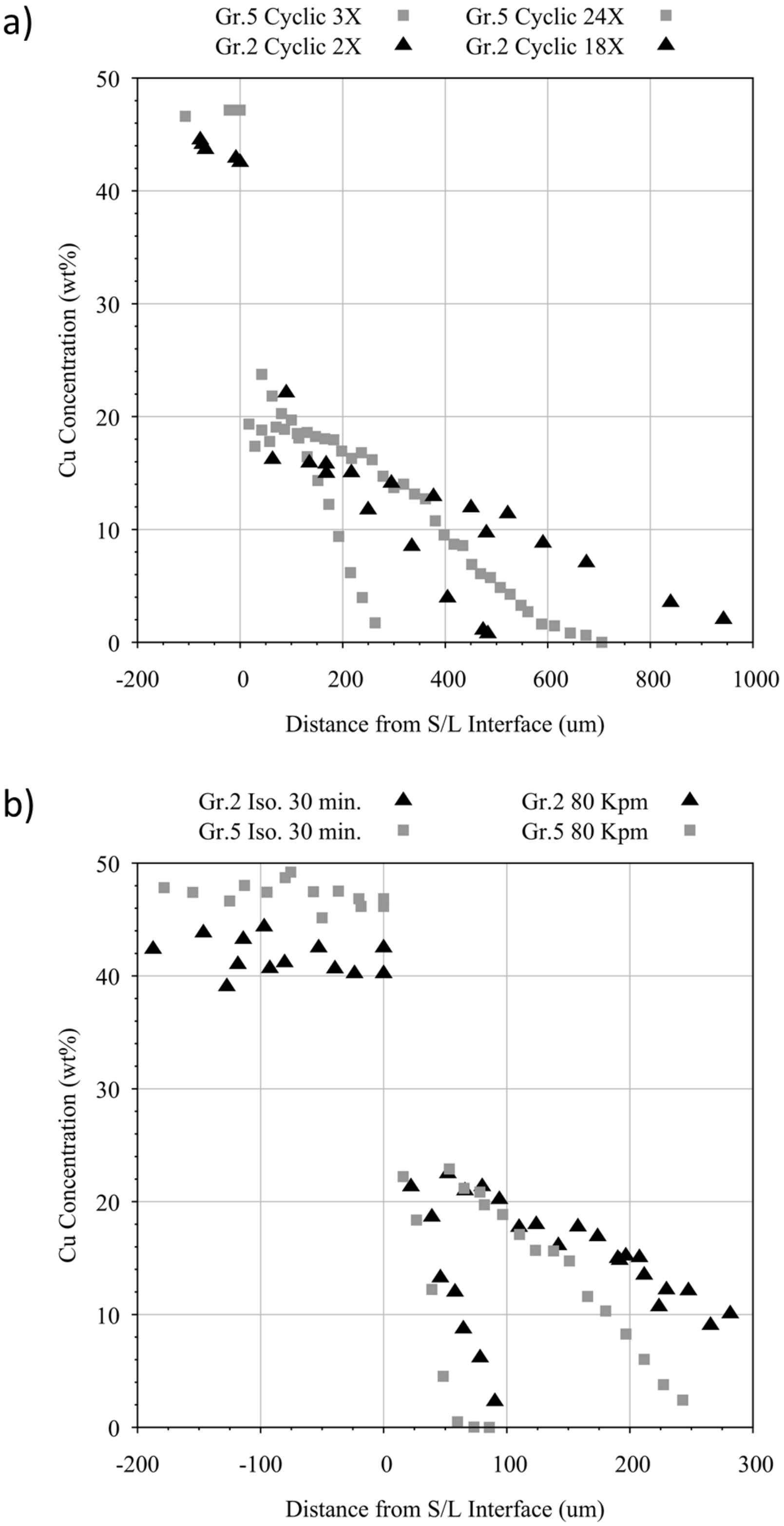

Figure 8.15 - Corrected Compositional Profiles Comparing Grade Two and Five Titanium Using Copper as an Interlayer (a) Comparing Cyclical Testing; (b) Comparing Isothermal Testing

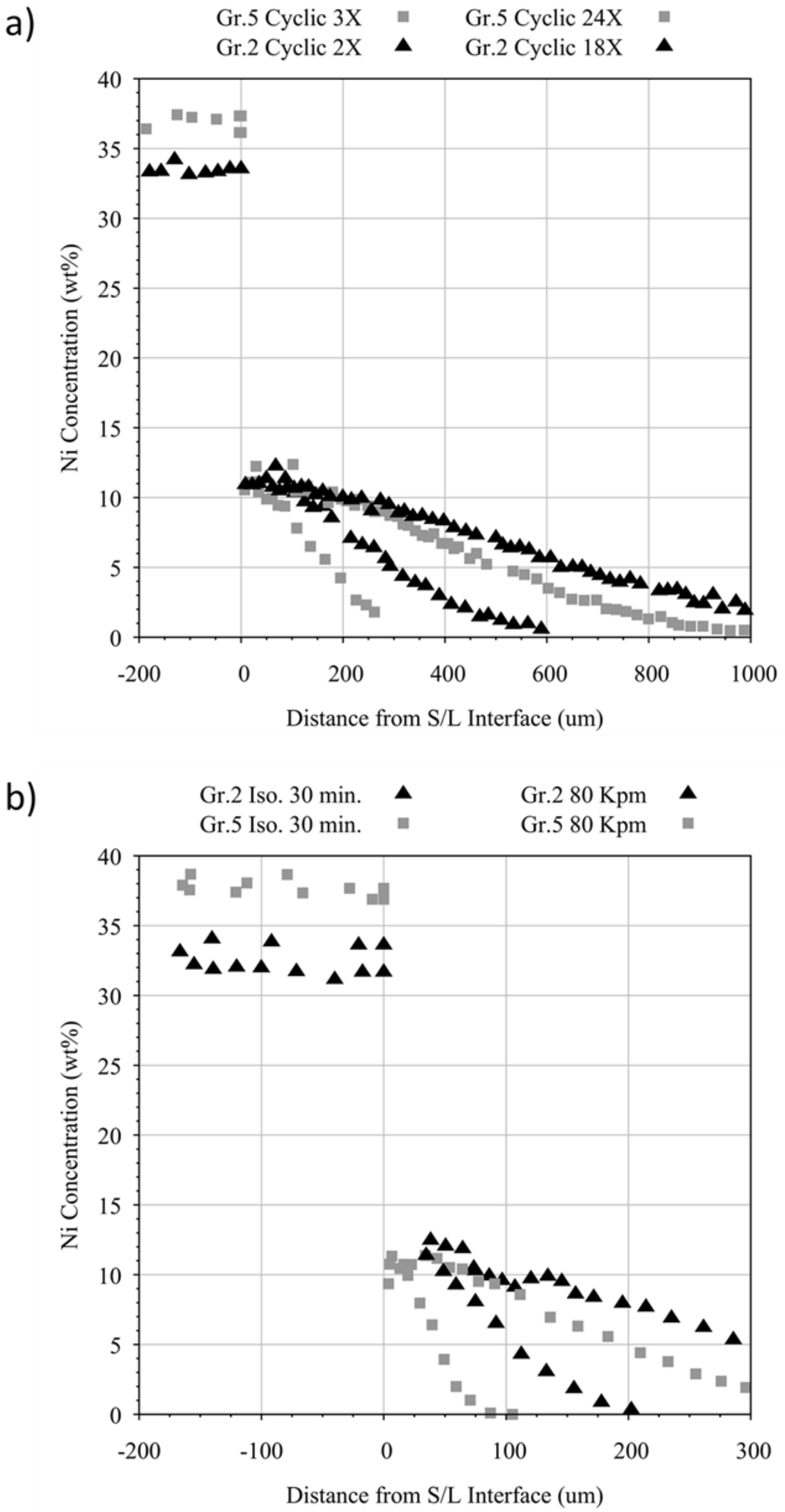

Figure 8.16 - Corrected Compositional Profiles Comparing Grade Two and Five Titanium Using Nickel as an Interlayer (a) Comparing Cyclical Testing; (b) Comparing Isothermal Testing

8.2.1 Diffusion Based Predictions of Isotheral Solidification Times

Experimental results in Chapters 6 and 7 have shown that diffusion in the base metal became sluggish when the Ti-6Al-4V alloy was implemented. No literature was found to describe the rate of diffusion of copper, or nickel, in grade five titanium and so a method is proposed here using equations from Tuah Poku *et al.* [21]. Equation 2.18 can be rearranged to the following form to find the time to isothermal solidification (t_{IS}):

$$t_{IS} = \frac{\pi W_{max}^2}{16 \cdot D_{sol.}} \left(\frac{C_{liq.}}{C_{sol.}} \right)^2 \tag{8.2}$$

Where W_{max} is the maximum width following dissolution and homogenization of the liquid, $D_{sol.}$ is the diffusion of solute in the solid, c_{liq} is the liquidus concentration, and $c_{sol.}$ is the solidus concentration. The values of the liquidus and solidus are taken from the phase diagram at 1050°C.

Equation 8.2 relies on the starting liquid width for accurate predictions of time to isothermal solidification. The calculated values for the maximum height of a cylinder would seem appropriate, however, these were never realized in actual application due to reasons discussed in Section 8.1 (dissolution behavior, solute uptake, etc.). A consistent observation during experimentation is the transient nature of dissolution and interaction in the base metal which leads to different responses for each system in terms of liquid fraction. This transient behavior tends to alleviate itself once the braze temperature has been reached and is restricted mostly to the heat up stage previously discussed.

Figures 8.14 and 8.17 have plotted the respective widths of the ISZ and ASZ with consideration of the heat up stage. Liquid duration is initially measured when the sample reaches the solidus composition (first onset of melting), or when interaction and melting occur at some higher temperature. Recall that there were large differences in these onsets (i.e. 970°C for Gr.2 Cu, 988°C for Gr.2 Ni, 880°C for Gr.5 Cu, and 1000°C for Gr.5 Ni). Therefore, there is a difference in the liquid duration for each system once the braze temperature is reached (i.e. Gr.5 Cu, 8.5 min. vs Gr.5 Ni, 2.5 min.). Figures 8.14 and 8.17 have removed all data prior to the braze temperature such that only data relevant to the isothermal solidification stage is plotted.

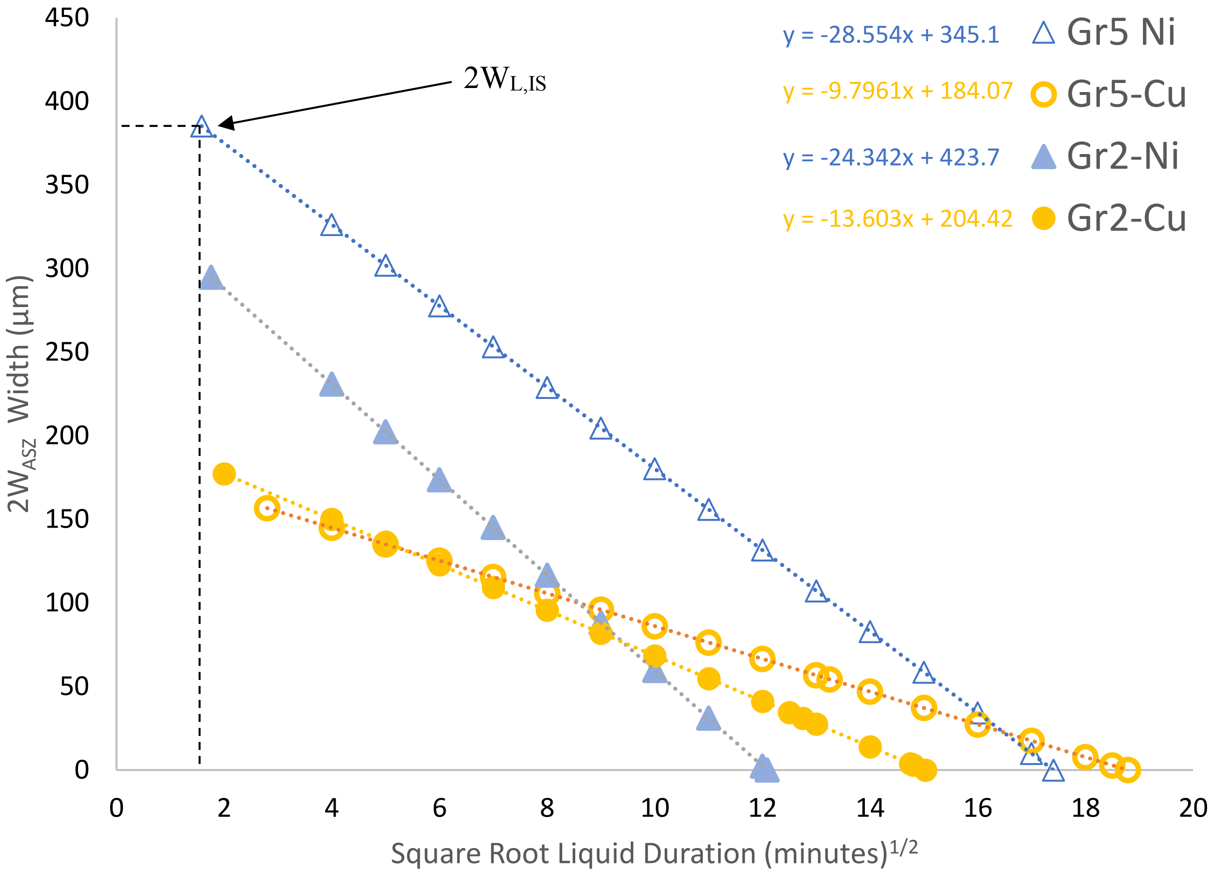

Figure 8.17 - Summary $2W_{ASZ}$ Curves for Copper and Nickel in Commercially Pure Titanium and Ti-6Al-4V

This is a convenient measurement since these graphs are now plotted with the starting liquid width and liquid duration at the onset of isothermal solidification. This starting liquid width that immediately follows heat up to the braze temperature has been termed $2W_{L,IS}$. This value is an accurate depiction of the available liquid such that V_{actual} in Figure 8.11 is represented. With this corrected liquid width, there is also an adjustment to liquid duration and the time to completion of isothermal solidification. This leads a term, $t_{IS,corr}$, which is the subtraction of the heat up liquid duration time from the total time to complete IS.

Equation 8.2 can now be rearranged with these terms to find the diffusion coefficient for each system. This allows for only experimental values to be used for $W_{L,\,IS}$ and $t_{IS,corr.}$ The new equation becomes:

$$\boldsymbol{D_{sol.} = \frac{\pi W_{L,IS}^2}{16 \cdot t_{IS,corr}} \left(\frac{C_{liq.}}{C_{sol.}}\right)^2} \tag{8.3}$$

An example calculation can be shown for grade two titanium and copper. The value for $W_{L,IS}$ was found to be 177.2 μm and the liquidus and solidus values are 0.4 and 0.18 respectively at the braze temperature of 1050°C. The time to complete isothermal solidification in this system is 222.4 minutes with a heat up stage lasting 4 minutes. Thus, the value for $t_{IS,corr}$ becomes 218.4 minutes, or 13,107 seconds. Inputting all known variables, the equation becomes:

$$\boldsymbol{D_{sol.} = \frac{\pi(0.01772)^2}{16 \cdot (13107)} \left(\frac{0.4}{0.18}\right)^2 = 2.322\ x\ 10^{-8}\ cm^2/s} \tag{8.4}$$

Table 8.1 outlines the resultant times of isothermal solidification, liquid widths, and diffusion coefficients found using Equation 8.3. Values from Table 2.5 have been used in the D_s column to represent values found from literature [52]. There very is good agreement when contrasted with the calculated diffusivities at 1050°C in grade two titanium.

Table 8.1 - Calculated Diffusivities for Copper and Nickel in Commercially Pure Titanium and Ti-6Al-4V

System	$t_{IS,corr}$ (min.)	$2W_{L,IS}$ (μm)	$D_{calc.}$ (10^{-8} cm^2/s)	D_S (10^{-8} cm^2/s)
Gr.2 Cu	**218.4**	**177.2**	**2.32**	**3.12**
Gr.2 Ni	**142.8**	**294.8**	**9.83**	**11.80**
Gr.5 Cu	**355.4**	**155.9**	**1.11**	**-**
Gr.5 Ni	**297.1**	**385.2**	**8.07**	**-**

Examining diffusivities in Ti-6Al-4V, nickel samples show a diffusivity close to the rate found in commercially pure titanium whereas copper samples show about half the value found in CP-Ti. Semiatin *et al.* noted that the pertinent diffusivities in ternary alloys were found to be about 80% of those estimated in binary diffusion experiments [84]. The ratio of calculated diffusion coefficients in quaternary (Ti-6Al-4V) versus binary systems in copper and nickel was found to be 47.8% and 82.1% respectively. Considering that both Ti64/Cu and Ti64/Ni are quaternary systems these diffusion coefficients are in good agreement.

With the apparent diffusion coefficients calculated for Ti-6Al-4V, it was now possible to compare to them to the rate of isothermal solidification. Figure 8.18 shows there is a strong correlation between the rate of isothermal solidification and the diffusion rate of the solute into the base metal. This provides support that the calculated values were close to experimental observations in terms of the diffusion of solute into the base metal.

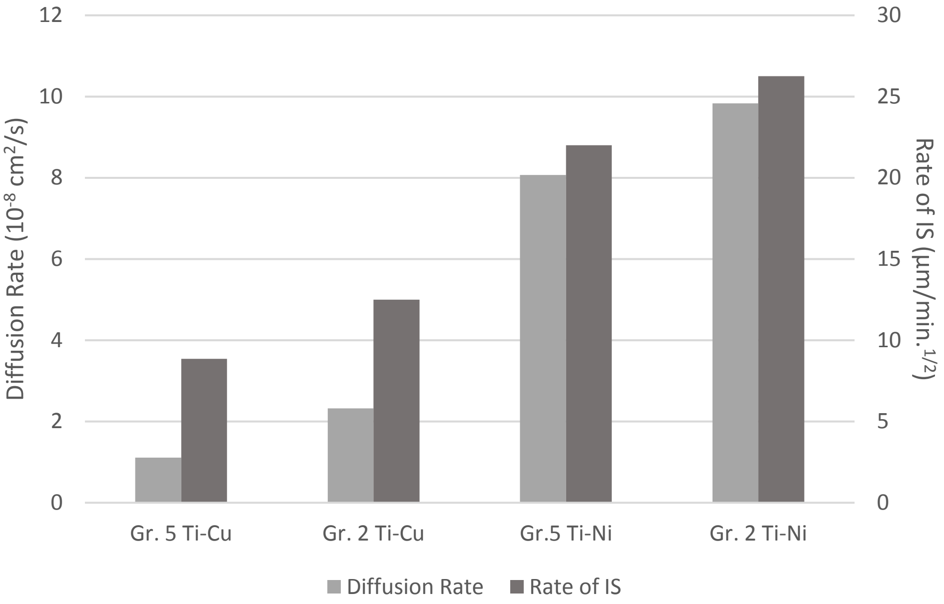

Figure 8.18 - Comparing Diffusion Rates and the Rates of IS for All TLPB Systems

9.0 Summary and Conclusions

Copper and nickel were examined as potential interlayers in transient liquid phase brazing (TLPB) of commercially pure titanium and Ti-6Al-4V. Experimental parameters were set such that the braze temperature was above intermetallic formation (1050°C) and was examined for all systems for the purpose of consistency. In addition, a foil width of 50 μm and a heating and cooling rate of 20 Kpm was used throughout experimentation. Using high temperature thermal analysis techniques (DSC, DIL), as well as microstructural observations (SEM, Optical Microscopy), the efficacy of these interlayers was monitored for levels of dissolution, rates of isothermal solidification, and the time to homogenization.

Wire Electrical Discharge Machining was used to reproduce similar volume titanium slugs for use in the DSC with commercially pure (N2.0) copper and nickel foils. DSC testing of both commercially pure titanium and Ti-6Al-4V titanium alloy showed only a small difference in the base metal correction factor making both materials comparable in thermal lag. Cyclical and isothermal testing was planned based on the length of time to isothermal solidification. Titanium plates were later fixtured into full joints with stainless steel balls by tack welding to prevent shifting of the assembly during dissolution and liquid flow. All samples were etched using Kroll's reagent.

Initial experimentation of grade two titanium and copper led to wetting of the alumina crucible and made conventional DSC testing of TLPB difficult. An undersized foil was adopted which led to dissolution of the base metal in a spherical cap geometry. Liquid volumes created by the interlayer were measured and modelled based on this geometry and it became necessary to project the width and height of the cap to the centre to find these values. To avoid any further issues with dissolution, or wetting, all foils used were undersized and placed as close to the center of the base metal surface as possible. This was also practiced for the creation of full joints. Experimental results agreed well with this model and, by assuming equal faying surface areas, it could be converted back to cylindrical values. This allowed the creation of $2W_{ISZ}$ curves such that the expected height of ASZ and ISZ could be mapped across all braze gaps and hold times at the braze temperature of 1050°C.

Examining copper and commercially pure titanium, initial heating shows the formation and melting of TiCu (L→TiCu) and a peritectic reaction coupled with an undercooled eutectic on cooling (L→TiCu+Ti_2Cu). Initial microstructures revealed an ASZ that transitions from a mixture of TiCu and Ti_2Cu into a predominantly Ti_2Cu layer in the interdendritic spaces of hypereutectoid dendrites. The ISZ consists of α + Ti_2Cu ranging from hypereutectoid compositions into hypoeutectoid and finally the grade two titanium base metal. The liquidus composition for an 80 Kpm sample was measured to be 39.3 wt% Cu where 51% of the liquid remained after reaching the braze temperature. The maximum depth of dissolution was calculated to be 201.3 μm for a cylinder and 395 μm for a spherical cap. Excess eutectic solidification halts at 150 minutes and the remaining peritectic reaction has undergone complete isothermal solidification after 222 minutes.

Liquid fraction data allowed the creation of $2W_{ISZ}$ curves where the y-intercept reveals the initial solute uptake into the base metal and the slope provides the rate of isothermal solidification in $\mu m/min^{1/2}$. In the titanium copper system, 99.1 μm of ISZ was predicted at the braze temperature which closely followed measured microstructural values for a half joint. Compositional profiles for isothermal and cyclic specimens revealed that the ASZ homogenizes to a composition of 40-43 wt% Cu with a maximum diffusion distance over 1000 μm when isothermal solidification has completed.

Full joints were fixtured and heated to the braze temperature as either capillary or pre-sandwiched assemblies. In the pre-sandwiched double foil experiment light porosity was observed due to the use of undersized foils which pulled liquid into empty sections of the braze gap. Region A was assumed to be where full dissolution of the foil occurred and showed agreement when modelled under those conditions. The assumptions of Region B where liquid at the liquidus composition entered at the braze temperature proved less consistent when modelled suggesting liquid was drawn prior to reaching the braze temperature. The $2W_{ISZ}$ curve was shown to be able to not only predict the height of the ISZ but also the ASZ and the duration of homogenization following isothermal solidification. Single foil capillary experiments showed copper wet easily into the braze gap where the sample reduced to 3 wt% Cu along the joint centreline following 75 minutes of homogenization. Hardness profiles showed Vickers hardness values comparable to the base metal regardless of the presence of Ti_2Cu.

TLPB brazing of grade two titanium and nickel showed an initial exothermic onset of 967°C and 984°C indicating the peritectic ($L+TiNi \rightarrow TiNi+Ti_2Ni$) and eutectic ($L \rightarrow TiNi+Ti_2Ni$) formation, though an entire band of Ni-rich intermetallics remained visible until 1000°C. Following complete dissolution of the nickel foil, the ASZ becomes a homogenous fine eutectic. The Ti_2Ni intermetallic shows difficulty nucleating from the liquid and was observed to undercool by as much as 100°C. Cyclical data showed complete isothermal solidification in 146 minutes.

Modelling the liquid layer at 28.41 wt% Ni, determined from 80 Kpm experimentation, yielded a predicted maximum dissolution depth of 572.7 μm. There was good agreement between liquid fraction data calculated based on a spherical cap and data from DSC measurement. The rate of IS was observed to be 2.2 times greater than copper in agreement with relative diffusion rates. Composition profiles show a eutectic composition of 32-34 wt% Ni with a maximum diffusion distance of 1500 μm on compete isothermal solidification. A two foil pre-sandwiched joint showed a large pore in the region where full dissolution occurred (Type A:Stage A). Again, predictions of the Type A joint showed agreement and the Type B joint assumption showed that liquid wet prior to reaching the braze temperature. Hardness profiles show a spike in hardness of 859 HV on Ti_2Ni in the ASZ. A single foil pre-sandwiched sample that was homogenized for 68 minutes showed a nickel composition of 4-5 wt% at the centreline.

Copper as an interlayer in Ti-6Al-4V brazing showed more Cu-rich intermetallics ($TiCu_4$, Ti_3Cu_4) on melting. Upon cooling the peritectic reaction from the binary phase diagram was observed as well as a dual peak structure of transient copper rich intermetallics. The peritectic reaction observed undercooling beyond the range of cyclic DSC testing for early liquid duration samples making it difficult to measure. A modified 10 Kpm cyclical temperature program was necessary to fully measure freezing events. These events occurred close to, or during, the β to α phase transformation such that Bezier and Sigmoidal baseline corrections became necessary (also implemented in the Ti-6Al-4V and nickel system). Microstructure agreed with DSC findings where Ti_3Cu_4 was observed in most initial, and even some cyclic, samples. Samples held for longer duration showed cyclical behavior similar to grade two titanium and isothermal solidification completed in 364 minutes.

Using a composition of 40.94 wt% Cu from 1050°C 80 Kpm samples, it was estimated that the maximum dissolution for a spherical cap was 386.4 µm. The $2W_{ISZ}$ results revealed a solute uptake similar to nickel in grade two titanium and the slowest rate of isothermal solidification. Two foil joints displayed minimal dissolution and limited porosity (only where liquid wet into Region B). Some TiCu is observable in the joint though most of the ASZ was Ti_2Cu. Again, no spike in hardness was observed for Ti_2Cu and the joint showed hardness values similar to the base metal. There was indication that the Ti-6Al-4V base metal had become enriched with oxygen due to a higher hardness value than literature. The intermetallic layer showed minimal incorporation of aluminum and vanadium. Aluminum and vanadium were commonly observed in the same ratio as the base alloy suggesting uniform dissolution.

Finally, nickel was implemented as an interlayer in Ti-6Al-4V which showed an onset at 1000°C where exothermic intermetallic formation was observed. Cooling traces showed a consistent peak at 942°C indicating the eutectic ($L \rightarrow TiNi+Ti_2Ni$) and a minor secondary peak which disappears after 100 minutes representing (β-Ti) dendrite formation. It was determined that this system behaves like the binary nickel system used with commercially pure titanium. No Ni-rich intermetallics were observed in initial microstructures and the compositions of 80 Kpm samples were similar to grade two titanium. Unlike the grade two titanium samples, there was no undercooling observed in the eutectic reaction and a cooling exotherm was always observed at the eutectic temperature. Additions of aluminum may improve the ability for the intermetallic Ti_2Ni to nucleate.

Cyclical data showed isothermal solidification would complete at 300 minutes which is comparable to copper in Ti-6Al-4V. Using the 80 Kpm composition of the ASZ (29.44 wt% Ni), a maximum dissolution depth of 565.1 µm was calculated. The $2W_{ISZ}$ curve revealed comparable levels of dissolution and solute uptake to grade two titanium. This was attributed to the large volumes of liquid generated in the system creating a larger ISZ. Composition profiles show the ASZ eutectic composition to be around 36 wt% Ni where this value drops to 32 wt% Ni when a finer eutectic is observed (i.e. Isothermal 60 min. sample). The maximum diffusion distance was 1000 µm following the completion of isothermal solidification. Two foil pre-sandwiched joints showed high dissolution but no porosity suggesting the excess liquid was enough to fill both region A and B at the braze temperature. A spike in hardness was again observed for Ti_2Ni in the ASZ in excess of 1000 HV. It was believed that Ti-6Al-4V was enriched with oxygen due to a higher hardness values than provided in literature [73].

It was found that Ti-Cu and Ti-Ni binary systems experience dissolution very differently when examining diffusion couples based on their respective phase diagrams. It was determined that Ti-Ni systems maintained intimate contact of the base metal and the liquid. This allowed for higher levels of solute uptake but lead to a slower homogenization of the liquid with the remaining Ni-rich IMC layer. Ti-Cu systems first melt between the copper foil and the Cu-rich IMC layer which forms. This in turn leads to rapid dissolution of the foil with minimal solute uptake. Above 1000°C, the Ti-rich IMC layer of TiCu and Ti_2Cu melts and there is a rapid injection of solute which lead to lower initial liquid fractions in Ti-Cu couples.

The dissolution of both systems has been documented microstrucurally. Ti-6Al-4V observed slower rates of homogenization of the liquid which continued into the braze temperature and isothermal solidification. Ti64/Ni couples were the slowest due to late interaction occurring at 1000°C between the foil and the base metal. The slower rates may be the result of lack of contact between foil and base metal due to the surface oxide layer.

Diffusivity values were calculated for titanium-copper and titanium-nickel liquids where it was found that nickel is 1.3 times faster during dissolution. Effective diffusivities were determined using a geometric mean of the solid and liquid diffusivities where titanium-copper and titanium-nickel were found to be 9.83×10^{-7} cm^2/s and 1.665×10^{-6} cm^2/s respectively. These values are important for considerations of homogenization of the ASZ prior to isothermal solidification. The ratio of the $D_{Cu}:D_{Ni}$ in the liquid is similar to those observed during solid state transport.

Knowing the times to isothermal solidification it was possible to find the diffusion coefficients of copper and nickel in Ti-6Al-4V using equations outlined in work by Tuah-Poku [21]. The coefficients were found to be 1.11×10^{-8} cm^2/s for copper and 8.07×10^{-8} cm^2/s for nickel. These values showed strong agreement with rates of isothermal solidification found from cyclical data.

Based on experimental findings, it was found that both copper and nickel are appropriate interlayers for TLPB of titanium and titanium alloys. Copper readily wets the titanium surface making it more applicable for capillary action-based joining. For use in pre-sandwich applications there is a lower amount of dissolution compared to nickel though under sized foils are recommended when brazing to prevent wetting outside the braze gap. Intermetallic formation does not significantly impact overall hardness of the joint cross section though complete isothermal solidification is recommended. At the very least, a eutectoid composition should be maintained. With an appropriate foil thickness, it is possible to completely isothermally solidify prior to reaching the braze temperature (as seen in single foil experiments) and achieve low levels of copper dispersed in the base metal with no change in hardness.

Nickel shows difficulty in nucleating Ti_2Ni in commercially pure titanium; however, this is not an issue in Ti-6Al-4V. A braze temperature lower than 1050°C could be used since the binary eutectic temperature is 942°C though the kinetics will be slower. However, to avoid Ti_2Ni formation it would need to be above 984°C. Use of a thinner foil would also be recommended as a much larger level of dissolution is observed and could lead to an excess of liquid. Nickel possesses a much higher diffusivity making it attractive due to the shorter braze times necessary to achieve complete isothermal solidification. Complete isothermal solidification is necessary to avoid deleterious Ti_2Ni intermetallics which lower the overall mechanical strength of the joint.

References

1. Shapiro, Alexander E., and Yury A. Flom. "Brazing of Titanium at Temperatures below 800°C: Review and Prospective Applications." *DVS BERICHTE* 243 (2007): 254.
2. Somi Seong, Obaid Younossi, Benjamin W. Goldsmith, *Titanium: Industrial Base, Price Trends, and Technology Initiatives.* RAND Corporation 2009.
3. Gerd Lütjering, James C. Williams, *Titanium: Second Edition.* Springer-Verlag Berlin Heidelberg 2007.
4. Veiga, C., J. P. Davim, and A. J. R. Loureiro. "Properties and Applications of Titanium Alloys: A Brief Review." *Reviews on Advanced Materials Science* 32.2 (2012): 133-148.
5. Peters, M., Kumpfert, J., Ward, C.H. and Leyens, C. "Titanium alloys for aerospace applications." *Advanced Engineering Materials* 5.6 (2003): 419-427.
6. Schauerte, Oliver. "Titanium in automotive production." Advanced Engineering Materials 5.6 (2003): 411-418.
7. Peter, William H., and Yukinori Yamamoto. "Near net shape manufacturing of new, low cost titanium powders for industry." *Oak Ridge National Laboratory*, Springfield (2013).
8. G. Humpston, David M. Jacobson, *Principles of Soldering and Brazing.* ASM International 1993.
9. Makkonen, Lasse. "Young's equation revisited." *Journal of Physics: Condensed Matter* 28.13 (2016): 135001.
10. Barozzi, G. S., and D. Angeli. "A note on capillary rise in tubes." *Energy Procedia* 45 (2014): 548-557.
11. ASM Specialty Handbook, *Brazing.* Materials Information Society 2003.
12. Sekulic, Dusan P., *Scaling of Molten Metal Brazing Phenomena: Prolegomena for Model Formulation.* Progress in Scale Modeling. Springer Netherlands, 2008. 391-402.
13. D. Sekulic, *Advances in Brazing: Science, Technology and Applications.* Woodhead Publishing 2013.
14. Amin, M. R., R. C. Gosh, and G. M. Bhuiyan. "Surface tension of liquid transition and noble metals." *Journal of Non-Crystalline Solids* 380 (2013): 42-47.

15. Onzawa, Tadao, Akio Suzumura, and Myoungwan Ko. "Structure and Mechanical Properties of CP-Ti and Ti-6Al-4V Alloy Brazed Joints With Ti-Base Amorphous Filler Metals." *Quarterly Journal of Japan Welding Society* 5.2 (1987): 21-27.

16. Wells, R. R. "Microstructural control of thin-film diffusion-brazed titanium." *Welding Journal* 55.1 (1976): 20.

17. Dunkerton, Sue. "Diffusion Bonding." *Joining Materials*, Norwegian University of Science and Technology, 2000, www.ansatt.hig.no/henningj/materialteknologi/Lettvektdesign/joining methods/joining-diffusion bonding.htm.

18. Cook, Grant O., and Carl D. Sorensen. "Overview of transient liquid phase and partial transient liquid phase bonding." *Journal of materials science* 46.16 (2011): 5305-5323.

19. MacDonald, W. D., and T. W. Eagar. "Transient liquid phase bonding." *Annual Review of Materials Science* 22.1 (1992): 23-46.

20. Zhou, Y., W. F. Gale, and T. H. North. "Modelling of transient liquid phase bonding." *International Materials Reviews* 40.5 (1995): 181-196.

21. Tuah-Poku, Isaac, M. Dollar, and T. B. Massalski. "A study of the transient liquid phase bonding process applied to a Ag/Cu/Ag sandwich joint." *Metallurgical Transactions A* 19.3 (1988): 675-686.

22. Kuntz, M. L., "Liquid Phase Bonding using Differential Scanning Calorimetry." Diss. PhD Thesis, University of Waterloo, Canada, 2006.

23. Joshi, Vydehi Arun. *Titanium Alloys: an Atlas of Structures and Fracture Features.* CRC Press, 2006.

24. Tiley, J., *et al.* "Quantification of Microstructural Features in α/β Titanium Alloys." *Materials Science and Engineering: A* 372.1 (2004): 191-198.

25. Ivasishin, O. M., *et al.* "Aging Response of Coarse and Fine-grained β Titanium Alloys." *Materials Science and Engineering: A* 405.1 (2005): 296-305.

26. Ahmed, T., and Henry J. Rack. "Phase Transformations during Cooling in α+ β Titanium Alloys." *Materials Science and Engineering: A* 243.1 (1998): 206-211.

27. Edwards, P., and M. Ramulu. "Peak temperatures during friction stir welding of Ti–6Al–4V." *Science and Technology of Welding and Joining* 15.6 (2010): 468-472.

28. H. Ahmed. "Titanium Database: Part 1." *ResearchGate*, 2005, https://www.researchgate.net/publication/316636275_Titanium_data_base_part1, (2005).

29. Lee, M.K., Kim, K.H., Lee, J.G. and Rhee, C.K. "Growth of isothermally-solidified titanium joints using a multi-component Zr–Ti–Cu–Ni–Be amorphous alloy as a brazing filler." *Materials Characterization* 80 (2013): 98-104
30. H. Baker, *ASM Handbook: Alloy Phase Diagrams. Volume 3.* ASM International (1992).
31. Okamoto, H. "Cu-Ti (copper-titanium)." *Journal of phase equilibria* 23.6 (2002): 549-550.
32. Kundu, S., Ghosh, M., Laik, A., Bhanumurthy, K., Kale, G.B. and Chatterjee, S. "Diffusion bonding of commercially pure titanium to 304 stainless steel using copper interlayer." *Materials Science and Engineering: A* 407.1-2 (2005): 154-160.
33. MacDonald, W. D., and T. W. Eagar. "Transient liquid phase bonding processes." *The Metal Science of Joining* (1992): 93-100.
34. Elrefaey, A., and W. Tillmann. "Solid state diffusion bonding of titanium to steel using a copper base alloy as interlayer." *Journal of materials processing technology* 209.5 (2009): 2746-2752.
35. Wang, T., Zhang, B., Feng, J. and Tang, Q. "Effect of a copper filler metal on the microstructure and mechanical properties of electron beam welded titanium–stainless steel joint." *Materials Characterization* 73 (2012): 104-113.
36. He, P., Zhang, J., Zhou, R. and Li, X. "Diffusion bonding technology of a titanium alloy to a stainless steel web with an Ni interlayer." Materials characterization 43.5 (1999): 287-292.
37. Hinotani, S., and Y. Ohmori. "The microstructure of diffusion-bonded Ti/Ni interface." *Transactions of the Japan institute of metals* 29.2 (1988): 116-124.
38. Kundu, S., and S. Chatterjee. "Interfacial microstructure and mechanical properties of diffusion-bonded titanium–stainless steel joints using a nickel interlayer." *Materials Science and Engineering: A* 425.1-2 (2006): 107-113.
39. Cheepu, Muralimohan, V. Muthupandi, and S. Loganathan. "Friction welding of titanium to 304 stainless steel with electroplated nickel interlayer." *Materials Science Forum*. Vol. 710. Trans Tech Publications, 2012.
40. Chatterjee, S., T. A. Abinandanan, and K. Chattopadhyay. "Microstructure development during dissimilar welding: case of laser welding of Ti with Ni involving intermetallic phase formation." *Journal of materials science* 41.3 (2006): 643-652

41. Deng, Y., Sheng, G., Wang, F., Yuan, X. and An, Q. "Microstructure evolution and mechanical properties of transient liquid phase bonded Ti–6Al–4V joint with copper interlayer." *Materials & Design* 92 (2016): 1-7.
42. Song, X.G., Cao, J., Chen, H.Y., Wang, H.Q. and Feng, J.C. "Contact reactive brazing of Ti53311S alloy using Cu foil as interlayer: interfacial microstructure and joining properties." *Materials & Design* 46 (2013): 895-901.
43. Norouzi, Ehsan, Masoud Atapour, and Morteza Shamanian. "Effect of bonding time on the joint properties of transient liquid phase bonding between Ti--6Al--4V and AISI 304." *Journal of Alloys and Compounds* 701 (2017): 335-341.
44. Kundu, S., Thirunavukarasu, G., Chatterjee, S. and Mishra, B. "Effect of bonding temperature on phase transformation of diffusion-bonded joints of duplex stainless steel and Ti-6Al-4V using nickel and copper as composite intermediate metals." *Metallurgical and Materials Transactions A* 46.12 (2015): 5756-5771.
45. Özdemir, N., and B. Bilgin. "Interfacial properties of diffusion bonded Ti-6Al-4V to AISI 304 stainless steel by inserting a Cu interlayer." *The International Journal of Advanced Manufacturing Technology* 41.5-6 (2009): 519-526.
46. Eroglu, M., T. I. Khan, and N. Orhan. "Diffusion bonding between Ti-6Al-4V alloy and microduplex stainless steel with copper interlayer." *Materials science and technology* 18.1 (2002): 68-72.
47. Zakipour, S., Halvaee, A., Amadeh, A.A., Samavatian, M. and Khodabandeh, A. "An investigation on microstructure evolution and mechanical properties during transient liquid phase bonding of stainless steel 316L to Ti–6Al–4V." *Journal of Alloys and Compounds* 626 (2015): 269-276.
48. Li, J. H., and R. Y. Lin. "Active joining of Ti–6Al–4V with electroplated Cu thin film." *Materials Science and Engineering: A* 381.1-2 (2004): 39-50.
49. Kundu, S., S. Sam, and S. Chatterjee. "Interfacial reactions and strength properties in dissimilar titanium alloy/Ni alloy/microduplex stainless steel diffusion bonded joints." *Materials Science and Engineering: A* 560 (2013): 288-295.
50. Atieh, Anas M., and Tahir I. Khan. "Transient liquid phase (TLP) brazing of Mg–AZ31 and Ti–6Al–4V using Ni and Cu sandwich foils." *Science and Technology of Welding and Joining* 19.4 (2014): 333-342.

51. Yan, J.C., Zhao, D.S., Wang, C.W., Wang, L.Y., Wang, Y. and Yang, S.Q. "Vacuum hot roll bonding of titanium alloy and stainless steel using nickel interlayer." *Materials Science and Technology* 25.7 (2009): 914-918.
52. Neumann, G. and Tuijn, C., *Self Diffusion and Impurity Diffusion in Pure Metals: Handbook of Experimental Data.* Pergamon, London, 2008.
53. Bastin, G. F., and G. D. Rieck. "Diffusion in the titanium-nickel system: I. occurrence and growth of the various intermetallic compounds." *Metallurgical Transactions* 5.8 (1974): 1817-1826.
54. Gupta, K. P. "The Hf-Ni-Ti (hafnium-nickel-titanium) system." *Journal of phase equilibria* 22.1 (2001): 69-72.
55. Cluff, D., "NiTi: An In-Situ Investigation of Sintering from Elemental Powders." Diss. PhD Thesis, Dalhousie University, Canada, 2016.
56. Murray, J. L. "The Cu− Ti (copper-titanium) system." *Bulletin of alloy phase diagrams* 4.1 (1983): 81-95.
57. Höhne, G., Hemminger, W., Flammersheim, H., *Differential Scanning Calorimetry: 2nd Edition.* Springer-Veriag Berlin Heidelberg 2003.
58. Tadgell, C., "Investigation of Plating Process Variability and Mechanism for Oxide Disruption in a Ni-Modified Fluxless Brazing Process for Aluminum Alloys." MS thesis. University of Waterloo, Canada, 2015.
59. Boettinger, W., Kattner, U., Moon, K., Perepezko, J., *DTA and Heat-flux DSC Measurements of Alloy Melting and Freezing.* National Institute of Standards and Technology, 2006.
60. Turriff, D. M., S. F. Corbin, and M. Kozdras. "Diffusional solidification phenomena in clad aluminum automotive braze sheet." *Acta Materialia* 58.4 (2010): 1332-1341.
61. E.D. Moreau, S. F. Corbin. "Predicting Maximum Brazing Clearance During Transient Liquid Phase Bonding of Ni-based Superalloys via Differential Scanning Calorimetry", *Metallurgical and Materials Transactions A* (2019) Pending.
62. Wanbing, G., Yulai, G., Qijie, Z. and Kuangdi, X. "DSC study on the undercooling of droplet solidification of metal melt." *Chinese Science Bulletin* 50.9 (2005): 929.
63. Mueller, B. A., and J. H. Perepezko. "The undercooling of aluminum." *Metallurgical Transactions A* 18.6 (1991): 1143-1150.

64. ASTM International. *B265-15 Standard Specification for Titanium and Titanium Alloy Strip, Sheet, and Plate.* West Conshohocken, PA, 2015. Web. 23 Sep 2019

65. Nicholas, M. G., T. M. Valentine, and M. J. Waite. "The wetting of alumina by copper alloyed with titanium and other elements." *Journal of Materials Science* 15.9 (1980): 2197-2206

66. Goldstein, Joseph, *et al.*, *Scanning Electron Microscopy and X-Ray Microanalysis.* Springer, 2018.

67. Porter, D., Easterling, K., *Phase Transformations in Metals and Alloys.* CRC Press, 2004.

68. Corbin, S. F., and P. Lucier. "Thermal Analysis of Isothermal Solidification Kinetics during Transient Liquid-Phase Sintering." *Metallurgical and Materials Transactions A* 32.4 (2001): 971-978.

69. Murray, D. C., and S. F. Corbin. "Determining the kinetics of transient liquid phase bonding (TLPB) of Inconel 625/BNi-2 couples using differential scanning calorimetry." *Journal of Materials Processing Technology* 248 (2017): 92-102.

70. Turchanin, M.A., Agraval, P.G., Fesenko, A.N. and Abdulov, A.R. "Thermodynamics of liquid alloys and metastable phase transformations in the copper-titanium system." *Powder Metallurgy and Metal Ceramics* 44.5-6 (2005): 259-270.

71. Nicholas, M. G., T. M. Valentine, and M. J. Waite. "The wetting of alumina by copper alloyed with titanium and other elements." *Journal of Materials Science* 15.9 (1980): 2197-2206.

72. Whitney, M., S. F. Corbin, and R. B. Gorbet. "Investigation of the mechanisms of reactive sintering and combustion synthesis of NiTi using differential scanning calorimetry and microstructural analysis." *Acta Materialia* 56.3 (2008): 559-570.

73. Oh, J.M., Lee, B.G., Cho, S.W., Lee, S.W., Choi, G.S. and Lim, J.W. "Oxygen effects on the mechanical properties and lattice strain of Ti and Ti-6Al-4V." *Metals and Materials International* 17.5 (2011): 733-736.

74. Povoden-Karadeniz, E., Cirstea, D.C., Lang, P., Wojcik, T. and Kozeschnik, E. "Thermodynamics of Ti–Ni shape memory alloys." *Calphad* 41 (2013): 128-139.

75. Uvarov, A.A., Semenov, A.N., Krestnikov, N.S., Lyushinskii, A.V. and Nikitina, E.V. "A Study of the Structure of Steel–Titanium Joints Formed by Diffusion Welding with the Use of Ultrafine Nickel Powder." *Metal Science and Heat Treatment* 59.7-8 (2017): 529-533.

76. Kundu, S., Chatterjee, S., Olson, D. and Mishra, B. "Effects of intermetallic phases on the bond strength of diffusion-bonded joints between titanium and 304 stainless steel using nickel interlayer." *Metallurgical and materials transactions* A 38.9 (2007): 2053-2060.
77. Zou, L., Guo, C., Li, C. and Du, Z. "Experimental investigation and thermodynamic modeling of the Ni–Ti–V system." *Calphad* 64 (2019): 97-114.
78. Senkevich, K.S., Knyazev, M.I., Runova, Y.E. and Shlyapin, S.D. "Special features of formation of a TiNi–VT6 diffusion joint." *Metal Science and Heat Treatment* 55.7-8 (2013): 419-422.
79. Xu, H.B., Meng, L.J., Xu, J., Li, Y. and Zhao, X.Q. "Mechanical properties and oxidation characteristics of TiNiAl (Nb) intermetallics." *Intermetallics* 15.5-6 (2007): 778-782.
80. Rosa, Casimir J. "Oxygen diffusion in alpha and beta titanium in the temperature range of 932 to 1142 C." *Metallurgical Transactions* 1.9 (1970): 2517-2522.
81. Malinov, S., W. Sha, and C. S. Voon. "In situ high temperature microscopy study of the surface oxidation and phase transformations in titanium alloys." *Journal of microscopy* 207.3 (2002): 163-168.
82. Gaskell, David R., and David E. Laughlin. *Introduction to the Thermodynamics of Materials*. 4th ed., CRC Press, Taylor & Francis Group, 2009.
83. Meyer, Andreas. "The measurement of self-diffusion coefficients in liquid metals with quasielastic neutron scattering." *EPJ Web of Conferences*. Vol. 83. EDP Sciences, 2015.
84. Semiatin, S.L., Brown, T.M., Goff, T.A., Fagin, P.N., Turner, R.E., Murry, J.M., Barker, D.R., Miller, J.D. and Zhang, F. “Diffusion Coefficients for Modeling the Heat Treatment of Ti-6Al-4V.” *Metallurgical and Materials Transactions A*, vol. 35, no. 9, 2004, pp. 3015–3018.
85. Raghavan, V. "Al− Cu− Ti (Aluminum-Copper-Titanium)." *Journal of Phase Equilibria and Diffusion* 27.2 (2006): 156-157.
86. Nash, P. G., V. Vejins, and W. W. Liang. "The Al− Ni− Ti (Aluminum−Nickel−Titanium) system." *Journal of Phase Equilibria* 3.3 (1982): 367-374.

Appendix A

Appendix A – Ti-Cu-Al and Ti-Ni-Al Ternary Phase Diagrams

Ternary diagrams were investigated to characterize Ti-Cu and Ti-Ni microstructures in grade five titanium with the additions of aluminum and vanadium. With aluminum being the more prevalent addition, the ternary phase diagrams examined were Ti-Cu-Al and Ti-Ni-Al. The only copper phase diagram found was an isothermal section at 850°C which is shown in Figure 11.1.

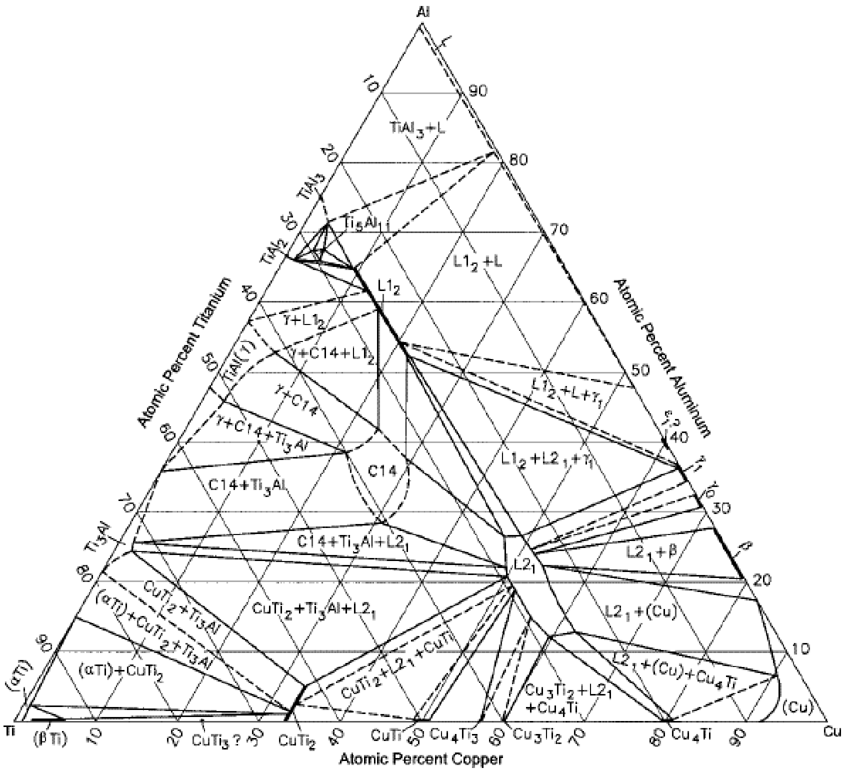

Figure 0.1 - Al-Cu-Ti Isothermal Section at 850°C [85]

For the formation of ternary intermetallics, at least 12 at% Al is needed to create $L2_1$ ($TiCu_2Al$). In addition, the phase is much more copper rich than what was observed in microstructure. The presence of Ti_3Al was never observed in the examination of copper and Ti-6Al-4V.

Figure 11.2 shows the liquidus projection for Ti-Ni-Al. Additions of 8-10 at% aluminum are required to generate H phase (TiNi2Al). This phase was not observed in any nickel and Ti-6Al-4V microstructure. Also, it is worth noting the increased solubility of beta titanium with increasing additions of aluminum, as well as the changing composition range of Ti2Ni.

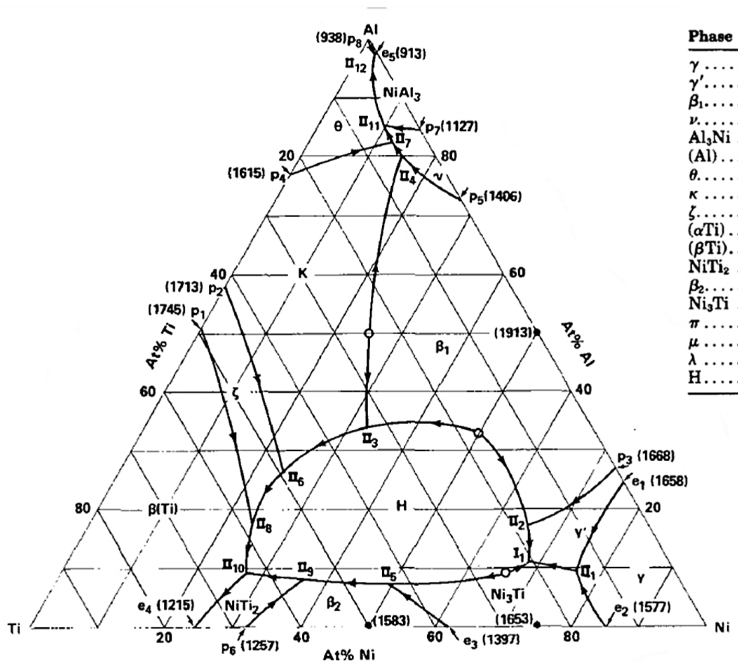

Phase	Description or alternate phase designation	Prototype	Pearson symbol
γ	Ni terminal solid solution	Cu	*cF*4
γ'..........	$AlNi_3$	$AuCu_3$	*cP*4
β_1..........	AlNi	CsCl	*cP*2
ν..........	Al_3Ni_2	Al_3Ni_2	*hP*5
Al_3Ni	Al_3Ni	Al_3Ni	*oP*16
(Al)........	Al terminal solid solution	Cu	*cF*4
θ..........	Al_3Ti	Al_3Ti	*tI*8
κ	AlTi	AuCu	*tP*4
ζ..........	$AlTi_3$	Ni_3Sn	*hP*8
(αTi).......	Ti terminal solid solution	Mg	*hP*2
(βTi).......	Ti terminal solid solution	W	*cI*2
$NiTi_2$	$NiTi_2$	CFe_3W_3	*cF*112
β_2..........	NiTi	CsCl	*cP*2
Ni_3Ti	Ni_3Ti	Ni_3Ti	*hP*16
π	$Al_{6.5}NiTi_{2.5}$	$AuCu_3$	*cP*4
μ	Al_2NiTi	(fcc)	...
λ	AlNiTi	$MgZn_2$	*hP*12
H..........	$AlNi_2Ti$	$AlCu_2Mn$	*cF*16

Figure 0.2 - Liquidus Projection of Ti-Ni-Al [86]